



SAPIENZA  
UNIVERSITÀ DI ROMA

## Indirect search for Dark Matter towards the Galactic Centre with the ANTARES submarine Cherenkov neutrino telescope

Scuola Dottorale in Scienze Astronomiche, Chimiche,  
Fisiche, Matematiche e della Terra "Vito Volterra"

Dottorato di Ricerca in Astronomia – XXV Ciclo

Candidate

Dr. Paolo Fermani  
ID number 698643

Thesis Advisors

Prof. Antonio Capone

Co-Advisor

Dr. Giulia De Bonis

Ph.D. coordinator

Prof. Roberto Capuzzo Dolcetta

A thesis submitted in partial fulfillment of the requirements  
for the degree of Doctor of Philosophy in Astronomy

1 December 2012

Thesis defended on 21 January 2013  
in front of a Board of Examiners composed by:

Prof. F. Ricci (chairman)

Prof. S. Capozziello

Prof. F. La Franca

Dr. O. Straniero

Dr. M. Castellani

---

**Indirect search for Dark Matter towards the Galactic Centre with the ANTARES  
submarine Cherenkov neutrino telescope**

Ph.D. thesis. Sapienza – University of Rome

© 2013 Dr. Paolo Fermani. All rights reserved

This thesis has been typeset by L<sup>A</sup>T<sub>E</sub>X and the Sapthesis class.

Version: 20 January 2013

Author's email: [paolo.fermani@roma1.infn.it](mailto:paolo.fermani@roma1.infn.it)

## Abstract

The aim of this thesis work is to search for neutrinos arising from Dark Matter particles annihilation in the Galactic Centre. To detect these neutrinos we used a large neutrino telescope: ANTARES.

In recent years several evidences (rotational velocity of stars in galaxies, existence of galaxy clusters, the evolution of cosmic structures, the famous example of the bullet cluster etc.) show the presence of an unknown invisible form of matter in our Universe (chapter 1), called Dark Matter. Since no standard model particles can satisfy the requirements for Dark Matter candidates (massive, stable and only gravitationally and weakly interacting), the most common hypothesis arises from the minimal supersymmetry extension of the standard model. In this theory the Dark Matter candidate is the lightest neutralino, identified with the WIMP (Weak Interacting Massive Particle) (chapter 2). WIMPs present into the galactic halo can self-annihilate as Majorana particles producing some standard model secondary particles like bosons and quarks that eventually decay producing neutrinos. These neutrinos carry on an energy that is of the order of one third of the energy of the original WIMP (thus for an example WIMP mass of  $100 \text{ GeV}$  the resulting neutrino has an energy of  $\approx 30 \text{ GeV}$ ), they travel free in space and can be detected here, on Earth, by large neutrino telescopes like ANTARES.

We are searching for neutrinos of astrophysical origin, but we have to distinguish them in the much bigger amount of background particles: atmospheric muons and neutrinos produced in the interaction of cosmic rays in the Earth atmosphere. Since neutrinos have also a small cross-section we need detectors with large instrumented volumes. ANTARES is a deep-sea Cherenkov based detector located in the Mediterranean sea near the south coast of France at roughly  $2400 \text{ m}$  depth (chapter 3). It is composed by twelve strings of photomultiplier tubes (PMT) that can detect the Cherenkov light induced by charged particles generated in neutrino interactions with the matter near the apparatus. ANTARES can detect all the three neutrino flavours, but the main task of the detector is to reveal muon neutrinos. These neutrinos interacting with the matter around the apparatus produce muons that can travel along large distances and can be seen by the PMTs of the instrumented detector volume. To minimise the background we search for up-going events (coming from below the detector horizon, so mainly from the southern hemisphere, that interact with the Earth in the vicinity of the bottom of the apparatus producing muons) for which the Earth acts like a shield against the atmospheric muons.

In this analysis we use the data collected by the apparatus in the period 2007-2010 (chapter 4). To take into account the detector and environmental status we determine a data quality assessment to select only data taken in good conditions. In the considered time interval we have a lifetime of  $\approx 588$  days of active detector in a good environmental conditions. We examine the data set and the Monte Carlo simulations of background and expected signal. The Monte Carlo (MC) simulations allow us to describe all possible physical background that mimic the signal (muon neutrinos from the direction of the Galactic Centre): atmospheric muons and neutrinos are the main background. The MC simulations are used also to represent the response of the detector to signal and background events: raw and

simulated data are then reconstructed with the same software (BBFit reconstruction algorithm). Muon neutrinos from point-like sources, or by WIMP annihilations, are expected to be very rare signals. So we impose tight cuts to select a sample of data with enriched signal: this is the most important part in the analysis. To build a valid MC of the signal arising from the Dark Matter annihilation into the Galactic Centre we use the `WIMPSIM` package. We choose to constrain three different annihilation channels ( $\chi\chi \rightarrow b\bar{b}, \tau^+\tau^-, W^+W^-$ ) with ten different WIMP masses, ranging from 50 *GeV* to 1 *TeV*, for a total of 29 Dark Matter models.

The search for muon neutrinos from Dark Matter in the Galactic Centre is a search for a point like source, therefore we decide to follow a "binned" search strategy. It means we search for signal events in cones of fixed angular apertures around the Galactic Centre direction. Indeed the only way to detect a neutrino signal from the Galactic Centre is to see a statistical excess of events over the underlying background. We search for the cuts optimization on the set of the parameters representing the track quality reconstruction and the angular bin cone aperture. To evaluate the statistical significance of the result, we use the Feldman and Cousins method (appendix A), evaluating the Model Rejection Factor (MRF) for each Dark Matter model chosen. With the best cuts we are able to minimise the MRF and, at the end, find the sensitivity of the ANTARES detector to all the selected Dark Matter models.

As an appendix, we describe the service task we have done in parallel for the ANTARES collaboration (appendix B). It consists of a calibration work concerning the charge calibration of the detector PMTs. Each PMT has two circuits, called ARS, that receive the analogue signal of the Cherenkov photons. The signal charge is measured together with its time of arrival. These signals are then digitised and sent to the shore. The ARSs undergo a cross-talk problem between the sections that measure time and charge. Our purpose is to study this effect and try to establish a universal correction to apply in all the data sets.

# Contents

<b>Introduzione</b>	<b>VII</b>
<b>1 The standard model of cosmology and Dark Matter</b>	<b>1</b>
1.1 Standard model of the Universe: first principles . . . . .	1
1.1.1 The cosmological principle . . . . .	1
1.1.2 The Universe is expanding . . . . .	2
1.2 The metric of the Universe . . . . .	3
1.3 The basis of the theory of the Universe . . . . .	4
1.3.1 The ruling equations of the Universe . . . . .	5
1.3.2 The components of the Universe . . . . .	6
1.3.3 The cosmological parameters . . . . .	7
1.4 Brief summary of the history of the Universe . . . . .	8
1.5 Dark Matter . . . . .	13
1.5.1 Dark matter properties and types . . . . .	14
1.5.2 Observational evidences . . . . .	15
1.5.3 The Galactic Centre . . . . .	17
1.6 The WIMP scenario . . . . .	18
1.6.1 The WIMPs relic . . . . .	18
1.7 WIMPs detection . . . . .	20
1.7.1 Neutrino from WIMP annihilation in celestial bodies . . . . .	20
1.7.2 Direct detection . . . . .	22
1.7.3 Indirect detection . . . . .	23
<b>2 The super-symmetry theory and dark matter</b>	<b>25</b>
2.1 Introduction to Supersymmetry . . . . .	25
2.2 The Minimal Supersymmetric Standard Model . . . . .	27
2.3 The lightest super-symmetric particle . . . . .	29
2.3.1 SUSY WIMP candidates . . . . .	29
2.3.2 The SUSY broken symmetry . . . . .	29
2.3.3 The lightest neutralino . . . . .	30
2.3.4 The minimal supergravity model . . . . .	31
<b>3 The ANTARES neutrino telescope</b>	<b>33</b>
3.0.5 Neutrino astronomy . . . . .	33
3.1 Detection principle . . . . .	35
3.2 Neutrino interactions . . . . .	36

3.2.1	Low energy interactions . . . . .	37
3.2.2	High energy interactions . . . . .	37
3.2.3	Different types of neutrino interactions in ANTARES . . . . .	38
3.3	The Cherenkov effect . . . . .	39
3.4	Light propagation in sea water . . . . .	40
3.5	Track reconstruction technique . . . . .	41
3.6	The detector response . . . . .	42
3.6.1	Angular response for $\nu_\mu$ interactions . . . . .	43
3.6.2	The detector energy response for $\nu_\mu$ interactions . . . . .	44
3.7	The detector design . . . . .	45
3.8	Detector general overview . . . . .	46
3.9	The detector string . . . . .	48
3.10	The optical module . . . . .	49
3.10.1	PMT characteristics . . . . .	50
3.11	Offshore electronics . . . . .	51
3.11.1	The front-end electronics . . . . .	52
3.11.2	Trigger logic . . . . .	52
3.12	Slow control . . . . .	53
3.13	Calibration . . . . .	53
3.14	Positioning . . . . .	54
3.15	Bioluminescence and K40 . . . . .	55
3.16	ANTARES observational characteristics . . . . .	56
3.16.1	Observable sky . . . . .	56
3.16.2	Effective area . . . . .	57
3.17	The current ANTARES detector . . . . .	57
<b>4</b>	<b>Analysis of the 2007-2010 data</b> . . . . .	<b>59</b>
4.0.1	Definition of "run" . . . . .	61
4.0.2	DATA and DATA scrambled . . . . .	61
4.1	The coordinate convention system . . . . .	62
4.2	Data . . . . .	65
4.2.1	Configuration of the detector . . . . .	66
4.2.2	Types of runs . . . . .	67
4.3	Data Quality selection of runs . . . . .	67
4.3.1	The detector lifetime of the data sample . . . . .	69
4.4	Construction of the detector simulation . . . . .	71
4.5	The background Monte Carlo . . . . .	72
4.5.1	Standard and low energy Monte Carlo . . . . .	72
4.5.2	Monte Carlo and Data Quality selection . . . . .	73
4.6	The reconstruction algorithm . . . . .	74
4.6.1	The choice of the reconstruction algorithm . . . . .	77
4.7	The event selection . . . . .	79
4.7.1	Basic cuts and efficiency . . . . .	79
4.8	Weights policy for MC background events . . . . .	81
4.8.1	The standard formalism for weights . . . . .	81
4.8.2	How to use the weights . . . . .	83
4.9	Data - Monte Carlo comparison . . . . .	84

---

4.9.1	Angular resolution . . . . .	89
4.9.2	The effective area . . . . .	90
4.10	Monte Carlo simulation of $\nu_\mu$ from Dark Matter . . . . .	90
4.10.1	The WIMPSIM package . . . . .	91
4.10.2	The annihilation spectra . . . . .	92
4.11	Weights policy for MC signal events . . . . .	93
4.11.1	The weight w2 in the v1r2p5 version of AntDST . . . . .	93
4.11.2	The signal weight convolution . . . . .	96
4.12	The selection of signal events . . . . .	97
4.12.1	Selection of $\nu$ candidates: the acceptance region . . . . .	97
4.12.2	Selection of $\nu$ candidates: the cut $t\chi^2 < b\chi^2$ . . . . .	98
4.13	The binned analysis . . . . .	100
4.14	The statistical analysis of 2007-2010 data . . . . .	104
4.14.1	The Model Rejection Factor . . . . .	105
4.14.2	The cuts to optimize . . . . .	106
4.15	Final results and conclusions . . . . .	108
<b>Conclusioni</b>		<b>113</b>
<b>A The Feldman and Cousins statistical approach</b>		<b>115</b>
A.1	Bayesian interval construction . . . . .	115
A.2	Classical Neyman's interval construction . . . . .	116
A.3	Poisson process with background and Feldman and Cousins ordering principle . . . . .	117
A.3.1	Our Feldman and Cousins construction of intervals . . . . .	118
<b>B The Cross-Talk effect in ANTARES ARS</b>		<b>123</b>
B.1	Structure and description of an ARS . . . . .	123
B.1.1	TVC . . . . .	125
B.1.2	AVC . . . . .	126
B.2	The cross-talk effect between the measures of time and charge . . . . .	127
B.3	The study of the time evolution of the cross-talk parameters . . . . .	129
B.3.1	The first part of the analysis . . . . .	130
B.3.2	The second part of the analysis . . . . .	133
<b>Bibliography</b>		<b>152</b>



# Introduzione

Lo scopo di questa tesi è la ricerca di neutrini provenienti dall'annichilazione di materia oscura nel centro galattico.

Nella nostra ricerca usiamo i neutrini come portatori di informazioni astronomiche. Potrebbe suscitare curiosità il motivo che ci spinge ad usare i neutrini (pochi e difficili da rivelare) invece dei più abbondanti fotoni. Certo i fotoni sono abbondanti e facilmente rilevabili, ma se vogliamo studiare le regioni più dense e calde del cosmo, motori di molte sorgenti astrofisiche, queste risultano opache ai fotoni e quindi non indagabili direttamente. Inoltre i fotoni possono subire anche l'effetto della radiazione cosmica di fondo (CMB) producendo, nell'interazione, coppie elettrone-positrone. Anche i protoni, se decidiamo di usarli per fare astronomia, risentono dell'interazione con la CMB. Oltretutto i protoni, essendo particelle cariche, vengono deviati dalla presenza dei campi magnetici (per energie  $< 10^{19}$  eV) perdendo l'informazione della sorgente originaria. I neutrini possono invece rivelarsi una buona scelta per condurre indagini astronomiche. Infatti essi sono debolmente interagenti, quindi penetrano le regioni opache ai fotoni; sono elettricamente neutri, non subiscono dunque l'influenza di campi magnetici; infine sono stabili e possono viaggiare per lunghe distanze inalterati. Come vedremo, essi costituiscono un valido oggetto d'indagine per la ricerca di annichilazione di particelle di materia oscura in oggetti astrofisici.

Negli ultimi decenni, numerose osservazioni di oggetti astrofisici di diverso tipo hanno portato all'ipotesi dell'esistenza di una forma di materia invisibile, perciò detta oscura, ma preponderante nel bilancio totale della materia presente nell'Universo (capitolo 1).

Le più note evidenze osservative della presenza di una forma di materia non bariónica nell'Universo sono: la curva di velocità rotazionale nelle galassie a spirale, curva che rimane costante ( $v_r \sim \text{cost}$ ) anche a grandi distanze  $r$  dal centro delle galassie, contrariamente all'andamento aspettato ( $1/\sqrt{r}$ ); l'esistenza stessa degli ammassi di galassie che, date le altissime velocità del gas intra ammasso ( $\sim O(1000 \text{ km/s})$ ), dovrebbero invece disgregarsi; la ormai celebre analisi dello scontro del "bullet cluster" con un altro ammasso, in cui le buche di potenziale tracciano la materia visibile (stelle) e non il gas caldo visibile nell'X che dovrebbe rappresentare la parte maggiore della materia di un ammasso; ed ultimo, la presenza stessa di strutture cosmiche nel nostro Universo, inspiegabile senza l'ipotesi di una forma di materia nuova che, disaccoppiandosi prima della materia ordinaria dall'Universo primordiale, avvia la formazione di aloni di materia oscura in cui poi andranno a cadere le particelle della materia ordinaria (barionica) che formano le strutture che oggi vediamo intorno a noi nell'Universo.

Posta l'evidenza di questa forma di materia oscura dobbiamo constatare che

non esiste nel modello standard alcuna particella che soddisfi le caratteristiche che dovrebbe avere tale forma di materia: elettricamente neutra, stabile e che interagisca solo per interazioni debole e gravitazionale. Per questo si ricorre a modelli che prevedano espansioni del modello standard delle particelle elementari.

Il modello usato più comunemente è quello della espansione supersimmetrica (SUSY) del modello standard (capitolo 2). In particolare nel modello supersimmetrico minimale (MSSM) le particelle di materia oscura vengono identificate con i neutralini più leggeri  $\chi$ . Queste particelle, che hanno le proprietà di particelle Majorana (quindi anti particelle di se stesse), vengono anche chiamate WIMP (Weak Interacting Massive Particles).

I WIMP dell'alone di materia oscura della galassia si accumulano nel centro incrementando la densità di materia oscura nel Centro Galattico; oppure possono essere attratti gravitazionalmente da oggetti massivi come le stelle (come il Sole) o i pianeti. In questi ultimi casi, per mezzo di successive collisioni elastiche, i WIMP vengono attratti nel centro di questi oggetti; qui si annichiliscono formando varie particelle secondarie (bosoni, quark, leptoni). La maggior parte di queste viene subito riassorbita, ma alcuni danno origine, decadendo, a neutrini che possono essere rivelati sulla Terra. Considerando i vari canali, la massa del neutrino risultante può andare da circa  $1/3$  a circa  $1/2$  della massa del WIMP. Considerando che i vari modelli supersimmetrici prevedono la massa del WIMP nell'intervallo  $100 \text{ GeV} - 1 \text{ TeV}$ , i neutrini risultanti hanno energie ben diverse da quelle tipiche dei neutrini solari (pochi  $\text{MeV}$ ) e possono essere rivelati qui, sulla Terra, per mezzo di telescopi per neutrini. Dati i piccoli flussi aspettati e la piccolissima sezione d'urto dei neutrini ( $\sigma_\nu \approx 10^{-38} \cdot E[\text{GeV}]$ ) necessitiamo di grandi volumi instrumentati per la rivelazione. Solitamente si usa la tecnica di rivelazione di luce Cherenkov, quindi un'altra necessità è disporre di un grande mezzo che sia trasparente: acqua e ghiaccio sono mezzi ottimali.

Nella nostra analisi utilizziamo i dati raccolti dall'esperimento ANTARES. ANTARES è un telescopio sottomarino per neutrini basato sulla tecnica Cherenkov (capitolo 3). Esso è composto da dodici stringhe, di  $350 \text{ m}$  di altezza, instrumentate con fotomoltiplicatori (PMT). Le stringhe sono ancorate al fondo marino a circa  $2400 \text{ m}$  di profondità al largo della costa mediterranea francese. I neutrini che interagiscono in corrente carica con la materia nei dintorni dell'apparato producono nell'interazione leptoni carichi che, attraversando il detector, possono essere rivelati per mezzo della luce Cherenkov che essi inducono. In questo modo è possibile ricostruirne la direzione di provenienza e l'energia. La rivelazione di neutrini muonici, che producono muoni nell'interazione con la materia, è l'obiettivo principale per cui è stato costruito l'apparato, anche se esso può rivelare anche gli altri sapori di neutrino.

Il problema principale è identificare gli eventi di segnale e distinguerli da quelli, molto più numerosi, di fondo. I tipi di fondo riscontrabili nell'esperimento ANTARES sono due: i muoni atmosferici ed i neutrini atmosferici prodotti nell'interazione dei raggi cosmici con l'atmosfera terrestre. Per minimizzare il fondo cerchiamo i cosiddetti eventi up-going cioè provenienti da sotto l'orizzonte del rivelatore (principalmente dall'emisfero sud). In questo modo la Terra agisce come uno scudo che elimina il fondo di muoni atmosferici dal basso ma non quello dei neutrini atmosferici che, interagendo con la materia sul fondo dell'apparato, producono muoni che vengono

rivelati dal detector. Bisogna però considerare che i neutrini atmosferici di fondo sono distribuiti isotropicamente mentre gli eventuali neutrini di segnale provengono da una ben precisa direzione. Quindi osservare un eccesso statistico di eventi di neutrino in una data direzione può costituire una evidenza di segnale. Le tracce di eventi provenienti dall'alto (muoni e neutrini astrofisici) vengono scartate in sede di analisi dati considerando anche che ANTARES è ottimizzato per la rivelazione di eventi dal basso. In aggiunta alle tracce di fondo occorre considerare anche la bioluminescenza naturale marina e il decadimento del potassio presente nel mare. Questo rumore ottico è minimizzato considerevolmente con l'ausilio di sofisticati sistemi di trigger studiati per l'apparato.

In questa analisi usiamo i dati raccolti dall'esperimento ANTARES nel periodo di presa dati 2007-2010 (capitolo 4). Per scartare i dati acquisiti in periodi con un ambiente marino in cattive condizioni e per selezionare solo dati presi con un apparato attivo e perfettamente funzionante si stabiliscono dei criteri di qualità da applicare alla totalità dei dati considerati. Nell'intervallo di tempo suddetto, dopo i tagli di qualità, il tempo attivo di presa dati risulta pari a circa 588 giorni di osservazione.

Nell'analisi abbiamo esaminato il set di dati e le corrispondenti simulazioni Monte Carlo (MC) del fondo e del segnale. Le simulazioni MC ci aiutano a descrivere tutte le forme di fondo fisico (muoni e neutrini atmosferici) che contaminano la rivelazione del segnale (costituito da neutrini muonici provenienti dall'annichilazione di materia oscura nel Centro Galattico). Le simulazioni MC vengono anche usate per rappresentare la risposta del rivelatore agli eventi di segnale e di fondo. Sia gli eventi di fondo simulati col MC sia i dati grezzi vengono ricostruiti tramite un programma di ricostruzione di eventi chiamato BBFit.

Neutrini muonici da sorgenti puntiformi, o da annichilazione di WIMPs, sono segnali molto rari. Dunque, imponiamo dei tagli stringenti, su determinati parametri fisici, per selezionare un campione di dati arricchito in segnale. Quest'ultima è la parte più importante dell'analisi.

Per costruire una realistica simulazione MC di segnale da annichilazione di materia oscura nel Centro Galattico usiamo il pacchetto WIMPSIM. In particolare abbiamo scelto di porre dei limiti sulla sensibilità dell'apparato per tre diversi canali di annichilazione dei WIMP ( $\chi\chi \rightarrow b\bar{b}, \tau^+\tau^-, W^+W^-$ ) e per dieci masse diverse da 50 GeV a 1 TeV per un totale di 29 modelli differenti di materia oscura.

La ricerca di neutrini da annichilazione di materia oscura nel Centro Galattico è una ricerca di sorgente puntiforme. Portiamo quindi avanti una ricerca detta "binned": cerchiamo eventi di segnale in coni angolari di apertura fissata centrati in direzione del Centro Galattico.

Come abbiamo detto, l'unico modo di rivelare un segnale di neutrini dal Centro Galattico consiste nel riscontrare un eccesso statistico di eventi sopra il sottostante fondo. L'ultimo passaggio dell'analisi dei dati 2007-2010 corrisponde alla ottimizzazione del set dei due parametri rappresentanti la qualità della ricostruzione della traccia di muone e la semiapertura del cono angolare centrato nel Centro Galattico. Per calcolare la significatività statistica del risultato usiamo l'approccio di Feldman e Cousins (appendice A) applicando il metodo dell'MRF (Model Rejection Factor) per ogni modello di materia oscura preso in considerazione. Con i valori dei tagli ottimizzati possiamo infine minimizzare l'MRF e valutare la sensibilità dell'esperimento

ANTARES alla rivelazione di flussi di neutrini provenienti dall'annichilazione di particelle di materia oscura nel Centro Galattico.

In appendice abbiamo descritto il lavoro di calibrazione svolto all'interno della collaborazione ANTARES (appendice B) parallelamente a quello di analisi di fisica. Questo lavoro concerne la calibrazione di circuiti, presenti in ogni PMT, che permettono di acquisire il segnale analogico dato dai fotoni Cherenkov e convertirlo in segnale digitale per poi spedirlo a terra per l'analisi. Questi circuiti, chiamati ARS, misurano anche la carica dei segnali ed i loro tempi d'arrivo sul fototubo. Gli ARS presentano un problema di "cross-talk" (diafonia) tra la parte del circuito che misura la carica e quella che misura il tempo. Lo scopo di questa nostra attività di calibrazione è cercare di studiare questo effetto e trovare una correzione universale, stabile nel tempo, da poter applicare a tutti i dati acquisiti dal rivelatore.

Ora descriviamo concisamente l'argomento di ciascun capitolo di cui si compone questa tesi.

Nel primo capitolo descriviamo in linea generale il modello standard dell'Universo. Partiamo dall'enunciazione del principio cosmologico e dalla constatazione dell'espansione dell'Universo (paragrafo 1.1). Descriviamo quindi la metrica che si usa per un universo omogeneo ed isotropo (paragrafo 1.2). Passiamo poi alla rassegna delle principali componenti in energia dell'Universo e alle equazioni che ne regolano l'espansione (paragrafo 1.3). Raccontiamo poi una storia sommaria della sua evoluzione dai tempi subito dopo l'istante iniziale ad oggi (paragrafo 1.4). Nella seconda parte del capitolo introduciamo le evidenze che permettono di ipotizzare la presenza di materia oscura come componente principale costituente la materia nell'Universo (paragrafo 1.5). Da ultimo introduciamo i WIMPs (paragrafo 1.6) e i metodi per una loro rivelazione (paragrafo 1.7).

Nel secondo capitolo introduciamo la teoria supersimmetrica di espansione del modello standard delle particelle elementari (paragrafo 2.1). Trattiamo brevemente il modello minimale supersimmetrico (paragrafo 2.2) nel cui ambito è definita la particella supersimmetrica più leggera che viene identificata con il neutralino più leggero. Questa particella è quella più comunemente presa a modello per comporre la materia oscura (paragrafo 2.3).

Nel terzo capitolo descriviamo in dettaglio il telescopio per neutrini ANTARES. Per prima cosa spieghiamo il principio di rivelazione dei neutrini con l'apparato (paragrafo 3.1) e le diverse tipologie di interazioni di neutrino visibili in ANTARES (paragrafo 3.2). Parliamo quindi brevemente dell'effetto Cherenkov (paragrafo 3.3) e della propagazione della luce in acqua (paragrafo 3.4), quindi schematizziamo la tecnica di ricostruzione delle tracce di eventi nell'apparato (paragrafo 3.5). Ci addentriamo poi nella descrizione del disegno del rivelatore (paragrafo 3.7), ne facciamo una panoramica generale (paragrafo 3.8) e passiamo in seguito a descrivere una stringa tipo (paragrafo 3.9). Nel seguito descriviamo la struttura e le caratteristiche dei fotomoltiplicatori (paragrafo 3.10) e l'elettronica di supporto (paragrafo 3.11). Segue la descrizione del sistema di "slow-control" dell'apparato (paragrafo 3.12), la calibrazione (para-

grafo 3.13), il sistema di posizionamento acustico delle stringhe (paragrafo 3.14) e l'analisi del rumore ottico di fondo dato dalla bioluminescenza marina e dal decadimento del potassio marino disciolto in acqua(paragrafo 3.15). Per concludere il capitolo mostriamo il cielo osservabile da ANTARES, l'area efficace dell'esperimento (paragrafo 3.16) ed il suo stato attuale (paragrafo 3.17).

Nel quarto capitolo definiamo il set di dati utilizzati (paragrafo 4.2) e la selezione di qualità applicata al set di dati per scartare quelli presi in periodi con un ambiente marino instabile (paragrafo 4.3). Ci occupiamo poi di descrivere come si costruisce una simulazione Monte Carlo dell'apparato (paragrafo 4.4). Dopo la definizione dei sistemi di coordinate usate per identificare una sorgente sulla sfera celeste (paragrafo 4.1), introduciamo il Monte Carlo che simula il fondo (paragrafi 4.5 e 4.8) e discutiamo in dettaglio l'algoritmo che ci permette di ricostruire le tracce di muoni rivelate dal detector (paragrafo 4.6). Quindi descriviamo la selezione di base degli eventi accettati (paragrafo 4.7) e mostriamo i grafici di confronto tra dati e Monte Carlo di fondo (paragrafo 4.9). Dopo il confronto tra i dati ed il MC di fondo passiamo alla costruzione del Monte Carlo di segnale che simula il segnale di neutrini aspettato dall'annichilazione di materia oscura nel Centro Galattico (paragrafi 4.10 e 4.11). Nell'ultima parte del capitolo trattiamo la selezione degli eventi di segnale (paragrafo 4.12), discutendone le ragioni e le finalità, quindi descriviamo l'analisi detta "binned" del set di dati (paragrafo 4.13), arrivando a definire la significatività statistica (secondo l'approccio di Feldman e Cousins) della nostra analisi (paragrafo 4.14) e mostrando i grafici della sensibilità di ANTARES a flussi di neutrini da annichilazione di WIMPs nel Centro Galattico (paragrafo 4.15).

Nell'appendice A è illustrato l'approccio statistico di Feldman e Cousins. Partendo dall'approccio classico di Neyman, passando per la statistica Bayesiana, si arriva a definire un nuovo metodo per la costruzione degli intervalli di confidenza per una misura sperimentale dato un certo livello di fondo.

Nell'appendice B descriviamo il lavoro di calibrazione dei circuiti ARS svolto all'interno della collaborazione ANTARES. Introduciamo i circuiti per la misura della carica e del tempo di arrivo dei segnali e la problematica dell'effetto di "cross-talk" tra questi due elementi. Quindi procediamo con la descrizione dello studio portato avanti per stabilire una correzione universale indipendente dal tempo per tutti i dati raccolti dall'esperimento.



# Chapter 1

## The standard model of cosmology and Dark Matter

In this chapter [125, 50, 56] the standard cosmological model is described. This model is currently considered the most appropriate to explain almost all the astrophysics observations available. As the base of this model there is the cosmological principle. From this first assumption one can add, thanks to the use [116] of the general relativity and of the Einstein equations in particular, all the diverse components that form all together the so called  $\Lambda$ CDM model.

After this brief description of the standard model of cosmology, that serves for contextualization, the dark matter scenario will be described. The different models and candidates for the role of dark matter particles will be shown.

### 1.1 Standard model of the Universe: first principles

In this section we will explain the cosmological principles, that are at the base of the standard model, the concept of redshift and the Hubble law, that describe the expansion of the Universe. With the Hubble law we can then evaluate in a simple way the age and the size of the Universe.

#### 1.1.1 The cosmological principle

In the first years of the XX century the knowledge about the distribution, composition and metric of matter in the Universe was very poor. Friedmann was the first to find the solution of the Einstein equations for a homogeneous distribution of matter, but he never hypothesised the cosmological principle.

Thus, in the lack of observational data and with the aim of finding a simple model to describe our Universe, that could be used as a foundation for mathematical and geometrical theories, one has recourse, at the end of '40 years, by Gamow [74, 17], to the formulation of the cosmological principle. This formulation has been revealed, thanks to the definition of new techniques that have brought to an incredible development of our knowledge of the Universe, correct.

The cosmological principle states:

**Theorem 1 (Cosmological principle)** *The Universe is homogeneous and isotropic on large scales ( $\geq 100 \text{ Mpc}$ ).*

It means that, in it, there not exist privileged positions or directions (following the Copernican principle). The concepts of homogeneity and isotropy appear to be strange to us in rapport to our perception of the Universe: stars, galaxies and other structures separates from each other by great empty spaces, thus a completely anisotropic and inhomogeneous scenario! This is the reason because, in the principle, one refers to the big scales<sup>1</sup>.

Thus, roughly above  $100 \text{ Mpc}$ , the Universe appear isotropic from our point of view in the space. But the isotropy in a given point in the space, combined with the cosmological principle, leads to the isotropy in any given point in the space, and the isotropy in any given point in the space implies the homogeneity of the Universe in any point.

### 1.1.2 The Universe is expanding

Let we take the spectrum of a galaxy and let us examine an absorption line of this spectrum. In a laboratory frame on Earth this line has a wavelength  $\lambda_e$ , while the wavelength we observe, for the same line, in another galaxy is generally different and equal to  $\lambda_o$ .

Now we define a quantity that has an enormous importance: the *redshift* ( $z$ ), defined by:

$$z = \frac{\lambda_o - \lambda_e}{\lambda_e}. \quad (1.1)$$

We need to specify that some galaxies show negative values of  $z$ , thus they undergo a blue-shift induced by their own motion, but almost all the galaxies show a red-shift of the spectral lines.

### The Hubble law

In 1929 Hubble measured [87] redshift and distances of a sample of galaxies reporting his results in a redshift-distances diagram.

He, hence, found the relation that has his name:

$$v = cz = H_0 d. \quad (1.2)$$

This is the Hubble law. More distant are the galaxies, more they are moving away from us. This regression is induced by their radial velocity  $v$ . In the formula 1.2 appears the *Hubble constant*  $H_0$ . It has a measured value equal to  $H_0 = (71.9 \pm 2.6) \text{ km/s/Mpc}$  [71, 58].

The meaning of this law is that the galaxies move away from us and from each other linearly with the distance.

---

<sup>1</sup>consider that  $100 \text{ Mpc}$  corresponds roughly to  $3 \times 10^{18} \text{ km}$

### The age of the Universe

Is interesting to note that, if today the galaxies are moving away from each other, there have been one moment in which they were very closed each other, all in the same point. In the absence of external forces the velocities of two galaxies, with a distance  $d$  between them, will be constants.

Thus, at a given time we have:

$$t_0 = \frac{d}{v} = \frac{d}{H_0 d} = H_0^{-1}, \quad (1.3)$$

where we made use of the Hubble law 1.2. The  $t_0$  time is called *Hubble time*. With the reported above value of the Hubble constant it is equal to  $t_0 = (13.69 \pm 0.13) \text{ Gyr}$  [95].

Thus, roughly 14 billions of years ago all the galaxies were forced in a point in the space. Consequently the Hubble time is a raw estimation of the age of the Universe. This value is also confirmed by the age of the most ancient stars that is compatible with it.

This is a simple scheme of the Big bang model, according to this theory, the Universe is evolved from a very little, dense and hot initial volume to the current enormous, rarefied and cold volume.

### The size of the Universe

As we did for the age of the universe, the Hubble law 1.2 can be also useful to define a scale of interest in cosmology. This scale corresponds to the maximum distance that a photon can cover from the Hubble time until today.

This distance is called *Hubble distance*:

$$d_H(t_0) = \frac{c}{H_0} = (4300 \pm 400) \text{ Mpc}. \quad (1.4)$$

It can be considered like a raw estimation of the maximum size of the Universe.

## 1.2 The metric of the Universe

Now we try to build models of the Universe that respect the cosmological principle and based on the general relativity. Since the general relativity [130] is also a geometrical theory let us now examine the geometrical properties of an homogeneous and isotropic space.

Let us assign to each point in the space the three space coordinates, constant in time,  $x^\alpha$  with  $(\alpha = 1, 2, 3)$  and one time coordinate  $(\alpha = 0)$ : the so called *proper time* (measured by a clock in motion with the point). The coordinates  $x^\alpha$  are called the *co-moving coordinates*.

If the matter distribution is uniform, then the space is homogeneous and isotropic and the proper time become the time measured by an observer that sees the Universe uniformly expanding around it, such as the three-dimensional space metric  $dl^2$  between space points is identical in any time, place and direction to respect the cosmological principle.

Thus, the expression for the metric, following the synchronous gauge, is  $ds^2 = (cdt)^2 - dl^2$ . Taken into account these geometrical considerations (for a complete treatment see [142]), the metric that describes, among all the possible choices, in the better way a Universe characterised by the cosmological principle is the *Friedmann-Robertson-Walker metric* (FRW), that has the form:

$$ds^2 = (cdt)^2 - a(t)^2 \left[ \frac{dr^2}{1 - Kr^2} + r^2(d\theta^2 + \sin^2\theta d\phi^2) \right]. \quad (1.5)$$

where  $(r, \theta, \phi)$  are the polar coordinates in the co-moving reference system (if the Universe's expansion is perfectly homogeneous and isotropic, then the co-moving coordinates of any point in space remains constants in time),  $t$  is the proper time,  $K$  is the *curvature constant*: it can assume the values 1,0 or -1 if the Universe has a closed, flat or open geometry respectively [121].

It is important to note besides the introduction of a new time dependent function:  $a(t)$  called the *scale factor*. It has the dimensions of a length and serves to describe the expansion or the eventual contraction of the Universe, and it is normalised in order to have today a value  $a(t_0) = 1$ . This means that a galaxy have, in its own co-moving reference system, coordinates that do not vary with time, the thing that vary with the time is the metric itself.

### 1.3 The basis of the theory of the Universe

To derive the equations ruling in the Universe we have to start from the expression of the Einstein equation [69]:

$$G_{\mu\nu} = R_{\mu\nu} - \frac{1}{2}g_{\mu\nu}R = 8\pi GT_{\mu\nu}, \quad (1.6)$$

where we have set  $c = 1^2$ .  $G_{\mu\nu}$  is the Einstein tensor,  $R_{\mu\nu} = R_{\mu\sigma\nu}^{\sigma}$  is the Ricci tensor (where  $R_{\mu\sigma\nu}^{\sigma}$  is the Riemann tensor that tells us if the space is flat or curve),  $g_{\mu\nu}$  is the metric tensor and  $T_{\mu\nu}$  is the energy-momentum tensor, that describes the distribution of matter and energy in the Universe.  $R = g^{\mu\nu}R_{\mu\nu}$  is the so called scalar curvature.

The left side of the equation describes the geometry of the space-time, while the right side of the equation<sup>3</sup> accounts for the energy contained in it. This is the main aim of the Einstein equation: to bond the matter (and energy) to the metric of the space-time.

First we define the *Hubble parameter*, that is an estimation of the expansion rate of the Universe. It tells us how much the scale factor varies with time:

$$H(t) = \frac{da/dt}{a(t)} = \frac{\dot{a}(t)}{a(t)}. \quad (1.7)$$

Following this notation the Hubble constant represents only the particular case  $H(t_0) = H_0$ . The Hubble law 1.2 can be rewrote in this way:  $v = H(t)d$ . This is

<sup>2</sup>From now on we will always consider  $c = 1$ .

<sup>3</sup> $G$  is the Newton gravitational constant, with the value  $G \simeq 6.673 \times 10^{-11} \text{ Nm}^2\text{kg}^{-2}$  [111]

the only velocity field compatible with the isotropy and homogeneity stated in the cosmological principle.

### 1.3.1 The ruling equations of the Universe

From the Einstein equation we can derive [56] the equation that governs the expansion of the Universe. This is the *Friedmann equation*:

$$H(t)^2 = \left(\frac{\dot{a}}{a}\right)^2 = \frac{8\pi G}{3}\rho - \frac{K}{a^2}, \quad (1.8)$$

where with  $\rho$  all the kind of energy densities of the components of the Universe (matter, radiation and dark energy) are taken into account.  $K$  is the curvature constant just explained above.

The Friedman equation alone can not specify the behaviour of the scale factor in time, because is an equation with two unknown variables ( $a(t)$  and  $\rho(t)$ ). Thus, we use the energy conservation law  $\partial T_\nu^\mu / \partial x^\mu = 0$ .

Considering an expanding, homogeneous and isotropic Universe we can derive, from the continuity and Euler equations that govern the evolution of the density  $\rho$  and of the pressure  $P$  respectively, the so called *fluid equation*:

$$\frac{\partial \rho}{\partial t} + 3\frac{\dot{a}}{a}(\rho + P) = 0. \quad (1.9)$$

Combining the Friedmann equation 1.8 with the fluid equation 1.9, with some passages we arrive to the second equation of Friedmann, also called *acceleration equation*:

$$\frac{\ddot{a}}{a} = -\frac{4\pi G}{3}(\rho + 3P). \quad (1.10)$$

From this equation is clearly visible that, if the energy density  $\rho$  is positive, then we will have a negative acceleration, that is a deceleration of the Universe.

Now we have three equations with three unknown variables:  $a(t)$ ,  $\rho(t)$  and  $P(t)$ . However the last equation 1.10 it is not independent from the others two, so we need a further equation.

The last equation we need is a state equation, of the type  $P = P(\rho)$ , that bonds together the pressure with the energy density of the components of the Universe.

For any components of cosmological interest the *equation of state* can be written in the simple form:

$$P = \sum_i w_i \rho_i, \quad (1.11)$$

where  $w$  is a dimensionless constant with values that differ with the type of components  $i$  considered. Our set of equations (1.8, 1.9, 1.10 and 1.11) describing the Universe is now complete.

### 1.3.2 The components of the Universe

In this section we take in consideration the principal components of the Universe: radiation, matter and dark energy. Combining the fluid equation 1.9, that holds for each component separately, with the equation of state 1.11 we obtain the evolution of the energy density for each component:

$$\rho_w(a) = \rho_{w,0} a^{-3(1+w)}. \quad (1.12)$$

With this equation we can evaluate the evolution of the energy density as a function of the scale factor and of the redshift.

From the different behaviour of the energy density  $\rho_i$  of the diverse components as a function of the scale factor it is possible to see that the Universe undergoes three different regimes in which was dominated by only one component each time. First there was the radiation domination, then the matter domination and last the dark energy domination.

#### Radiation

In the first part of its life the Universe was dominated by the radiation component. A non degenerate fluid of relativistic particles in thermal equilibrium has an equation of state parameter equal to  $w = 1/3$ .

Thus, from the state equation and the density evolution equation 1.24, using the relation that bonds redshift and scale factor ( $\frac{1}{a(t)} = 1 + z$ ), we can derive the trend of the radiation energy density as a function of the scale factor and of the redshift, and from the Friedmann equation we can derive the evolution of the scale factor with the time and the relative Hubble parameter:

$$\begin{aligned} \rho_r &= \rho_{0,r} a(t)^{-4} = \rho_{0,r} (1+z)^4 \\ a(t) &= \left(\frac{t}{t_0}\right)^{1/2} \\ H(t) &= \frac{1}{2t} \end{aligned} \quad (1.13)$$

#### Matter

After the radiation the matter component dominated the Universe. For the matter, considered as a non relativistic ideal gas with negligible pressure,  $w = 0$ .

This leads to:

$$\begin{aligned} \rho_m &= \rho_{0,m} a(t)^{-3} = \rho_{0,m} (1+z)^3 \\ a(t) &= \left(\frac{t}{t_0}\right)^{2/3} \\ H(t) &= \frac{2}{3t} \end{aligned} \quad (1.14)$$

### Dark energy

Recently the Universe has been started to be dominated by the dark energy component, which physical meaning is not yet understood [127]. Supposing the dark energy being fully described by the so called cosmological constant  $\Lambda$  (first introduced and then rejected by Einstein) that have a  $w = -1$ , we obtain:

$$\begin{aligned}\rho_\Lambda &= \text{constant} \\ a(t) &= \exp[H_0(t - t_0)] \\ H(t) &= H_0\end{aligned}\tag{1.15}$$

From the above reported behaviour of the scale factor, energy density and Hubble parameters we can derive the moments in which there were the passages of the domination phases between the different components.

As we have seen, the radiation energy density decreases more quickly than the matter one. The passage epoch is called *radiation-matter equivalence*. Equating the densities we obtain:

$$\begin{aligned}a_{rm} &= \frac{\Omega_{0,r}}{\Omega_{0,m}} \simeq 2.8 \times 10^{-4} \\ z_{rm} &= a_{rm}^{-1} \simeq 3600\end{aligned}\tag{1.16}$$

The second moment of equivalence, this time between matter and dark energy, happens at:

$$\begin{aligned}a_{m\Lambda} &= \sqrt[3]{\frac{\Omega_{0,m}}{\Omega_{0,\Lambda}}} \simeq 0.75 \\ z_{m\Lambda} &\simeq 0.33\end{aligned}\tag{1.17}$$

#### 1.3.3 The cosmological parameters

For a flat Universe, a critical density can be defined as:

$$\rho_{cr} = \frac{3}{8\pi G} H_0^2.\tag{1.18}$$

If the Universe has a critical density bigger than this value it will have a positive curvature ( $K = 1$ ), otherwise it will have a negative curvature ( $K = -1$ ). Currently the critical density has a value equal to  $\rho_{cr} = (9.2 \pm 1.8) \times 10^{29} \text{ g/cm}^3$  [77].

It is useful to introduce some new variables. Let us define the dimensionless density parameters:

$$\Omega_i = \frac{\rho_i}{\rho_{cr}}.\tag{1.19}$$

With  $\Omega(t) > 1$  ( $K = 1$ ) we have a closed Universe, with  $\Omega(t) < 1$  ( $K = -1$ ) we have an open Universe for  $\Omega(t) = 1$  we have a flat Universe. Remember that a Universe ruled by the Friedmann equation cannot change its curvature's sign.

With this new formalism the Friedmann equation, at the time  $t_0$ , becomes:

$$1 - \Omega_0 = \Omega_K.\tag{1.20}$$

In this formula is evident the dependence of the curvature of the Universe from its total energy density. Since we know that our Universe is flat ( $\Omega_K = 0$ ), thus described by an euclidean geometry, the Friedman equation can be rewrote in the following way taking into account all the contributes to the today Universe's energy density:

$$1 = \Omega_{0,tot} = \Omega_{0r} + \Omega_{0m} + \Omega_{0\Lambda}. \quad (1.21)$$

Then to describe in the correct way the behaviour of our Universe it is necessary to know the values of the main cosmological parameters ( $\Omega_{r0}$ : radiation,  $\Omega_{m0}$ : matter,  $\Omega_{0\Lambda}$ : dark energy) present in the above equation 1.21.

A lot of recent measures [34, 95, 25] posed constraints over these parameters.

- $\Omega_r = \Omega_\gamma(1 + 0.2271N_{ef})$ 
  - $N_{ef} \approx 3.04$
  - $\Omega_\gamma \approx 4.76 \times 10^{-5}$
- $\Omega_m \approx 0.258 \pm 0.030$ 
  - $\Omega_b h^2 \approx 0.02273 \pm 0.00062$
  - $\Omega_c h^2 \approx 0.1099 \pm 0.0062$
- $\Omega_\Lambda \approx 0.742 \pm 0.030$

Thus, as can be also seen from the parameters characterizing the dark energy component, the Universe expansion is accelerating exponentially. The acceleration is also confirmed by the *deceleration parameter*  $q_0$ <sup>4</sup>.

For a Universe containing the three major components described in the paragraph 1.3.2, this parameter can be expressed in the following way:

$$q_0 = - \left( \frac{\ddot{a}a}{\dot{a}^2} \right)_{t=t_0} = \Omega_{0,r} + \frac{1}{2}\Omega_{0,m} - \Omega_{0,\Lambda} \quad (1.22)$$

Thus a positive value of  $q_0$  corresponds to a negative acceleration and vice-versa. Recent measures of this parameter gave the value  $q_0 \simeq -0.55$ : an accelerating Universe.

## 1.4 Brief summary of the history of the Universe

In this section we will briefly describe [115] the history of the Universe with the diverse ages and their characterizing events.

The observed expansion of the Universe [135, 102], as we have seen in the section 1.3 and in the paragraph 1.1.2, is a natural result of any homogeneous and isotropic cosmological model based on general relativity and ruled by the Friedmann equations. However the Hubble expansion (1931) [87], by itself, does not provide sufficient evidence for what we generally call the Big-Bang model of the Universe. The

<sup>4</sup>This parameter has been called in this way because when it was first introduced (half of the XX century), scientists thought, because of the lack of observational data, that the Universe was decelerating.

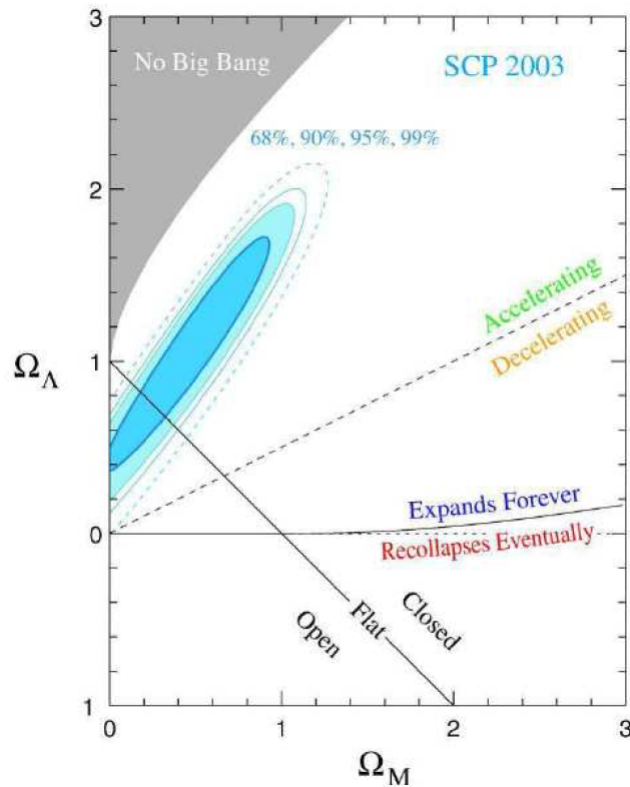


**Figure 1.1.** Probability contours for  $\Omega_\Lambda, \Omega_m$  in sky blue. Regions representing specific cosmological sceneries are illustrated: models of closed, flat or open Universe and the possible future evolutions. Data of the Supernova cosmology project. The region of maximum probability is consistent with an accelerated and dark energy dominated Universe [124].

formulation of the Big-Bang model began, as we said, in the 40s years by Gamow and his collaborators. They proposed that the early Universe was very hot and dense (enough to allow the nucleosynthesis (BBN) of the Hydrogen) and expanded and cooled step by step to its present state [74, 17]. Alpher predicted (1948) that, as a consequence of this model, a relic background radiation had to be survived [18, 19] with a temperature of roughly  $3\text{ K}$ . This radiation was then (1965) observed by Penzias and Wilson: it is the Cosmic Microwave Background (CMB) [117]. This confirmed the Big-Bang theory as the prime candidate to describe the Universe. But there were some problems with the initial conditions of the model. These were solved (1981) with the inflationary solution proposed by Guth [81].

## Inflation

Proposed by Guth to solve the horizon, flatness and monopoles problems (see [50] for details) the Inflation mechanism describes the behaviour of the Universe in the first moments of its life. It does not modify the sequent Big-Bang model of structure formation and evolution of the Universe. The Inflation states that from an age of the Universe equal to  $t_i = 10^{-36}\text{ s}$  until the age  $t_e = 10^{-32}\text{ s}$ , the Universe underwent

an accelerated expansion of the scale factor. Thus, in the short duration of only  $10^{-34}$  s the Universe expanded by the enormous factor  $10^{30}$ !

### The early times

At the beginning, in the first decimal of seconds, the temperature, the density and the pressure were so high that the matter, in the way we know it today, could not exist. The early Universe was a plasma made of relativistic elementary particles (quarks, neutrinos etc.) and photons. For the long time of the primordial life of the Universe, the interactions rate between these elements proceeded with such a big rapidity that all the particles were in thermal equilibrium and different species shared the same temperature. Thus, in the absence of external energy exchange, the expansion was *adiabatic*.

Due to the expansion of the Universe, certain rates may be too slow to either establish or maintain equilibrium. Quantitatively, for each particle type  $i$ , as a minimal condition for equilibrium, one requires that some rate  $\Gamma_i$  involving that type must be larger than the expansion rate (given by the Hubble parameter at that time) of the Universe  $H$ :  $\Gamma_i > H$ . Recalling (paragraph 1.1.2) that the age of the Universe is determined by the equation 1.3, this condition is equivalent to requiring that, on average, at least one interaction has occurred over the lifetime of the Universe.

Good examples of particles that were before in the thermal equilibrium and, when their rates became smaller than the expansion rate, decoupled proceeding autonomously with the evolution are the neutrinos and the photons. Neutrinos went out of the equilibrium before of the photons (this happened when the Universe was 1 s old at a temperature of  $9 \times 10^9$  K), then their background temperature is now smaller than that of photons:  $T_\nu \simeq 1.9$  K [143]. The neutrino density parameter is  $\Omega_\nu h^2 = 5 \times 10^{-4}$ , so the neutrino contribution to the matter budget is negligible.

### The baryogenesis

When the Universe was very hot and dense and the temperature was of the order of  $MeV/k_B^5$ , there were no neutral atoms or bonded nuclei. The radiation domination in such a hot ambient assured that each atom or nucleus produced have been immediately destroyed by an high energy photon.

When the temperature of the Universe become of the order of 1 MeV, the primordial cosmic plasma is composed of: relativistic particles in equilibrium (electrons and protons strongly coupled by the Compton scattering  $e^+e^- \rightarrow \gamma\gamma$ ), relativistic decoupled particles (neutrinos) and non relativistic particles (baryons).

The initial process of baryogenesis had an asymmetry in the numbers of baryons and anti-baryons of the order of  $10^{-10}$  constant along all the expansion. Under 1 MeV all the anti-baryons were annihilated, thus the *baryon to photon ratio* is  $\eta_b = n_b/n_\gamma = 5.5 \times 10^{-10}(\Omega_b h^2/0.020)$ .

---

<sup>5</sup>The Boltzmann constant has the value  $k_B \simeq 1.38 \times 10^{-23} JK^{-1} = 8.62 \times 10^{-5} eVK^{-1}$

### The nucleosynthesis

When the cooling of the Universe arrive at a temperature lower than that of the bound energy of the nuclei, the first *light elements* start to form [108].

The nuclear processes lead primarily to *Helium*  ${}^4\text{He}$ , with a primordial mass fraction of about 25%. Lesser amounts of the other light elements are produced: about  $10^{-5}$  of *Deuterium*  $D$  and Helium  ${}^3\text{He}$  and about  $10^{-10}$  of *Lithium*  ${}^7\text{Li}$  by number relative to the Hydrogen  $H$ . The abundances of the light elements (see figure 1.2) depend almost only from the baryon-photon ratio we have shown in the previous sub-paragraph. The nucleosynthesis happened from 1 s to roughly 200 s ( $T \simeq 7 \times 10^8 \text{ K}$ ) of the life of the Universe.

The few number of neutrons with respect to protons show the inefficiency of the BBN. Still today the 75% of the baryon matter is composed by free protons and almost the 24% of baryon objects, like stars and gas clouds, are composed by Helium.

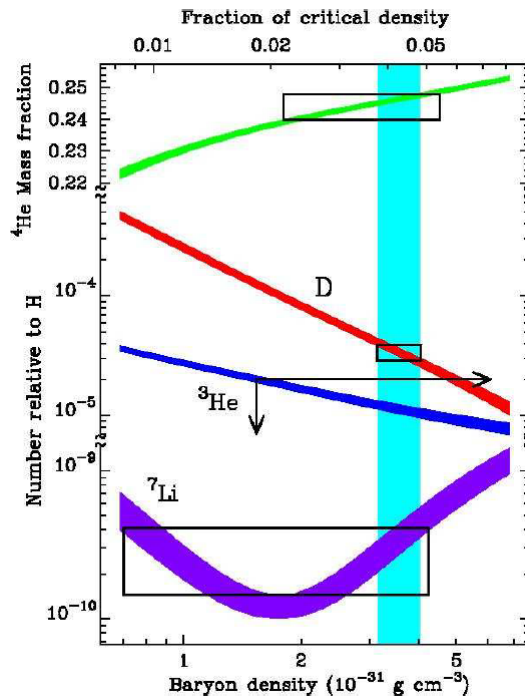


**Figure 1.2.** Constraint on the baryon density from Big Bang Nucleosynthesis. Predictions are shown for four light elements:  ${}^4\text{He}$ ,  $D$ ,  ${}^3\text{He}$  and  ${}^7\text{Li}$ . Spanning a range of ten order of magnitude. The solid vertical band is fixed by measurements of primordial Deuterium. The boxes are the observations; there is an upper limit on the primordial abundance of  ${}^3\text{He}$  [56].

### Recombination

It is the time in which the baryon component of the Universe passes from a totally ionised situation to a neutral one. It can be defined as the time in which the ions

numerical density is equal to the neutral atoms numerical density. The ionization rate can be expressed by the *ionization fraction*  $X = n_e/n_b$ .

The recombination took place for  $X = 1/2$  when the temperature of the Universe was of the order of  $T_{rec} = 3740 K$ . This happened at a redshift of  $z_{rec} = 1370$  that is when the Universe was 240000 age old; it last roughly for 70000 years: it is not an instantaneous process.

### Decoupling

It is the time at which the scattering rate of the photons over the electrons become smaller than the Hubble parameter, that represents the expansion rate of the Universe. The decoupling happen when  $\Gamma(z_{dec}) = H(z_{dec})$ . With  $z_{dec} \approx 1100$ , when the Universe was 350000 year old and the temperature was of the order of  $T_{dec} = 3000 K$ .

### Last scattering epoch (CMB)

It is the time at which a photon of the thermal bath undergo its last scattering from the free electron of the strongly coupled baryon-photon fluid. Thus each observer in the Universe has a last surface scattering around him. After this moment the photons has been free to travel in the space. This last scattering happened at  $z_{ls} \approx z_{dec} = 1100$ . It is important to note that the last three epoch described here: recombination, decoupling and last scattering happened after the radiation-matter equivalence time, thus in the matter dominated Universe. This implies also that these results are dependent from the cosmological model assumed.

The relic of the last scattered photons were first observed by Penzias and Wilson in 1965. They found an isotropic background of microwave radiation. The temperature, with a perfect Planck law of black body spectrum, of this *Cosmic Microwave Background (CMB)* was measured by the COBE satellite in 1992:  $T_{CMB} = (2.725 \pm 0.001) K$  [105].

Another observable quantity inherent in the CMB is the variation in temperature from one part of the microwave sky to another one [131, 149]. These anisotropies are of the order of  $\sqrt{\langle \Delta T/T \rangle^2} \approx 10^{-5}$  and were first observed by COBE and then better investigated by WMAP [86] and are one of the main aim of the Planck experiment (see figure 1.3).

### The structures formation

Before the decoupling age the strongly coupling of the baryon-photon fluid tend to destroy all the possible fluctuations in the density of the plasma. After the last scattering epoch we have two separated gases: baryons and photons. From now on the baryon component is free to collapse under its own gravity falling in the potential wells created by the dark matter (DM) component (see section 1.5). This collapse permit to form, in the time passed from the last scattering until today, all the cosmic structures we can see: from the giants clusters of galaxies till the smaller asteroid.

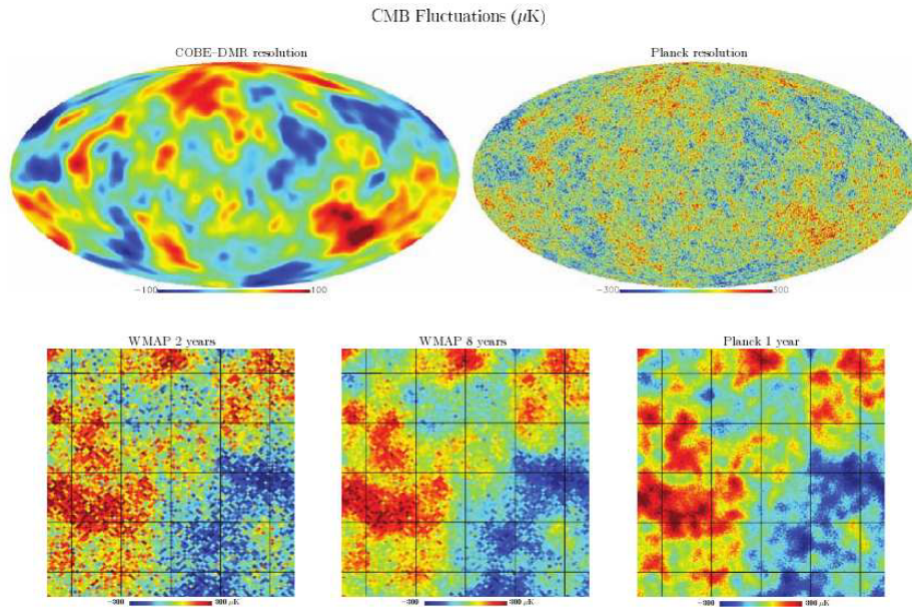


**Figure 1.3.** CMB temperature anisotropies maps. In the left upper plot the sky map observed by COBE while in the right upper plot the sky map resolution of Planck. In the bottom portions of sky maps resolution are showed for WMAP (2 and 8 years) and Planck (1 year prediction).

## 1.5 Dark Matter

The matter density parameter  $\Omega_m$  has a great importance, although it no more represents the dominant component in the Universe. With this parameter we can know the composition of matter in the Universe: how much matter in the Universe is under the form of stars, gas etc.?

Currently the value measured for the matter density parameter, as we seen in the paragraph 1.3.3, is  $\Omega_{0,m} \simeq 0.3$ . Now we try to evaluate the different types of ordinary baryon matter parameters to see in which amount they contribute to the total density matter parameter. The stars represent only the 0.5% of the total matter in the Universe:  $\Omega_{*,0} \simeq 0.004$  [125] (estimated through the data derived from the star formation theory).

Also galaxies and galaxy clusters contains baryon matter under the form of hot gas [16], with temperature of the order of  $10^6 K$ . They are not in the visible part of the light spectrum but in the X part [23, 101]. All these contributes form the baryon matter<sup>6</sup>. From the BBN arise some strict constraints:  $\Omega_{0,b} \simeq 0.0267$  [86]. The baryon matter parameter is too small to account for all the matter considered in the total matter density parameter, then the majority of this matter has a non baryon nature:  $\Omega_{DM} \simeq 0.21$ . It is not visible but it is necessary to explain a lot of phenomena that would not be existent. This is the reason why it is called *Dark Matter*.

<sup>6</sup>In cosmology the electrons also are considered baryons.

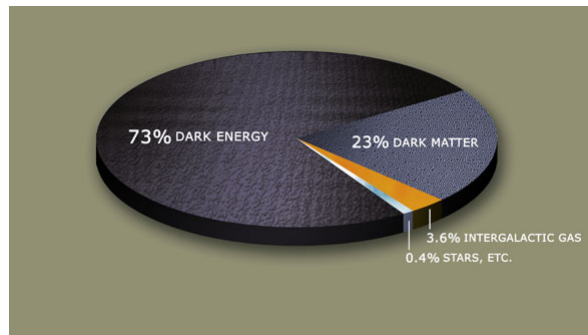


**Figure 1.4.** The pie scheme represents the divisions of the energy density in the Universe. As can be seen the dark matter represents the biggest part of the matter component of the Universe.

### 1.5.1 Dark matter properties and types

Candidates for non baryonic dark matter must satisfy several conditions:

- they must be stable on cosmological time scales;
- they must interact weakly with electromagnetic radiation;
- they must have the correct relic density.

Since the Universe is indeed dominated by non baryonic matter (see figure 1.4), it is obviously important to figure out the present density of various types of candidate particle expected to be produced in the early stages of the Big Bang. These relics are held in thermal equilibrium with the other components of the thermal bath of the Universe until they decouple. These relic candidates are divided into two classes: *Hot Dark Matter (HDM)* and *Cold Dark Matter (CDM)*. The former are relativistic when they decoupled, the latter are non relativistic at the time of the decoupling [50].

#### Hot Dark Matter

Examples of this type of relics are the neutrinos. However, a lot of different measures (CMB, SN and galaxy survey) show that the relic of cosmic neutrino background is too small to account for all the non baryonic dark matter component of the Universe. As we saw in the section 1.4  $\Omega_\nu < 0.048$  at 95% C.L. [86, 58] that pose an upper limit on the neutrino mass equal to  $m_\nu < 0.68 eV$  at 95% C.L., limits that are in agreement with those obtained in laboratory:  $m_\nu < 2 eV$  [111]. But, over all these reasons, there is the fact that, if the dark matter was composed of relativistic particles, no one of the cosmic structures we observe today would be formed in the structures formation process [137].

#### Cold Dark Matter

Possible cold (non baryonic) dark matter candidates could be represented by the axions or the primordial black holes etc. The primordial black holes have been postulated in some strange cosmological models [93] and they must be formed before

the BBN. Instead the axions [132] have been introduced to solve the strong CP problem of QCD; they naturally occur in super-string theories.

Then, the most diffuse and tested scenario is the Weak Interacting Massive Particle (WIMP) that will be described in the following section 1.6.

### 1.5.2 Observational evidences

In this paragraph we will describe some methods that are used to evidence the presence of dark matter in our Universe; we will see that dark matter is the dominant component among those that form the total matter distribution.

#### Rotational velocity of galaxies and the galactic halo

The classic approach to identify the presence of dark matter is the measure of the rotational velocity of stars in spiral galaxies. Consider a star in motion on a stable Keplerian orbit of radius  $r$ , which velocity is  $v$ , around the galactic centre. The star feels an acceleration given by  $\dot{v} = v^2/r$  directed toward the centre of the galaxy and originated by the gravitational attraction of all the matter  $M(r)$  contained in the sphere of radius  $r$ :  $\dot{v} = GM(r)/r^2$ .

Equating the two expressions we obtain the relation between velocity and mass:

$$v = \sqrt{\frac{GM(r)}{r}}. \quad (1.23)$$

If the only matter is the luminous matter, one expect that the velocity would decrease, for large values of the radius, as  $v(r) \propto 1/\sqrt{r}$ . However, following [57, 100], what one observe is that the velocity remains constant also until big values of  $r$  as can be seen in the figure 1.5.

In our own galaxy, for the solar orbit radius  $r \simeq 8.4 \text{ kpc}$ , the velocity is  $v \simeq 220 \text{ km/s}$  with little change out to the largest observable radius. Then it is usually assumed that the rotational velocity of the Sun corresponds to  $v_\infty$ .

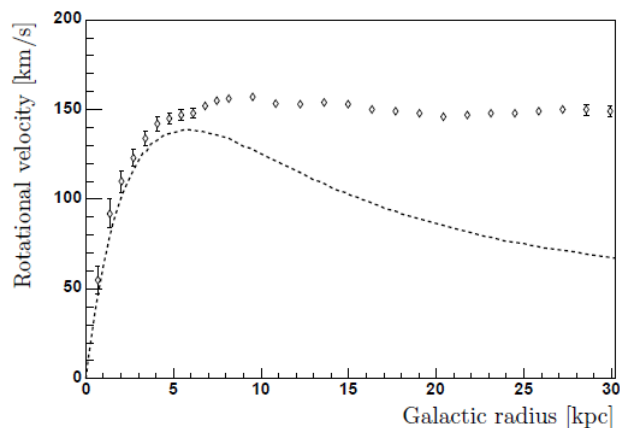


**Figure 1.5.** Observed rotational curve of the galaxy NGC 3198 (data points) compared to the prediction based considering only luminous matter (dashed line) [144].

This implies the existence of a *dark halo*. For a spherical matter distribution  $dM(r) = 4\pi r^2 \rho(r) dr$  we can obtain the density distribution of the halo using the concept of  $v(\infty)$  expressed above:

$$\rho(r) \propto \frac{v_\infty^2}{r^2} \quad (1.24)$$

The local dark matter halo density in the Sun's position has been estimated to be  $\rho_0 \simeq 0.3 \text{ GeV}/\text{cm}^3$  [111, 91]. At some point,  $\rho$  will have to fall off faster to keep the total mass of the galaxy finite, but we do not know at what radius it happens.

Since the formula 1.24 is singular for  $r = 0$ , there is uncertainty on the Galactic Centre position. This uncertainty is solved parametrizing the radial dark matter density profile distribution. One famous parametrization is the *Navarro Frank and White (NFW)* profile [112] (see paragraph 1.5.3).

### Clusters of galaxies and weak lensing

Another way to identify the presence of dark matter is to look at its gravitational influence on visible matter: for example from the observations of clusters of galaxies [38] one can estimate the luminous mass and compared it to the predicted virial mass. Zwicky was the first to perform this calculus for the COMA cluster. Starting from the *virial theorem*, that bounds the kinetic energy of the cluster  $T = m\langle v \rangle^2/2$  with its gravitational potential energy  $U = Gm^2/2r$  in statical equilibrium:  $2T + U = 0$ , he estimated the virial mass of the COMA cluster:  $M \propto r\langle v \rangle^2/G$ . Measuring the velocity dispersion of the galaxies in the COMA cluster he noticed that there was a bigger amount of matter with respect to the one calculated only considering the luminous matter.

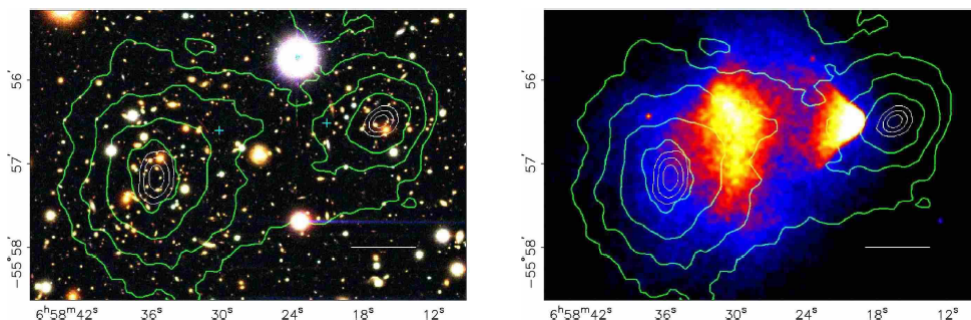


**Figure 1.6.** Shown above in the top panel is a color image from the merging bullet cluster 1E0657-558. The white bar indicate 200 kpc at the distance of the cluster. In the bottom panel is a Chandra image of the cluster. Shown in green contours in both panels are the weak lensing reconstruction. The white contours show the errors on the positions of the peaks and correspond to 68.3%, 95.5%, and 99.7% confidence levels. The blue crosses show the location of the centres used to measure the masses of the plasma clouds [49].

Measurements of the X-ray temperature of the hot gas in the cluster, which correlates with the gravitational potential felt by the gas, together with the study of weak gravitational lensing of background galaxies on the cluster can evidence the presence of dark matter [57].

A particular example of the described method involves the Bullet cluster which recently (on cosmological time scales) passed through another cluster. As a result, the hot gas forming most of the cluster's baryonic mass was shocked and decelerated, whereas the galaxies in the clusters proceeded on their trajectories. Gravitational lensing shows that the potential wells trace the visible matter distribution and not the hot thermal gas distribution that is supposed to be the big part of the matter in the absence of dark matter (see figure 1.6). This is a direct empirical proof of the existence of dark matter [49].

### 1.5.3 The Galactic Centre

The presence of a dark halo in the galaxy is almost sure (according to the observable evidences, some of them shown above), the problem arises when considering the dark matter profile in the inner region of the galaxy.

The usual parametrisation for a dark matter halo density is given by:

$$\rho(r) = \frac{\rho_0}{\left(\frac{r}{R}\right)^\gamma \left[1 + \left(\frac{r}{R}\right)^\alpha\right]^{\frac{\beta-\gamma}{\alpha}}}, \quad (1.25)$$

where  $r$  is the galacto-centric coordinate,  $R$  is a characteristic length (in the case of our galaxy is the galactic halo radius, roughly equal to 20 kpc [77]) and  $\alpha, \beta, \gamma$  are free parameters.  $\rho_0$  is the just defined galactic halo density ( $\approx 0.3 \text{ GeV cm}^{-3}$ ).

There is consensus, at present, about the shape of the profile in the outer parts of halos, but not in the innermost regions, due to loss of numerical resolution in N body simulations and to the poor resolution in observation of rotation curves of outer galaxies [33].

Navarro, Frank and White found [112], with N-body simulations, that the profile could be well approximated at small radii with a power-law  $\rho(r) = r^\gamma$ .

Observations of the velocity dispersion of high proper motion stars suggest the existence of a *Super Massive Black Hole (SMBH)* lying at the centre of our galaxy, with a mass  $M_{\text{SMBH}} \approx 3.6 \times 10^6 M_\odot$ , and accreting dark matter producing the so called spikes [79].

The existence of such spikes would produce a dramatic enhancement of the annihilation radiation from the galactic center and consequently a large uncertainties that are associated with predictions of annihilation fluxes.

Furthermore, the scattering of dark matter particles by stars in the dense stellar cusp observed around the SMBH could substantially lower the dark matter density near the Galactic center over  $10^{10}$  yrs, due both to kinetic heating, and to capture of dark matter particles by the SMBH [32].

In the region that contains also the GC (in an error circle of  $0^\circ.2$  radius) the EGRET satellite observed (around 1 GeV) an excess of gamma-ray radiation with respect to the expected emission of gamma-ray due to the interaction of primary cosmic ray with the interstellar medium (via  $p + X \rightarrow \pi^0$ ,  $He + X \rightarrow \pi^0$ , where  $X$  is an interstellar atom) [106].

Recently with the data of the Fermi satellite [1] (which has, with the LAT experiment, among one of its aims the indirect search for dark matter in the galactic

halo [68]) has been observed an excess of gamma-ray emission (at  $\approx 130$  GeV) in the direction of the central region of the galaxy. Several hypothesis has been done to interpret this excess. Currently there are no evidences that it can be due to dark matter annihilation. For discussion and more details, among the big numbers of published articles, see [138, 146, 48].

## 1.6 The WIMP scenario

Among the candidates for non baryonic dark matter (axions, primordial black holes etc.), that satisfied the three conditions reported in paragraph 1.5.1, the most diffused scenario is that of a dark matter made of the Weak Interacting Massive Particles (WIMPs).

The WIMP particles, indicated with  $\chi$ , have a mass ranging from 10 GeV up to few TeV, and with weak strength cross-sections. In the early Universe the WIMPs are in thermal and chemical equilibrium with the primordial plasma. In this scenario, their density would become exponentially suppressed when the Universe reached a temperature  $T < m_\chi$ . The WIMPs therefore freeze out of the thermal equilibrium once the rate of reactions, that change standard model particles into WIMPs and vice-versa, becomes smaller than the Hubble expansion rate of the Universe. After the freeze out, the WIMPs relic abundance remains constant accounting for the component of dark matter [57].

### 1.6.1 The WIMPs relic

The evolution of the number density of a generic species  $\chi$  in the Universe, is described (following [50, 137, 100]) by the Boltzmann equation:

$$\frac{dn_\chi}{dt} + 3\frac{\dot{a}}{a}n_\chi = -\langle\sigma_A \cdot v\rangle n_\chi^2 + \psi, \quad (1.26)$$

where the term  $\frac{\dot{a}}{a} = H$  is the Hubble rate that takes into account the expansion of the Universe,  $\langle\sigma_A \cdot v\rangle n_\chi^2$  is the rate of collisional annihilation ( $\sigma_A$  is the cross-section for annihilation reactions, and  $v$  is the mean particle velocity);  $\psi$  denotes the rate of creation of particle pairs. If the creation and annihilation processes are negligible, one has the expected solution:  $n_{\chi eq} \propto a^{-3}$ . This solution also holds if the creation and annihilation terms are non zero, but equal to each other, i.e. if the system is in (thermal) equilibrium:  $\psi = \langle\sigma_A \cdot v\rangle n_{\chi eq}^2$ .

Thus, the equation 1.26 can be written in the form:

$$\frac{dn_\chi}{dt} + 3Hn_\chi = -\langle\sigma_A \cdot v\rangle (n_\chi^2 - n_{\chi eq}^2). \quad (1.27)$$

The equilibrium abundance is maintained by annihilation with its antiparticle  $\bar{\chi}$  into lighter particles  $l$  ( $\chi\bar{\chi} \rightarrow l\bar{l}$ ) and vice versa ( $l\bar{l} \rightarrow \chi\bar{\chi}$ ). In our case, the WIMP  $\chi$  is a Majorana particle ( $\chi = \bar{\chi}$ ) [51].

The equilibrium density of WIMPs in the primordial plasma at temperature  $T$  and for a non relativistic specie is given, following the Boltzmann distribution, by:

$$n_{\chi eq} = \frac{g}{(2\pi)^3} \int d^3p_\chi e^{-E_\chi/T} \quad (1.28)$$

where  $g$  denotes the number of degrees of freedom of  $\chi$ ;  $E_\chi$  and  $p_\chi$  are the WIMP energy and momentum. The Boltzmann equation can be solved integrating it in two extreme regions, long before and long after the WIMP decoupling, and matching then the solutions. These solution are:  $n_{\chi eq} \simeq g (m_\chi T / 2\pi)^{3/2} e^{-m_\chi/T}$  for ( $T \ll m_\chi$ ) and  $T^3$  for ( $T \gg m_\chi$ ).

For the calculation details see [94, 61]. Here we report the result for the relic density today for a generic WIMP  $\chi$  [32]:

$$\Omega_\chi h^2 = \frac{m_{\chi,0} n_{\chi,0}}{\rho_{cr,0}} \approx \frac{1.07 \times 10^9 \text{ GeV}^{-1}}{M_P} \frac{x_f}{\sqrt{g_f}} \frac{1}{(a + 3b/x_f)} \approx \frac{3 \times 10^{-27} \text{ cm}^3 \text{ s}^{-1}}{\langle \sigma_A \cdot v \rangle} \quad (1.29)$$

where  $g_f$  counts for the relativistic degrees of freedom at the decoupling ( $f = \text{freeze out}$ ),  $M_P$  is the Planck mass,  $x_f = m_\chi/T_f$  with  $T_f$  the freeze out temperature and  $a, b$  are part of the parametrization in powers expansion of  $\langle \sigma_A \cdot v \rangle$ :

$$\langle \sigma_A \cdot v \rangle = a + b \langle v^2 \rangle + O(\langle v^4 \rangle) \simeq a + 6b/x. \quad (1.30)$$

The last line of 1.29 is an order of magnitude estimate and it shows that the relic abundance of a non relativistic decoupled specie strictly depends on the annihilation cross-section at freeze out [57].

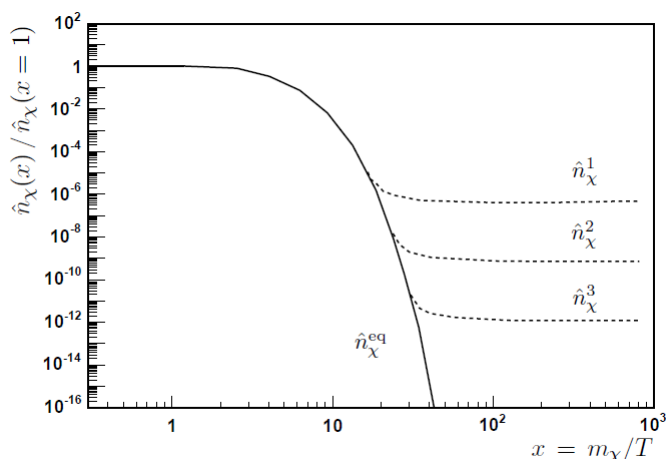


**Figure 1.7.** Time evolution of the comoving WIMP number density according to equation 1.27. The co-moving equilibrium WIMP number density  $n_{\chi eq}$  is shown by the solid line. It is constant for small values of  $x$  and decreases exponentially as the temperature drops below the WIMP mass. This is expected from the solution of the Boltzmann equation and the fact that in the radiation-dominated Universe  $T \propto a^{-1}$ . The three dashed lines show the comoving WIMP number-density for three different annihilation cross sections, where  $\sigma_1 < \sigma_2 < \sigma_3$  [94].

It is convenient to rewrite equation 1.27 in terms of the number of WIMPs per unit volume comoving with the expansion of the Universe  $\hat{n}_\chi = n_\chi a^3$ . In this way the equation can be solved for the comoving number density  $\hat{n}_\chi$  by using  $x = m_\chi/T$ , since in the radiation dominated Universe  $T \propto \frac{1}{a} \propto t^{-1/2}$ . Solutions for three different annihilation cross sections are shown in the figure 1.7. Here can be seen that the comoving WIMP number densities follow the equilibrium one until the

annihilation rate becomes smaller than the expansion rate. Thus, the bigger the WIMP annihilation cross-section is, the longer the WIMP number density follows the equilibrium value and the lower the final relic density is today.

This scheme is suitable for weak cross-sections. Therefore theories that predict interaction probabilities and particle masses similar to those of the weak interaction provide suitable dark matter candidates [100].

The WIMP freeze out happens at temperature  $T_f \simeq m_\chi/20$  almost independently of the properties of the WIMP. This means that WIMPs are already non relativistic when they decouple from the thermal plasma [57].

The WIMP neutralinos, created in the Big Bang, decoupled from ordinary particles at the temperature of SUSY symmetry breaking ( $\sim 1 \text{ TeV}$ ). They began to form the first structures under the influence of gravity: the future galactic halos. Then, the baryons, decoupled from radiation ( $\sim 0.25 \text{ eV}$ ) were attracted into the cold dark matter objects to build up the galaxies we see today.

## 1.7 WIMPs detection

WIMPs can be gravitationally trapped inside galaxies and have the correct density profile necessary to explain the rotational curves of outer stars in galaxies as we have seen in the paragraph 1.5.2.

Consider that the rms velocity of WIMPs in our galactic halo is roughly  $v_{rms} \simeq 270 \text{ km/s}$  (similar to that of stars). For these velocities WIMPs interact with ordinary matter through elastic scattering on nuclei.

Then, the main two ways [104] to experimentally detect the WIMPs of our galactic halo are based on these interactions. The first way is the direct search, which aims mainly to detect the recoil energy of the nuclei directly at Earth; the second way is the indirect search, based on the detection of the products (including neutrinos, gamma-rays, positrons, anti-protons etc.) of WIMP annihilations that happen in massive celestial bodies.

### 1.7.1 Neutrino from WIMP annihilation in celestial bodies

As we said in the paragraph 1.7.3, the galactic halo WIMPs can pass through massive celestial bodies because they only interact weakly with the ordinary matter. However, if a WIMP interacts with a nucleus in the object and it loses sufficient kinetic energy, so that its velocity after the collision is lower than the escape velocity of the object, the WIMP will be gravitationally bound to the object itself. For example the escape velocity of the Sun is  $\approx 60 \text{ km/s}$  and that of the Earth is  $\approx 11 \text{ km/s}$  [100].

WIMPs captured and accumulated in this way can annihilate therein producing some SM particles and subsequently neutrinos, that can be observed in large neutrino telescopes (see figure 1.8). The neutrino signal comes, in this way, from a fixed direction and is therefore much more easily distinguished from the background. Moreover the number density of WIMPs in the galactic halo is inversely proportional to the WIMP mass ( $n_\chi \propto m_\chi^{-1}$ ) and the annihilation rate in the halo is  $\propto n_\chi^2$  (while in the Sun is  $\propto n_\chi$ ) making the neutrino signal favoured for higher WIMP masses [90].

Thus, the better source to explore for the indirect dark matter annihilation are the Sun, the Earth and the Galactic Centre. The Sun [133] and the Earth are favoured because the neutrino flux is inversely proportional to the distance to the dark matter source squared, thus nearby objects are preferable. But in the Galactic Centre is supposed to be the peak of the distribution of dark matter into the galactic halo [79], thus also this source is very interesting (and the neutrino flux can be constrained by the gamma-ray flux [33]).

Quantitatively, the neutrino flux from neutralino annihilations depends on the details of the interaction-decay-propagation chain. It is fundamental to consider also the capture versus the annihilation balance in the core of the celestial body [51]. The differential neutrino flux is given by:

$$\frac{d\Phi_\nu}{dE} = \frac{\Gamma_A}{4\pi d^2} \sum_f B_\chi^f \left( \frac{dN_\nu}{dE} \right)_f, \quad (1.31)$$

where  $\Gamma_A$  is the annihilation rate,  $d$  is the distance from the source,  $f$  is the neutralino pair annihilation final state and  $B_\chi^f$  its branching ratio,  $(dN_\nu/dE)_f$  is the differential energy spectrum of neutrinos at the source surface, expected from channel  $f$ . Various annihilation channels are capable of producing high-energy neutrinos:  $W^+W^-$ ,  $Z^0Z^0$ ,  $\tau^+\tau^-$ ,  $b\bar{b}$  etc.

The neutrino energy spectra and angular distributions from WIMP annihilation in the Sun and the Earth are computed using the WIMPSIM simulation package as we will see in the paragraph 4.10.1.

### The case of the annihilation in the Sun and in the Earth

Here we briefly describe ([90, 51, 100]) the annihilation of WIMPs and the subsequent production of neutrinos into the Sun.

The determination of the energy spectra of neutrinos appearing in the equation 1.31 is complicated, as it involves hadronization of the annihilation products, interaction of particles with the surrounding medium and the subsequent interaction of neutrinos with it. This is the reason why the spectra of neutrinos from the Sun are different from those from the Earth [90].

The annihilation rate  $\Gamma_A$  must be computed through a parametrization of the WIMPs density into the core region of the Sun. The equation that describes the variation in time of the WIMPs number is given by [89]:

$$\frac{dN_\chi}{dt} = C - C_A N_\chi^2, \quad (1.32)$$

where  $C$  is the capture rate of the object (Sun in this case),  $N_\chi$  is the total number of WIMP in the object. The factor  $C_A$  is defined by the relation  $\Gamma_A = \frac{1}{2}C_A N_\chi^2$  where the factor 1/2 accounts for the vanishing of two WIMPs in one annihilation interaction.

The capture rate  $C$  depends on the nature of the WIMP (mass and WIMP-nucleus elastic scattering cross section), the properties of the dark matter halo (density and velocity dispersion) and the composition of the object in which the WIMPs are accumulating (density and chemical composition). The capture rate is

time-independent assuming the dark matter halo and the composition of the object remain constant in time.

The annihilation factor  $C_A$  in equation equals the WIMP annihilation cross section  $\sigma_\chi$  times the relative WIMP velocity  $v$  per unit volume, and depends on the WIMP distribution in the object. It can be approximated by [89]:

$$C_A = \frac{\sigma_\chi \cdot v}{V}, \quad (1.33)$$

where  $V$  is the effective volume of the object. The effective volume of the Sun is  $V_\odot \approx 5.8 \times 10^{30} m_\chi^{3/2} \text{ cm}^3$  and that of the Earth is  $V_\oplus \approx 1.8 \times 10^{27} m_\chi^{3/2} \text{ cm}^3$  with the WIMP mass in units of 1  $GeV$ .

The annihilation rate factor  $C_A$  of the Sun is higher than in the Earth, independent of the nature of the WIMP.

Solving the equation 1.32 for  $\Gamma_A$  gives:

$$\Gamma_A = \frac{C}{2} \tanh^2 \left( \frac{t}{\tau} \right), \quad (1.34)$$

where  $\tau = (CC_A)^{-1/2}$  is the equilibrium time scale between capture and annihilation rates in the object.

From equation 1.34 it can be seen that, for  $t \gg \tau$ , the annihilation rate depends only on the capture rate. In that case, it is the elastic scattering cross section and not the annihilation cross section that determines the annihilation rate. For both the Sun and the Earth, the relevant time scale is the age of the solar system ( $\approx 4.5 \times 10^9 \text{ yrs}$ ). The capture rate of the Sun is nine orders of magnitude larger than that of the Earth, while the effective volume of the Sun is only three orders of magnitude larger than that of the Earth. Hence the equilibrium time scale  $\tau$  for the Sun is always smaller than for the Earth, it means the equilibrium is always reached sooner in the Sun than in the Earth [100, 61].

Quantitatively, for the Sun  $\tau$  is much smaller than a few billion years, and therefore equilibrium is often a good approximation. This means that it is the capture rate which is the important quantity that determine the neutrino flux. For Earth, instead,  $\tau$  is usually of the same order as the age of the solar system and equilibrium has often not occurred [78].

### 1.7.2 Direct detection

The direct detection of dark matter is based on measures of the recoil energy of the nuclei of the detector on which WIMP particles hit. With expected WIMP masses ranging from 10  $GeV$  up to 10  $TeV$ , the typical nuclear recoil energies are of the order of 1-100  $KeV$ .

The shape of the nuclear recoil spectrum is given by the convolution of the WIMPs velocity distribution (Maxwellian) with the distribution of the angular scattering (peaked at high nuclear masses). The result is an exponential spectrum, the higher the WIMP mass the higher the exponential value. This points to the need for low nuclear energy threshold detectors. Usually the technique utilised can be temperature increase in cryogenic apparatus, ionization or scintillation. In

the experiments the observable is normally the scattering rate as a function of the energy;

The expected interaction rates depend on the local WIMP flux and on the interaction cross-section. It depends also from two unknown variables: the WIMP's mass and cross-section. The cross-section depends on the nature of the couplings. For non relativistic particles one has to distinguish between spin-dependent (SD) and spin-independent (SI) cross-sections [57].

The signal expected rate is of the order of 1 event  $day^{-1}kg^{-1}$ . Thus the problem is to separate the signal from the millions of background events, generated by cosmic rays and background radioactivity. For this purpose underground detectors are necessary. It is also customary to look for an annual modulation of the signal: considering the rotation of the Earth around the Sun, the WIMP flux should be greater in June (when the rotation velocity sums up to that of the Solar System with respect to the galaxy) than in December (when the two velocities are opposite) [51]. The total seasonal variation is roughly of 10%.

The sensitivity of the detectors usually have a maximum near the mass of the recoiling nucleus. Before the detector's threshold, and after the decreasing of the flux ( $\propto m_\chi^{-1}$ ) make the sensitivity drop.

Numerous are the experiments that direct search the WIMP: DAMA [31], CDMS [13], EDELWEISS [39], PICASSO among the others.

### 1.7.3 Indirect detection

The indirect search is based on the detection of the standard model particles produced into the WIMP annihilations. Its results are complementary to those of the direct search, they can explore high masses and different coupling scenarios.

WIMP annihilation in the galactic halo can give a continuous spectrum of gamma-ray and also mono-energetic photon contributions from the  $\gamma\gamma$  and  $\gamma Z$  channels. The resulting gamma-ray should have energies equal to the WIMP mass. However the size of this signal depends from the halo model, but it is expected to be very prominent in the Galactic Centre (GC).

Existing limits come from the EGRET satellite below 10  $GeV$  and from the WHIPPLE ground based telescope above 100  $GeV$  [55]. The Fermi-LAT satellite apparatus is now taking data toward the GC region, it will bring new better constraints on dark energy particle mass.

Other products of the WIMP annihilation in the galactic halo are constitute by anti-protons (detectable above the background only at very low energies) and positrons (possible cosmic ray positron flux excess). Experiments observing these products are PAMELA [9], HEAT [29] and also Fermi-LAT [8] among the others [57].

However, the main goal of the indirect detection of dark matter is the detection of neutrinos coming from the centre of massive astrophysical objects. As we said the WIMPs can be trapped in massive celestial bodies (like the Sun or the Earth) or just present into the Galactic Centre (where one thought there is a density peak of WIMP into the galactic halo [79]). Here they accumulate, enhancing their density, and annihilate producing diverse standard model particles (quarks, leptons, gauge bosons), The majority of the annihilation products are absorbed almost immediately,

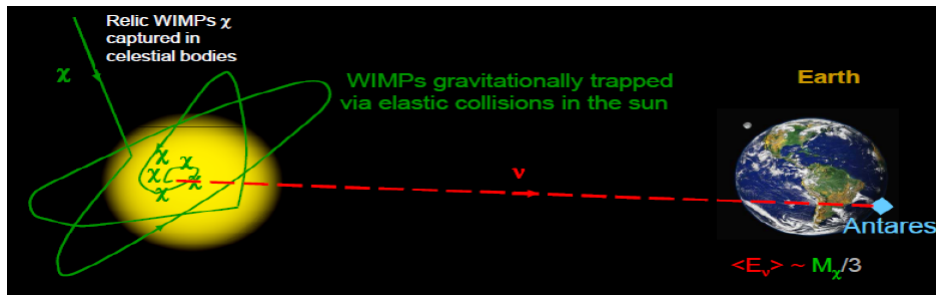


**Figure 1.8.** Mechanism scheme of how WIMPs are trapped into celestial bodies originating, after some intermediate standard model particles, neutrinos that can be detected at Earth by large neutrino telescope like ANTARES.

but some of them decay and produce mainly muon neutrinos [33], which can be detected in large neutrino telescopes such as IceCube [2, 30], ANTARES, MACRO and BAKSAN [37].

In fact, the interaction producing directly neutrinos (of the same energy of the WIMP mass) is suppressed for non relativistic particles.

Considering the different channels, the typical neutrino energy is roughly  $\frac{1}{3}$  to  $\frac{1}{2}$  the WIMP mass, far from the solar neutrino energies (few  $MeV$ ). A neutrino signal in the direction of the centre of the Sun, Earth or GC, with energy in the range of  $10 GeV$  to few  $TeV$ , can be a good experimental signature for dark matter.

## Chapter 2

# The super-symmetry theory and dark matter

In the Standard Model of particle physics there is a fundamental distinction between bosons and fermions, the former being the mediators of the interactions and the latter that are the constituents of matter. It is therefore natural to ask whether a symmetry exists which relates them, thus providing a sort of unified picture of matter and interactions [32].

Supersymmetry (SUSY) [147, 148, 126, 89] is a generalization of the space-time symmetries of quantum field theory that transforms fermions into bosons and vice-versa. Supersymmetry also provides a framework for the unification of particle physics and gravity, which is governed by the Planck energy scale  $M_P \approx 10^{19} \text{ GeV}$ , where the gravitational interactions become comparable, in magnitude, to the gauge interactions. In particular, it is possible that supersymmetry will finally explain the origin of the large hierarchy energy scales from the  $W$  and  $Z$  boson masses to the Planck scale (the so called gauge hierarchy) [82].

Supersymmetry or fermion-boson symmetry has not been observed in Nature yet.

In this chapter we will try to give [82, 103, 100, 32] some basics about the supersymmetry theory and the description of the supersymmetry candidate to assume the role of WIMP.

### 2.1 Introduction to Supersymmetry

The Poincaré group is the one that contains all the possible space-time symmetries of any quantum field theory: rotations, Lorentz boosts and translations in space and time. Its structure's algebra can be fully describe by the following expressions:

$$\begin{aligned} [M_{\mu\nu}, M_{\rho\sigma}] &= i(\eta_{\mu\sigma}M_{\nu\rho} - \eta_{\mu\rho}M_{\nu\sigma} + \eta_{\nu\rho}M_{\mu\sigma} - \eta_{\nu\sigma}M_{\mu\rho}); \\ [M_{\mu\nu}, P_\rho] &= i(\eta_{\nu\rho}P_\mu - \eta_{\mu\rho}P_\nu); \\ [P_\mu, P_\nu] &= 0; \end{aligned} \tag{2.1}$$

where  $M_{\mu\nu}$  is the generator of Lorentz transformations (rotations and boosts),  $P_\mu$  is the generator of space-time translations and  $\eta_{\mu\nu} = \text{diag}(1, -1, -1, -1)$  is the metric tensor.

The principal news of the SUSY theory is the introduction of a new operation, under which the Lagrangian is invariant, that is the rise of a new symmetry in nature. This operation was introduced to transform boson into fermions and vice-versa (that is the aim of the SUSY theory). The generator of this new operation is  $Q$ .

The SUSY transformations can be written as [32]:

$$Q|\text{fermion}\rangle = \text{boson} \quad \text{and} \quad Q|\text{boson}\rangle = \text{fermion}$$

Since the operators  $Q$  are of fermionic nature, they must carry spin 1/2. This implies that supersymmetry must be a space-time symmetry.

Thus, the algebra that involves  $Q$  (and its hermitian conjugate  $\bar{Q}$ ) is an extension of the algebra of Poincaré [103].

The anti-commutator of the operators are:

$$\begin{aligned} \{Q_a, Q_b\} &= 0 \\ \{\bar{Q}_{\dot{a}}, \bar{Q}_{\dot{b}}\} &= 0 \\ \{Q_a, \bar{Q}_{\dot{b}}\} &= 2(\sigma^\mu)_{a\dot{b}} P_\mu \end{aligned} \tag{2.2}$$

Instead, the commutator are:

$$\begin{aligned} [Q_a, P_\mu] &= 0 \\ [\bar{Q}_{\dot{b}}, P_\mu] &= 0 \\ [Q_a, M_{\mu\nu}] &= \frac{i}{4}(\sigma_\mu \bar{\sigma}_\nu - \sigma_\nu \bar{\sigma}_\mu)_a^b Q_b \\ [\bar{Q}_{\dot{a}}, M_{\mu\nu}] &= \frac{i}{4}(\bar{\sigma}_\mu \sigma_\nu - \bar{\sigma}_\nu \sigma_\mu)_{\dot{a}}^{\dot{b}} \bar{Q}_{\dot{b}} \end{aligned} \tag{2.3}$$

where  $Q_a, \bar{Q}_{\dot{a}}$  are the left-handed and right-handed two components Weyl spinors with indexes  $a, \dot{a} = 1, 2$ ;  $\sigma^\mu = \bar{\sigma}_\mu = (\mathbf{1}, \sigma^1, \sigma^2, \sigma^3)$  and  $\sigma_\mu = \bar{\sigma}^\mu = (\mathbf{1}, -\sigma^1, -\sigma^2, -\sigma^3)$ , where  $\sigma^i$  are the Pauli matrices and  $\mathbf{1}$  is the  $2 \times 2$  identity matrix.

The algebra of supersymmetry naturally guarantees the existence of new particles, with the required properties, associating to all of the particles of the Standard Model their super-partners, with the same mass and opposite spin-type (boson or fermion). The super-partners can be transformed one into another with a combination of  $Q$  and  $\bar{Q}$ .

All the single state particles are contained in the so called super-multiplets. They represent the irreducible representation of the supersymmetry algebra. Each super-multiplet contains both boson and fermion states with the same number of degrees of freedom.

The Standard Model gauge group is:  $SU(3)_{\text{color}} \times SU(2)_{\text{left}} \times U(1)_{\text{hypercharge}}$ . Since both  $Q$  and  $\bar{Q}$  commute with the SM group, all the particles in the same super-multiplet have the same gauge quantum number. This implies that the particles of the SM can not be super-partners of one another in a super-multiplet.

Thus, the supersymmetry theory predicts the existence of some new particles:

- *squarks*: Spin 0 super-partner for each right- and left-handed quark field;
- *sleptons*: Spin 0 super-partner for each right- and left-handed lepton field;
- *gauginos*: Spin 1/2 super-partner for each gauge boson field;
- *higgsinos*: Spin 1/2 super-partner for each Higgs boson field.

The super-partners of the same super-multiplet must also have the same mass, since  $P^2 = P_\mu P^\mu$  is a Casimir operator of the supersymmetry algebra. As we said, since none of the supersymmetric particles have been observed, SUSY must be a broken symmetry. Thus, one think that the supersymmetry is broken at the electro-weak scale [100].

The supersymmetry theory solves also some problems of the Standard Model as [82]:

1. A natural (i.e. one that is stable with respect to quantum corrections) explanation of the gauge hierarchy problem[136];
2. The unification of the three SM gauge couplings at a very high energy ( $M_U = 2 \times 10^{16} \text{ GeV}$ ): close to the Planck scale [118, 20];
3. The existence of dark matter, which makes up approximately one quarter of the energy density of the Universe (as we saw in the section 1.5) and that can not be explained within the SM [32].

### The R-parity

In the Standard Model, baryon and lepton numbers are conserved. This because the most general gauge-invariant and re-normalizable Lagrangian does not contain any baryon or lepton number violating interactions. For the supersymmetric Lagrangian this is not the case. But, combining the baryon number  $B$ , and the lepton number  $L$  it is possible to construct a new quantum number for a particle of spin  $S$ : the *R-parity* [65].

This new number is defined by:

$$R = (-1)^{2S+3(B-L)}. \quad (2.4)$$

The imposition of the R-parity conservation implies that the baryon and lepton number violating processes are forbidden. Furthermore, the definition is such that all Standard Model particles are R-parity even, while all their super-partners are R-parity odd.

As we will see the conservation of the R-parity make the lightest super-partner (LSP) stable.

## 2.2 The Minimal Supersymmetric Standard Model

The *Minimal Supersymmetric Standard Model (MSSM)* is the minimal supersymmetric extension of the Standard Model. This theory contains the smallest possible super-multiplets necessary to give rise to all the fields of the SM, and those,

allowed by the transformation invariance under the SM gauge symmetry group ( $SU(3)_C \times SU(2)_L \times U(1)_Y$ ), re-normalizable and R-parity conserving (see table 2.1).

This can be done in the following way [32]:

- Associating fermionic super-partners to all gauge fields. Gluons,  $W^\pm$ , and B bosons get fermionic partners called gluinos ( $\tilde{g}$ ), winos ( $\tilde{W}^i$ ) and binos ( $\tilde{B}$ ) respectively. They all share a common name: gauginos.
- Associating scalar partners to the fermions, i.e. quarks and leptons get scalar partners called squarks and sleptons as we just saw before.
- Introducing one additional Higgs field (for a total of two Higgs doublets, corresponding to five physical Higgs states) and associate one spin 1/2 Higgsino to each Higgs boson. This is done to give masses to both up and down-type quarks upon electroweak symmetry breaking and also preserve supersymmetry (therefore, we cannot use the conjugate of the Higgs as is done in Standard Model). Introducing another Higgs doublet also makes the theory anomaly free.

In the table 2.1 are shown all the particles of the MSSM model with their Standard Model particles.

**Table 2.1.** Standard model particles and their super-partners [61].

Standard Model particles and fields		Supersymmetric partners			
Symbol	Name	Interaction eigenstates Symbol	Name	Mass eigenstates Symbol	Name
$q = d, c, b, u, s, t$	quark	$\tilde{q}_L, \tilde{q}_R$	squark	$\tilde{q}_1, \tilde{q}_2$	squark
$l = e, \mu, \tau$	lepton	$\tilde{l}_L, \tilde{l}_R$	slepton	$\tilde{l}_1, \tilde{l}_2$	slepton
$\nu = \nu_e, \nu_\mu, \nu_\tau$	neutrino	$\tilde{\nu}$	sneutrino	$\tilde{\nu}$	sneutrino
$g$	gluon	$\tilde{g}$	gluino	$\tilde{g}$	gluino
$W^\pm$	$W$ -boson	$\tilde{W}^\pm$	wino	} $\tilde{\chi}_{1,2}^\pm$	} chargino
$H^-$	Higgs boson	$\tilde{H}_1^-$	higgsino		
$H^+$	Higgs boson	$\tilde{H}_2^+$	higgsino		
$B$	$B$ -field	$\tilde{B}$	bino	} $\tilde{\chi}_{1,2,3,4}^0$	} neutralino
$W^3$	$W^3$ -field	$\tilde{W}^3$	wino		
$H_1^0$	Higgs boson	$\tilde{H}_1^0$	higgsino		
$H_2^0$	Higgs boson	$\tilde{H}_2^0$	higgsino		
$H_3^0$	Higgs boson				

The MSSM is characterised by the so called super-potential, defined as:

$$\mathcal{W} = \epsilon_{ij} [y_e H_1^j L^i E^c + y_d H_1^j Q^i D^c + y_u H_2^j Q^j U^c] + \epsilon_{ij} \mu H_1^i H_2^j, \quad (2.5)$$

where  $i$  and  $j$  are  $SU(2)$  indices and  $y$  are the Yukawa couplings. Colour and generation indices have been suppressed in the above expression.

The super-potential represents a super-symmetrization of the standard Yukawa couplings plus a bilinear Higgs term. The super-potential enters in the Lagrangian of the theory through the following terms:

$$\mathcal{L}_{\text{SUSY}} = -\frac{1}{2}(W^{ij}\psi_i\psi_j + W_{ij}^*\psi^{i\dagger}\psi^{j\dagger}) - W^iW_i^*, \quad (2.6)$$

where  $W^i = \partial W/\partial\phi_i$ ,  $W_i^* = \partial W/\partial\phi^{i*}$  and  $W^{ij} = \partial^2 W/\partial\phi_i\partial\phi_j$  with  $\phi_i$  and  $\psi_j$  that are the scalar field and the fermion field respectively [32].

## 2.3 The lightest super-symmetric particle

In the MSSM model the R-parity must also be conserved.

All the Standard Model particles have R-parity  $R = 1$  and all their super-partners have  $R = -1$ . Thus, as a consequence of R-parity conservation, the sparticles can only decay into an odd number of sparticles (plus Standard Model particles).

From R-parity considerations arise that the currently best motivated WIMP candidate is the lightest super-particle in supersymmetric models (LSP) with exact R-parity (which guarantee the stability of the LSP).

### 2.3.1 SUSY WIMP candidates

Searches for exotic isotopes imply that a stable LSP has to be neutral.

This leaves only few candidates among the super-partners of ordinary matter:

- **sneutrino.** Sneutrinos have large annihilation cross-sections and masses (several hundreds GeV: uncomfortably heavy to be the lightest sparticle) to make them good candidates for dark matter.
- **axino and gravitino.** These two sparticles, that are the super-partners of SM axion and graviton, cannot be a priori excluded, they arise only in a subset of supersymmetric scenarios, but they are in contrast with some of the results of cosmology (like the measured light elements abundance). They also have very weak interactions and would be practically impossible to detect, making them less interesting from a phenomenological perspective.
- **neutralino.** Is the most widely studied WIMP candidate; in particular the lightest neutralino, that is stable and can only be destroyed by via pair annihilation. Detailed calculations [94] show that the lightest neutralino will have also the desired thermal relic density [57]

### 2.3.2 The SUSY broken symmetry

To describe the neutralino characteristics and its origin we have to consider the way in which the supersymmetry has been broken [100, 32].

In the MSSM there is a spontaneous electro-weak symmetry breaking. It occurs because the neutral components of the two Higgs doublets have non-zero vacuum expectation values while their charged counterparts have zero vacuum expectation values .

If supersymmetry was not broken, then each super-partner would have a mass identical to its Standard Model counterpart, which is clearly not the case. Thus, new terms which break supersymmetry must be added to the Lagrangian. One have

to pay attention in introducing these new terms: they must respect the hierarchy between the Planck and electro-weak scales. The new terms are:

$$\mathcal{L}_{\text{SOFT}} = -\frac{1}{2}M_\lambda^a \lambda^a \lambda^a - \frac{1}{2}(m^2)_j^i \phi_i \phi_j^{j*} - \frac{1}{2}(BM)^{ij} \phi_i \phi_j - \frac{1}{6}(Ay)^{ijk} \phi_i \phi_j \phi_k, \quad (2.7)$$

where  $M_\lambda^a$  represents the gaugino masses,  $m^2$  are soft scalar masses,  $B$  is the bilinear mass term and  $A$  is the trilinear mass term.

Electro-weak symmetry breaking induces a mixing between fields that have different  $SU(2)_C \times U(1)_Y$  quantum numbers but the same baryon, lepton and  $SU(3)_C \times U(1)_{em}$  quantum numbers. In the SM case the mixing operation leads to SM particles plus an additional CP-even Higgs scalar  $H^0$ , a CP-odd Higgs scalar  $A^0$  and two charged Higgs scalars  $H^\pm$ . Instead in the case of the super-partners fields there is a mixing between left-handed and right-handed sfermions and a mixing between the electro-weak gauginos and the higgsinos.

In particular, the mixing, due to electro-weak symmetry breaking, of the gauginos and the higgsinos is at the origin of the neutralino super-particles.

### 2.3.3 The lightest neutralino

In the MSSM model, as can be seen in the table 2.1 the the super-partners of the  $B$ ,  $W_3$  gauge bosons and the neutral Higgs bosons,  $H_1^0$  and  $H_2^0$ , are called binos ( $\tilde{B}$ ), winos ( $\tilde{W}_3$ ), and higgsinos ( $\tilde{H}_1^0$  and  $\tilde{H}_2^0$ ) respectively.

These states mixing originate four Majorana fermionic mass eigenstates, called neutralinos:  $\tilde{\chi}_1^0, \tilde{\chi}_2^0, \tilde{\chi}_3^0, \tilde{\chi}_4^0$  according to the increasing mass.

The lightest neutralino, thus the LSP, is  $\tilde{\chi}_1^0$ ; we will, from now on, call it by the simple form  $\chi$ .

In the so-called neutralino gauge eigenstate basis ( $\tilde{B}$ ;  $\tilde{W}_3$ ;  $\tilde{H}_1^0$ ;  $\tilde{H}_2^0$ ), the neutralino mass matrix  $M_\chi$  that appears in the MSSM Lagrangian can be written as:

$$\mathcal{M}_\chi = \begin{pmatrix} m_{\tilde{B}} & 0 & -c_\beta s_{\theta_W} m_Z & s_\beta s_{\theta_W} m_Z \\ 0 & m_{\tilde{W}} & c_\beta c_{\theta_W} m_Z & -s_\beta c_{\theta_W} m_Z \\ -c_\beta s_{\theta_W} m_Z & c_\beta c_{\theta_W} m_Z & 0 & -\mu \\ s_\beta s_{\theta_W} m_Z & -s_\beta c_{\theta_W} m_Z & -\mu & 0 \end{pmatrix} \quad (2.8)$$

where  $m_{\tilde{B}}$  and  $m_{\tilde{W}}$  are the bino and wino mass parameters;  $m_Z$  is the  $Z$  boson mass;  $c_{\theta_W} = \cos \theta_W$  and  $s_{\theta_W} = \sin \theta_W$  with  $\theta_W$  is the Weinberg electro-weak mixing angle;  $\mu$  is the higgsino mass parameter;  $c_\beta = \cos \beta$  and  $s_\beta = \sin \beta$  with  $\beta$  is the related to the vacuum expectation values of the neutral components of the two Higgs doublets by  $\tan \beta = \langle H_1^0 \rangle / \langle H_2^0 \rangle$ .

The neutralino mass matrix is a  $4 \times 4$  symmetric and Hermitian matrix. Thus it can be diagonalised through the unitary  $4 \times 4$  matrix  $N$  according to [82]

$$N^\dagger M_\chi N = \text{diag}(M_{\tilde{\chi}_1^0}, M_{\tilde{\chi}_2^0}, M_{\tilde{\chi}_3^0}, M_{\tilde{\chi}_4^0}). \quad (2.9)$$

where the right-hand side of the equation 2.9 is the diagonal matrix of (non negative) neutralino masses.

The matrix  $N$  is the neutralino mixing matrix that relates the neutralino mass eigenstates ( $|\tilde{\chi}_i^0\rangle$ , where  $i = 0, \dots, 4$ ) to the gauge eigenstates  $|\tilde{\chi}_\alpha^0\rangle = (\tilde{B}; \tilde{W}_3; \tilde{H}_1^0; \tilde{H}_2^0)$  by the relation:

$$|\tilde{\chi}_i^0\rangle = \sum_{\alpha=1}^4 N_{\alpha i}^* |\tilde{\chi}_\alpha^0\rangle \quad \Longleftrightarrow \quad |\tilde{\chi}_\alpha^0\rangle = \sum_{i=1}^4 N_{\alpha i} |\tilde{\chi}_i^0\rangle. \quad (2.10)$$

The four gauge eigenstate fractions of neutralino mass eigenstate  $|\tilde{\chi}_i^0\rangle$  are  $|N_{\alpha i}^*|^2$  for  $\alpha = (0, \dots, 4)$ .

With all we have just seen we can reconstruct the linear combination of the neutralino gauge eigenstates base that compose the lightest neutralino particle:

$$\chi = N_{11}\tilde{B} + N_{12}\tilde{W}_3 + N_{13}\tilde{H}_1^0 + N_{14}\tilde{H}_2^0. \quad (2.11)$$

The neutralino interactions most relevant for the purposes of dark matter are self annihilation and elastic scattering off of nucleons as we saw in the section 1.7. Neutralinos are expected to be extremely non relativistic in the present epoch, thus, we can use the power expansion of the annihilation cross-section 1.30. We can take only the  $a$  term in the expression and the  $b$  term must be used only to evaluate the relic density (see paragraph 1.6.1).

At low velocities, the leading channels for neutralino annihilation are annihilations to fermion-anti-fermion pairs (quarks and leptons) and gauge bosons pairs. In our analysis we will use only the three channels  $b\bar{b}, \tau^+\tau^-, W^+W^-$ .

Although extremely massive neutralinos are not favoured theoretically [27]. Neutralinos in the 100 GeV range may still be the better candidates for solving the problem of the presence of dark matter in our Universe [90].

### 2.3.4 The minimal supergravity model

The MSSM is rather impractical due to its many parameters (most of which representing masses and mixing angles). Thus the number of parameters which are considered must be reduced. This can be done with some assumption finalised to reduce the amount of free parameters.

One of the models that simplify things is the mSUGRA model [92], also called constrained MSSM (cMSSM). This expression stands for *minimal supergravity (mSUGRA)*. It is assumed that the gauge couplings unify at the grand unification scale, as well as the supersymmetry breaking parameters.

In mSUGRA, spontaneous electro-weak symmetry breaking is generated dynamically through quantum corrections: the conditions for electro-weak symmetry breaking contain the supersymmetry breaking Higgs mass parameters  $m_{H_u}^2$  and  $m_{H_d}^2$ . These are unified at  $m_0^2$  at the grand unification scale (see below). However, re-normalization group evolution drives the supersymmetry breaking Higgs mass parameter  $m_{H_u}^2$  to negative values at the electro-weak scale, which therefore spontaneously breaks the electro-weak symmetry. This process is called radiative electro-weak symmetry breaking.

The number of free parameters is reduced in this scenario by assuming that the MSSM parameters obey a set of boundary conditions at the Grand Unification scale:

- Gauge coupling unification:  $\alpha_1(M_U) = \alpha_2(M_U) = \alpha_3(M_U) = \alpha_U$ , with  $\alpha_i = g_i^2/4\pi$ ;
- Unification of the gaugino masses:  $m_{1/2}$ ;
- Universal scalar masses (for sfermion and Higgs boson):  $m_0$ ;
- Universal trilinear couplings:  $A_0$ .

By requiring the minimization of the Higgs potential (in order to recover electroweak symmetry breaking), we are left with five (four continuous and one discrete) free parameters:

$$\tan \beta, \quad m_{1/2}, \quad m_0, \quad A_0, \quad \text{sign}(\mu)$$

where  $\tan \beta$  is the ratio of the vacuum expectation values of the two Higgs fields and  $\mu$  is the higgsino mass parameter [32].

## Chapter 3

# The ANTARES neutrino telescope

The aim of the neutrino astronomy is to try to detect astrophysical objects by means of the neutrino fluxes produced by them. Since the neutrino interaction cross-section is very small ( $\sigma_\nu \approx 0.5 \times 10^{-38} \text{cm}^2 \times E_\nu(\text{GeV})$  for  $E_\nu < 10^4 \text{ GeV}$  [72]), neutrinos can be used as messengers of the Universe: they are able to carry on information, like direction and energy, on enormous distances. Thus, observations that would be impossible to perform only with the electromagnetic interaction, such as radio, visible or X-ray, can be done with neutrinos.

To detect neutrinos some neutrino telescope have been built in the recent years. This kind of telescopes are based on the revelation of the Cherenkov light induced by the propagation of relativistic muons generated by neutrino interactions in transparent means like water or ice. Given the small value of neutrino cross-section and the decrease of the flux with the increasing energy, only detectors of big mass are necessary.

Usually these big Cherenkov detectors are built in the sea, like ANTARES, or in the ice, like IceCube. In this chapter, after a brief introduction about the importance of the neutrino astronomy (paragraph 3.0.5), will be described the ANTARES neutrino Cherenkov telescope (ANTARES stands for Astronomy with a Neutrino Telescope and Abyss environmental RESearch) [139, 140, 141].

### 3.0.5 Neutrino astronomy

The bigger part of our knowledge of the Universe comes from the photons observations. In fact, the photons are stable and electrically neutral, they are also very easy to detect over a wide energy range and their spectrum can give information about the physical properties of the source. For these reasons they are commonly used as cosmic information carriers [51].

Unlikely, some regions of the Universe, in particular the hot and dense zones, such as the Active Galactic Nuclei (AGN) and other astrophysical sources (quasars, GRB etc.), are totally opaque to photons. Therefore these regions can not be investigated by a direct observation of photons.

Another effect that alters the photons transmission in the Universe is their interactions with the Cosmic Microwave Background (CMB), described in section

1.4 and Infra Red (IR) radiations. In these interactions electron-positron pairs are created. Thus, this effect prevents us from observing the sky over distances bigger than 100  $Mpc$  with high energy ( $> 10 TeV$ ) gamma rays (see figure 3.1).

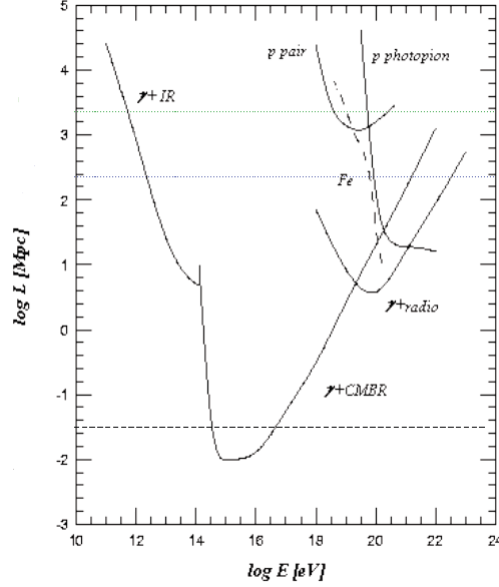


**Figure 3.1.** The figure shows how much protons and photons can propagate in the cosmic space (for several interactions, including the GZK cut-off) as a function of the energy.

The protons are also affected by the interaction with the matter and the radiation in the inter galactic space. For example, the GZK effect (from the names of the three physicists that found it first: Greisen-Zatsepin-Kuz'min) [80], [150] is caused by the interaction of high energy photons with the Cosmic Microwave Background radiation (CMB). Protons are also affected by magnetic fields and can not be used as messengers of the Universe for  $E_p < 10^{19} eV$ .

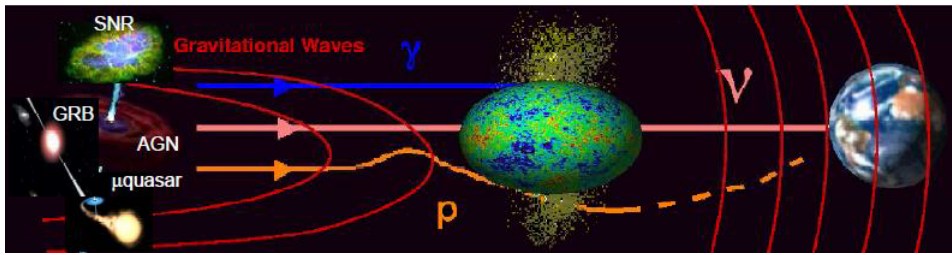


**Figure 3.2.** In this image is shown the importance of the neutrino astronomy. Neutrinos are the only particles that can travel over large distances in the Universe without losing the information on the source that they carry on with themselves.

To investigate the inner part of the hot and dense astrophysical objects and to have a description of the Universe over large distances and energy ranges, one needs to find a particle that is electrically neutral, in this way its trajectory will not be affected by magnetic fields, but also stable and weakly interacting, so that it will penetrate also the regions that are opaque to the photons. This particle is the

neutrino!

Neutrinos can be used to observe the core of the stars and the Supernova explosions (also if neutrino sources with an energy bigger than 10 GeV have never been observed) since they are foreseen by the cosmic ray properties; also Supernova remnants and AGN are expected to produce high energy neutrinos. As a matter of fact these objects are supposed to be the sources of the primary cosmic rays (composed by protons and, in a small part, heavy nuclei). The cosmic rays spectrum is extended up to  $10^{22}$  eV. Protons of these high energies interact with the matter and the radiation that surround the source and produce high energy pions. This pions, neutral and charged, then decay respectively giving gamma rays and neutrinos.

Another important target for the neutrino astronomy is the indirect search for dark matter particles. The most diffused theoretical model to explain the dark matter content of the Universe is the neutralino WIMP model, as we explained in chapter 2. Neutrino telescopes are sensitive to neutrinos produced in the decay of gauge bosons and other heavy particles arising from neutralino annihilations.

### 3.1 Detection principle

Since the Earth acts as a shield against all the particles except neutrinos, a neutrino telescope utilizes the detection of muons up-going (i.e. originated in the Earth below the detector) like a signature of a muon neutrino ( $\nu_\mu$ ) interaction.

The muon, travelling in water or ice, induces Cherenkov light that has to be revealed by the detector. Muons propagate in water leaving energy for Coulomb scattering and for bremsstrahlung. Typically a 1 TeV muon can propagate in water for  $\sim 2$  km, then it can be easily revealed in a "sparse" detector. The big range of distance covered by the muons, permit to observe also interactions that happened kilometres far from the detector.

Neutrinos of different flavours ( $\nu_e$  and  $\nu_\tau$ ) can also be detected, but with less efficiency and angular precision, because the travelled distances of the respective leptons ( $e$ ,  $\tau$ ) are short.

The muon neutrino detection technique requires to discriminate the up-going muons from the much bigger flux of muons due to atmospheric showers produced by High Energy Cosmic Rays (HECR): the so called down-going muons. Consequently, to simplify the discrimination, the detector must be placed under a big amount of water or ice: in the deep sea or under the polar icecap. In this way the water or ice, above the detector, acts like a shield against the down-going muon particles as can be seen in the figure 3.3.

Thus, the ANTARES detector is composed by twelve arrays of Optical Modules (OM), that are glass balls containing one photomultiplier (PMT), disposed on flexible lines and anchored to the sea floor at 2400 m depth.

The reconstruction of the muon tracks is based on measures of the arrival time of the Cherenkov photons on the OMs, which positions are known. As it will be described later, ANTARES is capable to detect muons with a minimum energy equal to 20 GeV, for well reconstructed muons.

Monte Carlo simulations also indicate that the directions of highly energetic neutrinos can be revealed with an accuracy of roughly  $0.3^\circ$  for energies beyond

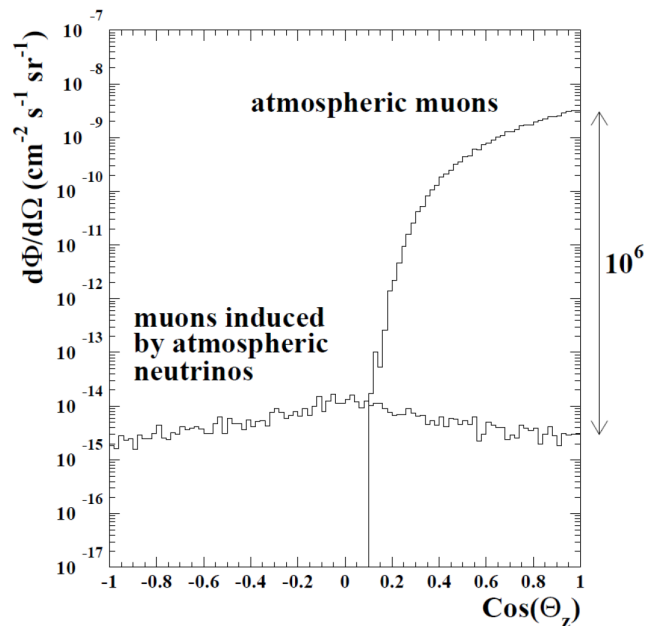


**Figure 3.3.** Zenith angle distribution of the muon flux above 1  $TeV$  for atmospheric muons and atmospheric neutrino induced muons at 2400m water equivalent depth [140].

10  $TeV$ .

### 3.2 Neutrino interactions

Neutrinos are neutral leptons, they can interact with matter only by weak interactions. Thus, their interaction length is very big, so neutrino detectors must have either a large volume or a high density matter [140].

There are only two possible channels of weak interaction for neutrinos: Charge Current (CC) and Neutral Current (NC) interactions .

- The weak CC interaction of a neutrino (or anti-neutrino) with a nucleon  $N$  of matter, produces a charge lepton  $l^\pm$  ( $l = e, \mu, \tau$ ) of the same flavour of the original neutrino and an hadron shower  $X$ :

$$\nu_l(\bar{\nu}_l) + N \xrightarrow{W^+(W^-)} l^-(l^+) + X. \quad (3.1)$$

- The weak NC interaction of a neutrino (or anti-neutrino) with a nucleon of matter do not produce any lepton in the final state of the interaction:

$$\nu_l(\bar{\nu}_l) + N = \nu_l(\bar{\nu}_l) + X. \quad (3.2)$$

The cases of interest for neutrino telescopes are the CC interactions producing a charged lepton in the final state, because these leptons can be revealed by the apparatus if they induce Cherenkov light.

The differential inclusive deep inelastic cross-section of this process (where the lepton mass is neglected) is given by [75]:

$$\frac{d^2\sigma_{\nu N}}{dxdy} = \frac{2G_F^2 m_N E_\nu}{\pi} \frac{M_W^4}{(Q^2 + M_W^2)^2} [xq(x, Q^2) + x(1-y)^2 \bar{q}(x, Q^2)] \quad (3.3)$$

where  $G_F$  is the Fermi constant,  $m_N$  and  $M_W$  are the nucleon and W boson masses, and  $Q^2$  is the square of the momentum transfer between the neutrino and muon.  $q(x, Q^2)$  and  $\bar{q}(x, Q^2)$  represent the probability to find a quark (anti-quark) in the nucleon. In the formula 3.3  $x = Q^2/2m_N\nu$  and  $y = (E_\nu - E_l)/E_\nu$  are the Bjorken variables [83, 119], where  $\nu = (E_\nu - E_l)$  is the lepton energy loss in the laboratory frame.  $\nu$  is the amount of energy that will be carried out by the hadronic content.

### 3.2.1 Low energy interactions

At energies such that  $E_\nu \ll M_W^2/2m_N \approx 3 \text{ TeV}$ ,  $Q^2$  can be neglected in the  $W$  propagator. In this case the average deep inelastic  $\nu N$  cross-section grows linearly with the neutrino energy (see figure 3.4):

$$\sigma_{DIS}(\nu N) \simeq 0.67 \times 10^{-38} E_\nu [\text{GeV}] \text{ cm}^2$$

$$\sigma_{DIS}(\bar{\nu} N) \simeq 0.34 \times 10^{-38} E_\nu [\text{GeV}] \text{ cm}^2$$

At even lower energies ( $E_\nu < 100 \text{ GeV}$ ), quasi elastic and resonant contributions to the charged current interactions have to be considered. In this case  $Q^2$  has to be small enough to allow a coherent interaction with the complete target nucleon, so these cross-sections are essentially constant with the energy. A fit to data above  $10 \text{ GeV}$  gives the following sums for the quasi elastic and resonant production processes [122]:

$$\sigma_{QE}(\nu_\mu N) + \sigma_{res}(\nu_\mu N) = 1.50 \times 10^{-38} \text{ cm}^2$$

$$\sigma_{QE}(\bar{\nu}_\mu N) + \sigma_{res}(\bar{\nu}_\mu N) = 1.58 \times 10^{-38} \text{ cm}^2$$

Between  $10 \text{ GeV}$  and  $500 \text{ GeV}$  the vertical  $\nu_\mu$  flux is approximately proportional to  $1/E_\nu^3$ . Integrating the cross-sections given above over this flux for  $E_\nu > 10 \text{ GeV}$  results in a quasi elastic and resonant contribution of 11% for  $\nu_\mu$  and 21% for  $\bar{\nu}_\mu$  interactions.

### 3.2.2 High energy interactions

At energies such that  $E_\nu \gg M_W^2/2m_N \approx 3 \text{ TeV}$ , quasi elastic and resonant contributions are completely negligible. On the other hand, the  $W$  propagator limits the growth of  $Q^2$  to  $\langle Q^2 \rangle \sim M_W^2$  and so the cross-section is dominated by the behaviour of distribution functions at small  $x$ .

The H1 [3] and ZEUS [4] collaborations at HERA measured the proton structure function  $F_2(x, Q^2)$  via charged current electron-proton scattering, for  $Q^2$  in the range from  $1.5$  to  $5000 \text{ GeV}^2$  with  $x$  ranging from  $3 \times 10^{-5}$  to  $2 \times 10^{-2}$  respectively [12].

These measurements can be translated into a neutrino-nucleon interaction cross-section at  $E_\nu \simeq 50 \text{ TeV}$  and can also be used as a guide to extrapolate the parton

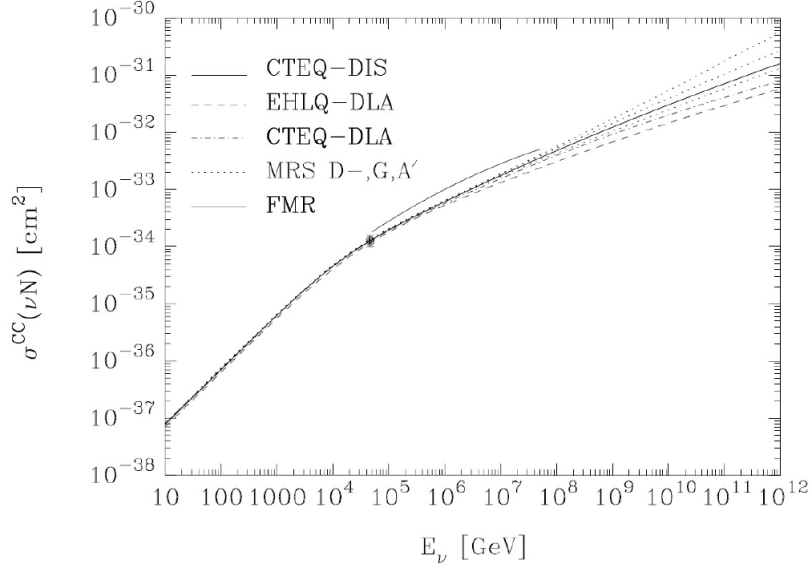


**Figure 3.4.** Averaged charged current cross-section for  $\nu N$  interactions for different sets of parton distribution functions [140]. The data point correspond to the average of the measurements by H1 and ZEUS at HERA.

densities beyond the measured ranges in  $x$  and  $Q^2$  to those required for higher neutrino energies. The figure 3.4 shows the behaviour of the average  $\nu N$  cross-section for different sets of parton distribution functions.

### 3.2.3 Different types of neutrino interactions in ANTARES

Thanks to the high energies observables, the ANTARES experiment can, in principle, see all the interaction processes of the neutrino with matter. The signal is given by the Cherenkov light induced in water by the propagation of the relativistic charged leptons originated in the CC interactions; Several kind of pattern of signals can be interpreted as the signature of different neutrino types [140].

- **$\nu_\mu$  interactions:** CC  $\nu_\mu$  interactions produce  $\mu^\pm$  leptons as well as point-like hadron shower. The  $\nu_\mu$  energy can be estimated from the measured  $\mu^\pm$  energy.

$$\text{In } \nu_\mu d \longrightarrow \mu^- u \text{ interactions, the average } E_{\mu^-} \sim \frac{1}{2} E_{\nu_\mu};$$

$$\text{In } \bar{\nu}_\mu u \longrightarrow \mu^+ d \text{ interactions, the average } E_{\mu^+} \sim \frac{3}{4} E_{\bar{\nu}_\mu}.$$

The  $\mu^\pm$  energy can be determined from the range for  $E_\mu < 100 \text{ GeV}$ , or from  $\frac{dE}{dx}$  for  $E_\mu > 1 \text{ TeV}$ . For  $\nu_\mu$  interactions inside the detector, additional information on the  $\nu_\mu$  energy is available from the hadron shower. The ANTARES detector is principally designed for the detection of these CC  $\nu_\mu$  interactions.

- **$\nu_e$  interactions:** CC  $\nu_e$  interactions give rise to electromagnetic and hadron showers with longitudinal dimensions of no more than a few metres, because the radiation length ( $\sim 36 \text{ cm}$ ) and the nuclear interaction length of water ( $\sim 83 \text{ cm}$ ) are below  $1 \text{ m}$  (the distance between the instrumented lines of

ANTARES is  $\sim 60 m$ ). On the scale of ANTARES, these are nearly point-like events. At energies above  $100 GeV$ , the energy resolution of these events is expected to be better than the one that can be obtained for muon-type events because the showers leave all of their energy inside the detector volume. On the other hand, their angular resolution will be poor compared to the one for muon-type events, due to the point-like character of the showers.

These interactions are contaminated by NC interactions of all three flavours of neutrino. The number of NC interactions is about  $\frac{1}{3}$  of the number of CC interactions. The neutrino type is not identified in the NC case, the energy resolution is poor due to the missing final state neutrino and the angular resolution is poor due to the point-like character.

- **$\nu_\tau$  interactions:** CC  $\nu_\tau$  interactions produce  $\tau^\pm$  leptons with electronic, muon and hadron decay modes. The  $\nu_\tau$  interaction vertex and the  $\tau^\pm$  decay vertex can not be separated for energies below  $\sim 100 TeV$ . The electronic and hadron modes will look like  $\nu_e$  CC or NC interactions. The muon decays  $\tau^- \rightarrow \mu^- \bar{\nu}_\mu \nu_\tau$ , with branching ratio of 17%, will be visible in ANTARES, but such events can not be distinguished from CC  $\nu_\mu$  interactions.

### 3.3 The Cherenkov effect

The Cherenkov effect happens when charged particles pass through a transparent medium with a velocity that exceeds the speed of light in the medium [119, 72]. This causes the polarization of the molecules of the medium along the trajectory of the particle (see figure 3.5), with a consequent emission of induced electromagnetic radiation that propagates with a conic wave-front as it is shown in the figure 3.6. This light is emitted under a characteristic angle: the Cherenkov angle  $\theta_C$  [140].

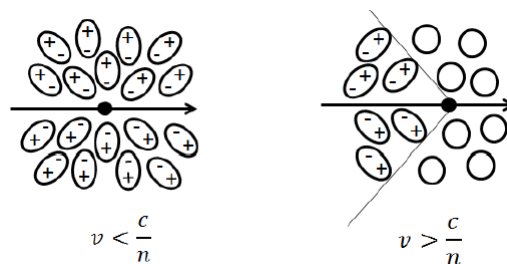


**Figure 3.5.** The effect of the medium molecules polarization when a charged particle pass through the medium with a velocity that exceeds the speed of light in the medium.

This angle  $\theta_C$  is related to the particle velocity  $\beta$  and the refractive index of the medium  $n$ :

$$\cos \theta_C = \frac{1}{n\beta}. \quad (3.4)$$

In the energy range interesting for ANTARES ( $E > 20 GeV$ ), secondary particles will generally be ultra-relativistic with  $\beta \simeq 1$ . The refractive index of the sea water is  $n = 1.35$  for a wavelength of  $450 nm$  therefore the Cherenkov light is emitted under a  $42^\circ$  angle for this wavelength.

This simple geometrical pattern of light emission allows a precise reconstruction of tracks from the measurement of only few hits (times of arrival) at different space points (PMT) of the apparatus.

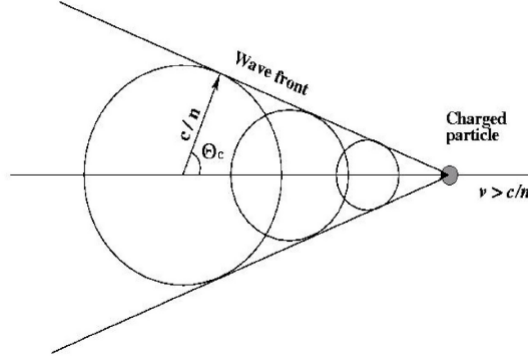


**Figure 3.6.** This image show the cone of Cherenkov light induced in the medium.

The number of photons produced along a flight path  $dx$  in a wavelength bin  $d\lambda$  for a particle carrying unit charge is:

$$\frac{d^2 N}{d\lambda dx} = 2\pi\alpha \frac{\sin^2 \theta_C}{\lambda^2}. \quad (3.5)$$

At wavelength of  $400 - 500 \text{ nm}$  the efficiency of the photomultiplier as well as the transparency of the water are maximal. Within  $1 \text{ cm}$  flight path 100 photons are emitted in this wavelength bin. Between  $285 - 400 \text{ nm}$  twice as many photons are emitted, however they contribute less to the detected signal. At a perpendicular distance of  $40 \text{ m}$  from a charged track the density of photons between  $400 - 500 \text{ nm}$  is still 1 per  $340 \text{ cm}^2$ , neglecting absorption and scattering effects.

For  $\beta = 1$  the Cherenkov light yield is independent of the energy of the charged particle. This means that the Cherenkov radiation does not allow to measure the energy of the particle that originated it. However when hadronic or electromagnetic showers are produced the electrons originated in the showers induce Cherenkov radiation. The number of  $e^\pm$  is proportional to the shower energy, so the total Cherenkov light emitted can allow an energy estimate of the event. This allows some calorimetric measurements if the neutrino vertex is inside the active detector volume or for muon tracks above  $1 \text{ TeV}$  where radiative processes dominate its energy loss.

### 3.4 Light propagation in sea water

The processes of absorption and scattering characterise the transmission of light in water. They are parametrised by the absorption length  $\lambda_a$ , the scattering length  $\lambda_s$  and the scattering function  $\beta(\theta_s)$  which describes the angular distribution of the volume scattering angle  $\theta_s$  [109].

The relevant window of wavelength for a sea water Cherenkov detector is centred on blue light. Deep sea water transparency is maximal in the blue, with typical values of  $60 \text{ m}$  for  $\lambda_a$ , and a scattering function peaked in the forward direction with

an average value for the cosine of the scattering angle  $\langle \cos \theta \rangle \simeq 0.9$ , as shown in figure 3.7.

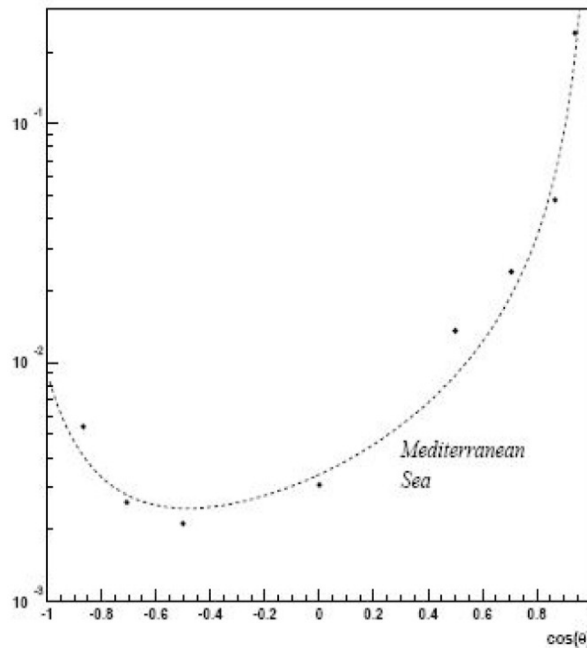


**Figure 3.7.** The angular distribution of light scattering in the deep Mediterranean Sea for  $(400 \leq \lambda \leq 500) \text{ nm}$  [109].

Seasonal variations are expected to affect these values, especially the scattering parameters which are governed by the amount of suspended particulate matter.

### 3.5 Track reconstruction technique

For muons with energy bigger than  $20 \text{ GeV}$  it is possible to approx the trajectory with a line and the velocity with the speed of light in vacuum  $c$ . We want to reconstruct the muon trajectories in a Cartesian coordinate system  $(x, y, z)$  centred in the detector center. In this system the muon track is completely determined by the point  $\vec{p} = (x_0, y_0, z_0)$  in which the muon passes at the reference time  $t_0$  and by the direction cosines:

$$\vec{d} = [\cos \phi \sin \theta, \sin \phi \sin \theta, \cos \theta], \quad (3.6)$$

with  $\phi$  and  $\theta$  that are respectively the Azimuth angle and the zenith angle (see figure 3.8). Let's define  $\theta_C$  the angle between the directions of the Cherenkov photon and the muon and  $\vec{q}_i = (x_i, y_i, z_i)$  the position of the  $i$ th PMT of the detector. The time of arrival of the photon on the PMT is given by:

$$t_{PMT}^i = t_0 + t_1 + t_2, \quad (3.7)$$

where, with respect to the figure 3.8,  $t_1 = \overline{OA} \cdot \frac{1}{c}$  is the time employed by the muon to travel from  $a$  to  $B$  and  $t_2 = \overline{AB} \cdot \frac{n}{c}$  is the propagation time in the medium with refractive index  $n$ .

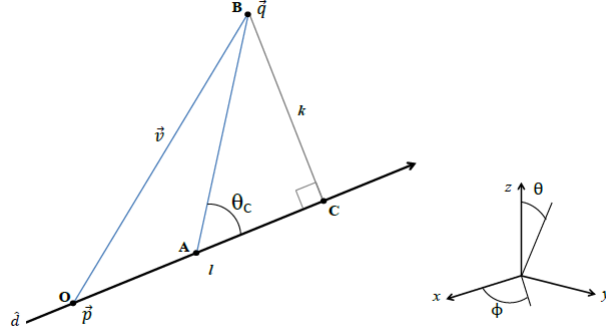


**Figure 3.8.** The track reconstruction scheme is shown. The arrow indicate the muon's trajectory,  $\theta_C$  is the angle under which the Cherenkov photons are emitted,  $B$  represents the position of the  $i$ -th PMT. The reference system is also reported.

Defining:

$$\vec{v} = \vec{q} - \vec{p} = \overline{OA}, \quad (3.8)$$

one has:

$$\vec{l} = \vec{v} \cdot \vec{d} = \overline{OC}, \quad (3.9)$$

thus, using the previous definitions 3.8 and 3.9, one has:

$$k = \sqrt{|\vec{v}|^2 - l^2}. \quad (3.10)$$

is the minimum distance between the track and the  $i$ -th PMT. Then the time of arrival, in  $\vec{q}(t_i)$ , of the photon is:

$$t_i = t_0 + \frac{1}{c} \left( l - \frac{k}{\tan \theta_C} \right) + \frac{1}{v_g} \frac{k}{\sin \theta_C}, \quad (3.11)$$

where  $v_g = \frac{c}{n}$  is the group velocity of light in water.

The relation 3.11, for each quintuple  $(x_0, y_0, z_0, \theta, \phi)$  that univocally identify the muon's track, allows to evaluate the time of arrival of the Cherenkov photons on the PMT of the apparatus. What really the detector measures are the times of arrival of Cherenkov photons on the single PMT (the hits). It is, then, possible to define a  $\chi^2$  function, as a function of the quintuple cited above, as the root mean square between the theoretical hit (for the assumed quintuple) times and the effectively measured ones. The minimization of this function permits to reconstruct the track.

For more details about the reconstruction strategy and the minimization procedure see the section 4.6 in the analysis chapter.

### 3.6 The detector response

The physical processes involved in the neutrino and muon interactions place limits both on the angular resolution (see paragraph 3.6.1) and the energy resolution (see paragraph 3.6.2) possible with a neutrino telescope. These limits must be taken into consideration when optimizing the detector design [140].

### 3.6.1 Angular response for $\nu_\mu$ interactions

The angular resolution of the detector in measuring the incoming neutrino direction is crucial for the identification of point sources of neutrinos. Three factors determine the detector response:

1. The angle between the neutrino and the muon in the neutrino interaction;
2. The deviation of the muon direction due to multiple scattering;
3. The intrinsic detector angular resolution.

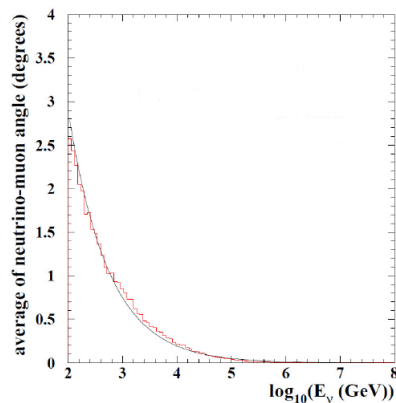


**Figure 3.9.** Angular difference between the initial neutrino direction and that of the reconstructed muon track at the detector; the observed energy dependence (solid curve) well reproduces what is expected by the kinematics [140].

The deviation of muons due to multiple scattering is negligible if compared to the other factors. The average of the neutrino-muon angle, due to kinematics, can be expressed by the formula:

$$\bar{\Theta}_{\mu\nu} \approx \frac{0.7^\circ}{\sqrt[0.6]{E_\nu [TeV]}} \quad (3.12)$$

At 1  $TeV$  the average difference between the original neutrino and the produced muon is about  $0.7^\circ$ . The difference decreases with increasing  $\nu$  energy, then the major contribution to the angular resolution will be due to the intrinsic properties of the detector.

The intrinsic angular detector resolution is determined by the quality of the alignment of the detector components, the time resolution of the photomultipliers, the global timing of the readout system and the quality of the muon reconstruction algorithm. The reconstruction will be affected by light coming from background ( $^{40}K$ , bioluminescence both described in section 3.15), by secondary particles (that propagates in diverse directions with respect to the muon one) and by scattered light. Monte Carlo studies show that, for  $E_\nu \geq 10 TeV$ , an angular resolution of  $0.2^\circ$  is possible. This means that above 10  $TeV$  the total angular resolution is dominated by the detector effects, whereas below 10  $TeV$ , the resolution is dominated by the angular distribution of the neutrino interactions.

Simulations show that, for point-like sources with energy spectrum equal to  $E^{-2}$ , roughly half of the events are in a region of radius  $\sim 2^\circ$ , centred in the source itself. Above  $10 \text{ TeV}$ , as can be seen in the figure 3.10, the angular resolution no more depends on the neutrino-muon angle, but only by the uncertainty deriving from the track reconstruction.

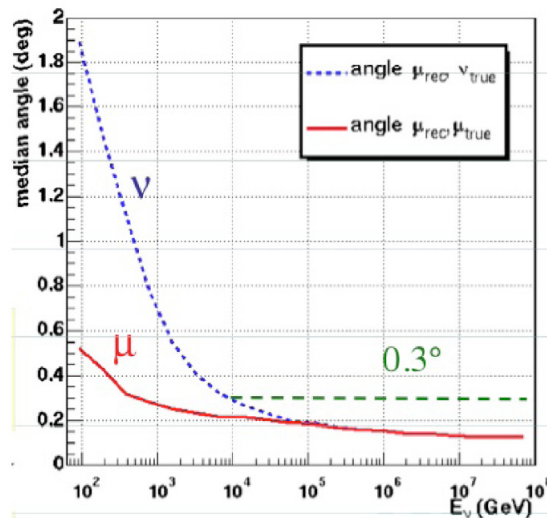


**Figure 3.10.** The angular resolution as a function of the neutrino energy. The red solid line represents the angle between the muon track reconstructed and the track generated in the MC simulation. The blue dashed line, instead, represents the angle between the neutrino direction and the one of the produced muon [139].

### 3.6.2 The detector energy response for $\nu_\mu$ interactions

The reconstruction of the interacting neutrino energy, in a Cherenkov detector like ANTARES, is possible only if the energy is deposited in the detector volume and the resulting showers tracks do not escape. In this case the instrumented volume allows a "calorimetric" evaluation of the energy as a function of the number of hits, and of the charges measured by the PMTs. Unfortunately the number of neutrino interactions in the detector volume is limited.

The search for neutrino sources can be done identifying tracks going through the detector even if they are not contained. In this case it will be possible to estimate the muons energy measuring the Cherenkov light associated to the bremsstrahlung showers that accompany the muons and that increases as the  $\log(E_\mu)$ .

The detector energy resolution is determined by the energy fraction transferred to the muon in the neutrino interaction, the energy lost by the muon outside the detector and the energy resolution of the detector. The muon energy determination requires different techniques in different energy ranges [140].

- **$E < 100 \text{ GeV}$ :** muons lose energy mainly by Coulomb scattering, so the energy of contained events, with start and end points measured inside the detector, can be determined accurately from the muon range. The threshold for this method is about  $5 - 10 \text{ GeV}$  for vertical tracks, depending on the

vertical distance between groups of optical modules, and about 15  $GeV$  for more isotropic events, depending on the horizontal distance between lines.

- **100  $GeV < E < 1 TeV$ :** the range cannot be measured because of the limited size of the detector, but the visible range determines a minimum energy that can be used for the analysis of partially-contained events: starting events in which the vertex point is measured inside the detector, and stopping events in which the endpoint is measured.
- **1  $TeV < E < 1 PeV$ :** stochastic processes (bremsstrahlung, pair production,  $\delta$ -rays) are dominant, and the muon energy loss becomes proportional to the energy. On the other hand, the detection efficiency increases with energy because of the additional energy loss. The correlation between measured muon range and neutrino energy is reported in figure 3.11. Monte Carlo studies have shown that the neutrino energy determined within a factor 3 above 1  $TeV$  from the average energy loss.
- **$E > 1 PeV$ :** the Earth becomes opaque to up-going vertical neutrinos. However, higher energies are accessible closer to the horizon. Very high energy  $\nu_\tau$  can be observed because the  $\tau^\pm$  produced in  $\nu_\tau$  interactions decay before they are absorbed, producing  $\nu_\tau$  of lower energy which continue along the original  $\nu_\tau$  flight path, but with decreasing interaction probability, resulting in an accumulation of events at the highest detectable energies.

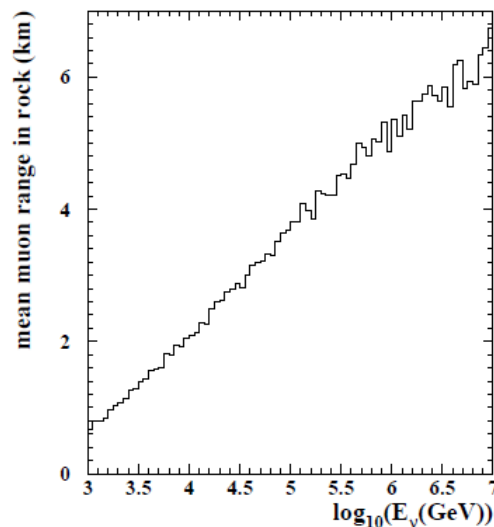


**Figure 3.11.** Average range of the muon in standard rock as a function of the initial neutrino energy [140].

### 3.7 The detector design

The ANTARES detector was built mainly to search for neutrino events of astrophysical origin. In particular, as we said before, muon neutrinos that produce muons in

CC interactions. The cross-section for neutrino CC interactions is very small, thus we need a detector of very large volume to try to detect these particles.

Otherwise the apparatus was built to main detect high energy neutrinos resulting in high energy muons in order to distinguish the neutrino signal over the background. High energy muons travel in water for long distances, inducing Cherenkov light that propagates for roughly  $50 - 100 m$ . Thus the detector is composed of strings of PMTs that are at a mean distance of  $60 m$  between strings.

The detector design [140] has also taken into account other important parameters:

- The environmental conditions at the site, which influence:
  - the spacing of optical modules;
  - the mechanical structure of detector strings;
  - the expected background rates.
- The requirement for a high level of reliability.

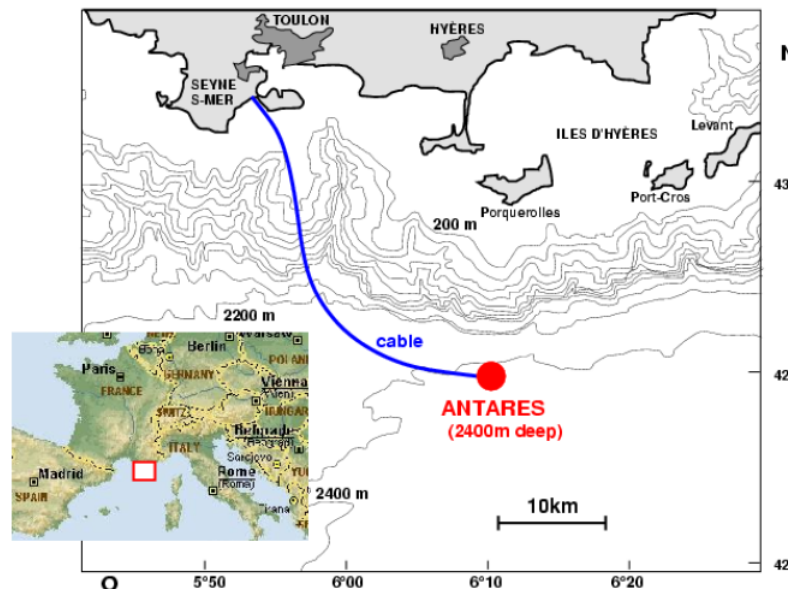


Figure 3.12. The location of the ANTARES experiment

All the detector parts and their characteristics will be described in the next sections.

### 3.8 Detector general overview

The ANTARES detector [140] has been built into the Mediterranean Sea, near the south cost of France, roughly at  $40 km$  offshore from the city of Toulon at a depth of roughly  $2400 m$ , as is shown in the figure 3.12.

The detector consists of an array of approximately 900 photomultiplier tubes disposed in 13 vertical strings (12 standard strings plus one Instrumented Line,

called IL). These lines are spread over an area of about  $0.1 \text{ km}^2$  forming a cylindrical instrumented volume with an active height of about  $0.3 \text{ km}$  and a diameter of roughly  $0.2 \text{ km}$ .

The figure 3.13 shows a schematic view of part of the detector array indicating the principal components of the telescope. The basic unit of the detector is the *Optical Module (OM)*, consisting of a PMT, various sensors and the associated electronics, housed in a pressure resistant glass sphere. The electronics includes a digital electronic circuit which captures and stores waveforms, pulse heights and timing information (see paragraph 3.11.1 the appendix B), as well as as the *High Voltage (HV)* power supply for the PMT tubes and the network nodes for data transmission and slow control.

The optical modules are grouped together in the so called storeys of three modules and interconnected via an electro-mechanical cable.

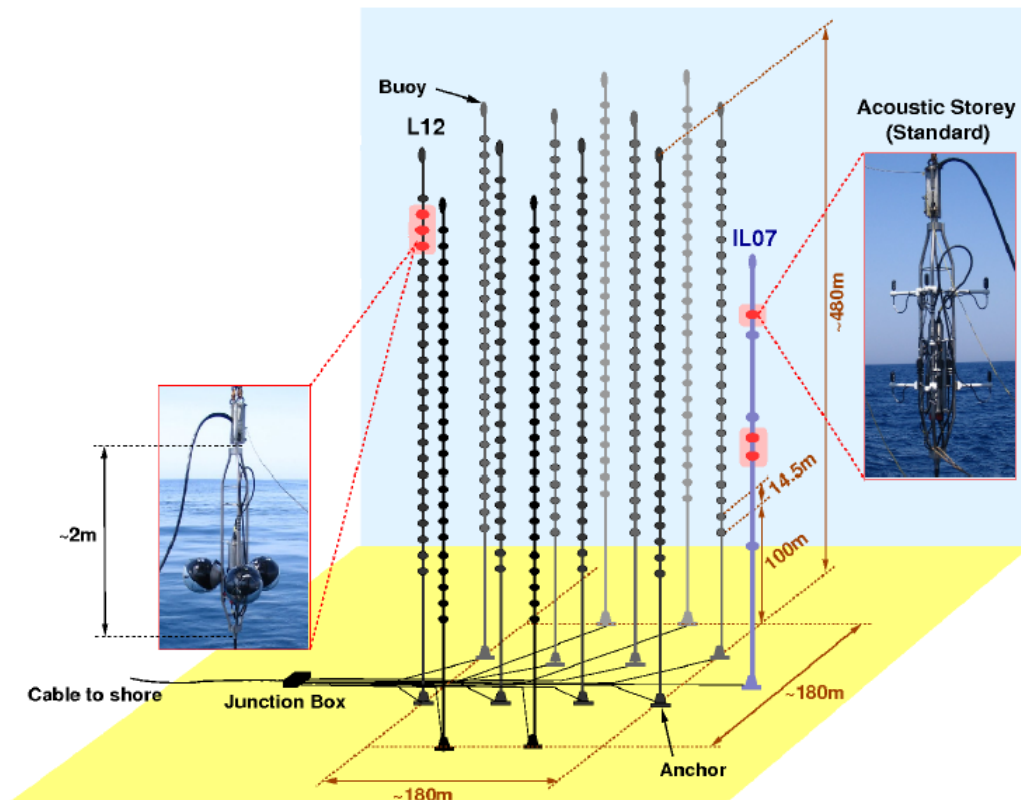


**Figure 3.13.** Scheme of the detector array. The structure of the 12 standard lines and the IL is shown. In the little photo are showed also the storeys.

The optical modules in a storey are arranged with the axis of the PMT tubes  $45^\circ$  below the horizontal one. The angular acceptance of the optical modules is broad, falling to half maximum at  $\pm 70^\circ$  from the axis. This means that this arrangement of OMs detects light in the lower hemisphere with high efficiency, and has some acceptance for muon directions above the horizontal. In the lower hemisphere there is an overlap in angular acceptance between modules, permitting an event based on coincidences from this overlap.

The relative positions of all the optical modules in the detector are given in real time by a positioning system that will be described in the section 3.14.

Each string is instrumented with several electronics containers. At every storey there is a *Local Control Module (LCM)* and, at the base of each string, there is a *String Control Module (SCM)*. Special containers house acoustic and calibration equipment. Each of these containers constitutes a node of the data transmission network, receiving and transmitting data and slow control commands. The functions which they support include reading sensors, adjusting slow-control parameters, the trigger and the distribution of power, clock and reset signals to the front-end electronics.

The individual SCM are linked to a common junction box by electro-optical cables. A standard deep sea telecommunication cable links the junction box with a shore station where the data are filtered and recorded.

The trigger logic in the sea is planned to be as simple and flexible as possible. It will be described later in the paragraph 3.11.2. Here one can say that there are some first levels of trigger that are based on coincidences of hits in adjacent OMs and storeys in one or more floors. A more refined level of trigger, imposing tighter time coincidences over larger numbers of OMs, are made in a farm of processors on shore. The readout rate is expected to be several  $kHz$  and the corresponding data recording rate less than 100 events per second.

Each day ANTARES collects about 3 atmospheric neutrino events.

### 3.9 The detector string

The detector strings are maintained vertically by their own buoyancy and anchored on the sea bed. Between the buoy and the anchor, the active detector part of the string comprises a series of elementary detector segments.

The design of the string [140] components meets basic specifications such as corrosion resistance, required because of the prolonged immersion in salt water, resistance to high pressure and water tightness. All the detector components have been selected for a minimum lifetime of 10 years. The main elements of each string are showed in the figure 3.14.

The *Bottom String Socket (BSS)* anchors the string to the sea bed, facilitates the electrical connection of the string to the network and permits the release and subsequent retrieval of the string. The BSS is instrumented for acoustic positioning.

The *Electro-Mechanical Cable (EMC)* provides mechanical support for the string as well as enabling the electrical interconnection of the detector string elements. Electrical cables and optical fibres run through the EMC. They enable power distribution and the transmission of signals between two consecutive electronic containers (LCM or SCM).

Each string is composed of 25 floors, each floor represents an *Elementary Segment (ES)*. It consist the *storey* of three optical modules, one local control module and one *Optical Module Frame (OMF)*.

The OMF supports the various elements placed within it, namely the OMs, the LCM container and possibly a hydrophone for acoustic positioning.

The top of the string consists of a buoy. Its dimensions and geometry are

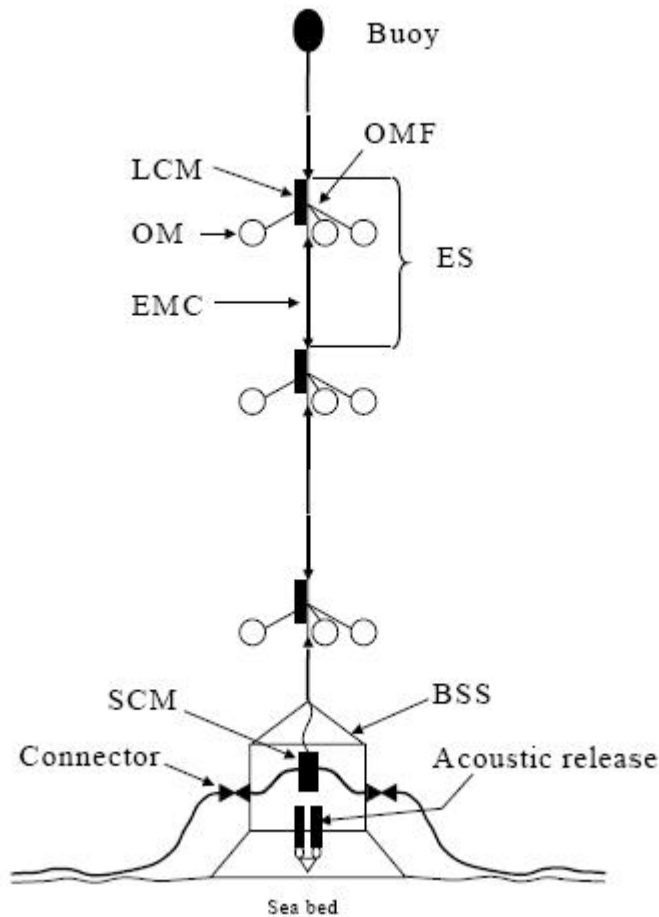


**Figure 3.14.** Scheme of a detector string with all the principal components shown. The acronyms are presented and described in the text. [140]

optimised to minimize hydrodynamic effects such as dragging and vibration whilst maintaining a suitable tension in the string. In addition, the buoyancy should be sufficient to ensure a controlled resurfacing of the string during retrieval.

### 3.10 The optical module

The basic element of the ANTARES strings is the optical module [140] that contains the photomultiplier tube represented in the figure 3.15. The PMT and its associated electronics are housed in a 43 cm diameter, 15 mm thick, Benthos sphere, which can withstand pressures of up to 700 bar. The sphere is made of two halves, one of which is painted black on its inner surface to give to the OM some minimal directionality with respect to Cherenkov light detection without degrading its acceptance. The two halves of the sphere have machined edges which form a seal when subjected to an external over-pressure. Attenuation of light at  $\lambda \geq 350 \text{ nm}$  due to the sphere was measured to be less than 5%.

A silicone gel ensures both optical coupling and mechanical support of the PMT.

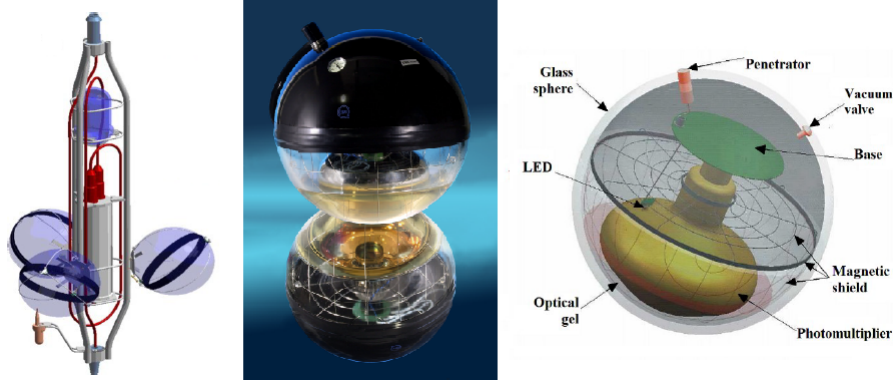


**Figure 3.15.** In the left image is shown the scheme of a storey with the three OMs, in the centre a picture of an OM over a mirror, in the right image the different components of an OM are reported.

The refractive index of the gel ( $n_{gel} = 1.40$ ) does not exactly match that of the sphere itself ( $n_{glass} = 1.48$ ) but is higher than the refractive index of water ( $n_{water} = 1.35$ ) and so the amount of light reflected out of the OM is minimised. The silicone gel covers the entire photo-cathode area; its attenuation length is given as a function of wavelength in figure 3.16 [73].

The Earth's magnetic field ( $46 \mu T$  in the ANTARES site) significantly degrades the collection efficiency of photo-tubes by bending the trajectories of electrons, mainly between the photo-cathode and the first dynode. A cage made of  $1.1 \text{ mm}$  thick high permittivity alloy wire is used to shield the PMT and to minimize the dependence of the OM response with respect to its angle with the magnetic North. The mesh size of the cage ( $6.81 \text{ mm}$ ) was optimised to reduce the non uniformity of the PMT angular response to less than 5% while the fraction of light lost due to the shadow on the photo-cathode [107].

### 3.10.1 PMT characteristics

ANTARES utilize as PMT the Hamamatsu 10" R7081-20 with a sensible area having an hemisphere form.

Several test benches have been set up to measure and compare the main features of different PMT and to provide detailed characteristics of the OM response [24].

The effective photo-cathode area ( $A_{EFF}^{PC}$ ) is defined as the detection area of the photo-cathode weighted by the collection efficiency. It was measured by scanning the entire photo-cathode surface with a collimated blue LED.

Electromagnetic interference in the optical module induces noise at the PMT anode. It is expected that will not exceed a value of  $rms < 5 \text{ mV}$ . This noise rules the gain at which the PMT is operated. A factor of 10 between the average pulse height for a *Single Photo-Electron (SPE)* and the noise is sufficient to ensure efficient discrimination of the signal. This corresponds to an effective working gain of the order of  $5 \times 10^7$ . In view of PMT ageing and possible variations in specifications a maximum gain of at least  $10^8$  is required.

The *Peak to Valley ratio (P/V)* is computed from the observed charge spectrum of single photo-electrons with the high voltage adjusted to give  $50 \text{ mV}$  amplitude

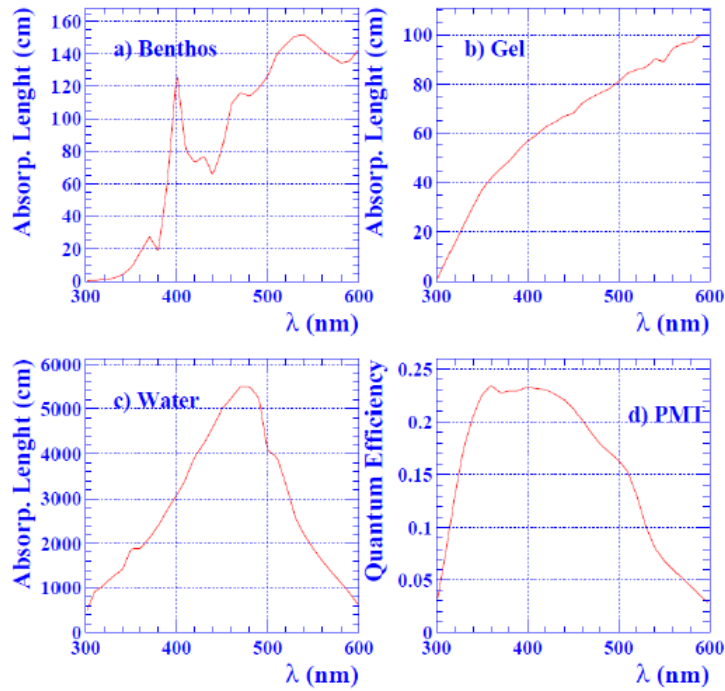


**Figure 3.16.** Attenuation length of: Benthos sphere (a), silicone gel (b), sea water (c), quantum efficiency (d) for the Hamamatsu PMT tubes [73].

for SPE. The  $P/V$  is required to be bigger than 2.

Due to imperfections in the electron optics of the photo-cathode, the SPE transit time between the photo-cathode and the anode has a measurable width, usually referred to as the *Transit Time Spread (TTS)*. This defines the timing resolution of the PMT, which is required to be comparable to that from the overall positional accuracy and the timing precision in the readout electronics, that is  $1.3 \text{ ns}$  (rms) or  $3 \text{ ns}$  (FWHM). The measurement of the TTS is performed over the whole photo-cathode area with the PMT operating at a gain of  $5 \times 10^7$ .

### 3.11 Offshore electronics

The distance between the detector and land precludes a point to point connection between each optical module and the shore station. On the contrary, an electro-optical cable from the shore station supplies electrical power to the detector array and permits data to flow in both directions. The electro-optical cable offshore ends into a junction box where cables coming from the several strings are connected. A star topology network architecture is used, from the SCM to the OMs via the LCMs. A digital scheme has been developed for the necessary data multiplexing. This network is used to distribute power, collect data, broadcast slow control commands and master clock signals and form the trigger [140].

### 3.11.1 The front-end electronics

The OM electronics must consume little power, be reliable and long lived and be inexpensive. An *Application Specific Integrated Circuit (ASIC)* meets these requirements. The ASIC developed for the digital front end electronics is called *Analogue Ring Sampler (ARS)*. This circuit samples (with a clock) the PMT tube signal continuously, then holds the analogue information and digitised it by an external 8 bit ADC.

Since the 99% of the pulses are SPE the ARS has been developed also to reduce the dead times and the data flow. A pipeline memory is implemented to store the information about the hits long enough to match the trigger check.

The ARS circuit and its components and characteristics are described in detailed depth in the appendix B.

### 3.11.2 Trigger logic

The input to the trigger process is based on the ARS raw data, time and charge information of the PMT hits, taking into account the detector geometry and the calibration values. The raw data are organised in the so called time slices, which consist of frames containing the data provided by the ARS in a time window of 13 *ms* [51].

The trigger program first performs a 0 level trigger called *L0* that occurs when the output of a PMT crosses a threshold corresponding to the 30% of a single photo-electron amplitude. In order to deal with the high counting rate in the sea, a level 1 trigger, called *L1*, is built out of a tight time coincidence between two *L0* triggers from the same storey. Also more complex level 2 triggers (*L2*) can be formed by requiring multiple *L1* triggers in coincidence gate whose width is of the order of that needed for a track to pass through the entire detector [140].

In the following a summary of all the first level triggers and some of the second level are reported with some brief explanation [15]

- **L0.** When the electrical signal passes the threshold of 0.3 photo-electrons;
- **L1.** Two types of *L1* can be distinguished:
  - When the electrical signal passes the High Threshold (3 or 10 photo-electrons) the *L0* becomes *L1*;
  - The coincidence of at least two *L0* from different OMs of the same storey, inside a 20 *ns* time window. The time window is such that the delays due to different positions of the PMT and scattering effects are taken into account.
- **T3.** Is a cluster of *L1* [47]. There are two possible way in which the *T3* can trigger:
  - The coincidence of two *L1* in adjacent floors, in 80 *ns* time window;
  - The coincidence of two *L1* in next to adjacent floors, in 160 *ns* time window.

- **3N** also called **3D\_SCAN** [53]. It requires at least 5 L1 in the time window corresponding to a muon track;
- **2T3**. It requires at least two T3;
- **K40**. Used for the in situ calibration. It requires two L0 on two OM of the same storey within a 50 ns time window;
- **TST**. The Transit Sources Trigger is activated when an alert is sent by  $\gamma$ -ray satellites such SWIFT or Fermi via the GCN network [5]. In this case 2 minutes of data around the trigger are saved without any filtering.

Trigger rates due to random coincidences of optical background have been estimated assuming a 0 level trigger rate of 60 kHz; the level 1 trigger yield a rate about 500 Hz per storey. A level 2 trigger can at maximum yield a total of 10 kHz over all the apparatus. These trigger rates levels can be reduced significantly with more strict combination of second level triggers.

The easiest way to reduce the trigger rate is to increase the number of level 1 triggers required within the level 2 coincidence gate. For example, for the simple string triggers, requiring three level 1 triggers would reduce their contribution to the level 2 trigger to about 30 Hz: a reduction of a factor 100. For the array triggers, requiring four level 1 triggers in coincidence would reduce the level 2 rate to about 600 Hz: a reduction of a factor 10.

### 3.12 Slow control

The slow control system is intended for the monitoring of variables which change relatively slowly. Also serves to control various aspects of the detector operations. PMT voltage, temperature and power supply voltages are read from the OMs. Dedicated instruments provide information on string attitude and orientation, water current velocity, acoustic positioning information and other control data.

Parameters to be adjusted during the detector operations include the PMT voltage, threshold involved in pulse detection and triggering and various calibration systems. The slow control system thus gives, to a user at the shore station, all the information needed to monitor and control the detector, as well as providing the calibration information necessary to reconstruct events.

Slow control data acquisition and execution of slow control commands are carried on by the processors on the motherboard of the relevant electronics container: OM, LCM, SCM, etc.

### 3.13 Calibration

The pointing accuracy of the detector is largely determined by the overall timing accuracy of each event.

This is a quadratic sum of terms due to

- The precision with which the spatial positioning and orientation of the optical modules is known:  $\sigma_{geom}$ ;

- The accuracy with which the arrival time of the photons at the OMs is measured:  $\sigma_{PMT}$ ;
- The precision with which the local timing of individual OM signals can be synchronised with respect to each other:  $\sigma_{align}$ .

Thus:

$$\sigma_t^2 = \sigma_{geom}^2 + \sigma_{PMT}^2 + \sigma_{align}^2. \quad (3.13)$$

Furthermore, in situ calibration of the optical modules efficiency as a function of time is necessary in order to measure and correct changes in the response due to factors such as the optical fouling.

### 3.14 Positioning

The choice to build the detector in the deep sea cause that the strings on which are positioned the optical modules, constitutes by a flexible electro-optical cable, constantly undergo the variations of the submarine sea currents.

The reconstruction of the muon trajectory is based on the differences of the arrival times of the photons between optical modules. As such, it is sensitive to the distances between the optical modules. In order to avoid degrading in the reconstruction, it is necessary to monitor the position of each optical module with a precision of about 20 *cm*, equivalent to a precision of 1 *ns* in the determination of the arrival times of the photons.

The reconstruction of the muon trajectory and the determination of its energy also require the knowledge of the OMs orientation with a precision of the order of one degree. The precise absolute positioning of the whole detector has to be guaranteed to point to individual sources.

The absolute position of the detector's components as a function of time is obtained through two different systems:

- **Acoustic positioning.** An *High Frequency Long Base Line* system (*HFLBL*) returns the three dimensional position of the hydrophones distributed along the strings. These positions are obtained by an acoustic triangulation of the signals emitted from the hydrophones, with transponders posed in the bottom of the sea bed and by transmitters that are at the bases of the strings themselves.
- **Orientation system.** A set of compass sensors permit to determine the inclination (called tilt angle) of the singles storeys with respect to the vertical axis of the string (pitch and roll parameters) and their orientation with respect to the Earth North Magnetic Pole (heading parameter). The determination of the orientation is obtained through a fit of the measures get in different points along the strings.

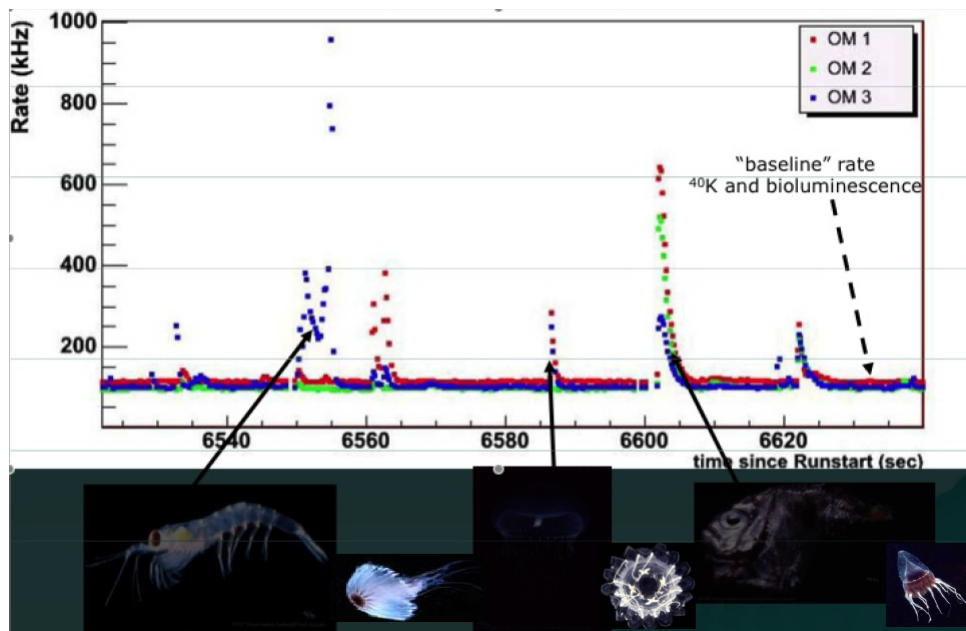
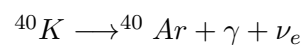


**Figure 3.17.** In the figure the two main contribution to the optical noise on the PMT are shown. The constant line represents the contribution of the Potassium decay, while the peak are caused by the sea fauna.

### 3.15 Bioluminescence and K40

The ANTARES detector has been built in the deep sea. This cause the presence of two environmental components that must be taken into account in the evaluation of the neutrino background: the  $^{40}\text{K}$  (sea Potassium) decay and the marine bioluminescence.

The principal decay channels of the Potassium 40 are:



The activity of the Potassium can be determined in base of the saltiness of the sea in the detector site, the percentage of Potassium with respect to the other salts, the relative abundance of the Potassium and the mean lifetime of the Potassium itself.

The bioluminescence instead is due to some species that constitutes the sea fauna, that are capable to emit light signals that can disturb the detector observation (see figure 3.17). This noise can be significantly reduced applying the trigger levels (described above, in the paragraph 3.11.2) that involve more coincidences between PMT of different floors and strings and also considering that muon particles travel at a velocity very next to the speed of light and the lighting fishes no!

### 3.16 ANTARES observational characteristics

Here we examine two quantities that play an important role in the physics performance of the detector: the fraction of visible sky that can be observed and the effective area in which the detector is sensible.

#### 3.16.1 Observable sky

The ANTARES detector has been optimised for the revelation of up-going neutrinos. Given the exact position of the apparatus it is possible to determine the fraction of observable sky [140].

Situated at a latitude of  $42^{\circ}47'.935$  North and at a longitude of  $6^{\circ}09'.942$  East (the position reflects the barycentre of the detector) and thanks to the rotation of the Earth it is able to observe the majority of the sky (about  $3.5 sr$ ).

Declinations below  $-47^{\circ}$  are always visible, while those above  $+47^{\circ}$  are never visible. Declinations comprised between  $-47^{\circ}$  and  $+47^{\circ}$  are visible for part of the sidereal day<sup>1</sup>. Most of the Galactic plane is visible, and the Galactic Centre is visible most of the sidereal day.

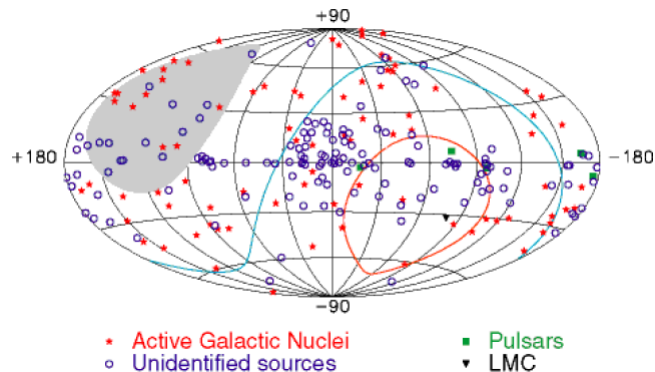


**Figure 3.18.** Sky observable by ANTARES in galactic coordinates. Some high energy sources are reported. The area in the inner of the red curve is always visible, while the grey zone is never seen by the detector. The sources comes from the third EGRET catalogue [55].

Since the neutrino telescope IceCube, located at the South Pole, is sensitive to positive declinations, the two detectors will have a reasonable area in common for cross checks (about  $1.5 sr$ ).

At energies bigger than  $\simeq 40 TeV$ , the interaction length becomes smaller than the Earth's diameter for  $\nu_{\mu}$  traversing the dense core of the Earth. Above  $10 PeV$  only nearly horizontal  $\nu_{\mu}$  are visible. If the field of view can be extended to  $10^{\circ}$  above the horizon at these energies where the background is greatly diminished, a non negligible fraction of the sky can be kept observable even at these energies.

In the figure 3.18 the sky observable by the ANTARES detector is shown.

<sup>1</sup>definition[77]

### 3.16.2 Effective area

One of the fundamental properties for the ANTARES detector is the evaluation of the effective area. In fact the capability of the detector to identify the muon tracks is identify by the mean of this parameter: the effective area ( $A_{eff}$ ). With effective area one intend the area around a section of the apparatus within which the passing muons are revealed.

The effective area can be estimated knowing the revelation efficiencies. Another way to evaluate it is through Monte Carlo simulations. Given a reference area, on which calculate the muon flux that pass through it, the better reconstructed tracks are counted. The fraction of reconstructed events multiplied the geometric area of generation gives the value of the effective area. The geometric area of reference must be bigger than the area that contain all the detector, usually with a five attenuation length margin.

The effective area depends, besides from the muon energy, also from the detector geometry (for example from the distance between the PMT with respect to the attenuation length of photons in water and from the algorithm used for the filtering process and the events reconstruction).

An estimation of the muon effective area as a function of the energy is reported in figure 3.19. Multiplying the muon effective area for the expected flux and the observation time window one obtain the total number of expected events for that period.

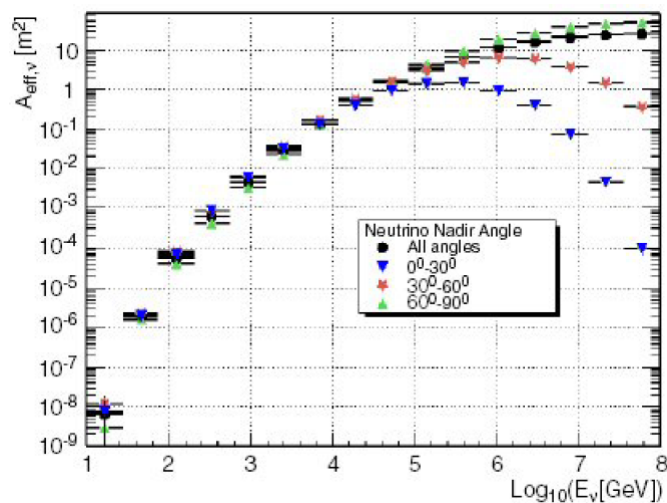


Figure 3.19. The muon effective area as a function of the energy.

## 3.17 The current ANTARES detector

The ANTARES detector soon started to take data with the connection of the line 1 only, in March 2006. Then the line 2 followed in the construction in September 2006. Lines 3,4 and 5 were placed in January 2007. Other five lines were added: the 6,7,8,9 and 10 in December 2007. Finally the last two lines: 11 and 12 were posed

in May 2008 when the detector was completed.

In addition to the 12 lines detector, the instrumented line MILOM was installed in the ANTARES site to measure and study different parameters. It was operational from March 2005 to June 2007. It was, then, removed, modified and redeployed with a new name: IL-07.

Because of cable problems the line 10 was disconnected in January 2009 and line 12 in March 2009. Both were reconnected in November 2009.

Last time, lines 9 and 6 were disconnected in July and October 2009 respectively and both reconnected at the end of 2010 [15]. Now the apparatus is completely active and working.

## Chapter 4

# Analysis of the 2007-2010 data

In this chapter we will treat the analysis work we have done for this thesis. Good examples of the analysis procedure followed into the ANTARES collaboration can be found in these references: [43] for neutrino oscillations, [36] for point sources search, [99] for dark matter search. The chapter is divided in sections and paragraphs in order to take everything into account.

In this chapter we will present the data sample selected for the analysis and the relative Monte Carlo simulation to compare with.

### Introduction

First, (paragraph 4.0.1) we will describe the data sample, made up by short (roughly 2 hours) periods of data collection named "run". We will describe how these data have been used for a blind analysis (paragraph 4.0.2) after a "scrambling" procedure. We will also define the coordinate convention system used in ANTARES (section 4.1).

Then we will define the data set used to obtain the final result (section 4.2). We will use the data took by the ANTARES apparatus in the period ranging from the January 2007 up to the December 2010: that is almost four years of data.

The configuration of the detector, during these 4 years has evolved, so the number of instrumented lines changed and this is very important to characterize the acquired data sets (paragraph 4.2.1).

In particular we will also see the diverse kind of data taken by the experiment for optical calibration, acoustic calibration and physics analysis (paragraph 4.2.2).

As we just mentioned, multiple data types and detector configuration exist, and this will force us to determine some data quality assessment to judge which data sets has been taken in good conditions and which were not (section 4.3).

As a direct consequence of the data quality criteria, we will derive the lifetime of the detector corresponding to the data sample that survived the selection (paragraph 4.3.1).

After examining the data sets, we will describe how to construct a Monte Carlo production to simulate the detector performances (section 4.4).

The Monte Carlo (MC) simulation (section 4.5 section) will allow us to describe all possible physical background that will mimic the signal (muon neutrinos from the Galactic Centre): atmospheric muons and neutrinos are the main background. The MC simulation will be used also to represent the response of the detector to signal and background events: raw and simulated data have been then reconstructed with the same software (the BBFit reconstruction algorithm described in section 4.6) so great effort has been put on the part of the MC that represent the behaviour of the detector, of the trigger system and of the surrounding environment.

The ANTARES MC simulation is normally used to describe the background to the search for  $\nu_\mu$  originated in point-like sources. Then, since the search is easier for  $E_\nu > 1 \div 10 \text{ TeV}$ , the MC simulated sample of data is rich in this energy domain. Searching for  $\nu_\mu$  from neutralinos annihilation will imply to accept also events in the lower energy window ( $10 < E_\nu < 3000 \text{ GeV}$ ). A dedicated MC production has been done on this purpose.

Then two different type of Monte Carlo will be available: one for the high energy particles, the other for the low energy ones (paragraph 4.5.1). Both must go through the same quality selection criteria used for the DATA (paragraph 4.5.2).

ANTARES reveals roughly 3 atmospheric neutrinos and about  $10^6$  muons per day.  $\nu_\mu$  from point-like sources, or by  $\chi$  annihilations, are expected to be very rare signals. So we will have to impose tight cuts to select a sample of data with enriched signal.

The most important analysis step will be represented by the events selection (section 4.7), based both on good reconstruction strategies (paragraph 4.6.1) and on cuts (4.7.1 paragraph).

The energy spectrum of the astrophysical muon neutrinos and of the atmospheric background ( $\mu$  and  $\nu_\mu$ ) show strong dependence on the energy. The background flux varies as  $\sim E^{-3.1}$  while the signal is proportional to  $E^{-2 \div 2.2}$ . Muon neutrinos from neutralinos annihilation have a spectrum that is characterised by the decay kinematics and the neutralino mass.

In order to simulate by MC the  $\nu_\mu$  from  $\chi$  we use spectra foreseen by WIMPSIM, a dedicated software.

The simulation of events following a  $E^{-3.1}$  dependence in energy would be very time consuming, so MC events are usually simulated according to a softer energy dependence ( $E^{-1.4}$ ): in this manner the whole energy range ( $0.1 \div 10000 \text{ TeV}$ ) can be simulated in a reasonable time. In order to reproduce the "real" spectrum a statistical weight will be then applied to each event (section 4.8). The same MC sample can then be used to simulate atmospheric and astrophysical  $\nu_\mu$ .

To test the goodness of our MC production to simulate the detector and its performances, we will check for the comparison between the MC simulation and the DATA events to see how much they agree (section 4.9).

To build a good signal MC arising from the dark matter annihilation (section 4.10) into the Galactic Centre we will use the WIMPSIM package (paragraphs 4.10.1 and 4.10.2). We will use three diverse annihilation channels ( $\chi\chi \rightarrow b\bar{b}, \tau^+\tau^-$ ,

$W^+W^-$ ) with ten different  $\chi$  masses, ranging from  $50\text{GeV}$  up to  $1\text{TeV}$ , for a total of 29 dark matter models that we will study.

Also the MC signal events have to be weighted (section 4.11), and it will be much more complex than the background weighting (paragraphs 4.11.1 - 4.11.2): the weights will take into account also the annihilation spectra.

The search for  $\nu_\mu$  from dark matter in the Galactic Centre, that is the aim of this thesis work, is a search for a point like source, therefore a binned search (section 4.13): we will search for signal events in cones of different angular apertures around the Galactic Centre direction.

The only way to detect a neutrino signal from the Galactic Centre is to see a statistical excess of events over the underlying background.

To evaluate the statistical significance of the result, we will use the Feldman and Cousins method (appendix A). We will describe in details this method in the paragraph A.3.

To obtain the final result, we will evaluate the so called Model Rejection Factor (MRF) for each dark matter mass selected and for each annihilation channel model chosen (paragraph 4.14.1).

The last step of the analysis of the 2007-2010 ANTARES data (section 4.14) will be to search for the cuts optimization on the set of the parameters representing the track quality reconstruction and the bin cone aperture (paragraph 4.14.2).

With the best cut we will be able to minimize the MRF and, at the end, find the sensitivity of the ANTARES detector to all the dark matter models selected (4.15 paragraph).

#### 4.0.1 Definition of "run"

The detector is immersed in water at a depth of roughly 2500 m, the condition of the environment and of the detector itself can change, also with big changes, in a short period of time. Thus, in order to take into account all these changes in the output files, the session of data taking is divided in short sub sessions called **runs**. Each run has a duration of about 2 hours. All the analysis is based on such kind of small data taking sessions.

#### 4.0.2 DATA and DATA scrambled

In this analysis we used the so called scrambled DATA.

The true DATA represent the events with the true time of arrival and their exact coordinate positions.

The **scrambled DATA** are obtained replacing, in the raw data, the event time: this time is selected randomly from the collected data sample. Data<sup>1</sup> are stored in

---

<sup>1</sup>With the word "data" in lower case we mean, simply, a run that contains events whatever their origin is (e.g. Monte Carlo). With the word in capital letters, DATA, we intend only the runs of data events (not Monte Carlo).

ROOT format [40].

We analysed files that contain raw data and results of the reconstruction software; information is stored in the **AntDST** (Antares Data Summary Tapes) format.

Since our analysis is still a **blind analysis**, we are forced to use scrambled DATA events instead of true DATA events. Thus, from now on, when we will use the word DATA we will always mean scrambled DATA.

## 4.1 The coordinate convention system

The AntDST library is used to read the ANTARES output files of the acquisition system, as we said in section 4.3. In these files some useful parameters are stored; these parameters give us important information about the reconstructed event tracks. Among the others there are also the direction of provenance of the event: i.e. the angles that univocally define the event in a given coordinate system.

To perform a physical analysis of an astronomical object it is fundamental to know exactly its space position during the time passing. Otherwise, since we are performing a search for up-going events (to reduce the atmospheric muons contamination) we need to know the exact position of the source during the day; i.e. if it is above or under the detector horizon.

In the ANTARES output files four different systems of coordinates are available [77, 145, 100]. In general the celestial coordinate systems can be divided in two categories: local systems and absolute systems. The first are dependent from the position of the observer and from the time of the observation, while the second type of systems are independent from these quantities.

- Local systems:
  - **Local coordinates**  $(\phi, \theta)$ . Reconstructed tracks in ANTARES are defined in the local system whose centre is the location of ANTARES on the Earth. The Cartesian coordinate  $x$  points to the East,  $y$  points to the North and  $z$  is directed upwards. In the local system, a direction is defined with two angles: the track zenith angle  $\theta$ , defined as the angle with respect to the positive  $z$ -axis ( $0^\circ \leq \theta \leq 180^\circ$ ), and the track azimuthal angle  $\phi$ , defined as the counter-clockwise angle in the horizontal plane with respect to the positive  $x$ -axis ( $0^\circ \leq \phi \leq 360^\circ$ ).
  - **Horizontal coordinates**  $(A, z)$ . This system is centred in the Earth, the Cartesian coordinates  $x$ ,  $y$  and  $z$  are directed towards the North, the East and in the upward direction, respectively. As in any spherical system, each position on the celestial sphere can be described by a longitudinal and a latitudinal angle. In this case the Azimuth  $A$ , defined as the counter-clockwise angle in the horizontal plane with respect to the North ( $0^\circ \leq A \leq 360^\circ$ ), and the elevation  $h$ , measured from the celestial horizon positive if the position is above the horizon and negative if the position is located below the horizon ( $-90^\circ \leq h \leq 90^\circ$ ). The complement angle with respect to the elevation is called zenith  $z$ , defined by:

$$z = 90^\circ - h,$$

positive with respect to the  $z$ -axis ( $0^\circ \leq z \leq 180^\circ$ ).

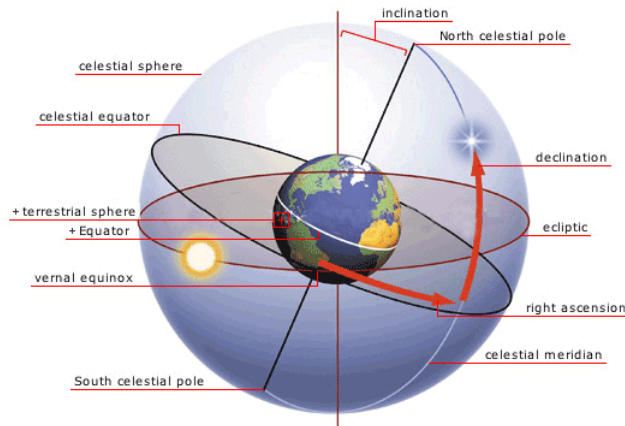


**Figure 4.1.** The equatorial coordinates system [6].

- Absolute systems
  - **Equatorial coordinates**  $(\alpha, \delta)$ . This system is based on the projection of celestial objects onto a sphere (the celestial sphere) in which the Earth sits at the centre. The equatorial system is fixed to this sphere, while the Earth rotates in the centre. The definition of the positional angles is done with respect of the projection of the Earth's poles and equator on the celestial sphere (see figure 4.1). In the Cartesian system the coordinate  $x$  points to the vernal point  $\gamma$ , that is the crossing point of the celestial equator and the Ecliptic (the apparent annual path of the Sun on the celestial sphere due to the Earth's rotation around the Sun when the Sun moves from below to above the equator),  $y$  points to the West and  $z$  to the North Pole following the line joining the poles. The longitudinal and latitudinal angles are referred to as right ascension  $\alpha$ , measured anti-counter-clockwise in hours ( $0^h \leq \alpha \leq 24^h$ ), and declination  $\delta$ , measured from the celestial equator positive if the position is above the horizon and negative if the position is located below the horizon ( $-90^\circ \leq \delta \leq 90^\circ$ ). The declination coordinate is independent from the position and time of observation, thus it has an absolute meaning. However, since the Earth's rotation is influenced by the effects of precession and nutation, the positions of celestial objects in the equatorial system are not completely time independent. Hence, the position of a celestial object is always stated with respect to the epoch of observation, expressed now by the parameter J2000<sup>2</sup>
  - **Galactic coordinates**  $(l, b)$ . In this system the references are the plane of the Galaxy and the vertical to this plane (see figure 4.2). The galactic

<sup>2</sup>J2000 is approximately noon January 1, 2000 (Gregorian calendar) at the Royal Observatory in Greenwich); this is equivalent a Julian date 2451545.0 or January 1, 2000, 11:58:55.816 UTC. When dates or times are expressed as years with a decimal fraction from J2000, the years are of exactly 365.25 days, which is the average length of a year in the Julian calendar.

plane is defined by the median plane of the distribution of the neutral hydrogen on the galactic disk. The Cartesian coordinate system is defined right-handed with  $x$  that points to the Galactic Centre<sup>3</sup>. The angles that define the position of a given point on the celestial sphere are: the galactic longitude  $l$ , defined anti-counter-clockwise ( $0^\circ \leq l \leq 360^\circ$ ) and the galactic latitude  $b$ , measured with respect to the galactic equator positive if the position is above the horizon and negative vice-versa ( $-90^\circ \leq b \leq 90^\circ$ ).

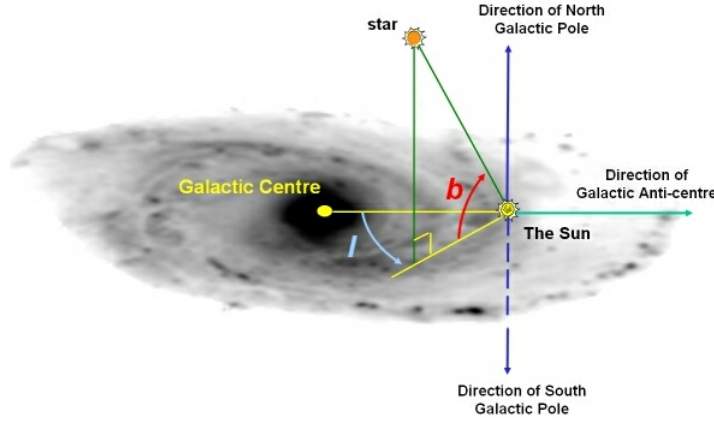


**Figure 4.2.** The galactic coordinates system [7].

We used the library of functions available in the ANTARES collaboration (`ConvertCoordinates.hh`) to pass from one coordinate system to the other. This library is based on the usual equations of coordinate transformation on a sphere. The only things we need to know are the position of the ANTARES detector (reported in section 4.13) and the time of observations of the events.

### The Hammer-Aitoff projection

To plot the distribution of the event positions as seen on the celestial sphere we use the Hammer-Aitoff projection. This projection is an equal-area projection method to map points on a sphere on to a plane. The longitude angle  $\varphi$  and the latitude angle  $\vartheta$  on a sphere can be transformed to the  $x_A$  and  $y_A$  coordinates of the projection through the formula:

$$x_A = \frac{2\sqrt{2} \cos(\varphi) \sin(\vartheta/2)}{\sqrt{1 - \cos(\varphi) \cos(\vartheta/2)}} \quad \text{and} \quad y_A = \frac{\sqrt{2} \sin(\varphi)}{\sqrt{1 - \cos(\varphi) \cos(\vartheta/2)}}. \quad (4.1)$$

To use the coordinates with this projection we need to have them in the range  $(-180^\circ < \varphi \leq 180^\circ)$  and  $(-90^\circ < \vartheta \leq 90^\circ)$ . An example for each coordinate system described above is shown in the following two figures 4.3 and 4.4. These plots represent the up-going events collected from the DATA set by the ANTARES

<sup>3</sup>the GC position in the equatorial coordinates is  $\alpha = 17^h 42^m .4$ ,  $\delta = -28^\circ 55'$  at 1950. The position of the GC in galactic coordinates is reported in section 4.13

detector for a sample period of time.

Since we are searching for up-going events (that come from the southern hemisphere), we remove from these plots all the down-going events (that have a  $\cos(z) < 0$ ). The red-yellow zones are those in which ANTARES has the best sensitivity (due to the exposure and to the detector octagonal design of the strings). The empty zones are those that are not visible by the ANTARES detector (regions above the detector horizon, thus mainly the northern hemisphere).

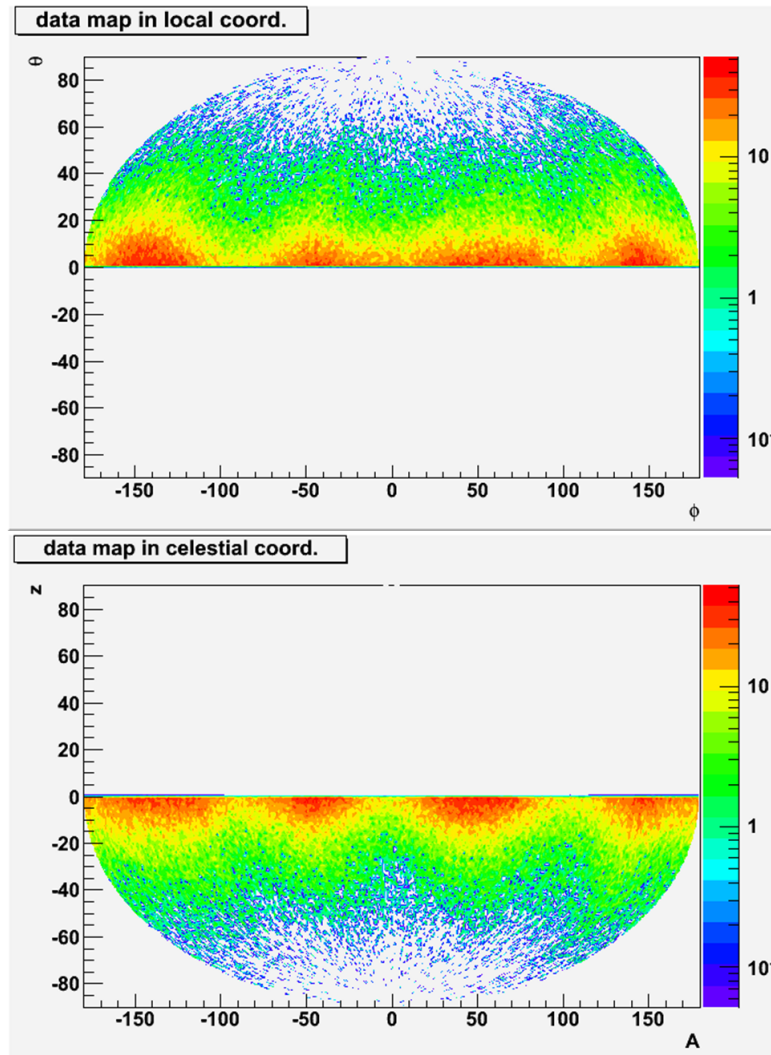


**Figure 4.3.** The DATA distributions in four different coordinates systems. Top: local detector coordinates; bottom: horizontal coordinates.

## 4.2 Data

In this paragraph we show the different lines configuration phases in which the detector has been during the time taken into account in this analysis.

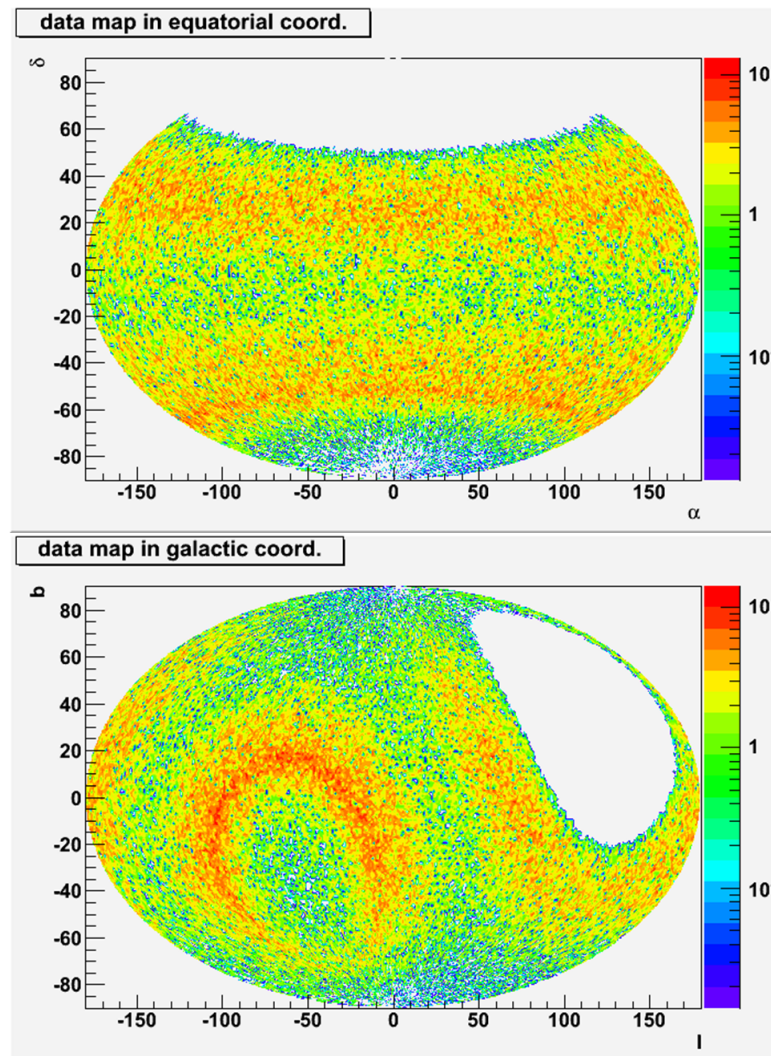


**Figure 4.4.** The DATA distributions in four different coordinates systems. Top: equatorial coordinates; bottom: galactic coordinates.

Data have been collected using several different "trigger conditions" and scopes. The detector needs a continuous calibration and monitoring. So periods of "physics runs" are alternated to calibration (acoustical, optical) runs.

The diverse categories of runs are described. Then we introduce the concepts of Data Quality and run selection to distinguish between the run's categories and the good and bad periods of data taking. The lifetime evaluation is also described in this section.

#### 4.2.1 Configuration of the detector

In this thesis work we used the physics data collected by the ANTARES experiment in the period of time from January 2007 to December 2010. During these years the detector had different configurations in instrumented lines: starting with a 5 line detector in 2007 to the 12 line configuration reached in 2008 with the end of the

construction phase of the apparatus, as reported in the table 4.1.

**Table 4.1.** The different configurations in lines of the apparatus with their durations for the data sample used in this analysis.

configuration	first run #	last run #	first day #	last day #
5 Line	025669	030460	27-01-2007	04-12-2007
10 Line	030508	032491	07-12-2007	03-03-2008
9 Line	032529	034417	03-03-2008	25-05-2008
12 Line	034419	054250	28-05-2008	31-12-2010

We have to consider that the number of lines in each period refers to the total installed lines at that time, and not to the lines actually working during that period.

### 4.2.2 Types of runs

As mentioned above, not all the runs took by the experiment are runs that can be used in a physical analysis. In effect there are three different categories of run:

1. **Physics runs**, tagged as "Line 1-12 Physics Trigger [trigger type]...";
2. **Acoustic runs**, tagged as "IL-07-Amadeus Test";
3. **Calibration runs**, tagged as "Line 1-12 [calibration check type]...".

The first category, the *Physics runs*, contains all the runs taken with the aim to perform physics with them. So these are the runs we are going to analyse in this work.

The second, the *Acoustic runs*, refers to data taken (by the hydrophones of the apparatus) to perform specific acoustic analysis, they are longer than those of Physics, and are not taken into account in our analysis.

The third category is that of the *Calibration runs*. These runs are taken to perform the time and optical calibration of the detector. There are different types of calibration runs that corresponds to the diverse detector components checks. All the calibration runs are discarded from the analysis applying some selection criteria.

## 4.3 Data Quality selection of runs

The main task of the ANTARES analysis is to distinguish signal from background. This is obtained by means of selection criteria and, on a statistical basis, searching for an excess of events in a map where are represented the origin of all collected tracks.

The better is the angular resolution of the detector, the powerful is the signal to background separation. The angular resolution is function of the detector behaviour, of the environmental conditions (sea current, bioluminescence, optical transparency etc. see chapter 3). For these reasons a selection on the detector and environment status affect the quality of the data analysis.

As we mentioned above, there are different types of runs taken by the detector. To discriminate between them, selecting only the true Physics runs, it is mandatory to apply some selection criteria about the quality of the data.

First of all, the output of the acquisition system is given to a .root file, that can be read in the ROOT software with the aim of the library AntDST developed in the ANTARES collaboration [129, 128].

The Acoustic runs are stored in a diverse place with respect of the other two categories, that are stored in the same one.

In order to select only Physics runs with a good quality of the environment conditions, two variables have been defined: ScanFlag and QualityBasic.

The **ScanFlag** is a parameter that discriminates Calibration (marked with the word SCAN or PRELIM in the set-up Data Base) runs from the others. It allows to select runs acquired for "physics".

The flag can assume four values:

- **-1**, for all runs until run 25746 included;
- **1**, for all runs having the word SCAN or PRELIM in their set-up (since run 25800);
- **10**, for runs which were originally SCAN/PRELIM but were recovered into the sample of good runs after data quality scrutiny;
- **0**, otherwise (since run 25800).

The **QualityBasic** (QB) is a flag that has been introduced to perform a first selection of the non-pathological runs that can be used for the analysis. It essentially concerns low-level of Data Quality criteria.

It can assume the following four values:

- **1**, basic selection: minimum requirement for a run to be included in the analysis;
- **2**, QB=1 and at least 80% of the OMs expected to work at the time of the run are effectively working;
- **3**, QB=2 and BaseLine  $\leq$  120 kHz and BurstFraction  $\leq$  40%;
- **4**, QB=3 and BaseLine  $\leq$  120 kHz and BurstFraction  $\leq$  20%.

The parameter *BaseLine* [64] represents the mean value of a Gaussian distribution fitted on the rising slope of the counting rate distribution, the *BurstFraction*, based on the previous fit, is obtained as the fraction of entries in the histogram giving a rate higher than the mean value of Gaussian distribution plus 20%.

In this analysis work we used the selection criteria that discard all the runs that are not Physics runs. Thus, all the runs that have:

$$\text{ScanFlag} \neq 1;$$

$$\text{QualityBasic} \geq 3.$$

We analysed only the so called silver and golden Physics runs: the runs taken with the best detector and environment conditions.

The first thing to do to proceed with the analysis, is to check if all the ROOT data files have the information about the Data Quality (DQ) stored in them.

In the following, we show, for each lines configuration, the run numbers that have not DQ information.

- **5 Line**, 2 runs without DQ:  
030092, 028563;
- **10 Line**, no run without DQ;
- **9 Line**, 1 run without DQ:  
032659;
- **12 Line**, 10 runs without DQ:  
046483, 038172, 053714, 038125, 036291, 049393, 036755, 035264, 049683, 038724.

We have also to notice that there are some files without general information about the data events (**EventInfo**). These are two in the 5 Line period (026832, 025705) and three in the 12 Line period (045555, 045416, 045493). These runs have been removed from our list of analysis runs together with all the runs without Data Quality.

It is important to say, that, if one run file has not DQ information in the DATA, the correspondent MC files must be removed, also if they have DQ information, and vice versa. Otherwise it will be impossible to perform a comparison between DATA and MC.

The final situation is reported, for the DATA, in the table 4.2.

**Table 4.2.** Total number of runs for each configuration period. Only runs with DQ used

configuration	total runs	no DQ runs	runs with DQ	fraction
5 Line	1390	2	1388	18.7%
10 Line	375	0	375	5.0%
9 Line	355	1	354	4.8%
12 Line	5307	10	5297	71.5%

Thus, in total, we have 7414 DATA runs to analyse.

### 4.3.1 The detector lifetime of the data sample

It is useful to evaluate the lifetime of each run used in the analysis. First, to see the effective lifetime on which the analysis will be performed, secondly, the information

about the value of the lifetime will be used in the calculus of the weights to apply to the Monte Carlo simulations, as we will see in the paragraph 4.8.

We have to consider that the lifetime is a characteristic of the runs file and not of the events.

To be more precise, it is better to evaluate the lifetime of a run in this way:

$$\text{lifetime [s]} = (\text{FrameTime} \cdot \text{NSlices})/10^3, \quad (4.2)$$

where NSlices is the number of time slices in the run and FrameTime [ms] is the Duration of one time slice (or frame). The data acquisition system collects events in time slices for convenience and then distribute them to the "trigger system" for an on-line analysis.

It is important to say that the lifetime evaluated in this way is the true effective lifetime of data taking of the detector. Instead, the parameter called run duration, stored in the ROOT file among a lot of other parameters, characterizing the run and the events, represents the duration of the run as computed from the Start time and the Stop time of the run itself. So it includes also small dead times. In general, the run duration is longer of roughly 10 s, compared to the lifetime calculated like in the equation 4.2.

Now we show the impact of our selection choice 4.3 for Data Quality. We have first evaluated the lifetime before the DQ selection, then we do the same after this selection.

The results are shown in the table 4.3.

**Table 4.3.** Comparison of the data lifetimes before and after the Data Quality selection.

configuration	total runs	lifetime before [days]	lifetime after [days]	discarded data
5 Line	1388	230.8	164.0	28.9%
10 Line	375	46.0	38.3	16.7%
9 Line	354	46.4	37.9	18.3%
12 Line	5297	544.2	347.3	36.2%

so the total lifetime, before the DQ selection, amounts to: 867.4 days, while, after the DQ selection is equal to: 587.5 days.

$$867.4 \text{ days} \implies 587.5 \text{ days} \quad (\sim 67.8\%)$$

This means that the  $\sim 67.8\%$  of data are accepted, and the  $\sim 32.2\%$  are discarded because they have low DQ level.

### The lifetime trigger bug for the 5 Line period

One thing to notice is that a hidden but non-negligible dead-time has been found in the core of the trigger processor.

The main effect can be summarised as a 15% - 25% loss of data, depending on the singles rates (50 kHz and 100 kHz, respectively). This effect holds only for the

older data, that is for those runs preceding run 030412: thus only the 5 Line data taking period.

To correct this effect an additional weight is applied to the Monte Carlo events, multiplying for 0.8 event by event. Where we have done a mean between the two rates, resulting in a 20% loss of data.

## 4.4 Construction of the detector simulation

A full simulation of the detector response to the atmospheric neutrinos and the atmospheric muons is performed, including random optical background. In all the simulation steps, that are described below, the detector lines are assumed to be perfectly vertical [100].

### 1. Generation of atmospheric neutrinos and muons;

- The generation of atmospheric neutrino events is done with the **GENHEN** package [110]. Only events arising from CC interactions are simulated with the **LEPTO** package. The generation is isotropic and in the energy range between  $10 - 10^8$  GeV, with a power law spectrum  $S(E) \propto E^{-1.4}$ .
- The generation of atmospheric muon events is done using the **MUPAGE** package [45, 46] or with the **Corsika** package [96]. In this analysis we use the **MUPAGE** production, that is based on a parametrised description of the underwater muon flux. The muons at the detector volume are generated as an isotropic down-going flux.

### 2. Propagation of particles and emitted photons;

- A full simulation of the response of the ANTARES detector to the passage of high energy muons including the effect of photon scattering in the water is provided by the **KM3** package [113, 26]. This is obtained by building photon tables, which store the distributions of the numbers and arrival times of PMT hits at different distances, positions and orientations with respect to a given muon track or electromagnetic shower.
- The ANTARES software package to simulate the detector response (hits) to particle showers is **GEAsim** [42], based on **Geant 3.21**. It computes and propagates the Cherenkov light produced at the passage of particle tracks in water.
- The particle propagation until the detector position is performed through the **MUSIC** package.

### 3. Response of the detector electronics;

- The program used to process the Monte Carlo data through the ANTARES software trigger system is **Trigger Efficiency** [54]. In the simulation, the main characteristics of the PMT and the ARS are taken into account. With a hit simulator package, the observed PMT counting rates are converted into unbiased PMT signal rates (it means they are corrected for ARS thresholds) and a sequence of signal and background hits are

generated, prior to the simulation of the ARS, to insert random optical background in the simulation. The last step is to simulate the trigger setting and data filtering.

#### 4. Calibration parameters assignment;

- This step is obliged, both for DATA and MC. Both the DATA and the simulation results are processed with the `CalReal` package [120] to calibrate the time, charge and position for each hit of each event of Physics. In the case of DATA, the `CalReal` program selects, with an automatic procedure, the most appropriate calibration set corresponding to the data files. In the case of simulated events the default values for time and charge are considered.

### 4.5 The background Monte Carlo

For each run of data taking there is a Monte Carlo file to simulate the response of the apparatus. This type of MC, called *run by run*, takes into account the diverse conditions both of the detector and the environment that can modify the data acquisition. The aim is to reproduce as close as possible, for each run, realistic conditions of optical background and detector configurations and settings [76].

In each MC file are stored also a lot of parameters, characterizing the detector and environment status, like the number of active OMs, their counting rate, the bioluminescence noise etc.

The simulation of the cosmic ray flux is isotropic in space. Thus, there are no privileged directions in the local reference system  $(\varphi, \vartheta)$ . However, given the spatial configuration of the lines of the apparatus, the MC simulated events are not uniform in the track azimuth angle  $\varphi$  as it is in the track zenith angle  $\vartheta$ . This means that the particular geometry of the detector leads to diverse efficiencies in reconstruction in  $(\varphi, \vartheta)$ .

#### 4.5.1 Standard and low energy Monte Carlo

For each run of data taking, several files have been generated, one for each type of particle that contribute to the background of the experiment: atmospheric muons ( $\mu^\pm$ ), atmospheric neutrinos ( $\nu$ ) and anti-neutrinos ( $\bar{\nu}$ ):

- 3 **MC standard** files with an energy range  $100 - 10^8$  GeV;
- 2 **MC low energy** files, only for neutrino and anti-neutrino, with an energy range  $10 - 3000$  GeV.

The low energy Monte Carlo have been performed for data analysis like the "neutrino oscillations" and the indirect search for dark matter. For this reason these low energy files have a denser sampling in energy.

The two samples have a little overlapping in energy between the two regimes in the zone  $100 - 3000$  GeV. Thus, since the two MC production have a different seed, this overlapping region must be carefully treated.

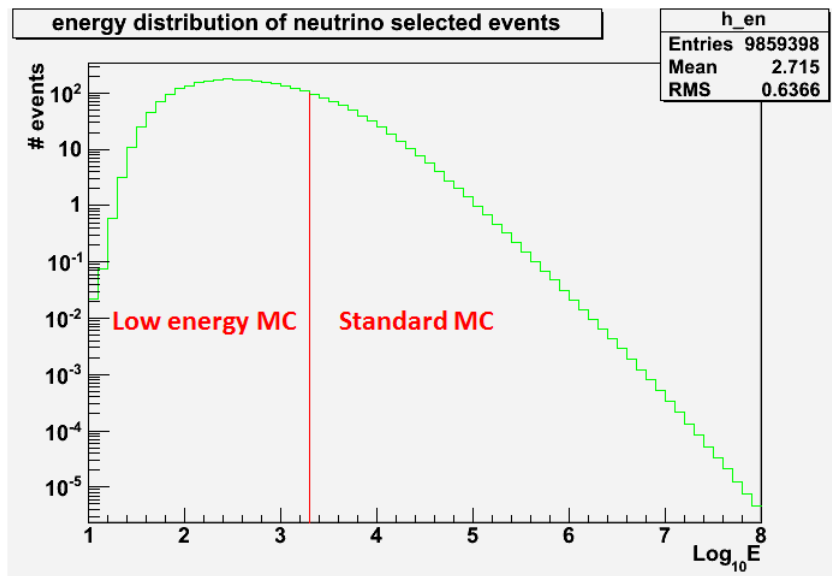


**Figure 4.5.** The Monte Carlo energy distribution for neutrinos. Our selection choice is shown.

In our analysis we removed the lower part of the standard MC production, maintaining all the low energy production (See figure 4.5). This because we are interested, for the dark matter analysis, to have an higher sampling in the low energy part of the distribution.

#### 4.5.2 Monte Carlo and Data Quality selection

The Monte Carlo production reproduces the "run" structure of the DATA. To each MC file has been attributed the same QualityBasic and ScanFlag of the corresponding DATA file. So we applied to the MC the same selection criteria applied to DATA and described in section 4.3.

The selection gave the results shown in the table 4.4 for the standard MC production and in the table 4.5 for the low energy production.

**Table 4.4.** Standard MC runs for each configuration period. Only runs with DQ used

configuration	total runs	no DQ runs	runs with DQ	fraction
5 Line	4170	0	4164	18.7%
10 Line	1125	0	1125	5.0%
9 Line	1065	0	1062	4.8%
12 Line	15921	1	15891	71.5%

Furthermore, if the DATA runs have no DQ information, the correspondent MC (both standard and low energy) files must be removed, also if the MC files have the DQ information. This because, in that case, the comparison DATA-MC would be impossible.

For example, there is one run without DQ in the 12 Line period, both in the MC

**Table 4.5.** Low energy MC runs for each configuration period. Only runs with DQ used

configuration	total runs	no DQ runs	runs with DQ	fraction
5 Line	2776	0	2776	18.7%
10 Line	750	0	750	5.0%
9 Line	708	0	708	4.8%
12 Line	10614	1	10594	71.5%

standard and MC low energy files: 046483. Consequently, it has been removed from the DATA files.

As arise from the table 4.4, the total number of runs for the standard type Monte Carlo is equal to 22242.

While, the total number of runs for the low energy type Monte Carlo is equal to 14828, as can be seen in table 4.5.

We have also to notice that there are two runs in the 5 Line period that have not the EventInfo stored in the ROOT file (026832, 025705). Also in the 12 Line period there is one run without the EventInfo (046483). It is useful to consider that one run with no DQ or EventInfo in the DATA set corresponds to 3 standard MC files and 2 low energy MC files, as we have explained above in the paragraph 4.5.1.

## 4.6 The reconstruction algorithm

Once we have the DATA and MC files, we have to reconstruct, if any, the tracks of the events. Paragraph 3.5 describes the basic concepts of track reconstruction.

The reconstruction program is inserted in the software framework SeaTray [59]. This software was developed by the ANTARES collaboration starting from the one built for the IceCube collaboration, called IceTray.

In the ANTARES collaboration there are two different methods both included in the SeaTray framework, to perform this reconstruction: AAFit [84] and BBFit [44, 43]. In the following we will not discuss both methods. We chose to use the BBFit method because it is faster and valid at lower energies (being search for dark matter a low energy particle search) producing reliable results without precise positioning calibration.

Now we are going to describe the BBFit reconstruction strategy. The basic concept is that, both the lines of the detector than the muon tracks, can be considered as straight lines in space. The only problem arise if the two lines are parallel, that is the case of vertical tracks (but, as we will see in the paragraph 4.7.1, these tracks will be removed).

The method starts [11] searching for the point of closest approach between the detector line and the muon track. The majority of the Cherenkov light, induced by the muon particle, will be in the vicinity of this point. From this principle descends the selection of the track hits and the consequent fit of the track.

In the fit are considered only the Cherenkov photons, while scattering effects and electromagnetic activity are ignored, this is the reason why the fit is simple and fast.

Only one hit per storey is allowed in the fitting procedure. The calibrated hit times  $t_i$  are given in *nsec* and their hit amplitudes  $a_i$  are given in photoelectrons. All the hits from the same storey are time ordered; then the hits which are closer in time for less than 20 nsec are merged, adding their amplitudes and keeping the time of the earlier hit; when hits from different OMs are merged, the merged hit obtains a bonus charge of 1.5 photoelectrons. This gives a higher weight to coincidences between two hits on different OMs than one single high charge pulse. This is the way in which the hits list is formed.

After that, the L1 trigger is redefined as an amplitude cut, set to 2.5 photoelectrons. So the coincidences will pass the cut if their combined amplitude is larger than 1 pe: so most of the time. The T3 trigger is defined by the coincidence of 2 L1 in two adjacent floors within 80 nsec or 160 nsec in two next to adjacent floors. All the hits which pass the T3 step are added to the hit list, together with the single L0 hits on the 1pe level.

The detector geometry is invariable. A file describing the position of each OM (the 2008:V2.6) with a 12 lines detector is used. The nominal geometry uses the measured BSS<sup>4</sup> position from acoustic triangulation and two important approximations:

1. Lines are considered perfectly vertical: sea current distortions are ignored;
2. Geometry of the three optical modules on each storey is ignored: each storey is considered as a point in space centred on the detector line.

After the hits list is acquired, the fitting procedure starts. As we said before, a particle track is considered as a straight line in space. The particle is assumed to move with the speed of light.

All the space-time points which are part of the track can be parametrised as:

$$\vec{p}(t) = \vec{q}(t_0) + c(t - t_0)\vec{u}. \quad (4.3)$$

These particle passes through the point  $\vec{q}$  at time  $t_0$  and moves in the direction  $\vec{u}$ . The vector  $\vec{q}$ , that represents the position of the particle along the track, can be shifted along the track by  $t_0$ . Thus, the track is defined by five parameters: three to fix the position in space  $\vec{q}$  at a given time and two angles for the definition of  $\vec{u} \equiv (\cos \theta \cos \phi, \cos \theta \sin \phi, \sin \theta)$  with  $\theta$  the elevation angle and  $\phi$  the azimuth angle.

As we said, we consider the detector formed by only vertical axis along the z-axis: (0,0,z) at fixed horizontal positions ( $L_x, L_y$ ). The point of closest approach between the track and the vertical detector lies in:

$$z_c = \frac{q_z - u_z(\vec{q} \cdot \vec{v}) + u_z(L_x u_x + L_y u_y)}{1 - u_z^2}. \quad (4.4)$$

The particle passes through this point at the time:

$$t_c = t_0 + \frac{1}{c}(L_x u_x + L_y u_y + z_c u_z - \vec{q} \cdot \vec{u}), \quad (4.5)$$

---

<sup>4</sup>BSS means bottom string socket that is the anchor of the strings as we explained in the section 3.9 in the chapter 3.

and at a distance equal to:

$$d_c = \sqrt{(p_x(t_c) - L_x)^2 + (p_y(t_c) - L_y)^2} \quad (4.6)$$

In the case of perfectly vertical track (parallel to the detector line) we have  $t_c = t_0$  and  $z_c = q_z$ . The track can be re-parametrised by only four parameters:  $z_c$ ,  $t_c$ ,  $d_c$  and  $v_z$ . For a single-line fit the detector line can be placed at the coordinate origin  $(L_x, L_y) = (0, 0)$ .

To build the fitting function, for a Cherenkov photon of a given wavelength, we have to know the arrival time of the Cherenkov photons  $t_\gamma$ :

$$t_\gamma(z) = (t_c - t_0) + \frac{1}{c} \left( (z - z_c)u_z + \frac{n^2 - 1}{n} d_\gamma(z) \right) \quad (4.7)$$

on the line position  $(0,0,z)$ , the corresponding travel path  $d_\gamma$ :

$$d_\gamma(z) = \frac{n}{\sqrt{n^2 - 1}} \sqrt{d_c^2 + (z - z_c)^2(1 - u_z^2)}, \quad (4.8)$$

and its angle with respect to the detector line  $\cos \theta_\gamma$ :

$$\cos \theta_\gamma(z) = (1 - u_z^2) \frac{z - z_c}{d_\gamma} + \frac{u_z}{n}. \quad (4.9)$$

Where  $n$  is the refractive index with a value equal to  $n = 1.38$ . All the other effects like dispersion and group velocity are ignored.

A similar procedure, not reported here, is followed in the `BBFit` program, also for the bright point. A bright point is a point-like source which emits, isotropically, a single light flash at a given moment. Typically it is related to the electromagnetic showers events.

The fitting  $\chi^2$  function uses the differences of time between the arrival hits times  $t_i$  and the expected arrival times of the photons  $t_\gamma$  from the track or from the bright point. The quality function is extended with a term that accounts for measured hit charges  $a_i$  and the calculated photon travel distances  $d_\gamma$ .

The quality of the fit is expressed by the formula:

$$t\chi^2 = \sum_{i=1}^{N_{hit}} \left[ \frac{(t_\gamma - t_i)^2}{\sigma_i^2} + \frac{A(a_i)D(d_\gamma)}{\langle a \rangle d_0} \right], \quad (4.10)$$

where  $\sigma_i$  is the timing error (setted to 10 ns for  $a_i > 2.5$  photoelectrons or to 20 ns otherwise) and  $\langle a \rangle$  is the average amplitude that compensate for the fact that higher energy tracks or showers produce more light at the same distance.  $d_0 = 50$  m balance the weight between the two terms in the equation 4.10. This method penalizes the combination of high amplitudes and large distances.

The amplitudes are then corrected for the angular acceptance of the floor:

$$a'_i = \frac{2a_i}{\cos \theta_\gamma + 1}. \quad (4.11)$$

With these new amplitudes it is possible to evaluate the average amplitude expression:

$$\langle a \rangle = \frac{1}{N_{hit}} \sum_{i=1}^{N_{hit}} a'_i. \quad (4.12)$$

Furthermore, charges are protected against extreme values by the following function:

$$A(a_i) = \frac{a_0 a'_i}{\sqrt{a_0^2 + a_i'^2}} \quad (4.13)$$

The function  $A(a_i)$  introduces an artificial saturation such that for  $a'_i \ll a_0$ , the charge is relatively unaffected, i.e.  $A(a_i) \approx a'_i$ , whereas for  $a'_i \gg a_0$ , the charge saturates at  $A(a_i) \approx a_0$  the chosen saturation value.

The photon travel distance is similarly protected using the function:

$$D(d_\gamma) = \sqrt{d_1^2 + d_\gamma^2} \quad (4.14)$$

which introduces a minimal distance  $d_1$ . For large distances ( $d_\gamma \gg d_1$ )  $D(d_\gamma) \approx d_\gamma$ , whereas for very small distances ( $d_\gamma \ll d_1$ )  $D(d_\gamma) \approx d_1$ . This avoids an excessive pull of the fitted trajectory towards the detector line.

The equations 4.7, 4.8 and 4.9 are used in the track fit (similar equations are used for the bright point fit) to obtain  $t_\gamma$ ,  $d_\gamma$  and  $\cos\theta_\gamma$  respectively. There may be two type of fit: single-line and multi-line. Usually particle fitted along only one line are rejected by the cuts we will show (see 4.7.1 paragraph). Here we consider only the multi-line fit. In this case all the detector lines, which have selected hits, are considered. The multi-line fit breaks the rotational symmetry, thus all the five parameters are needed to determine the track.

After the minimization, performed with the MINUIT package [88], the value of the fit quality  $t\chi^2$  defined with the equation 4.10 is conserved into a particular tree of the ROOT file of both DATA and MC together with other parameters, arising from the reconstruction of tracks and bright point.

#### 4.6.1 The choice of the reconstruction algorithm

We have now to choose which reconstruction algorithm to use to reconstruct the events tracks. As we said, there are two possible method: **AAFit** and **BBFit**. Both the algorithms are optimised for up-going tracks, because the up-going events are the target events to select in an common analysis. In this analysis we use the **BBFit** program described in the section 4.6.

Another choice is the one for the reconstruction strategy to use within the **BBFit** program. There are three possible strategies: the one we call normal **BBFit** strategy optimised for the tracks reconstruction, the bright point reconstruction and the M-estimator reconstruction.

Each of these three strategies, have its own parameter to evaluate the goodness of the fit that discriminate between good and bad reconstructed events. The names of these parameters are:  $t\chi^2$ ,  $b\chi^2$  and  $M$  respectively. In this analysis we choose the

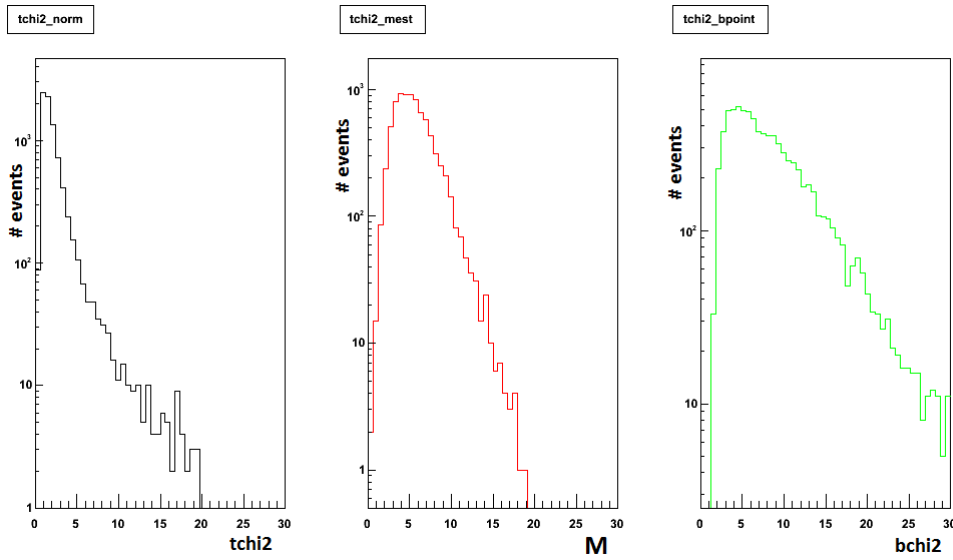


**Figure 4.6.** Comparison of the three parameters which point out the goodness of the fit quality ( $t\chi^2$ ,  $b\chi^2$  and  $M$ ) for a sample selection of runs belonging to the 12 lines period.

*normal track fit reconstruction*, which fit parameter is  $t\chi^2$ . More or less large cuts on this parameter discriminate between good and bad reconstructed tracks.

The different distributions of these three parameters are shown in the figure 4.6.

From the calculus of the integral of these distribution can be seen that, the value of the integral from 0 to 5 of the normal track strategy is equal to the value of the integral between 0 and 13 of the  $M$  estimator, and to the value of the integral between 0 and 23 of the bright point parameter. This means that a  $t\chi^2 < 5$  cut is equal to the  $M < 13$  cut and to the  $b\chi^2 < 23$  cut.

In the analysis of the up-going neutrino tracks (see 4.14.2 paragraph), the cuts on the track fit quality parameter, are applied to try to minimize the ratio between signal and background. Where the background is represented by the atmospheric muons.

Now we have to explain the importance and the significance of the track fit quality estimator parameter. In the reconstruction phase there are some down-going muon events that are bad reconstructed as up-going. In this way there is a contamination of the neutrino background and then of the possible neutrino signal. The only method to put away almost all the bad reconstructed muons is to cut on the track fit quality parameter. It means to cut the tail of the  $t\chi^2$  distribution to reject these the noisy particles. In particular, one of the main issue of the analysis is to choose the better cut.

However, before to treat the analysis of this cut in section 4.14, some others cuts are applied.

## 4.7 The event selection

Here below we will describe the background rejection obtained applying, to the sample of DATA and MC selected with the Data Quality (as described in section 4.3), further selection criteria.

### 4.7.1 Basic cuts and efficiency

We will search for  $\nu_\mu$  signals in the sample of "up-going" tracks in order to reduce the large atmospheric muon background. We will search for high quality tracks in order to have the possibility to apply a narrow cut around the direction of the Galactic Centre without losing too many events.

Requiring high quality tracks, as we discussed above, rejects also the "down-going" muon tracks badly reconstructed as up-going.

In this analysis we select only the events that pass all the following conditions. Thus the resulting events will be up-going events, taken from good conditions environment and well reconstructed.

- **$\cos(\mathbf{z}) \leq 0$** , This cut serves to remove all the down-going events, that are the events that come from above the horizon, considering the coordinate definition explained in 4.1;
- **$\mathbf{nhit} > 5$** , This means to consider only events that caused at least five hits on the PMT of the apparatus to avoid the selection of noisy events;
- **$\mathbf{nlines} > 1$** , In this way only the events reconstructed with more than 1 line are selected. In effect with the single line events (most of them are the vertical tracks we mentioned in the section 4.6), because of the cylindrical symmetry of the line, is not possible to determine the azimuth angle of the track ( $\varphi$ ) that is necessary to reconstruct the exact direction of the track event;
- **$\mathbf{t}\chi^2 \leq 5$** , This is a first cut on  $t\chi^2$  used to remove the majority of events with a very bad reconstruction. The more accurate analysis, to choose the better value to cut, will be performed later considering all the  $t\chi^2$  values up to 4.6. This pre-selection choice has been made for computational reasons, that is to have shorter computing time;
- **T3 and 3D\_SCAN triggers**, As most of the time several triggers were active in parallel, a choice on the considered trigger must be made to confront the data with simulations. Two triggers have been chosen [43], which descriptions can be seen in the paragraph 3.11.2. We select only the events that have been triggered at least by one of these two triggers. This means to select only muon tracks reconstructed with a cleaner environmental situation thus with an higher efficiency.

The effects of some of these cuts are shown in the figure 4.7 for the  $t\chi^2$  distribution for a DATA sample of the 9 lines period.

Referring to that plot, the black curve represents the DATA distribution only after the Data Quality selection; the red curve represents the distribution after a

more strict selection of the DQ ( $DQ > 3$ ); the green curve adds also the lines selection to the previous DQ cuts. Finally the blue zone is excluded with the pre-selection on  $t\chi^2$ .

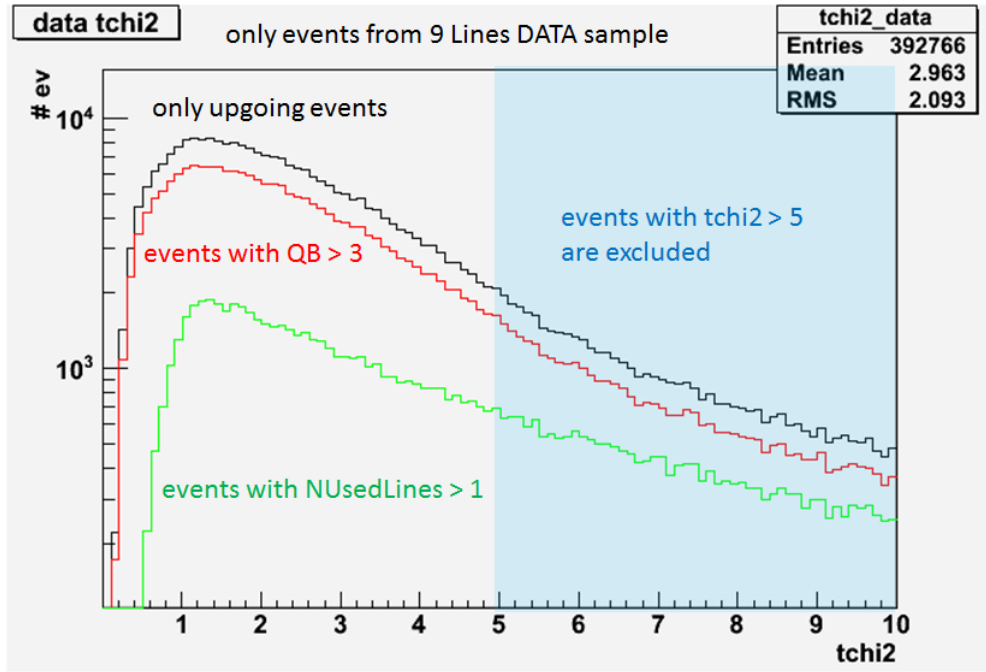


**Figure 4.7.** The effects of some types of cuts on the  $t\chi^2 = tchi2$  distribution of a 9 period DATA sample.

Next step is to apply these cuts to the DATA and MC events. The results of this operation is reported in the table 4.6. In this table is possible to see the percentage of events selection for each line configuration and type of event (DATA, MC and MClowE) and particle ( $\mu$ ,  $\nu$ ,  $\bar{\nu}$ ).

In the first column is reported the configuration in lines of the detector (5, 10, 9, 12), then the second and third columns show the total number of events and the selected one after applying the basic cuts previously shown. Finally the last column reports the efficiency in the data selection.

As can be seen from the table 4.6 there are periods of time in which there was a bigger efficiency in reconstructing the particle tracks. Usually this is caused by the better condition of the environmental and detector status.

Another cause of good efficiency is the number of lines used to detect tracks. Obviously more are the lines better is the efficiency.

One have the better efficiency for the DATA for the 10 lines configuration and, for the muon and neutrino/anti-neutrino MC also in the 10 lines case.

**Table 4.6.** Selected events for each detector line configuration, event and particle type.

configuration	DATA events			MC $\mu$ events		
	total	selected	efficiency	total	selected	efficiency
5 Line	$1.11 \times 10^8$	$5.67 \times 10^4$	$5.09 \times 10^{-4}$	$2.64 \times 10^6$	$1.23 \times 10^4$	$4.65 \times 10^{-3}$
10 Line	$1.44 \times 10^7$	$2.65 \times 10^4$	$1.84 \times 10^{-3}$	$1.48 \times 10^6$	$5.18 \times 10^3$	$3.50 \times 10^{-3}$
9 Line	$2.46 \times 10^7$	$2.30 \times 10^4$	$9.35 \times 10^{-4}$	$2.33 \times 10^6$	$4.26 \times 10^3$	$1.83 \times 10^{-3}$
12 Line	$9.60 \times 10^8$	$2.74 \times 10^5$	$2.85 \times 10^{-4}$	$3.62 \times 10^7$	$4.94 \times 10^4$	$1.37 \times 10^{-3}$
configuration	MC $\nu$ events			MC $\bar{\nu}$ events		
	total	selected	efficiency	total	selected	efficiency
5 Line	$5.13 \times 10^5$	$1.20 \times 10^5$	$2.34 \times 10^{-1}$	$5.25 \times 10^5$	$1.23 \times 10^5$	$2.34 \times 10^{-1}$
10 Line	$2.37 \times 10^5$	$6.86 \times 10^4$	$2.89 \times 10^{-1}$	$2.45 \times 10^5$	$7.16 \times 10^4$	$7.16 \times 10^{-1}$
9 Line	$2.53 \times 10^5$	$6.19 \times 10^4$	$2.45 \times 10^{-1}$	$2.61 \times 10^5$	$6.35 \times 10^4$	$6.35 \times 10^{-1}$
12 Line	$4.24 \times 10^6$	$8.26 \times 10^5$	$1.95 \times 10^{-1}$	$4.41 \times 10^6$	$8.50 \times 10^5$	$1.93 \times 10^{-1}$
configuration	MC LowE $\nu$ events			MC LowE $\bar{\nu}$ events		
	total	selected	efficiency	total	selected	efficiency
5 Line	$2.35 \times 10^6$	$7.66 \times 10^5$	$3.26 \times 10^{-1}$	$2.52 \times 10^6$	$8.43 \times 10^5$	$3.34 \times 10^{-1}$
10 Line	$1.66 \times 10^6$	$6.55 \times 10^5$	$3.95 \times 10^{-1}$	$1.81 \times 10^6$	$7.34 \times 10^5$	$4.04 \times 10^{-1}$
9 Line	$2.15 \times 10^6$	$5.14 \times 10^5$	$2.39 \times 10^{-1}$	$2.35 \times 10^6$	$5.76 \times 10^5$	$2.45 \times 10^{-1}$
12 Line	$4.33 \times 10^7$	$8.34 \times 10^6$	$1.92 \times 10^{-1}$	$4.8 \times 10^7$	$9.42 \times 10^6$	$1.96 \times 10^{-1}$

## 4.8 Weights policy for MC background events

We have described in which way the MC production was constructed in the section 4.4. In this section we will see the necessary weights to apply to the Monte Carlo background events and the way to use them.

In ANTARES the neutrino events simulation is given by the GENHEN package, as we mentioned in the section 4.4. GENHEN does not generate neutrino fluxes to simulate their interaction in the vicinity of the detector, but, to not consume machine time and disk space, simulates interacting neutrinos.

the GENHEN output consist of a neutrino of energy  $E$  that interacts in a given point into the generation volume while it's travelling to a certain direction. For each generated interacting neutrino, the output also reports the result of the interaction, that is the list of particles produced and their respective kinematics parameters.

Moreover, GENHEN associates to each event two numerical weights: the "generation weight" and the "global weight". These weights take into account the assumptions made by GENHEN in generating the events. In the following we will describe these weights and how to apply them to MC events.

### 4.8.1 The standard formalism for weights

The use of the ANTARES Monte Carlo events to reproduce signal or background is possible using weights that take into account the detector geometry, the generated

neutrino spectra, the actual spectrum of the sample to be simulated. Three weights can be applied for these purposes to the MC events [41]:

- **w1** contains the can volume [ $m^3$ ] for neutrino interaction in a volume or the angular dependent effective surface [ $m^2$ ] for neutrino and muon fluxes entering the detector.
- **w2** is the generation weight. For event generation of neutrino interactions, flat in cosine of the zenith angle and flat in  $E^{-\gamma}$ , w2 contains:

$$w2 = V \cdot I_\theta \cdot I_E \cdot E^\gamma \cdot \sigma(E) \cdot \rho \cdot N_A \cdot P_\oplus \cdot F, \quad (4.15)$$

where:

- $V[m^3]$  is the can volume w1 for volume drawing or equivalently  $w1 \cdot R_\mu$  (the product of effective surface and muon range) for surface drawing;
- $I_\theta[\text{sr}]$  is the angular phase space factor  $2\pi \cdot (\cos \theta_{\max} - \cos \theta_{\min})$ ;
- $I_E$  is the energy phase space factor, that can be:

$$\begin{cases} \frac{E_{\max}^{1-\gamma} - E_{\min}^{1-\gamma}}{1-\gamma} & \text{for } \gamma \neq 1 \\ \log\left(\frac{E_{\max}}{E_{\min}}\right) & \text{for } \gamma = 1; \end{cases}$$

- $E^\gamma$  takes into account that the random extraction has been done flat in  $E^{-\gamma}$ .  $I_E \cdot E^\gamma$  is measured in GeV;
- $\sigma(E)[m^2]$  is the total neutrino cross section for neutrino energy E. Here it is assumed that the events are drawn with the correct differential distributions;
- $\rho \cdot N_A$  is the number of target nucleons per  $m^3$ ;
- $P_\oplus$  represents the probability for neutrinos to survive crossing the Earth (depending on the energy and Zenith angle);
- $F$  is the number of seconds per year.

w2 has the units [ $\text{GeV} \cdot m^2 \cdot \text{sr} \cdot s \cdot \text{yr}^{-1}$ ]. For a point-like generation w2 has the units [ $\text{GeV} \cdot m^2 \cdot s \cdot \text{yr}^{-1}$ ].

- **w3** is called the global weight, and is defined as:

$$w3 = w2 \cdot \Phi, \quad (4.16)$$

where  $\Phi$  is the differential flux of neutrinos before penetrating the Earth or muons at the detector in [ $\text{GeV}^{-1} \cdot m^{-2} \cdot \text{sr}^{-1} \cdot s^{-1}$ ]. Therefore w3 has the simple unit [ $\text{yr}^{-1}$ ], which can be understood as the "rate per year".  $\gamma$  should be chosen to obtain global weights of similar magnitude, for example, for the simulation of atmospheric neutrino interactions below 1 TeV,  $\gamma = 2$  would be adequate, as  $\Phi \sim E^{-3}$  and  $\sigma = E$ .

### 4.8.2 How to use the weights

Now we discuss how to apply the weights we have described above to correctly use the Monte Carlo events, in order to simulate the distributions of atmospheric neutrinos and muons.

#### Neutrinos

To evaluate the absolute number of neutrino/anti-neutrino background events we need to know, for each run, two important pieces of information:

- Detector lifetime [yr] corresponding to the selected data sample. The method to evaluate the lifetimes has been described in the paragraph 4.3.1.
- Number of generated events. This parameter can vary run by run but, usually, it has a fixed value equal to  $N_{gen} = 5 \times 10^8$ , that is the number of events generated with the generation program **GENHEN** (see section 4.4).

For the atmospheric neutrino background events we use the  $w3 [yr^{-1}]$  weight described above in the paragraph 4.8.1. The total weight has to be dimensionless, thus it has to be multiplied by a factor with a dimension of [yr], this factor is the lifetime.

The way to use this weight is reported here:

$$w = w3[yr^{-1}] \cdot \frac{\text{lifetime [yr]}}{N\text{GenEvents}}. \quad (4.17)$$

#### Muons

A different treatment has to be done for background due to atmospheric muons. The muon flux is simulated according to its measured energy dependence. Since the number of events due to down-going muons exceed the number of atmospheric neutrinos by a factor  $\sim 10^5 \div 10^6$ , we should simulate an enormous sample of background muons.

We estimated that with only 10% of this sample we can well study and characterize this background. So only one event out of the ten collected in reality has been simulated.

The weight to apply to the atmospheric muon background events is simply a number: 10!

In the loop on the events, performed in the analysis program, one has to multiply each event for:

$$w = 10, \quad (4.18)$$

to simulate properly the MC muon events.

We have to notice that, in both cases (neutrinos and muons), one has to consider the lifetime trigger bug for the 5 line events, as we mentioned in the sub-paragraph 4.3.1: all the runs with a number  $< 030412$  have to be multiplied by 0.8.

## 4.9 Data - Monte Carlo comparison

The comparison between the DATA and the Monte Carlo events is necessary to evaluate the similarity and correspondence between the two distributions. This is important to know if the Monte Carlo simulates the detector behaviour in a good way.

We performed a Monte Carlo simulation of all the possible background sources that contaminate the collected data and make difficult the signal identification.

The main background sources that hinder the revelation of neutrino signal are:

- from the *down-going* direction:
  - atmospheric muon flux;
  - atmospheric neutrino flux.
- from the *up-going* direction:
  - atmospheric neutrino flux.

As we will see in the next sections, for a point-like source detection analysis, as it is in our case, the only possible method to see any signal events, is to search for a statistical excess of events, over the predominant background noise, from the expected direction of the source. For this reason, is very important that the background MC well simulates the DATA.

Since the search for neutrino signal events is performed looking only for up-going events (that are not contaminated by the down-going muon flux) and being all the Monte Carlo, as we saw in the section 4.4, built in an isotropic manner, there are no privileged directions in which to search for the signal event. Thus if we find a significant excess from the direction of our interest it may be interpreted as a statistical signal identification.

In the following are shown some DATA-MC comparison plots. These plots are useful to determine the agreement between the DATA (plotted with the own statistical errors) and the Monte Carlo distributions. If the Monte Carlo distributions are superimposed on the DATA distribution this means that the MC simulates well the detector response.

We show first the distributions of the  $t\chi^2$  and  $b\chi^2$  parameters. The first represent the  $\chi^2$  for the neutrino events that are reconstructed as muon tracks (plots 4.8-4.9), while the second refers to the neutrino events that are reconstructed as electron showers (bright point) (plots 4.10-4.11). Then we show the distributions of the number of hits (plot 4.12) and lines (plot 4.13) used in the reconstruction fit. Last we show the distribution of the events as a function of the  $\cos(\text{zenith})$  angle (plots 4.14-4.15). For each parameter, except the number of used lines and hits, we show the plots for two different cut on the  $t\chi^2$  parameter. First we show the plot with an higher value of cut, then the plot with a tighter value of  $t\chi^2$  cut.

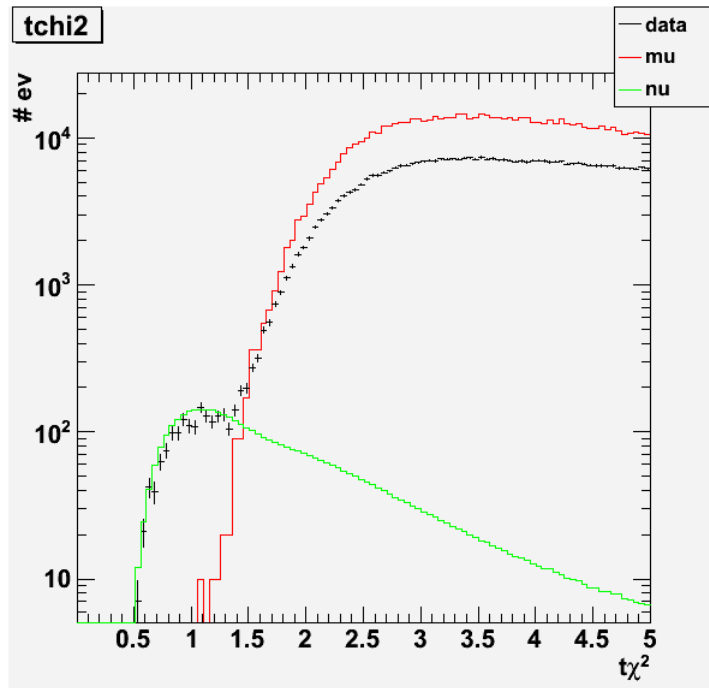


Figure 4.8. The DATA-MC comparison for the  $t\chi^2$  parameter. Only events with  $t\chi^2 < 5$  are considered.

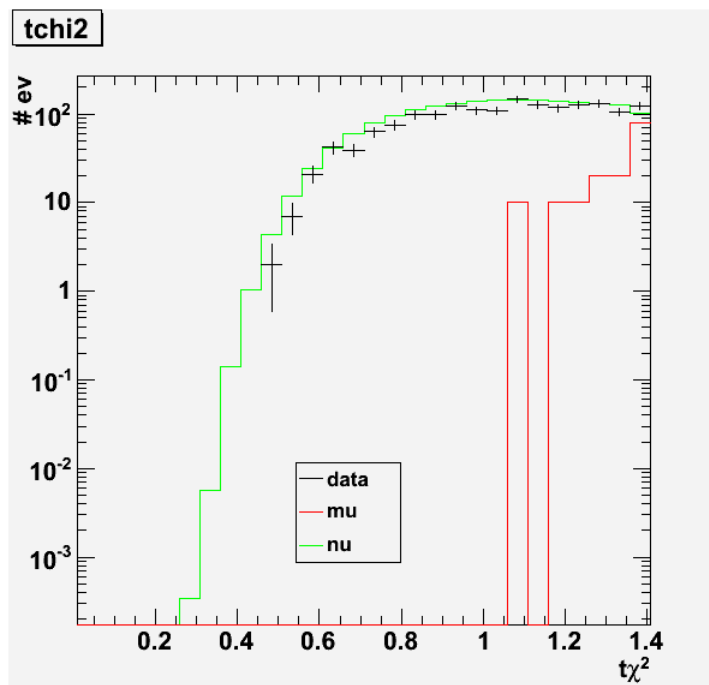
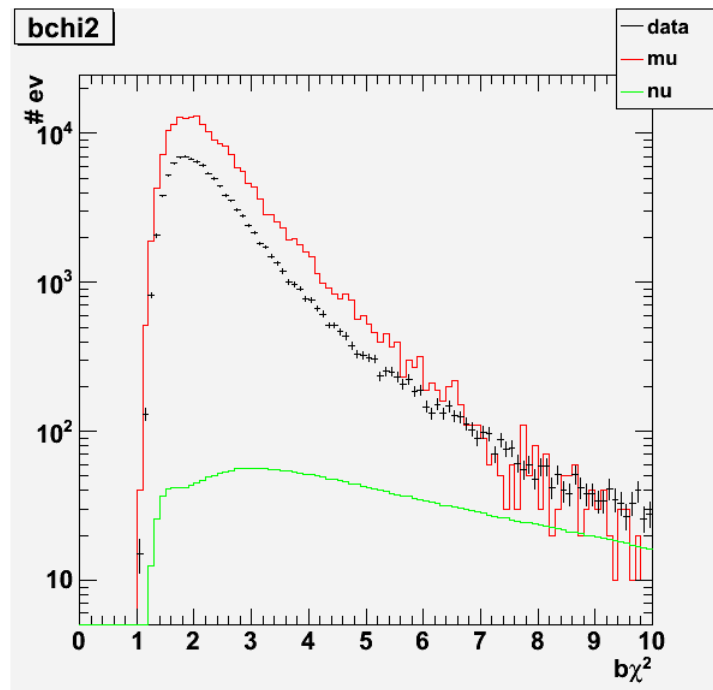
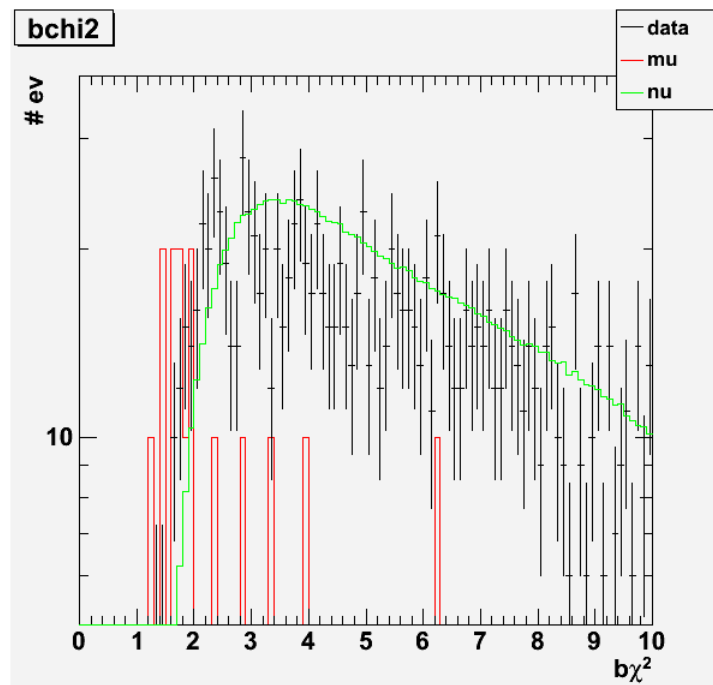


Figure 4.9. The DATA-MC comparison for the  $t\chi^2$  parameter. Only events with  $t\chi^2 < 1.4$  are considered.



**Figure 4.10.** The DATA-MC comparison for the  $b\chi^2$  parameter. Only events with  $t\chi^2 < 3$  are considered.



**Figure 4.11.** The DATA-MC comparison for the  $b\chi^2$  parameter. Only events with  $t\chi^2 < 1.4$  are considered.

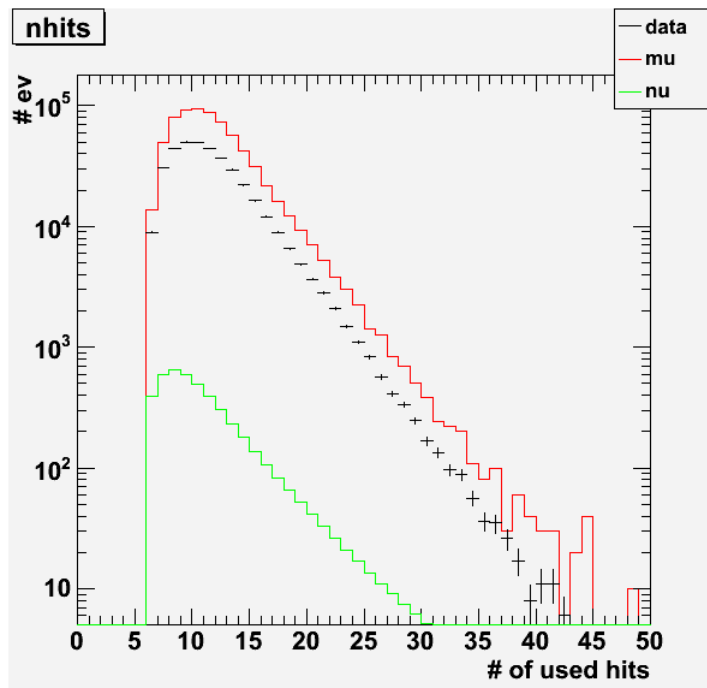


**Figure 4.12.** The DATA-MC comparison for the number of used hits in the reconstruction fit. Only events with  $t\chi^2 < 5$  are considered.

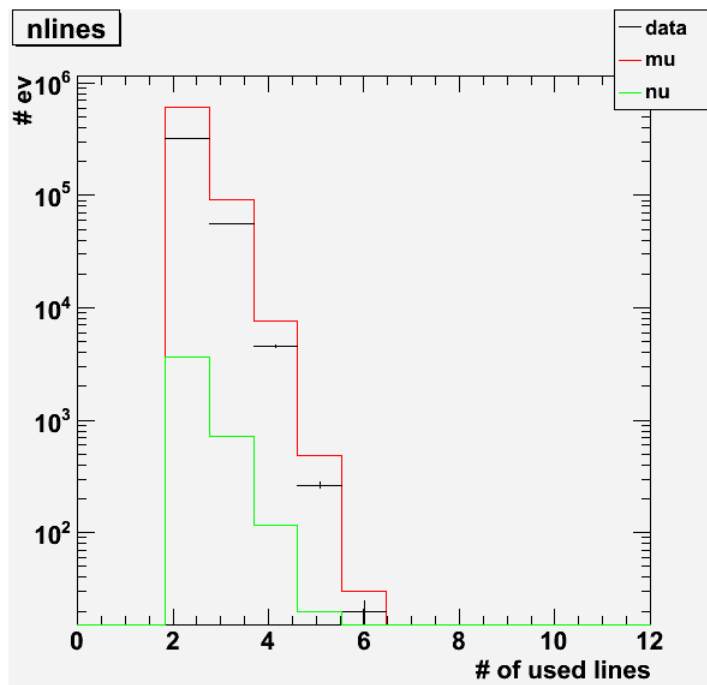


**Figure 4.13.** The DATA-MC comparison for the number of used lines in the reconstruction fit. Only events with  $t\chi^2 < 5$  are considered.

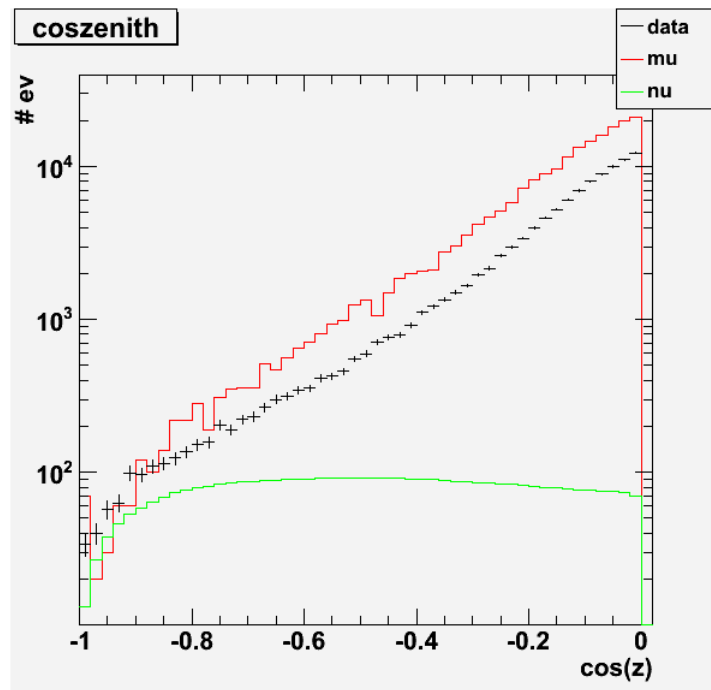


**Figure 4.14.** The DATA-MC comparison for the  $\cos(\text{zenith})$  parameter. Only events with  $t\chi^2 < 3$  are considered.

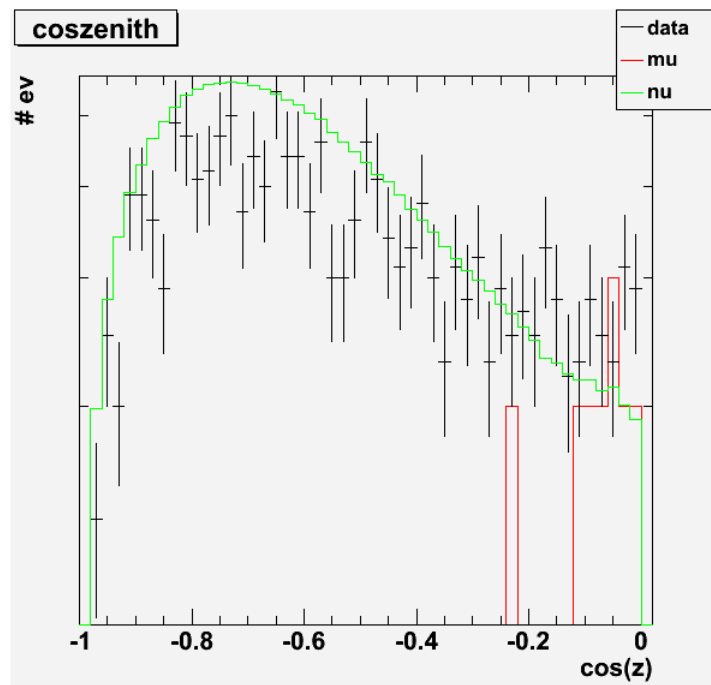


**Figure 4.15.** The DATA-MC comparison for the  $\cos(\text{zenith})$  parameter. Only events with  $t\chi^2 < 1.4$  are considered.

Summing up we can conclude that there is a good agreement between DATA and Monte Carlo for low values of  $t\chi^2$ . As a consequence of this good agreement we decided to use the scrambled DATA to emulate the background (see section 4.13).

The excess of the muon Monte Carlo over the DATA, seen in the plots with an high value of the  $t\chi^2$  cut, is of two orders of magnitude. It is know from previous analysis. This fact it is not worrying because, as it is shown in the plots with the cut  $t\chi^2 < 1.4$ , this excess is removed applying a tighter cut on the track fit quality parameter rejecting all atmospheric muon down-going events bad reconstructed as up-going.

### 4.9.1 Angular resolution

As we have shown in the previous paragraphs, the MC description of the expected background is remarkable. The selection signal-background is at this point possible only looking at the direction of the incoming track. So the angular resolution of the track reconstruction algorithm plays a fundamental role.

We do expect that the signal will be contained in a cone with aperture angle  $\sim 3\sigma$  where  $\sigma$  quantify the angular resolution. The amount of background is directly proportional to the cone aperture.

We described the meaning of angular resolution in the chapter 3. From MC simulated events we evaluate the detector angular resolution.

Applying the formula:

$$\Theta_{\mu-\nu} = \arccos [\sin(\theta_\mu) \sin(\theta_\nu) \cos(\phi_\mu - \phi_\nu) + \cos(\theta_\mu) \cos(\theta_\nu)], \quad (4.19)$$

which defines the angle between two given direction  $\Theta_{\mu-\nu}$ , we evaluate any difference between the original track  $(\phi_\nu, \theta_\nu)$  and the reconstructed one  $(\phi_\mu, \theta_\mu)$ .

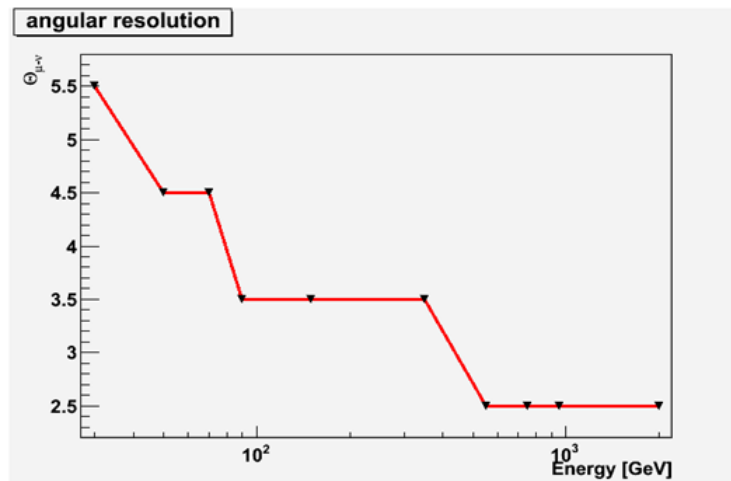


**Figure 4.16.** The angular resolution for an example set of neutrino MC events.

In figure 4.16 we show the angle between the MC  $\nu_\mu$  direction and the reconstructed  $\mu$  track, as a function of  $E_\nu$ . From this distribution we can evaluate the angular resolution for different interval of  $\nu$  energy.

Obviously for lower energies the angle is bigger than for the higher. This is due to  $\nu_\mu$  CC kinematics (see the angular resolution equation 3.12).

### 4.9.2 The effective area

In order to evaluate the amount of signal and background events we usually quote the "effective area" of the detector. This quantity if multiplied by the flux of incoming particles returns the number of events.

To evaluate the effective area we start from the definition of  $w_2$ . The effective area has the dimension of  $[m^2]$ . From the definition of  $w_2$  (see paragraph 4.8.1) we can write:

Then, for each event energy  $E$ , the effective area is equal to:

$$A_{eff} = \frac{w_2}{I_\theta \cdot I_E \cdot E^\gamma \cdot F}, \quad (4.20)$$

with  $\gamma = 1.4$ ,  $I_\theta = 4\pi$  (angular phase space),  $F = 3.15 \times 10^7$  (number of seconds in one year) and  $I_E$  (energy phase space) is the integral of  $E^{-\gamma}$ . All these quantities are defined in the paragraph 4.8.1.

In the following figure 4.17 is shown the effective area for neutrino MC events.

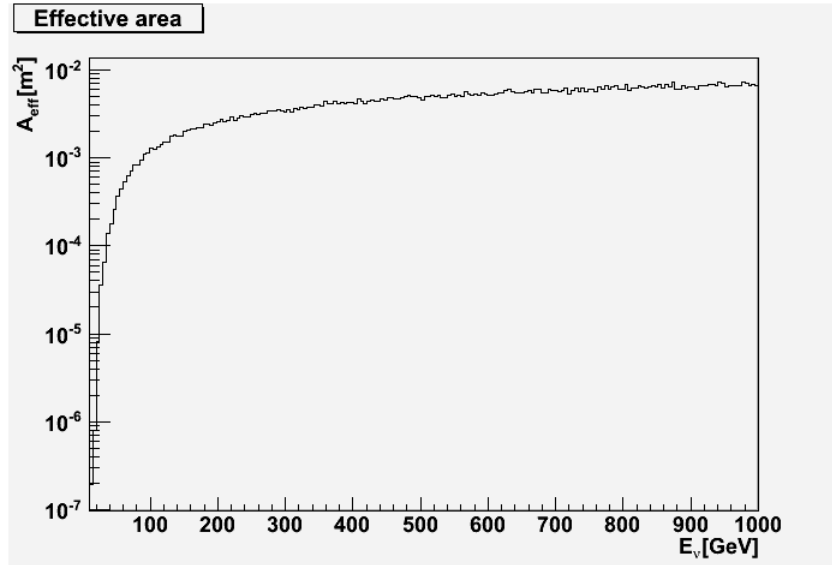


Figure 4.17. The effective area for neutrino MC events of line 9 configuration.

## 4.10 Monte Carlo simulation of $\nu_\mu$ from Dark Matter

In this section we describe how to construct the Monte Carlo signal simulation.

As for background we used the official ANTARES MC chain (shown in section 4.5) to simulate the interactions of neutrinos arising from the dark matter annihilation into the Galactic Centre.

The MC simulates an isotropic background diffuse flux of neutrino events. We convolute that flux with the spectra of neutrino from WIMP annihilation in order to have a neutrino energy distribution compliant with what expected for neutrinos from dark matter annihilation.

Now we have neutrinos according to the expected spectrum but isotropically distributed over the space.

Then, to obtain a localised flux deriving from a particular point source direction (the GC) we will only use those neutrinos coming from a region of the sky close to the GC coordinates.

To take into account the dark matter annihilation spectra we use the WIMPSIM package.

#### 4.10.1 The WIMPSIM package

The WIMPSIM package [63, 35] was used to simulate the WIMP annihilation in both the Sun and the Earth and the neutrino propagation to the neutrino telescope. WIMPSIM consists of two parts: `WimpAnn` and `WimpEvent`.

The program `WimpAnn` simulates WIMP annihilation in Sun and Earth with the help of the `Pythia` package [134], the neutrino interactions in the Sun are simulated with `nusigma` [62].

The output is given event by event, which is suitable for interfacing to a neutrino telescope Monte Carlo.

#### The WIMPSIM parameters

A full three flavour neutrino oscillations are also included in the simulations as well as the Neutrino regeneration from  $\tau$  decay arising in charged current interactions on the way out of the Sun.

`WimpAnn` generate neutrino events at 1 AU from the Sun and in the center of the Earth. The event files created by `WimpAnn` can be read by `WimpEvent`, that takes these neutrinos and propagates them to a neutrino telescope, including neutrino oscillations on their way. At the detector, neutrino interactions are simulated with `nusigma`.

The reason why there are these two programs is that `WimpAnn` can generate event files without having to know about a particular detector location: this last part of simulation is done with `WimpEvent`. Both these programs take into account the three neutrino flavours for neutrino and anti-neutrino events.

As reported in the WIMPSIM internet site [60], the two programs have been made run for 2.5 million events for 18 different WIMP masses, from 10 GeV to 10 TeV, and for several different annihilation channels.

The output was focused on the IceCube detector, but the results would not change significantly for any other detector.

In our analysis we have chosen the standard parameter oscillation scenario.

In the following table 4.7 the values of the main oscillation parameter in the B case are reported.

**Table 4.7.** Oscillation parameters considered in the WIMPSIM B scenario [60]

$\theta_{12}$	$\theta_{13}$	$\theta_{23}$	$\delta$	$\Delta m_{21}^2$	$\Delta m_{31}^2$
33.2	0.0	45.0	0.0	$8.1 \times 10^{-5}$	$2.2 \times 10^{-3}$

As can be seen in table 4.7 the  $\theta_{13}$  parameter was set to zero for the standard oscillation scenario. In the next new versions of WIMPSIM the new values of the oscillation parameters will be taken into account [70].

### MC simulation of $\nu$ from Dark Matter annihilation in the Galactic Centre

As we said a lot of time we have to perform a search for dark matter from the Galactic Centre. Unfortunately the WIMPSIM package does not provide the neutrino spectra arising from WIMP annihilation in the GC, but only the spectra from Earth and Sun Centre and Sun surface.

In order to investigate in the GC direction, the ANTARES collaboration decided to use the Earth Centre spectra because it can be considered more similar to the GC spectra. Instead the Sun spectra undergo some effects due to the interactions of neutrinos in the Sun medium like the  $\tau$  lepton regeneration into the Sun medium.

Another reason we do not use a GC-based MC is that we don't know in an exact way how the GC is made and its characteristics (for example the density distribution and so on) 1.5.3.

Moreover what it is truly important is the shape of the annihilation spectrum and not the number of events that is only a multiplicative constant. One have to consider that the shape of the spectrum is the same in the GC, in the Earth core and so on, because it depends from the annihilation reaction and the correspondent WIMP mass and not from other characteristics.

What can modify the spectrum is the effect of an high density medium like in the Sun's core. In effect the neutrinos from neutralino annihilation spectra at the surface of the Sun show the effects of the electronic capture and other absorption effects that cause an oscillation in the shape of the spectra. But this is not the case of the Galactic Centre, as a matter of fact, usually the common used halo density is  $0.4 \text{ GeV}/\text{cm}^3$ .

#### 4.10.2 The annihilation spectra

The WimpAnn output consists of two files: one for the Sun's core and the other for the Earth's centre. Each file has a header stating information about the simulation (like versions of programs used, oscillation parameters and date).

After the header, the earth summary files contains six lines, with 200 numbers each. These numbers are the differential yield,  $dN/dz$  [ $\text{ann}^{-1}$ ] in 200 bins in unity of annihilation<sup>-1</sup>.

$z = E_\nu/M_{WIMP}$  is the neutrino energy fraction in units of the WIMP mass.

The six lines are for the six different neutrino and anti-neutrino flavours [60]: the first line is  $\nu_e$ ; the second represents the  $\bar{\nu}_e$ ; the third is  $\nu_\mu$ ; the fourth represents the  $\bar{\nu}_\mu$ ; the fifth column represents  $\nu_\tau$  and the sixth the  $\bar{\nu}_\tau$ .

Thus we have to take into account the oscillation between the GC and the Earth. We see the case of neutrino (for anti-neutrino is the same).

We have the three spectra:

$$\frac{dN}{dz}(\nu_e), \frac{dN}{dz}(\nu_\mu), \frac{dN}{dz}(\nu_\tau). \quad (4.21)$$

In order to take into account the standard oscillation partition (1:1:1), since the GC is  $\approx 8.4$  kpc distant from the Earth, we sum the spectra and divide them by 3:

$$\frac{dN}{dz}(\nu) = \frac{\frac{dN}{dz}(\nu_e) + \frac{dN}{dz}(\nu_\mu) + \frac{dN}{dz}(\nu_\tau)}{3}. \quad (4.22)$$

In this analysis we choose to evaluate the sensitivity of the ANTARES detector to many different models of dark matter. In particular we choose 3 diverse annihilation channels and 10 diverse WIMP masses.

The three chosen annihilation channels are:

- $b\bar{b}$ , it is a soft energy channel, since the  $b$  quark is a light quark with a mass of  $m_b = 4.19^{+0.18}_{-0.06}$  GeV [111] ;
- $\tau^+\tau^-$ , it is a hard energy channel; the  $\tau$  lepton mass is  $m_\tau = 1776.82 \pm 0.16$  MeV [111] ;
- $W^+W^-$ , is the hardest energy channel used in this analysis, being the  $W$  boson mass is equal to  $m_W = 80.399 \pm 0.023$  GeV [111] .

The ten different values of mass that we selected to test the detector sensitivity are:

- |             |             |
|-------------|-------------|
| • 50 GeV;   | • 250 GeV;  |
| • 80.3 GeV; | • 350 GeV;  |
| • 100 GeV;  | • 500 GeV;  |
| • 176 GeV;  | • 750 GeV;  |
| • 200 GeV;  | • 1000 GeV. |

Thus, in total, we have 29 different models. The total number is not 30 because for the 50 GeV mass it not available the  $WW$  channel (since the  $W$  mass is to high for the  $b$  mass).

In the figures 4.18, 4.19, 4.20 and 4.21 can be seen some example of the neutrino spectra from the WIMP annihilation for different WIMP masses and channels.

## 4.11 Weights policy for MC signal events

As well as the Monte Carlo background events, also the signal Monte Carlo events have to be weighted, to use them for analysis purpose. To weight the simulated signal events we use the  $w_2$  weight defined in 4.8.1. Then, after the correction explained in 4.11.1, we convolute this weight with the spectrum obtained from the WIMPSIM simulation and partially show in figures 4.18-4.21.

### 4.11.1 The weight $w_2$ in the v1r2p5 version of AntDST

As we mentioned in the section 4.8, in the standard ANTARES analysis chain the  $w_2$  weight has the dimensions, for point-like sources, of  $[GeV \cdot m^2 \cdot s \cdot yr^{-1}]$ . The data

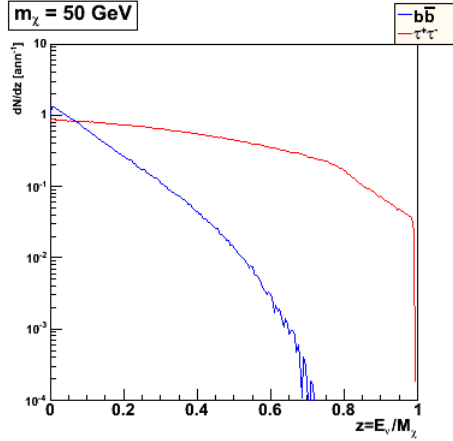


**Figure 4.18.** The neutrino spectra for the WIMP mass of 50 GeV and the two available annihilation channels:  $b\bar{b}$  and  $\tau^+\tau^-$ .

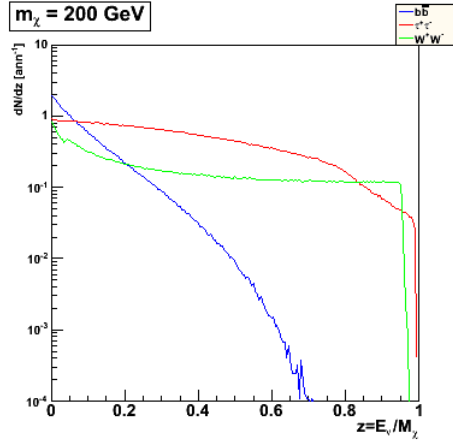


**Figure 4.19.** The neutrino spectra for the WIMP mass of 200 GeV and the three available annihilation channels:  $b\bar{b}$ ,  $\tau^+\tau^-$  and  $W^+W^-$ .

sample analysed in this thesis has been pre-processed officially by the ANTARES collaboration and is available in the format `AntDST` where few reconstructed quantities are added to the raw data.

Among the parameters related to the simulation there are the weights. Unfortunately the quantity `w2` for such data production is defined in a different way: it has, for point-like sources, the dimensions  $[GeV \cdot cm^2 \cdot s]$  [41].

The weight inserted in the `AntDST` files is `w2'` defined as:

$$w2' = \frac{w2}{3.15 \times 10^3} = \frac{w2}{3.15 \times 10^7 \cdot 10^{-4}}. \quad (4.23)$$

The factor  $3.15 \times 10^3$  simply derives from taking into account the number of seconds in a year, that is:  $3.15 \times 10^7$ , and the obvious transformation between  $cm^2$  and  $m^2$ .

Following the ANTARES procedure each simulated signal event, in `GENHEN`, has

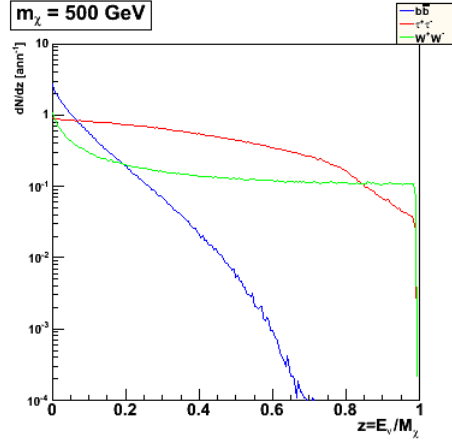


**Figure 4.20.** The neutrino spectra for the WIMP mass of 500 GeV and the three available annihilation channels:  $b\bar{b}$ ,  $\tau^+\tau^-$  and  $W^+W^-$ .

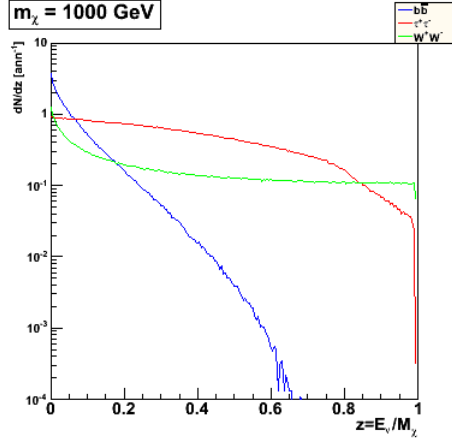


**Figure 4.21.** The neutrino spectra for the WIMP mass of 1 TeV and the three available annihilation channels:  $b\bar{b}$ ,  $\tau^+\tau^-$  and  $W^+W^-$ .

to be multiplied by the weight:

$$w = 3.15 \times 10^3 \frac{w2}{N_{gen}} \Phi [GeV^{-1} \cdot m^{-2} \cdot s^{-1}], \quad (4.24)$$

to get the rate of events in a specified time interval  $\Delta T[yr]$  in year corresponding to the active detector lifetime of the considered analysis.  $N_{gen}$  is the number of generated events in GENHEN,  $\Phi [GeV^{-1} \cdot m^{-2} \cdot s^{-1}]$  is the flux of  $\nu_\mu$  or  $\bar{\nu}_\mu$ .

On the contrary, considering the differences in the units, the weight that has to be attributed to each event in AntDST is:

$$w = \frac{w2'}{N_{gen}} \Phi [GeV^{-1} \cdot cm^{-2} \cdot s^{-1}]. \quad (4.25)$$

In this last case, indeed, one has to consider the flux in  $cm^{-2}$  and the active detector lifetime of the considered analysis  $\Delta T[s]$  expressed in seconds. The two ways

to evaluate weights for Monte Carlo events of neutrino interactions give equivalent results.

#### 4.11.2 The signal weight convolution

We have now to convolute the neutrino flux  $\Phi$  from dark matter annihilation with the w2 weight. Since we have two different MC productions of neutrino interactions (one for neutrinos and another one for anti-neutrinos), we have to multiply each distribution for the correct WIMPSIM spectrum:  $dN/dz(\nu)$  for neutrino MC and  $dN/dz(\bar{\nu})$  for anti-neutrino MC.

To remove the energy dependence of the weight we have to convert our  $dN/dz$  spectra in  $dN/dE$  spectra<sup>5</sup>. Using  $z = E/M_\chi$ , and  $dz = dE/M_\chi$ , we proceed in this way:

$$\frac{dN}{dz} = M_\chi \frac{dN}{dE} \implies \frac{dN}{dE} = \frac{1}{M_\chi} \frac{dN}{dz}.$$

To have the values of  $dN/dE$  we have to redraw the previous plot of  $dN/dz$  (see paragraph 4.10.2). First, we multiply  $z$  for the WIMP mass  $M_\chi$ , in this way we have only  $E$  on the abscissa. Then, for each given value of the energy of the event in the ANTARES MC we extrapolate, with an interpolation between the different bins, the correspondent value of  $dN/dE$ .

It is also important to evaluate the integral of the sum of the two spectra of neutrinos and anti-neutrinos given by WIMPSIM:

$$\begin{aligned} I(\nu + \bar{\nu}) &= \int \frac{dN}{dE} dE = \int \frac{1}{M_\chi} \frac{dN}{dz} M_\chi dz = \\ &= \int \frac{dN}{dz} dz = \int \left( \frac{dN}{dz}(\nu) + \frac{dN}{dz}(\bar{\nu}) \right) dz. \end{aligned} \quad (4.26)$$

This integral will be used to take into account the units of measures in the final computation of the sensitivity we will see in paragraph 4.14.1.

Thus, taking into account the generation weight defined in paragraph 4.11.1, the global event weight is given by:

$$w = w2[GeV \cdot m^2 \cdot s \cdot yr^{-1}] \cdot \frac{\Delta T[yr]}{N_{gen}} \cdot \Phi[GeV^{-1} \cdot m^{-2} \cdot s^{-1}], \quad (4.27)$$

where  $\Phi$  is the signal flux of neutrinos deriving from Dark Matter annihilation,  $N_{gen}$  is the total number of generated events ( $5 \times 10^8$  for standard MC and  $10^9$  for Low energy MC) and  $\Delta T[yr]$  is the total active detector lifetime for the considered analysis ( $\Delta T(dy) \sim 478.15$  days for 7903 runs when the GC is below the ANTARES horizon). For the study of the Dark Matter neutrino signal from the Galactic Centre, the considered time is the sum of the durations of the runs included in the selection

<sup>5</sup>Notice that, from now on:  $E_\nu \rightarrow E$  and  $M_{WIMP} \rightarrow M_\chi$ .

(paragraph 4.3.1) taking into account only those periods during which the GC is below the ANTARES horizon. Indeed, the formula 4.27 has to be intended as the sum over all the neutrino interaction events and it results in the total number of signal events  $n_s = rate \times \Delta T$ .

The signal flux used in the formula 4.27 has the following expression:

$$\Phi = \frac{\Gamma_A [ann \cdot s^{-1}]}{D^2 [m^2]} \cdot I(\nu + \bar{\nu}) [ann^{-1}] \cdot \frac{1}{M_\chi [GeV]} \frac{dN}{dz}, \quad (4.28)$$

where  $D = 8.4 \text{ kpc} = 2.5919692665 \times 10^{20} \text{ m}$  is the distance between the Earth and the Galactic Centre<sup>6</sup>,  $M_\chi$  is the WIMP mass considered each time and  $\Gamma_A$  represents the annihilation rate in the GC, that we consider as an unknown variable. The integral of the WIMPSIM spectra  $I(\nu + \bar{\nu})$  is introduced to preserve the dimension of  $[ann^{-1}]$  and can be interpreted as a branching ratio for the different channels.

## 4.12 The selection of signal events

According to the flux of neutrinos foreseen by WIMPSIM we use, from the sample of MC neutrino interacting events, only those events which energy ranges between 0 and  $M_\chi$ . All the other MC events are ignored. For example, in the case of  $M_\chi = 50 \text{ GeV}$  we can not use events with an energy bigger than  $50 \text{ GeV}$  to weight the MC signal.

So the first event selection applied is:

- $E < M_\chi$ .

### 4.12.1 Selection of $\nu$ candidates: the acceptance region

For the accepted events we modified the weight in order to reproduce the WIMPSIM energy spectra. The interacting neutrino MC (used for all analysis in ANTARES) foresee a uniform isotropic diffuse neutrino flux while the neutrinos from Dark Matter annihilation in Galactic Centre are expected from a fixed position at a given time.

In order to create a sample of simulated neutrino interactions to be used as "simulated signal" in our analysis we applied a cut on the neutrino incoming direction.

We then selected a region of acceptance, around the trajectory of the Galactic Centre, in the sky visible by the detector. To select this region we can apply diverse methods: use a Gaussian point spread function around the GC position or a rectangular one. The size of this angular interval must take into account the ANTARES angular resolution.

In this case we use a rectangular acceptance interval. Let us now define  $\Delta\xi$  the half-size of this allowed interval. We take, event by event,  $\Delta\xi = 5^\circ$ .

Thus, for each event we calculate, at a given time, the position of the GC following the method explained in the section 4.13, and we accept all the events that come from the allowed region of half-amplitude  $\Delta\xi$  around the GC direction.

---

<sup>6</sup>This distance was derived by the subtraction of the distance between the Earth and the Sun ( $d_{\odot\oplus} = 149597870700 \text{ m}$ ) [111] with the distance between the Sun and the GC ( $d_{\odot GC} = 8.4 \text{ kpc} = 2.591969268 \times 10^{20} \text{ m}$ ) [111].

So we have a  $\Delta\xi \times \Delta\xi$  zone around each GC position from which we accept the events, weighting them with the signal MC weight we describe in the paragraph 4.11.2.

The origin of the accepted events is shown in the figure 4.22, for only the anti-neutrino signal events in the (Azimuth,zenith) coordinate space.

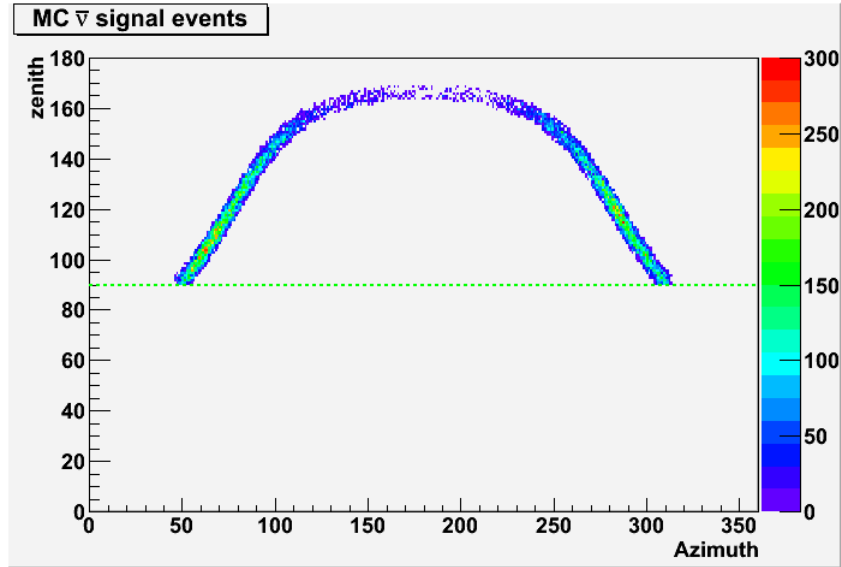


**Figure 4.22.** The stripe of signal around the Galactic Centre motion in the horizontal coordinates (A,z). Only for the anti-neutrino signal events.

The green dashed line represent the horizon of the detector for up-going events (that is zenith  $z = 90^\circ$ ).

#### 4.12.2 Selection of $\nu$ candidates: the cut $t\chi^2 < b\chi^2$

Before to proceed with the most accurate analysis on the two parameters  $t\chi^2$  and half-cone angle, analysis in which we will see which will be the best optimised cuts on these two parameters, we now apply a new cut.

As stated before, we apply some basic cuts to both DATA and Monte Carlo events. These cuts are defined in the paragraph 4.7.1. We know that the data sample we used in this analysis is composed both of events that are reconstructed as muon tracks and events that are reconstructed as electron shower. The first kind of events have a low value of the track fit quality parameter, that accounts for the goodness of the fit performed to reconstruct the events of the track type; the second, instead, have a low value of the bright point quality parameter, that accounts for the goodness of the fit performed to reconstruct the events of the shower type.

In order to clean our data sample, rejecting the surviving muon background events, and with the aim to select the majority of the simulated signal events, we decided to apply this new cut:

- $t\chi^2 < b\chi^2$ .

This means that we take all the events that have a probability to be due to a track higher than the probability to be due to a shower. Thus we take only events that are well reconstructed as a track and bad as a bright point.

The importance of this cut resides in the fact that it allows us to remove the majority of the background muon events conserving the bigger part of the neutrino signal events and, of course, of the background neutrino events. As can be seen in the figure 4.23 for the 9 line set of events.

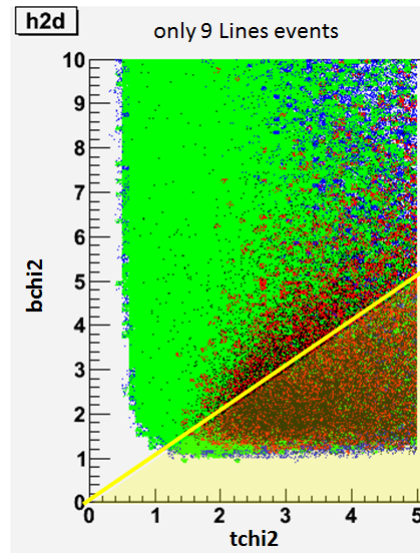


**Figure 4.23.** The plot show the effect of the  $t\chi^2 < b\chi^2$  cut. The black point represents DATA events, the red point the muon events, the green points the background neutrino events and the blue points the signal neutrino events.

In the figure 4.23 the black point represent the DATA events; the red points the MC muon events; the green points the MC background neutrino events and the blue points stands for the MC signal neutrino events. The yellow line separates the two regimes, the one under the line is the region rejected.

In this way we are able to remove the bigger part of the muon background events conserving a large fraction of the neutrino events, as we said above.

If we combine this cut with a more restricted cut on the track fit quality parameter, e.g.  $t\chi^2 < 1.4$ , all the muon events disappear. As a matter of facts a cut  $t\chi^2 < 1.4$  would remove all muon background events (see paragraph 4.14.2).

It means we found a criteria to remove all the muon background that affect the neutrino revelation but we have to be sure that we do not cut too much on neutrinos sample. We will optimize the cut value in order to maximize our search sensitivity.

Into the figure 4.24 is more easy to see the effect of this cut on the neutrinos signal and the muons background. Here is represented on the abscissa the subtraction  $t\chi^2 - b\chi^2$ .

In this plot 4.24 we compare normalised distributions for the several contributions. The green line represents the cut and the green region is the zone in which are all the accepted events.

From this plot we can do some simple evaluation to confirm that this cut (that

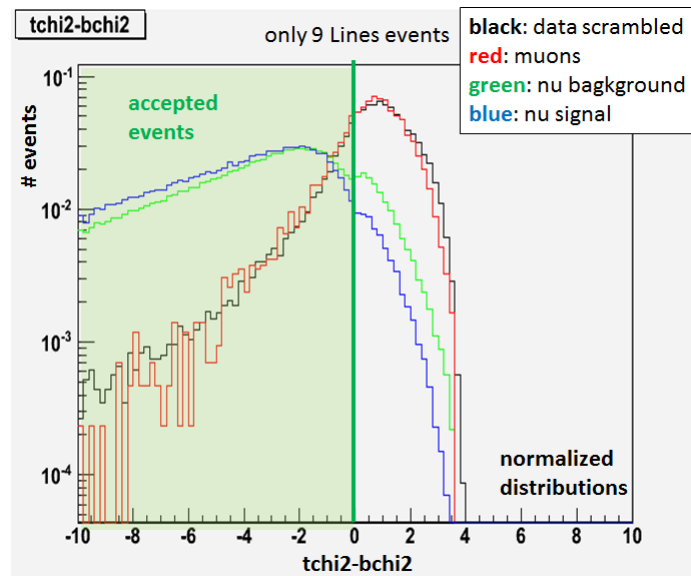


**Figure 4.24.** The distributions of the different types of particles: DATA, MC muons, MC background neutrinos and MC signal neutrino.

here figures as  $t\chi^2 - b\chi^2 < 0$ ) has the better ratio between selected neutrino signal events and discarded background muon events.

In fact, with this choice of cut we remove the 95% MC muon background events and at the same time discarding only the 7% of the MC neutrino signal events.

Thus, from now on, we apply always this cut to all the DATA and MC background and signal events (for both muons and neutrinos).

### 4.13 The binned analysis

In this section we describe how we will search for a signal once the candidate event sample will be defined. We will project all reconstructed tracks on the galactic coordinates and we will search for a statistical excess of events in a predefined angular interval: a binned analysis.

So, the main task of our binned analysis is to look for an excess of events in the GC direction under certain given cuts.

Using the ROOT subroutine `ConvertCoordinates.hh` we are able to calculate the position of the GC at any time in the space for any given coordinate system (galactic, equatorial, horizontal, local).

In order to have this result, having the position of GC in galactic coordinate system, we need to know the exact time and the position of the detector in longitude and latitude. The time is expressed in Julian Date (JD), very useful to report observations that go on for long interval of times. This means to express the time in mean solar days and decimal fractions starting from (for convention) the mean Greenwich noon of the first day of January of the year 4713 B.C.. By definition one Julian Year is equivalent to 365.25 Julian Days [77].

The exact position of the **Galactic Centre (GC)** in the galactic coordinate system<sup>7</sup> (l,b), where l represents the galactic longitude and b the galactic latitude, is:

$$l_{GC} = 359^\circ.944306, \quad b_{GC} = -0^\circ.46194.$$

The position of the ANTARES detector, in Azimuth and Zenith, is:

$$A_{ANTARES} = 6^\circ.1657, \quad z_{ANTARES} = 42^\circ.798917.$$

The definition of the Julian Date, that results in a decimal number, is [21]:

$$\begin{aligned} \text{JD} = & 367Y - \text{Int} \left\{ 7 \left[ \frac{Y + \text{Int} \left( \frac{M+9}{12} \right)}{4} \right] \right\} - \text{Int} \left\{ 3 \left[ \frac{\text{Int} \left( \frac{Y + \frac{M-9}{7}}{100} \right) + 1}{4} \right] \right\} \\ & + \text{Int} \left( \frac{275M}{9} \right) + D + 1721028.5 + \frac{\text{UT}}{24}, \end{aligned} \quad (4.29)$$

where  $Y$ ,  $M$  and  $D$  stand for Year, Month and Day; Int means integer part and UT is the Universal Time: a time scale based on the rotation of the Earth [77]. For more details on the Julian Date and the relative algorithms and transformations see the reference [21].

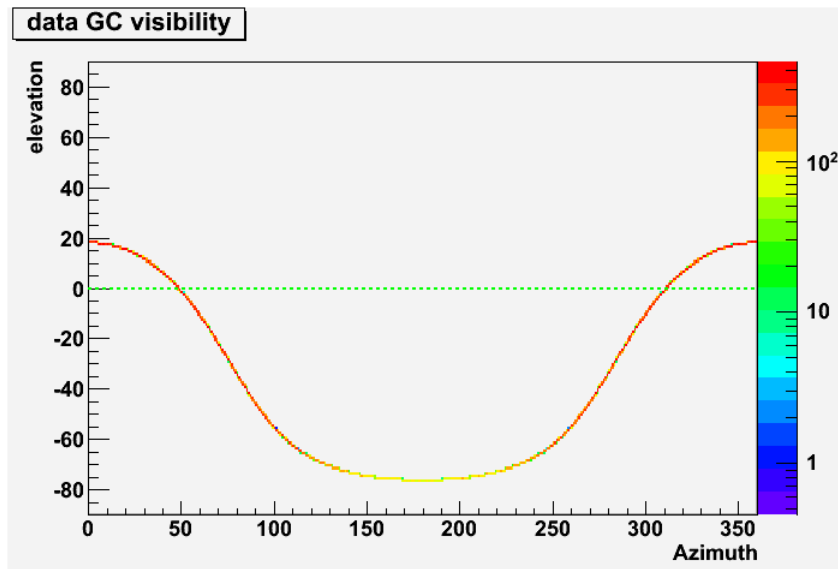


**Figure 4.25.** The Galactic Centre visibility in the horizontal system (A,h).

In the figure 4.25 is reported the GC motion in the coordinate system (Azimuth, elevation). The GC position in this reference system follows, day by day, always the same trajectory.

<sup>7</sup>Note that in this coordinate system the GC has obviously a fixed position.

In the figure it is possible to see the horizontal green dashed line of the horizon of the ANTARES detector. It represents also one of our applied cuts: as we said in the paragraph 4.7.1, in order to reduce the background from atmospheric muons, we accepted in our sample of candidates only the up-going events. They have an elevation lower than  $0^\circ$ .

The color scale represents the number of DATA events found in the exact direction of the Galactic Centre for each given time.

In the figure 4.26 are represented the evolution of the GC position and the distribution of the up-going neutrino events in horizontal coordinates (the conversion between elevation and zenith is  $z = 90 - h$  as we show in the section 4.1). It is easy to see that there are zones in which we have a lower rate of events and zones in which there are much more events.

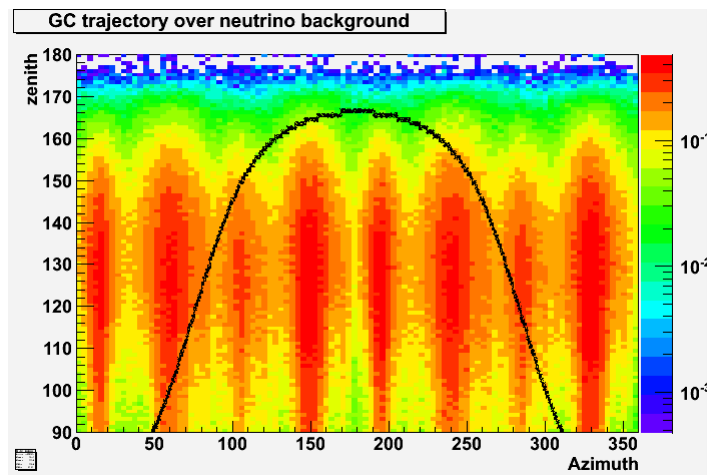


**Figure 4.26.** The trajectory of the GC plotted over the distribution of the up-going neutrino events in the horizontal coordinate system space  $(A, z)$ .

From the figure 4.26 are clearly visible also the zones that are preferred for the event identification and reconstruction due to the octagonal (cylindrical) symmetry of the ANTARES detector.

Our analysis will consist in searching for an excess of events in an angular region (a cone of a chosen **half-cone angle**) around the true neutrino coming from the Galactic Centre position (see figure 4.22). The angle aperture of that cone has to be defined in order to maximize the signal over background fraction, i.e. in order to maximize the detector sensitivity.

The number of background events is defined by the number of scrambled DATA events that fall inside the search cone. The number of signal events ( $n_s$ ) is evaluated, assuming a reference neutrino flux  $\Phi$ , as the number of events that fall inside the cone.

Of course the neutrino from GC will be only spread due to detector resolution (see section 4.12.1 while the background is uniformly distributed).

To derive the formula of the half-cone angle aperture, first we consider two points in the three dimensional space:  $(x_1, y_1, z_1) = (\phi_1, \theta_1)$  and  $(x_2, y_2, z_2) = (\phi_2, \theta_2)$ . Let's

put ourself in the center of the reference system and trace two vector pointing in these two directions. These two vectors are:  $\vec{r}_1$  and  $\vec{r}_2$  and the angle between them is  $\Delta$ .

The scalar product of these two vectors is:

$$\begin{aligned}\vec{r}_1 \cdot \vec{r}_2 &= |r_1| \cdot |r_2| \cos \Delta \\ &= (x_1 \cdot x_2 + y_1 \cdot y_2 + z_1 \cdot z_2).\end{aligned}\quad (4.30)$$

Now we use the spherical coordinates system:

$$\begin{cases} x = |r| \sin \theta \cos \phi \\ y = |r| \sin \theta \sin \phi \\ z = |r| \cos \theta.\end{cases}$$

Obtaining  $\cos \Delta$  from the equation 4.30, and substituting there the spherical coordinates, it follows that:

$$\begin{aligned}\cos \Delta &= \frac{x_1 \cdot x_2 + y_1 \cdot y_2 + z_1 \cdot z_2}{|r_1| \cdot |r_2|} \\ &= \frac{|r_1| \sin \theta_1 \cos \phi_1 |r_2| \sin \theta_2 \cos \phi_2 + |r_1| \sin \theta_1 \sin \phi_1 |r_2| \sin \theta_2 \sin \phi_2 + |r_1| \cos \theta_1 |r_2| \cos \theta_2}{|r_1| \cdot |r_2|} \\ &= \sin \theta_1 \cos \phi_1 \sin \theta_2 \cos \phi_2 + \sin \theta_1 \sin \phi_1 \sin \theta_2 \sin \phi_2 + \cos \theta_1 \cos \theta_2 \\ &= \sin \theta_1 \sin \theta_2 (\cos \phi_1 \cos \phi_2 + \sin \phi_1 \sin \phi_2) + \cos \theta_1 \cos \theta_2 \\ &= \sin \theta_1 \sin \theta_2 \cos(\phi_1 - \phi_2) + \cos \theta_1 \cos \theta_2.\end{aligned}\quad (4.31)$$

Where we used (in the fifth step) the trigonometrical property of the difference of cosines.

From the just derived formula 4.31, explicit the  $\Delta$  angle and using the horizontal coordinate system (Azimuth, zenith) described in the section 4.1, we obtain the half-cone angle between the true neutrino from the Galactic Centre direction and its reconstructed originated muon:

$$\Delta = \arccos [\sin(z) \sin(z_{GC}) \cos(A - A_{GC}) + \cos(z) \cos(z_{GC})]. \quad (4.32)$$

In the figures 4.27 and 4.28 the DATA and MC (of atmospheric muons and neutrinos) events distribution for the whole set of data is shown as a function of the half-cone angle  $\Delta$  [°]. As can be seen, for the tighter cut on  $t\chi^2$  all the muon events are rejected and the DATA distribution traces well the neutrinos MC distribution.

So we decided to use the Scrambled DATA to emulate the background events. Moreover, in order to cancel out the stepping behaviour of the Scrambled DATA events (seen in figure 4.28) we decided to perform a multiple scrambling: i.e. we scrambled the Julian Date of each event 5000 times randomly obtaining 5000 replica of each event and thus having an expanded sample of DATA<sup>8</sup>.

At the end, when we evaluate the number of background events, starting from the SD, in the half-cone angle we divide this number by the number of scrambling operations (5000). This trick serves only to smooth the scabbled DATA distribution in order to improve the agreement of the tracking of SD distribution with respect to the neutrino Monte Carlo one.

<sup>8</sup>We performed this multiple scrambling operation taking, for each event, the corresponding JD and calculating 5000 times the GC position for the JDs computed as follows:  $JD = JD \times (JD_{random} - 0.5) * 1$ , where 1 stands for one JD.

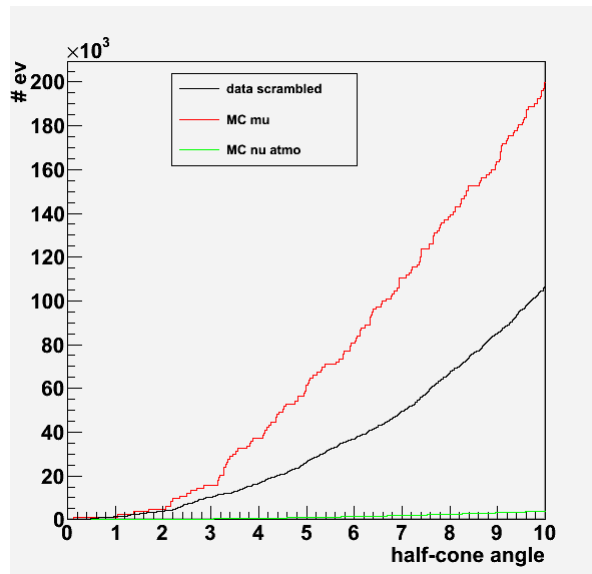


**Figure 4.27.** The distribution of DATA and MC events as a function of the half-cone angle for the whole data set. A  $t\chi^2 < 3$  cut was applied. The agreement, as already noticed, is not sufficient for larger values of  $t\chi^2$ .

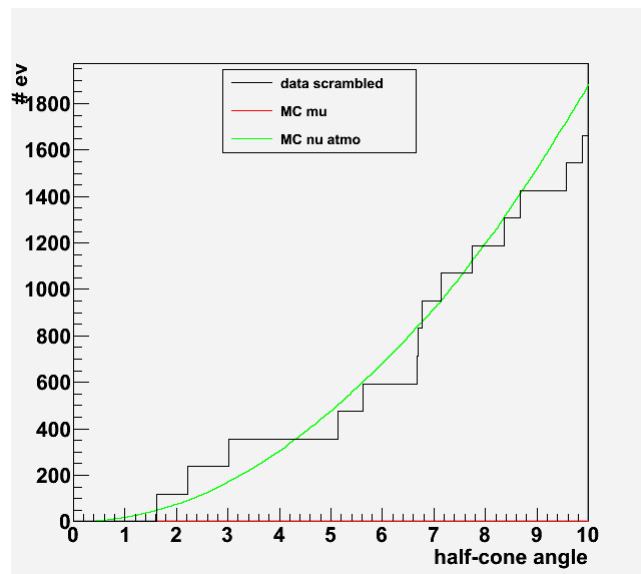


**Figure 4.28.** The distribution of DATA and MC events as a function of the half-cone angle for the whole data set. A  $t\chi^2 < 1.4$  cut was applied.

#### 4.14 The statistical analysis of 2007-2010 data

The DATA and Monte Carlo samples obtained so far, after all cuts already applied, still contain the neutrino signal from Dark Matter annihilation and some level of background due to atmospheric  $\nu_\mu$  and  $\mu$ .

The cut in  $t\chi^2$  could improve the signal to background ratio but the choice of the cut is not straightforward. Indeed our goal is to optimize the sensitivity of the

detector. The method to perform this optimization (called *Model Rejection Factor: MRF*) will be described in next paragraph 4.14.1.

The selection signal-background can be now performed requiring that the reconstructed tracks originate in a region close to the Galactic Centre position. Also in this case the aperture (the half cone angle defined with the formula 4.32) of the search cone, opened around the true neutrino coming from the GC position to define the "signal region", will affect the detector sensitivity.

Increasing the angle we allow more background (isotropically distributed); reducing too much the opening angle we could discard part of the signal. This parameter, the opening of the search cone, as well as the  $t\chi^2$  cut, will be fixed optimizing the detector sensitivity using the MRF technique.

#### 4.14.1 The Model Rejection Factor

This analysis technique has been developed [85] to optimize the sensitivity of an experiment to a discovery under the assumption that no signal will be detected [14]. This technique does not depend on the experimental data. The final signal-background selection criteria have to be chosen before ("prior") looking at the data sample. For this reason we analyse the sample of scrambled DATA also in agreement with the blinding policy of ANTARES experiment.

As described in the appendix A, the 90% confidence interval  $\mu_{90} = (\mu_1, \mu_2)$  is a function of the number of observed events  $n$  and of the expected background  $b$ :  $\mu_{90}(n, b)$ . We will consider  $\mu_{90}$  as an upper limit, taking only the high value of the confidence interval. Performing a measurement that results in  $n$  observed events, the corresponding upper limit on the source flux  $\Phi^{theo}(E, \theta)$  can be found scaling the expected source flux by the ratio of the upper limit to the signal expectations [123]:

$$\Phi_{90\%}(E, \theta) = \Phi^{theo}(E, \theta) \frac{\mu_{90}(n, b)}{n_s}. \quad (4.33)$$

A low value of the ratio leads to a strong constraint on the selected model, therefore one should optimise the cuts to minimize this ratio. As specified, the upper limit depends on the number of observed events  $n$ , that is not known until the experiment was performed (and the optimised cuts applied). For my analysis, the value of observed events  $n$  is unknown since the DATA are still scrambled. We only know the value of background  $b$  and we can evaluate the expected number of signal assuming the WIMPSIM model. Therefore we evaluate an average upper limit [66] to take place of  $\mu_{90}$  in the equation 4.33.

Following the Feldman and Cousins approach (described in the appendix A) we define the value  $\bar{\mu}_{90}(b)$  as the average 90% C.L. upper limit for the observed number of events in the hypothesis that  $b$  is the expected number of background events, evaluated from scrambled DATA using the given selection criteria, and no signal is present ( $n_s = 0$ ).

The average upper limit is the sum of these expected upper limits, weighted by their

Poisson probability of occurrence:

$$\bar{\mu}_{90}(b) = \sum_{n=0}^{\infty} \mu_{90}(n, b) \frac{b^n}{n!} \exp(-b). \quad (4.34)$$

If the number of events observed exceeds  $\bar{\mu}_{90}(b)$ , the null hypothesis (no signal) is rejected at 90% C.L.. This means that we can evaluate the minimum flux of neutrino signal from DM that would allow to reject the null hypothesis.

Our cuts on the  $t\chi^2$  and on the half-cone angle aperture will result in the number of background events  $b$  (obtained applying the selection criteria to the scrambled DATA) and in the number of signal events  $n_s$  that we could expect if a flux of neutrinos (from Dark Matter annihilation) with a known reference intensity (assumed according to the WIMPSIM simulation) would reach the detector.

Over an ensemble of identical experiments, the strongest constraint on the expected signal flux  $\Phi^{theo}$  corresponds to the set of cuts that minimizes the **Model Rejection Factor**:

$$\text{MRF} = \frac{\bar{\mu}_{90}}{n_s}, \quad (4.35)$$

and hence minimizes the average flux upper limit  $\bar{\Phi}_{90\%}$ :

$$\bar{\Phi}_{90\%} = \Phi^{theo} \times \text{MRF}, \quad (4.36)$$

where  $\Phi^{theo} = \frac{\Gamma_A}{D^2} \frac{dN}{dE} I(\nu + \bar{\nu})$ , that is the same flux described in the paragraph 4.11.2.

#### 4.14.2 The cuts to optimize

Our analysis represents the classical case of a search for a few events of neutrino signal, over a very large background, composed by atmospheric muons and neutrinos.

The experimental measure consists of counting the number of events in fixed angular bins around the selected source of signal, in our case the Galactic Centre, having fixed some cuts over fit and data quality parameters.

In this analysis we search the MRF optimization for two set of parameter values: the track fit quality  $t\chi^2$  and the half-cone angle  $\Delta$ . We choose a lot of different values for these two parameters:

For the  $t\chi^2$  we select 20 values:

- 0.8;
- 1.0;
- 1.2;
- 1.4;
- 1.6;
- 1.8;
- 2.0;
- 2.2;
- 2.4;
- 2.6;
- 2.8;
- 3.0;
- 3.2;
- 3.4;
- 3.6;
- 3.8;
- 4.0;
- 4.2;
- 4.4;
- 4.6.

For the half-cone angle also we select 20 values:

- 0.5;
- 1.0;
- 1.5;
- 2.0;
- 2.5;
- 3.0;
- 3.5;
- 4.0;
- 4.5;
- 5.0;
- 5.5;
- 6.0;
- 6.5;
- 7.0;
- 7.5;
- 8.0;
- 8.5;
- 9.0;
- 9.5;
- 10.0.

In the figure 4.29 can be seen the behaviour of the  $\bar{\mu}_{90}$  as a function of the half-cone angle for different values of  $t\chi^2$ . The stepping behaviour of the curves for the higher values of the track fit quality parameter is due to the fact that for lower values of the parameter the contribution to the background come only from atmospheric neutrinos, while for higher values of  $t\chi^2$  also atmospheric muons contribute. Let's remember (4.12.2) that  $t\chi^2 < 1.4$  rejects all muon background.

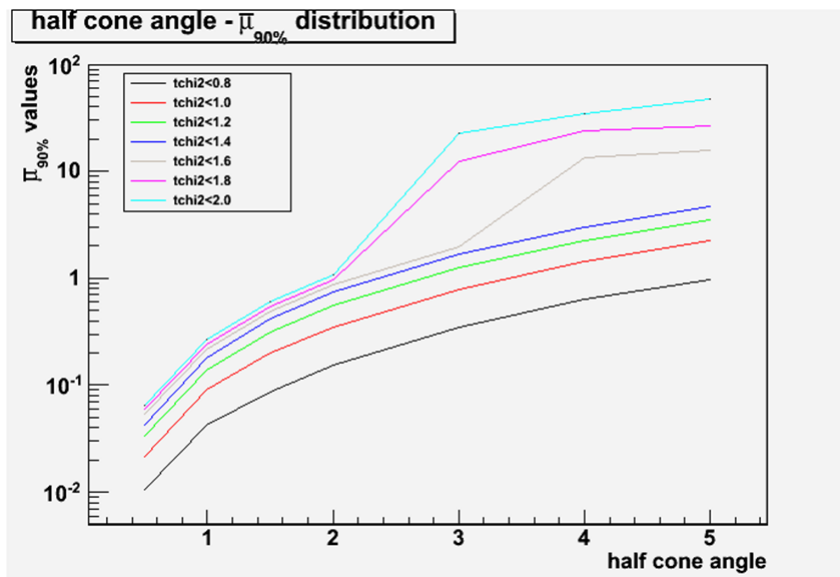


**Figure 4.29.** The behaviour of  $\bar{\mu}_{90}$  as a function of the half-cone angle for different values of  $t\chi^2$ .

The interval for  $t\chi^2$  and  $\Delta$  have been chosen such to have a similar parameter space to investigate a quite large interval of parameters values.

Thus, in total, we have 400 different combination of cuts. In fact we have to examine for each given value of  $t\chi^2$  all the events, of total MC signal ( $\nu + \bar{\nu}$ ) and total MC background ( $\nu + \bar{\nu} + \mu$ ), that fall inside the 20 different aperture of the half-cone angle.

Moreover this procedure has to be repeated for each model of Dark Matter we take into account. Considering that we use 3 annihilation channels and 10 possible WIMP masses, we have to analyse 11600 combinations (having seen that the  $W^+W^-$  channel has not the 50 GeV mass, it follows that we have 29 model and not 30).

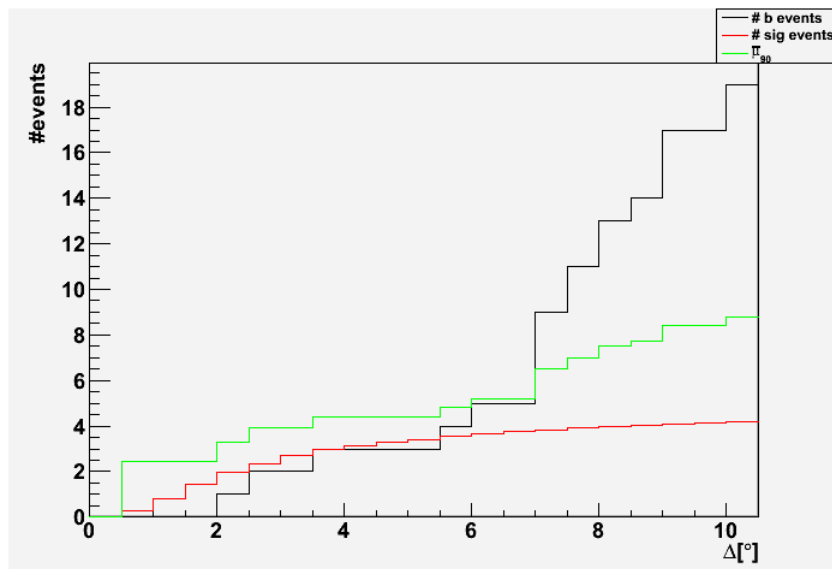


**Figure 4.30.** The different distributions of  $\bar{\mu}_{90}$ ,  $b$  and  $n_s$  (in units of  $10^5$ ) as a function of the half-cone angle  $\Delta[^\circ]$  for  $t\chi^2 < 1.6$  and  $M_\chi = 500 \text{ GeV}$  for  $W^+W^-$  channel.

In the figure 4.30 the different distributions of the number of background (from scrambled DATA) events, the signal events (in units of  $10^5$ ) and the  $\bar{\mu}_{90}$  are shown, in the case of a WIMP mass equal to  $500 \text{ GeV}$  for the  $W^+W^-$  channel, as a function of the half-cone angle  $\Delta[^\circ]$  for the optimized cut of  $t\chi^2 < 1.6$ .

## 4.15 Final results and conclusions

For each pair of values of  $\Delta$  and  $t\chi^2$  we obtain the value  $n_b(\Delta_i, t\chi_i^2)$  and  $n_s(\Delta_i, t\chi_i^2)$ .

Actually we tried to evaluate the background in two different ways with the idea to compare the results: from scrambled DATA and from  $\mu + \nu_\mu + \bar{\nu}_\mu$  MC events.

We noticed that, for the same set of cuts, the number of background events counted in the half cone angles are bigger in the case of using background MC than using the scrambled data.

As we explained in section 4.13, we assume that the background is evaluated with the sample of multiple scrambled DATA.

We built several matrices with the values  $n_b(\Delta_i, t\chi_i^2)$ ,  $n_s(\Delta_i, t\chi_i^2)$  one for each value of  $M_\chi$  and for each annihilation channel ( $b\bar{b}$ ,  $\tau^+\tau^-$ ,  $W^+W^-$ ).

For each pair of  $(n_b, n_s)$  we evaluate first the  $\bar{\mu}_{90}$  and then, assuming as "reference flux" the WIMPSIM output for the given  $M_\chi$  and annihilation channel, we compute the MRF (according to the formula 4.35).

Spamming over the whole phase space of  $t\chi^2$  and  $\Delta$  we search for the minimum value of MRF. This is shown for  $M_\chi = 500 \text{ GeV}$  and the  $W^+W^-$  channel in the figure 4.31.

Combining all the values that minimize the MRF for all the Dark Matter masses and annihilation channels we build the plot of the sensitivity of the ANTARES detector simply reporting these values as a function of the WIMP mass.

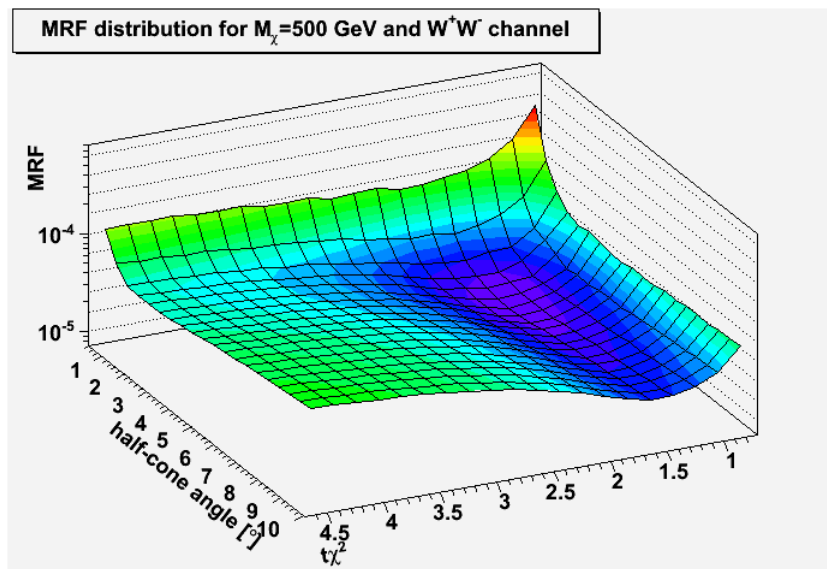


**Figure 4.31.** The MRF distribution in the  $t\chi^2$ -half-cone angle parameter space for a Dark Matter composed by WIMP with mass = 500 GeV and for the hard annihilation channel  $W^+W^-$ .

In the figure 4.32, 4.33 the sensitivity plots are shown in two different unity of measures.

In this analysis we use the data collected by the ANTARES detector in the period 2007-2010 (with different configurations of the detector ranging from 5 to 12 detector lines). After the Data quality cuts, applied to take into account the detector and environment conditions, in the considered time interval we have a lifetime of  $\approx 588$  days of active detector in a good environmental status.

We examine the DATA set and the Monte Carlo simulations of the background (using official ANTARES production) and of the expected signal (built starting from the WIMPSIM output spectra) and we reconstruct the DATA and the simulated events with the BBFit reconstruction algorithm.

We find a good agreement between DATA and MC for small values of the track fit quality parameter  $t\chi^2$ . Then we impose some tighter cuts on physical parameters: we select only up-going events (to reject the atmospheric down-going muons flux), well reconstructed ( $t\chi^2 < 5$ ), with a sufficient number of hits ( $> 5$ ) and with more than one line.

In this study we consider three channels of annihilation of WIMPs:  $\chi\chi \rightarrow b\bar{b}, \tau^+\tau^-, W^+W^-$ . For each of these channels we investigate ten different WIMP masses, from 50 GeV to 1 TeV. Thus, in total, we test 29 models of Dark Matter annihilation (the channel  $W^+W^-$  is forbidden for the 50 GeV mass due to energy reasons).

Since we search for muon neutrinos from Dark Matter in the Galactic Centre, we perform a binned search towards a point-like source. It means we search for signal events in cones of different angular apertures (the half-cone angle) around the

Table 4.8. Optimization values.

optimization $b\bar{b}$ channel			
$\chi$ mass [GeV]	$t\chi^2$	half-cone angle [°]	MRF <sub>min</sub> value
50	1.8	4	852.96
80.3	1.4	4.5	14.96
100	1.4	5.5	4.07
176	1.4	5	0.29
200	1.4	4.5	0.18
250	1.4	4.5	0.084
350	1.4	4.5	0.031
500	1.4	4.5	0.013
750	1.6	3.5	0.005
1000	1.6	3.5	0.002
optimization $\tau^+\tau^-$ channel			
$\chi$ mass [GeV]	$t\chi^2$	half-cone angle [°]	MRF <sub>min</sub> value
50	1.4	7.5	0.81
80.3	1.4	5	0.064
100	1.4	5	0.025
176	1.4	4.5	0.0038
200	1.4	4.5	0.0027
250	1.4	4.5	0.0015
350	1.6	3.5	0.00063
500	1.6	3.5	0.00028
750	1.6	3.5	0.00012
1000	1.6	3	$6.41 \times 10^{-5}$
optimization $W^+W^-$ channel			
$\chi$ mass [GeV]	$t\chi^2$	half-cone angle [°]	MRF <sub>min</sub> value
80.3	1.4	7.5	0.33
100	1.4	4.5	0.054
176	1.4	4.5	0.0065
200	1.4	4.5	0.0048
250	1.6	3.5	0.0026
350	1.6	3.5	0.0011
500	1.6	3.5	0.00051
750	1.6	3	0.00022
1000	1.6	3	0.00013

Galactic Centre direction.

As we said, the only way to detect a neutrino signal from the Galactic Centre is to see a statistical excess of events over the underlying background. To evaluate the statistical significance of the result, we use the Feldman and Cousins approach.

The final result is obtained with an evaluation of the Model Rejection Factor

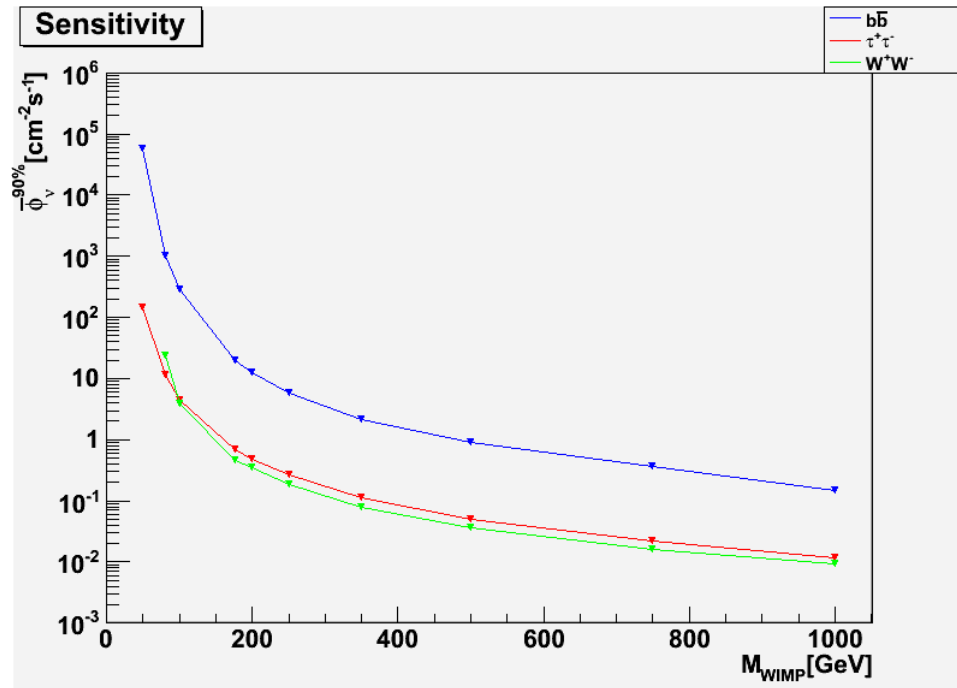


Figure 4.32. The sensitivity (in  $cm^{-2}s^{-1}$ ) of the ANTARES detector as a function of the WIMP mass for the three different annihilation channels chosen.

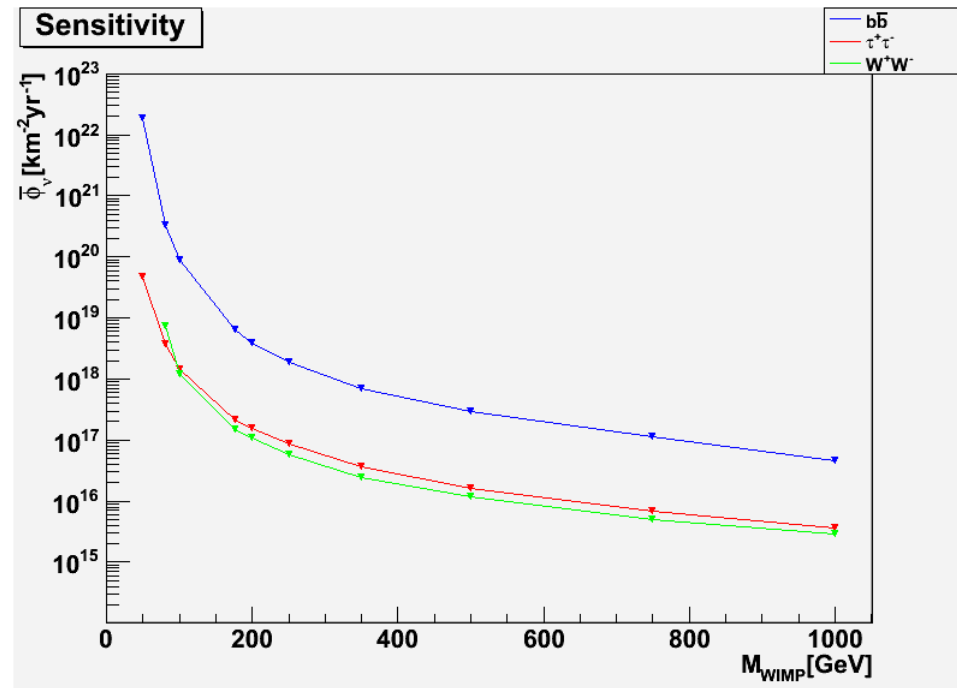


Figure 4.33. The sensitivity (in  $km^{-2}yr^{-1}$ ) of the ANTARES detector as a function of the WIMP mass for the three different annihilation channels chosen.

(MRF) for each Dark Matter model chosen. The MRF method is used in the analysis of the 2007-2010 ANTARES data to search for the cuts optimization on the bi-dimensional set of the parameters representing the track quality reconstruction and the half-cone angle.

The optimised cuts depend on the WIMP mass, but in the majority of cases, as can be seen in table 4.8, they are a  $3.5^\circ$  angle for the half-cone aperture with a  $t\chi^2 < 1.6$  cut. For each optimised cuts pair we obtain the minimum of the MRF.

Then, after the selection of the theoretical flux expected, with the best cuts just found, we were able to minimize the MRF and, at the end, to find the sensitivity of the ANTARES detector to all the selected Dark Matter models (see plots 4.32, 4.33). These plots of the sensitivity of the ANTARES experiment constitute the final result of this thesis work for the "blind" analysis.

We will soon ask to the ANTARES collaboration the "unblinding" of the data. In this way it will be possible to compute the true limits on the neutrino fluxes arising from Dark Matter annihilation into the Galactic Centre.

Some improvement can still be possible in the next future. In the ANTARES collaboration, an official Monte Carlo simulation of the Dark Matter annihilation in the Galactic Centre will be soon available. This MC will be computed at the source, and at the Earth surface taking into consideration the full standard oscillation scenario. Also the annihilation rate into the GC, that is an unknown variable in our analysis, will be taken into account. So, at the end we will expect better limits for the ANTARES sensitivity in the detection of neutrinos arising from Dark Matter annihilation in the Galactic Centre.

# Conclusioni

In questa tesi abbiamo presentato l'analisi dei dati, raccolti dall'esperimento ANTARES nel periodo 2007-2010, effettuata per ricercare la sensibilità dell'apparato alla rivelazione di neutrini muonici provenienti dall'annichilazione di particelle di materia oscura nel Centro Galattico.

Ci siamo serviti di un modello di materia oscura diffusamente usato: quello dei WIMP (Weak Interacting Massive Particles). Queste particelle vengono identificate con i neutralini più leggeri previsti all'interno della teoria supersimmetrica a minimale (MSSM).

I WIMP presenti nel Centro Galattico, avendo la proprietà di essere particelle Majorana (quindi antiparticelle di se stesse) possono annichilirsi producendo delle particelle intermedie (come bosoni, quarks, leptoni) che poi, decadendo, producono dei neutrini. Questi neutrini possono essere rivelati sulla Terra da telescopi di grande volume (dati i piccoli flussi aspettati e la piccola sezione d'urto) come l'esperimento ANTARES.

ANTARES, come abbiamo visto, è un telescopio sottomarino per neutrini che usa la tecnica di rivelazione di luce Cherenkov indotta dai leptoni carichi originati dalle interazioni dei neutrini nei dintorni dell'apparato.

Nella nostra analisi abbiamo per prima cosa applicato dei tagli di qualità sul set di dati scelto. Questo perché le condizioni dell'ambiente marino e del detector non sono sempre ottimali, bisogna quindi scartare tutti i dati presi in condizioni "cattive" dell'ambiente o dell'apparato: per questo abbiamo scelto dei tagli di qualità che "puliscano" il campione di dati selezionati per l'analisi.

Dopo questi tagli, nel periodo di presa dati 2007-2010, rimangono circa 588 giorni equivalenti di dati utilizzabili per l'analisi.

Come abbiamo ripetuto più volte, i principali fondi fisici per l'esperimento sono costituiti dai muoni atmosferici e dai neutrini atmosferici. Per ovviare alla contaminazione dei muoni atmosferici selezioniamo solo eventi detti up-going, cioè che vengono dal basso. In questo modo la Terra agisce come uno scudo per i muoni che vengono dal basso; allo stesso tempo rigettiamo quelli ricostruiti come provenienti dall'alto. I neutrini atmosferici invece non possono essere fermati e la selezione segnale-fondo avviene utilizzando criteri statistici descritti più avanti.

Tutti gli eventi visti dall'apparato vengono ricostruiti da un algoritmo di ricostruzione dedicato chiamato BBFit. Questo programma individua il tipo di evento distinguendo le tracce prodotte da neutrini muonici o dagli sciami indotti dall'interazione di neutrini elettronici) e ne ricostruisce le caratteristiche fondamentali come, ad esempio, la direzione di provenienza.

Siccome gli eventi di segnale aspettati sono scarsi e affogati nei sovrabbondanti

eventi di fondo l'unica possibilità di avere un'evidenza di segnale è riscontrare un eccesso statistico in una data direzione, dato che il fondo di neutrini atmosferici è distribuito in maniera isotropa.

Per costruire il Monte Carlo del segnale atteso abbiamo usato il pacchetto WIMPSIM da cui ottenere gli spettri in energia dei neutrini derivanti dall'annichilazione di WIMP per diversi canali d'annichilazione e per diversi valori di massa.

Per selezionare un campione di eventi "arricchito" in segnale abbiamo applicato dei tagli su alcuni parametri fisici per rigettare i muoni down-going mal ricostruiti come up-going ed eventuali altri eventi spuri. Abbiamo selezionato solo eventi che provengono dal basso, ben ricostruiti con almeno una linea e un minimo di 5 hit. Così abbiamo definito il nostro set di dati per la fase finale dell'analisi. La nostra analisi ricerca eventuali eventi di neutrino da annichilazione di materia oscura in direzione del Centro Galattico. Quindi è quella che si definisce una ricerca di sorgente puntiforme. Per questo abbiamo portato avanti una strategia di analisi detta "binned", cioè abbiamo cercato eventi di segnale all'interno di un cono angolare di ampiezza fissata centrato nel Centro Galattico.

In questa analisi abbiamo considerato tre diversi canali d'annichilazione dei WIMP ( $\chi\chi \rightarrow b\bar{b}, \tau^+\tau^-, W^+W^-$ ) per dieci masse diverse, da 50 GeV a 1 TeV, per un totale di 29 modelli differenti di materia oscura.

Per valutare la significatività statistica del nostro risultato d'analisi usiamo la tecnica di Feldman e Cousins per la costruzione degli intervalli di confidenza.

In seguito abbiamo ottimizzato, per l'insieme dei dati 2007-2010, i tagli del set di parametri bidimensionale composto dal parametro di qualità del fit di ricostruzione delle tracce ( $t\chi^2$ ) e dalla semiapertura del cono angolare centrato nel Centro Galattico. Il risultato finale è stato quindi ottenuto grazie alla stima del Model Rejection Factor (MRF), che ci dà il massimo numero di eventi di segnale osservabili con un dato fondo. Abbiamo valutato il MRF per ogni modello di materia oscura considerato.

Il valore risultante dei tagli ottimizzati, riportato in tabella 4.8, dipende dalla massa del WIMP considerata e dal canale di annichilazione. Nella maggior parte dei casi il valore ottimizzato corrisponde ad un  $t\chi^2 < 1.6$  e ad un'apertura angolare di  $5^\circ$ . Per ogni coppia di tagli ottimizzati otteniamo il valore minimo dell'MRF. Una volta trovati i tagli ottimizzati e, per essi, il minimo dell'MRF, consideriamo il flusso teorico atteso per i neutrini da annichilazione di materia oscura nel Centro Galattico e con questo calcoliamo la sensibilità di ANTARES per tutti i diversi modelli di materia oscura presi in considerazione. I grafici della sensibilità sono mostrati nelle figure 4.32 e 4.33 in funzione della massa dei WIMPs. Questi grafici rappresentano il risultato del nostro lavoro di tesi portato avanti con i dati "blind".

Al più presto verrà sottoposto alla collaborazione ANTARES il risultato definitivo di questa analisi per ottenere l'"unblinding" dei dati. Saremo quindi nella condizione di valutare i limiti dell'esperimento ANTARES con i dati veri e non "scrambled".

Nel prossimo futuro notevoli miglioramenti della sensibilità saranno anche possibili. Infatti è quasi pronta una simulazione Monte Carlo, prodotta ufficialmente all'interno della collaborazione, del segnale di neutrini da annichilazione di materia oscura nel Centro Galattico propagato fino al detector, che quindi sarà più realistica rispetto a quella che abbiamo usato in questa tesi. Unendo questi due fattori ci aspettiamo un miglioramento dei limiti posti sui flussi di neutrini da annichilazione di materia oscura nel Centro Galattico.

## Appendix A

# The Feldman and Cousins statistical approach

Classical confidence intervals are the usual way to report errors on results of experiments. To constrain the ANTARES limits on the neutrino flux from WIMP annihilation we used the Feldman and Cousins statistical method [66]. This method gives a classical confidence belt construction which unifies the treatment of upper limits for null results and two-sided confidence intervals for non-null results. This approach solves the problem that the choice of upper limit or two-sided intervals leads to intervals which are not confident with a choice based on the data.

This was obtained using the Neyman's scheme [114] in a new way to obtain the unified set of classical confidence intervals. The new method represents a new choice for the ordering principle based on the likelihood ratios. In this way it is possible to have confidence intervals which are never non-physical or empty.

In the following subsections, following the Feldman and Cousins approach [66], we will show the difference between the Bayesian way to intend confidence intervals and the Neyman's one, and the detailed construction of the intervals. This is a very useful process to learn how the statistical method we choose to analyse our data works.

It must also be specified that, during the development of this thesis work, we reproduced exactly all the results obtained by Feldman and Cousins, extended them to higher values of background. In particular, the Feldman and Cousins published analysis stops at a background level equal to 15, while in our calculations we arrived up to a background level of 875!

### A.1 Bayesian interval construction

Suppose [66] to make an inference about a parameter  $\mu$  whose true value  $\mu_t$  is unknown. Assume to do this by making a single measurement of an observable  $x$ , such that the probability density function (pdf) for obtaining  $x$  depends on the unknown parameter  $\mu$  in a known way:  $P(x|\mu)$ .

Now suppose that the single measurement of  $x$  gives the value  $x_0$ .  $P(x_0|\mu)$  is known

as the likelihood function. It is possible to make inference using the posterior pdf, which is the conditional pdf  $P(\mu_t|x_0)$  for the unknown  $\mu_t$ , given the result  $x_0$ . The posterior is related with the likelihood by the Bayes's theorem:

$$P(\mu_t|x_0) = P(x_0|\mu_t)P(\mu_t)/P(x_0), \quad (\text{A.1})$$

where the denominator  $P(x_0)$  is a constant and the most difficult thing is to evaluate the so called prior pdf  $P(\mu_t)$ . The real power of Bayesian inference lies in its ability to incorporate good prior information.

A Bayesian interval  $[\mu_1, \mu_2]$  corresponding to a **confidence level**  $\alpha$  can be constructed from the posterior pdf by requiring

$$\int_{\mu_1}^{\mu_2} P(\mu_t|x_0)d\mu_t = \alpha. \quad (\text{A.2})$$

## A.2 Classical Neyman's interval construction

In the classical Neyman's construction [114, 66] there is no prior, hence the intervals are limited to the statements derived from  $P(x|\mu)$ . In this case a **confidence interval**  $[\mu_1, \mu_2]$  is a member of a set such that the set has the property:

$$P(\mu \in [\mu_1, \mu_2]) = \alpha, \quad (\text{A.3})$$

where  $\mu_1$  and  $\mu_2$  are functions of the observable  $x$ . For a set of confidence intervals the equation A.3 is true for every allowed  $\mu$ . So, the intervals contain the fixed unknown  $\mu_t$  in a fraction  $\alpha$  of the experiments. This is different from saying, like in the Bayesian case A.2, that the degree of belief that  $\mu_t$  is in  $[\mu_1, \mu_2]$  is  $\alpha$ .

If there is any value of  $\mu$  for which  $P(\mu \in [\mu_1, \mu_2]) > \alpha$ , the intervals over-cover for that  $\mu$ . A set of intervals is called **conservative** if it over-covers for some values of  $\mu$  while under-covering for no values of  $\mu$ . Conservatism allows a loss of power to reject false hypothesis.

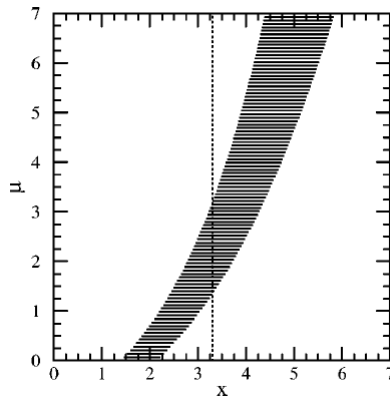


**Figure A.1.** Confidence belt construction and its use [66].

Referring to figure A.1, which shows the mean values  $\mu$  as a function of the observable

$x$ , an interval selection  $[x_1, x_2]$  such that

$$P(x \in [x_1, x_2] | \mu) = \alpha \quad (\text{A.4})$$

is called **acceptance region** for  $\mu$ . Such intervals are drawn as horizontal segments in the figure.

For  $P(x < x_1 | \mu) = 1 - \alpha$  we have **upper confidence limits**, instead for  $P(x < x_1 | \mu) = P(x > x_2 | \mu) = (1 - \alpha)/2$  we have **central confidence intervals**. The construction is complete when horizontal acceptance intervals are drawn for each value of  $\mu$ . Measuring  $x$  we obtain  $x_0$  and draw a vertical line passing by  $x_0$  (the dotted line in figure A.1). The confidence interval is the union of all the values of  $\mu$  for which the corresponding horizontal interval is intercepted by the vertical line, the result is a connected interval  $[\mu_1, \mu_2]$ .

By construction the equation A.3 is satisfied for all  $\mu$ , thus also for  $\mu_t$  which is unknown.

### A.3 Poisson process with background and Feldman and Cousins ordering principle

In this thesis work, we used the statistical approach of Feldman and Cousins [66], derived by the Neyman's classical construction we have seen before, to analyse our results.

Consider the case of a Poisson<sup>1</sup> process with background, that is the case of our interest, since neutrino detection is the search for a discrete number of neutrino events under certain conditions. Let  $x$  be the observable,  $n$  the total number of observed events with mean values  $\mu$  and known mean background  $b$ .

That is:

$$P(n | \mu) = (\mu + b)^n \exp[-(\mu + b)/n!], \quad (\text{A.5})$$

where  $n$  must be an integer.

For each  $n$ , let  $\mu_{best}$  be the value of the mean signal  $\mu$  which minimizes  $P(n | \mu)$ . The only requirement for  $\mu_{best}$  is that it has to be physically allowed, that means it has to be non-negative:

$$\mu_{best} = \max(0, n - b). \quad (\text{A.6})$$

A ratio of likelihoods is the new ordering principles when selecting those values of  $n$  to place in the acceptance interval.

The ratio is:

$$R = P(n | \mu) / P(n | \mu_{best}). \quad (\text{A.7})$$

Thus,  $R$  is the ratio of the likelihood of obtaining  $n$  given the actual mean  $\mu$  and the likelihood of obtaining  $n$  given the best fit physically allowed mean  $\mu_{best}$ . Values of  $n$  are added to the acceptance region for a given  $\mu$  in decreasing order of  $R$ , until the sum of  $P(n | \mu)$  meets or exceeds the desired confidence level. In our analysis we select a confidence level equal to 90%, so a 90% C.L. Because of the discreteness of

<sup>1</sup>The standard expression of the Poisson probability distribution, with parameter  $\lambda$ , for the variable  $x$  is:  $P(x)_\lambda = \lambda^x \exp(-\lambda/x!)$ , with the property:  $\lambda = E(x) = \text{Var}(x)$ .

$n$ , the acceptance region contains a summed probability greater than 90%, leading to confidence intervals which are conservative.

The construction proceeds by finding the acceptance region for all the values of  $\mu$  for each given value of  $b$ .

### A.3.1 Our Feldman and Cousins construction of intervals

We decided to apply the Feldman and Cousins statistical approach because of the advantages of this method [66] the new ordering principle yields intervals which automatically change over from upper limits to two-sided intervals as the "signal" becomes more statistically significant. This eliminates undercoverage caused by basing this choice on the data. This introduction of Bayesian methods was at least partly motivated by problems with the traditional classical intervals (non physical or empty-set intervals) which the new constructed intervals solve.

Thus, we followed the Feldman and Cousins approach in a program for computing confidence intervals using the ordering principle of the ratio of likelihoods explained above. We construct confidence intervals spanning the number of background events  $b$  from 0 to 895 with a step choice showed here below:

- step = **0.5** ( $0 \leq b < 5$ );
- step = **1.0** ( $5 \leq b < 50$ );
- step = **2.0** ( $50 \leq b < 100$ );
- step = **5.0** ( $100 \leq b < 895$ ).

Thus, there is a "fine tuning" for smaller values of  $b$  and an increasing step for larger values of  $b$ . The goal of our computation is to extend the result reported in the article up to larger values of background  $b$ .

As described above, the 90% confidence interval  $\mu_{90} = (\mu_1, \mu_2)$  is a function of the number of observed events  $n$  and of the expected background  $b$ :  $\mu_{90}(n, b)$ . We consider  $\mu_{90}$  as an upper limit, taking only the high value of the confidence interval. However, the upper limit depends on the number of observed events  $n$ , that is not known until the experiment was performed (and the cuts applied). Then we evaluate an average upper limit  $\bar{\mu}_{90}$  (also known as Feldman and Cousins sensitivity) to take place of  $\mu_{90}$  (see equation 4.34).

Once we constructed the confidence intervals suitable for our expected background, we then evaluate the  $\bar{\mu}_{90}$  upper limit for different values of the background  $b$ . The obtained values are in agreement with Feldman and Cousins table reported in the article [66] up to the value  $b = 15$ , that is the maximum value considered by the authors. For larger values of the background, the result shows a trend in agreement with the published result.

In addition, we tested also the effect of using Poisson and Gauss distributions for the construction of confidence intervals. In constructing our algorithm to calculate the table following the Feldman and Cousins approach, we used a Poisson distribution until the background value equal to 24 and a Gaussian distribution up to the end

of our sample background. This is justified by the application of the central limit theorem, that states:

**Theorem 2 (Central limit theorem)** *Given certain conditions, the mean of a sufficiently large number of independent random variables, each with finite mean and variance, will be approximately normally (Gaussian) distributed.*

This means that, for large values of the Poisson parameter  $\lambda$  (that in this case is  $\mu + b$ ), the Poissonian distribution can be well approximated by a Gaussian function<sup>2</sup>.

The reason why we did this choice is that, for larger values of background  $b$ , the computing time grows a lot. The difference of the two distribution is negligible, in agreement with theorem 2, and confirmed by plots reported in the figures A.2 and A.3.

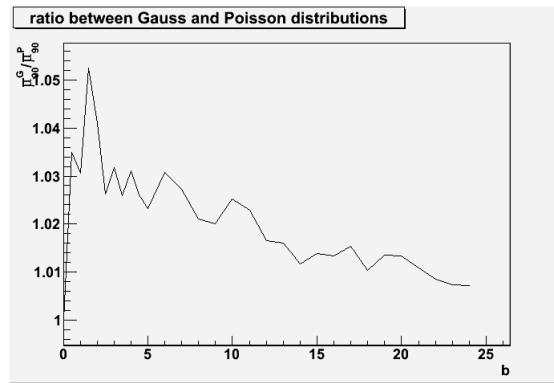


Figure A.2. Ratio between Gauss and Poisson distributions.

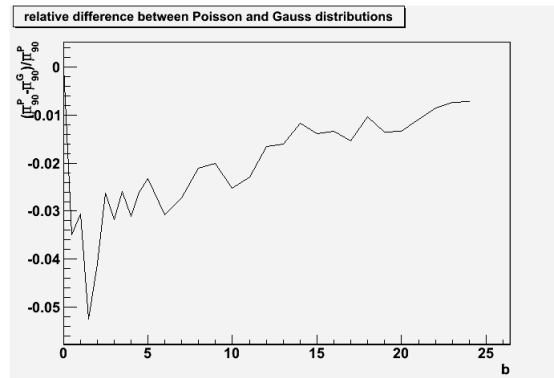


Figure A.3. Relative difference between Poisson and Gauss distributions.

In these figures the distributions of the ratio  $\bar{\mu}_{90}^{Gauss} / \bar{\mu}_{90}^{Poisson}$ , and the relative difference  $(\bar{\mu}_{90}^{Poisson} - \bar{\mu}_{90}^{Gauss}) / \bar{\mu}_{90}^{Poisson}$  are shown.

It is clearly visible that the trend of the ratio distribution tends to 1 as it must be when the difference between the two distributions tends to 0. The same thing can be seen in the trend of the relative difference, where the difference tends to 0.

<sup>2</sup>The Gauss distribution has the expression:  $g(x) = \frac{1}{\sqrt{2\pi\sigma^2}} e^{-\frac{(x-\mu)^2}{2\sigma^2}}$ , where  $\mu$  is the expected value and  $\sigma^2$  is the variance.

To test the difference between the behaviour of a Poisson distribution with respect to a Gauss distribution, we show the distribution of the average upper limit  $\mu_{90}$  as a function of the background  $b$ . We perform this calculus with a sample set of  $b$  values considering  $b = 10$  as a threshold for the passage between the two different regimes.

As can be seen in figure A.4 the difference between the two regimes is very little, and it tend to become infinitesimal with increasing values of  $b$ .

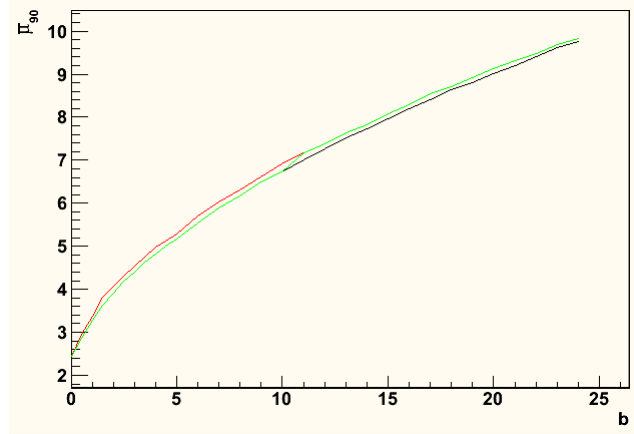


**Figure A.4.** Here an example for the average upper limit  $\bar{\mu}_{90}$  as a function of the background  $b$ . The black curve represents the Poisson distribution, the red one the Gauss distribution. The green curve show the behaviour of the mixed regime: Poissonian until  $b = 10$  and Gaussian up to the end. In the thesis we chose a value  $b = 24$ .

In the figure A.5 the behaviour of the  $\bar{\mu}_{90}$  as a function of the background is shown. As expected there is an increasing trend with the background  $b$ .

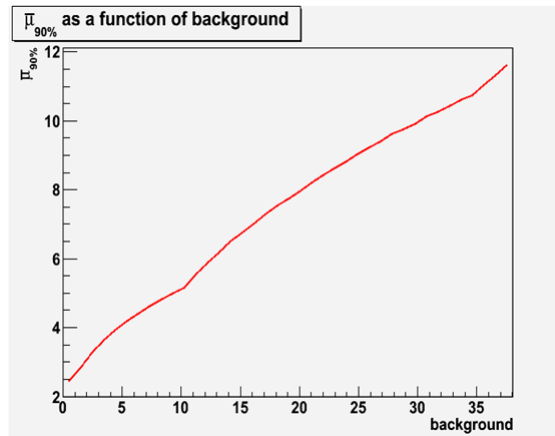


**Figure A.5.** The trend of  $\bar{\mu}_{90}$  as a function of the background.

Here we used our final choice consisting on the use of a Poissonian distribution until a background value  $b = 24$  and a Gaussian distribution hereinafter.

**Table A.1.** Upper limits for a required 90% C.L. as a function of the background  $b$ .

The first column represent the background, the second the average upper limit, the third the number of steps necessary for convergence and the last the C.L. probability reached at the moment of the convergence. As can be seen a lot of upper limits are conservative.

$b$	$\bar{\mu}_{90}$	$steps$	$P$	$b$	$\bar{\mu}_{90}$	$steps$	$P$
0.0	2.44	1	0.91	31.0	10.95	54	0.90
0.5	2.86	6	0.90	32.0	11.12	55	0.91
1.0	3.27	7	0.91	33.0	11.28	56	0.90
1.5	3.62	9	0.91	34.0	11.42	58	0.91
2.0	3.91	10	0.91	35.0	11.60	59	0.90
2.5	4.20	11	0.91	36.0	11.71	60	0.91
3.0	4.41	12	0.91	37.0	11.84	62	0.90
3.5	4.63	13	0.90	38.0	11.99	63	0.91
4.0	4.82	14	0.91	39.0	12.15	64	0.90
4.5	5.00	15	0.91	40.0	12.26	66	0.91
5.0	5.17	16	0.91	41.0	12.41	67	0.90
6.0	5.53	18	0.91	42.0	12.54	68	0.91
7.0	5.88	20	0.91	43.0	12.68	69	0.91
8.0	6.18	22	0.90	44.0	12.81	71	0.90
9.0	6.49	23	0.91	45.0	12.92	72	0.91
10.0	6.74	25	0.90	46.0	13.04	73	0.90
11.0	7.01	27	0.91	47.0	13.19	75	0.91
12.0	7.27	28	0.90	48.0	13.29	76	0.90
13.0	7.51	30	0.91	49.0	13.43	77	0.90
14.0	7.74	31	0.90	50.0	13.55	78	0.90
15.0	7.96	33	0.91	52.0	13.80	81	0.91
16.0	8.19	34	0.90	54.0	14.03	84	0.90
17.0	8.41	36	0.91	56.0	14.28	86	0.90
18.0	8.63	37	0.91	58.0	14.48	89	0.90
19.0	8.81	39	0.91	60.0	14.75	91	0.91
20.0	9.02	40	0.91	62.0	14.94	94	0.90
21.0	9.21	42	0.91	64.0	15.17	96	0.90
22.0	9.41	43	0.90	66.0	15.39	99	0.90
23.0	9.61	45	0.91	68.0	15.58	101	0.90
24.0	9.76	46	0.90	70.0	15.82	104	0.90
25.0	10.03	45	0.90	72.0	15.99	106	0.90
26.0	10.18	47	0.91	74.0	16.20	108	0.91
27.0	10.33	48	0.90	76.0	16.40	111	0.90
28.0	10.51	49	0.91	78.0	16.59	113	0.90
29.0	10.67	51	0.90	80.0	16.82	116	0.90
30.0	10.80	52	0.91	82.0	16.98	118	0.90



## Appendix B

# The Cross-Talk effect in ANTARES ARS

During the development of the thesis, as usual in the ANTARES collaboration, we have worked also on a particular technical aspect of the detector.

It is important to notice that, to have a good reconstruction of muon's trajectories, the precise measure both of the time of arrivals of the photons on the PMT and their charge have a big influence .

In particular the charge measure is relevant to establish a good measure of the time threshold passage (and also the amplitude) of the signal and the control of the PMT gain as a function of time.

This measures and their digitization happen in a particular circuit inserted in each LCM of the apparatus, called ARS.

First a short introduction [10] on the base structure and working of this circuit will be presented (B.1 section).

In the following [97] we will talk about the structure and working mode of only two objects among all the others that compose one ARS: the TVC that measures the time (B.1.1 paragraph) and the AVC that measures the charge (B.1.2 paragraph).

This because they are responsible for a little systematic that can afflict the measure of the charge of the signal events: a cross-talk effect between time and charge in the circuit (B.2 section).

This effect have to be corrected each time a calibration is done. In this technical appendix to the main research topic of this thesis work, we will try to obtain an universal estimation of the main parameters characterizing this effect, in order to do not perform this evaluation for each calibration no more (B.3 section).

### B.1 Structure and description of an ARS

As we mentioned in the chapter 3, about the description and operation of the detector, the position of the apparatus is roughly 40 km distant from the shore control station. Thus, there is the necessity of transmitting the raw data signal taken by the detector's photomultiplier (PMT) along that distance. This impose the

local digitization of the signal before the arrival on earth, to avoid the distortion and attenuation of the analogue signal. This task is taken over by the **ARS ("Analogue Ring Sampler")** circuit [98]. There are two ARS circuit for each optical module (OM) in order to reduce the dead times in acquisition of the signals.

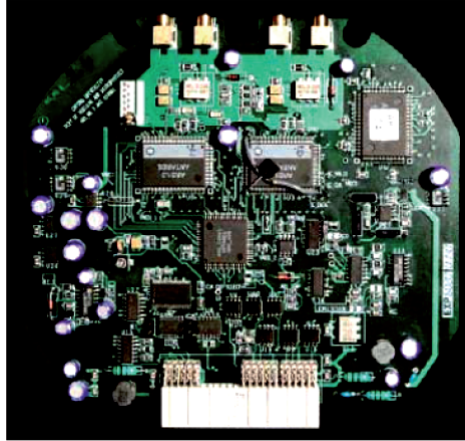


**Figure B.1.** The ARS circuit scheme [10].

The main purpose of the ARS circuit is: the selection of the analogue signals below a given threshold and the digitization of their time of arrival and charge. The signal so treaty is temporary safeguarded into the circuit before being transmitted: the circuit works in an asynchronous way.

The ARS structure is composed by:

- 24 digital to analogue converter (DAC);
- 1 sampler to see PMT signals;
- 1 Time-Voltage Converter (TVC);
- 1 integration module;
- 16 analogue-digital memories cells, called "pipeline"
- 2 8-bit Analogue to Digital Converter (ADC).

The pipelines are used for the temporary safeguard of the signals.

The majority of signals (>95%) have a charge equal to 1 photo-electron (1pe)<sup>1</sup>, in this case (Single Photo Electron: SPE mode), to avoid the rapid congestion of the acquisition system, only the charge and the time of passage of the signal under a certain threshold are transmitted. In the other cases also the form of the signal is transmitted (Wave Form: WF mode) [52].

<sup>1</sup>1pe is equal to the charge held by one electron extracted from the photo-cathode of a PMT by one arriving photon.

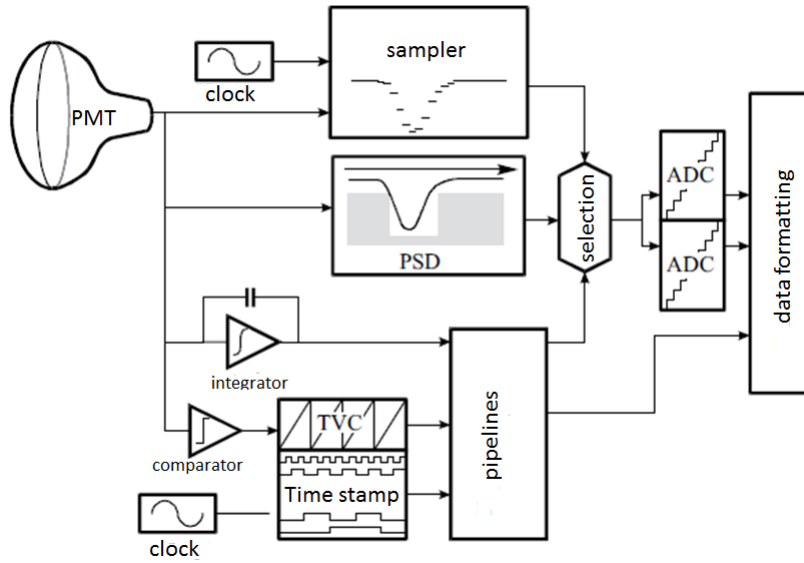


Figure B.2. ARS structure and working principle [10].

In the figure B.2 is shown the way in which an ARS work. Once the anode signal of one PMT exceeds the trigger threshold, it is treated. Thus the current value of the clock (with a cycle of 25 ns), called Time Stamp (TS), is registered. Between two clock cycles, the TVC gives an analogue signal with an amplitude proportional to the time of threshold passage. The TVC ramp, that provides the fine measure of the time, is of 50 ns. The signal is also integrated in parallel.

At the end of the integration passage ( $\sim 30$  ns), there is the discrimination (PSD: "Pulse Shape Discriminator") between SPE and WF modes. In both cases the information about the time (TVC and TS) and the integrated charge (AVC that states for "Analogue to Voltage Converter") is stored into the pipelines. If the signal is of the WF type the sampling process continues just to fill all the cells of the sampler (128).

In the two cases the dead times are of the order:

- SPE mode:  $\sim 300$  ns;
- WF mode:  $\sim 200$   $\mu$ s.

The pipelines have 16 cells, thus they can store up to 16 SPE events.

Exiting from the pipelines, the signals are digitised by the ADC and formatted .

### B.1.1 TVC

In a clock period the time is given by the time-voltage converter (TVC), which has a voltage ramp proportional to the time, with a total duration of 50 ns and a 40 ps precision. The conversion factor of the ramp is variable between 10 and 140

mV/ns with the help of 4-bit DAC (default value: TVC\_BIAS = 4 equivalent to 35.6 mV/ns). The exit voltage is converted by a 8-bit ADC.

In the case of voltage variation is better to leave a 30 ADC channel margin forward and below the voltage values of the ramp, in such a way that all the 50 ns duration of the ramp can be encoded in to the ADC range. See figure B.3. The first encoded channel is called TVC\_MIN and the last encoded channel is TVC\_MAX.

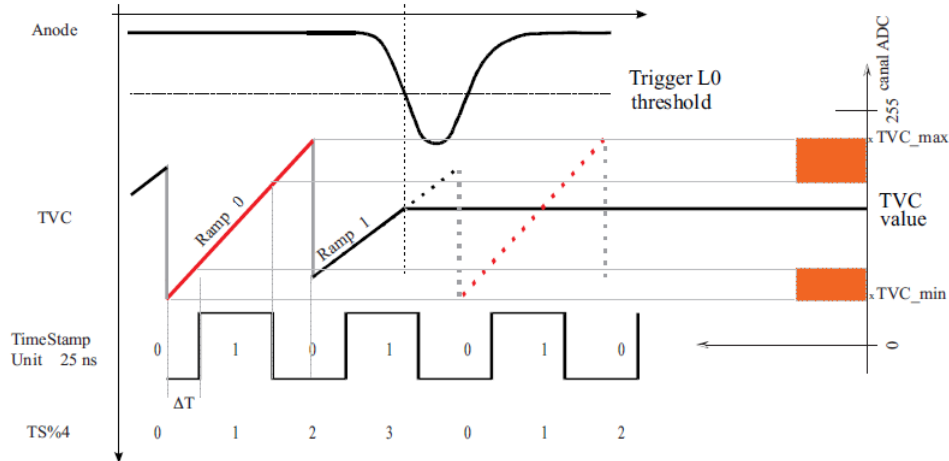


**Figure B.3.** The TVC working scheme [97].

The figure B.3 show the synchronization between the two ramps 0 and 1: there are two alternating ramps to avoid some edge effects, the ramps are also with a different slope to better distinguish between them. The clock is represented by the Time Stamp bit. The delay  $\Delta T$  between the ramp start, together with the variation of the Time Stamp bit, allow us to uniquely identify the ramp.

### B.1.2 AVC

The charge measure is provided by the integrator. Consider that the time L0 threshold passage (see paragraph 3.11.2) is not so obvious.

The integration port is optimised to describe as good as possible the signal. However, like in the figure B.4, this device not assures the integration of the signal before the threshold passage, underestimating in this way the total accumulated charge. Thus, as can be seen in the figure B.5, an integration by parts is performed.

The first integration part correspond to the signal before the threshold crossing, integrated with a duration that corresponds to an integration cycle ( $\sim 8$  ns). The second integration part covers the signal after the threshold crossing with a longer duration. The final result is the sum of the two charge integration. There are three cycle, each cycle with three phases (with the aim of three capacitors): I (integration), M (memorization), E (erasing).

During each phase one capacitor is in integration, another is memorizing the previous part signal and the third capacitor erases the signal it memorised before. The final charge result (called AVC) derives from the sum of the two phases I and M.

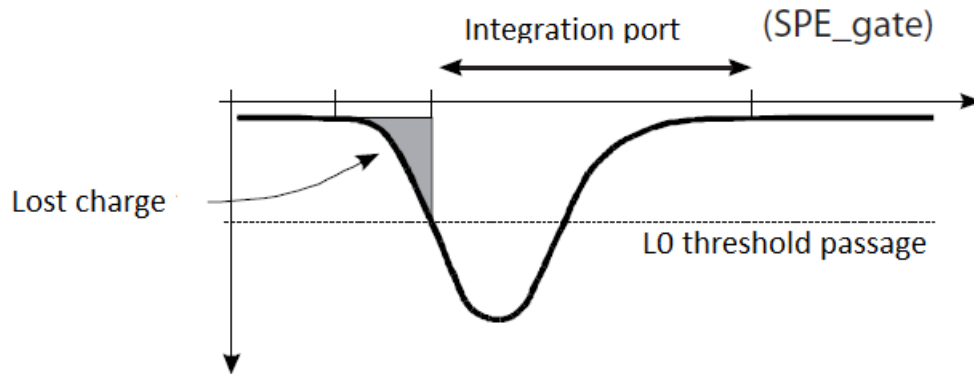


**Figure B.4.** The working method of the integrator when a signal pass the L0 threshold [97].

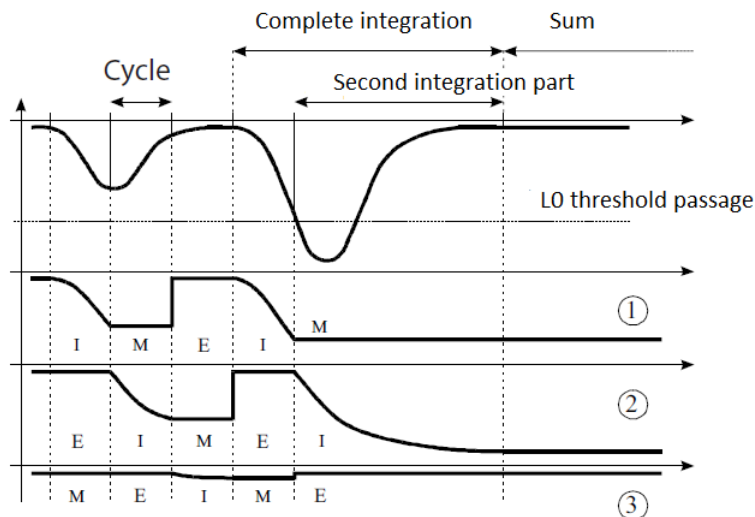


**Figure B.5.** The integration by parts of the charge signal [97].

The charge is stored into the pipeline and then digitised. Usually is convenient to leave a little margin between the continuous level of the integrator and the first ADC channel. Thus is possible to define the minimum value of the AVC identified with the parameter `AVC_OPE`, called "pedestal", that is the zero level of the integrator.

## B.2 The cross-talk effect between the measures of time and charge

After processed and waiting for the response of the trigger that choice which signal has to be digitised, the signal characteristics are stored in to the pipelines. Each pipeline has 16 memory cells. Among the others there are the two cells that store the analogue values of TVC and AVC.

The memories are formed by commuted capacitors. The proximity of the two cells and so of the two capacitors is at the base of the cross-talk (XT) effect.

The result is that the integrator's response for a given signal is dependant from the time of arrival of the signal itself. As can be seen from the figure B.6, there is a periodicity in the AVC channel of the ARS, with an observed period of 50 ns, that is the exact duration of the TVC voltage ramp. This implies a correlation between AVC and TVC.

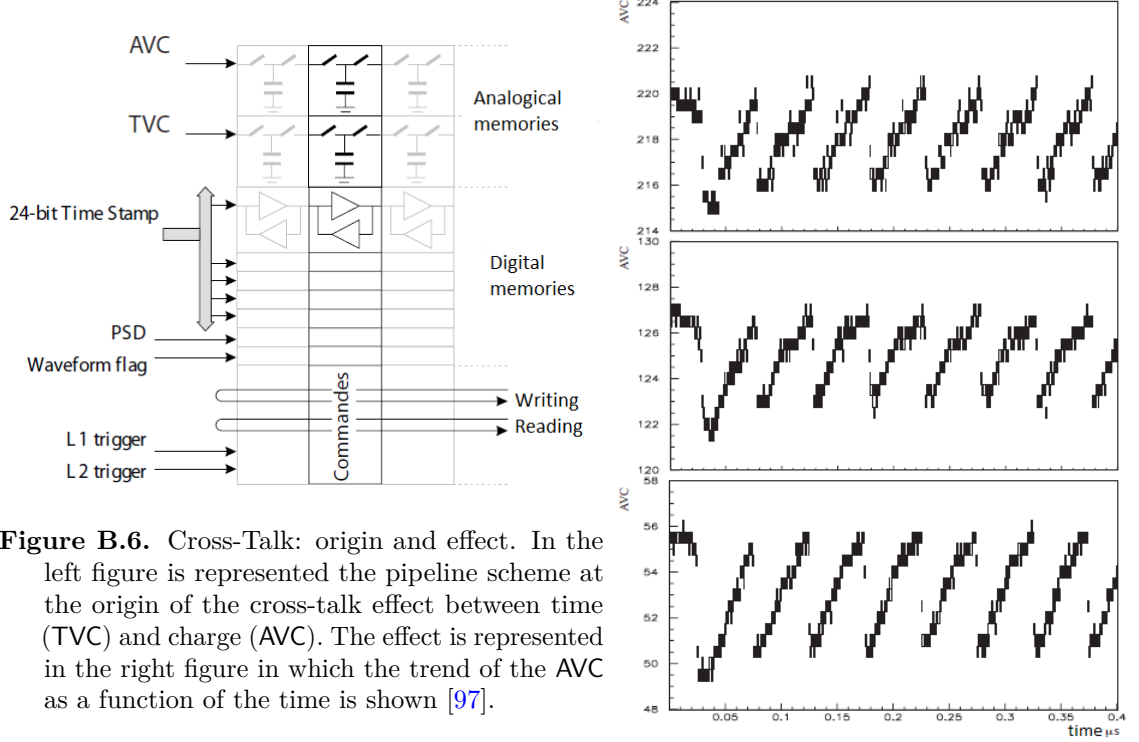


**Figure B.6.** Cross-Talk: origin and effect. In the left figure is represented the pipeline scheme at the origin of the cross-talk effect between time (TVC) and charge (AVC). The effect is represented in the right figure in which the trend of the AVC as a function of the time is shown [97].

The influence of the TVC over the AVC ranges from 4 to 5 AVC channel (see figure B.6). This effect degrades the precision of the measure of little charges (around 1pe), because its value is roughly 1/3 pe. Thus, this effect must be corrected.

The correction takes place in situ for each ARS as we will see. In addition there is also the effect of the influence of the AVC on the TVC; but this effect is of the second order, so is difficult to estimate it and will not be corrected.

Luckily the effect is linear, however an event by event correction is necessary to use data for physics analysis. The correction is performed, with a linear fit of the distribution AVC versus TVC, for each ARS.

The correction is given by the expression:

$$\begin{aligned} AVC_{corr} &= XT\_SLOPE \times (TVC - TVC\_MEAN) \\ &= XT\_SLOPE \times \left( TVC - \frac{(TVC\_MAX + TVC\_MIN)}{2} \right), \end{aligned} \quad (B.1)$$

where  $XT\_SLOPE = \frac{dAVC}{dTVC}$  is the slope of the fit line, and  $TVC\_MEAN$  is the mean of the TVC range. An example of the fit is shown in the figure B.7, where can be seen that the cross-talk correction is performed together with the measure of the

photo-electron peak.

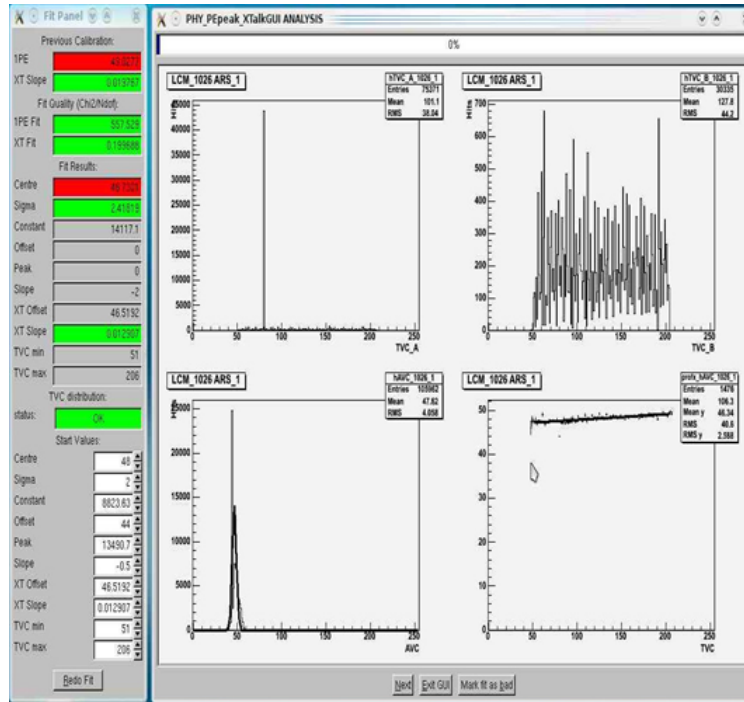


**Figure B.7.** An example of the fit to correct the cross-talk effect (bottom right) together with the measure of the 1pe peak (bottom left).

### B.3 The study of the time evolution of the cross-talk parameters

As we said before, the correction is applied for each ARS and changes after each calibration session. The main purpose of this work is to establish a general correction that not varies with the new calibrations. It means that the correction parameters have to be stable in time. Next will follow the study performed to check the stability of these parameters and the correspondent results.

The analysis starts with the calibration procedure [67], performed with the help of the CalibFW program developed by Antoine Kouchner. Before to proceed to describe the analysis work, it is better to explain the meaning of some concepts that are very important in the rest of the study.

**version\_id:** represent the identifier of a calibration session correspondent to an ANTARES run of data taking. Generally, blocks of *version\_id*, are used to perform the calibration of the ARS and evaluate the values of the main parameters like the cross-talk ones.

**calibOK:** is a flag, assigned, for each ARS, during the calibration by the CalibFW program, representing the goodness of the actual calibration compared to

the previous performed one. One calibration is good if the new obtained parameters are within the space of two sigma in the comparison with the previous performed calibration.

CalibOK can have three different values:

- **0**, for bad calibrations;
- **1**, for good calibrations;
- **2**, when the values of the previous calibration are taken, usually in the case of any mistakes during the ARS calibration.

After the end of the calibration process, for each version\_id, the output parameters: XT\_SLOPE, TVC\_MEAN, CalibOK are written on the ANTARES Data Base tables [22].

To go on with the analysis, is necessary to write Java programs to read the Data Base to extract the parameters values registered there for the version\_ids selected.

### B.3.1 The first part of the analysis

In the first phase of the study we selected 19 version\_id of XT calibration runs from the period 2007-2010 as reported in the table B.1.

**Table B.1.** The first block of the 19 selected version\_id. The first column represent the version\_id number. In the second column the version\_id number identifiers are reported, while in the third column there are the correspondent dates.

#	version_id	date
1	5394631	20/08/2007
2	5424518	07/12/2007
3	7707857	11/12/2007
4	10757966	11/04/2008
5	10776109	23/05/2008
6	15100193	05/06/2008
7	16718626	16/09/2008
8	59186564	07/09/2009
9	59186544	23/11/2009
10	50201176	25/06/2010
11	50201208	26/06/2010
12	50201234	27/06/2010
13	50253263	28/06/2010
14	50402408	05/07/2010
15	50403545	06/07/2010
16	50421269	08/07/2010
17	50421296	09/07/2010
18	56548993	04/11/2010
19	56470388	14/11/2010

In the figure B.8 the diverse distribution of the occurrence of the different values of the parameter CalibOK are shown.

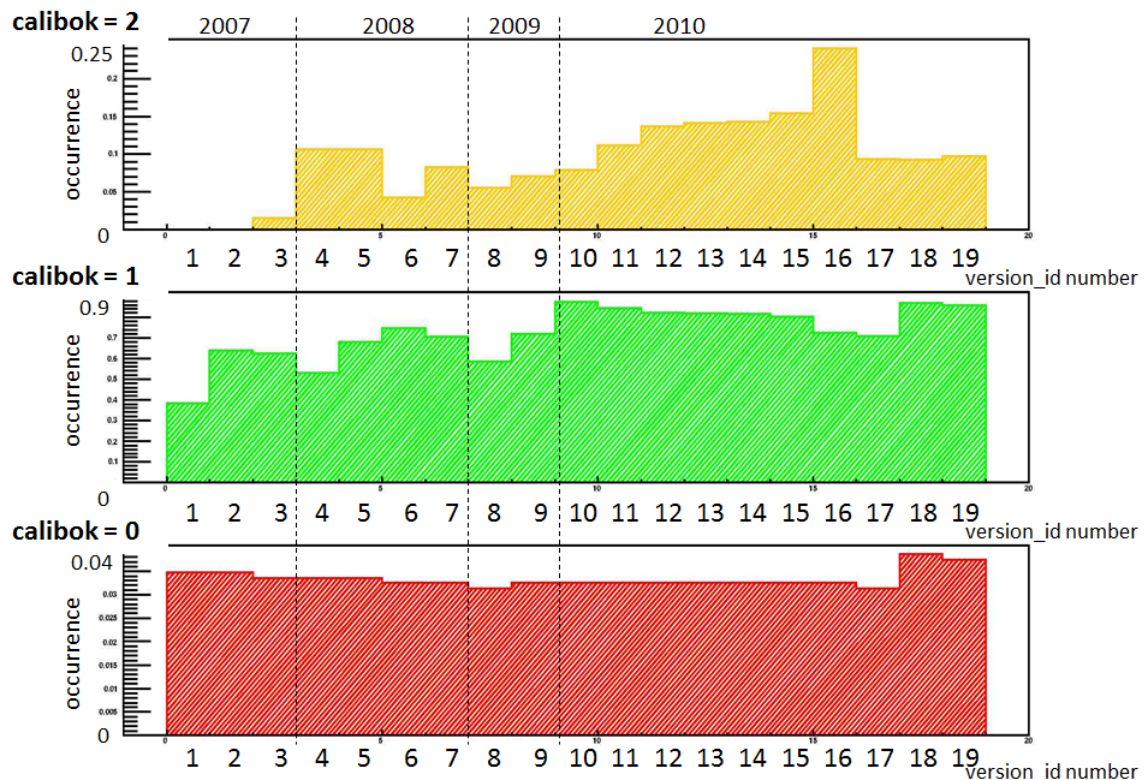


Figure B.8. The distribution of the CalibOK parameters occurrences

After that, we introduced two new calibOK flag:

- -10. This flag accounts for the version\_ids that have a number of lines lower than that of the full detector configuration. This because we need to report, for computational reasons, which ARS are not present;
- 4. This flag was introduced to account for the ARS that should not be in the detector; for example those of disconnected lines.

In the figure B.9 the percentage division of these parameters we describe above for the 19 version\_ids taken into account for this first analysis step. The different values are reported with different colors to make the plot more readable.

As can be seen the large majorities of the version\_ids have a calibOK equal to 1, so they exit from a good calibration.

Instead, in the figure B.10 the distribution of the calibOK parameter values as a function of the different version\_ids is shown. The color scale takes into account the occurrence percentage for each value.

Before to proceed with the analysis we have to check which ARS are present in the detector and which are well or bad working.

We consider not well working ARS those ARS which have a calibok value different from 1 and 2. That is to avoid only the bad calibrations and not existing ARS.

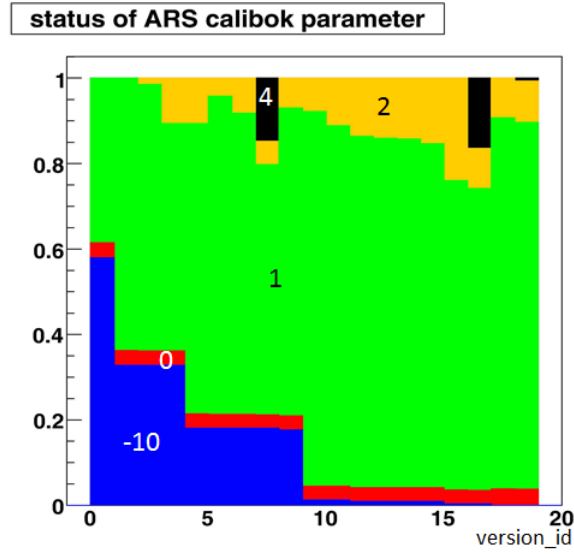


Figure B.9. The percentage of occurrence of the calibOK new flags.

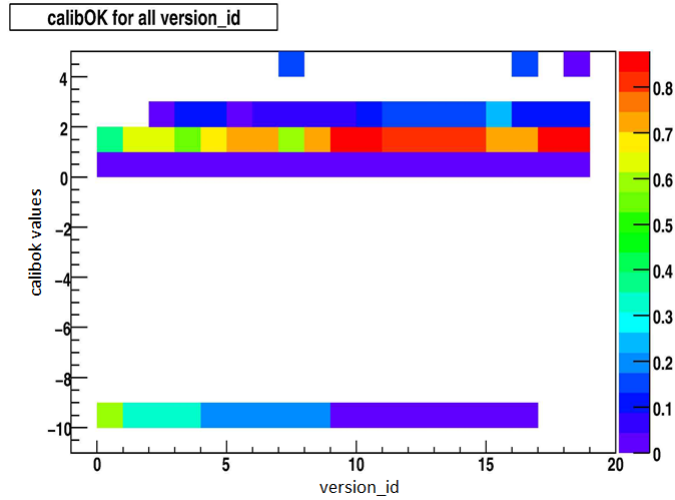


Figure B.10. The distribution of the calibOK values as a function of the selected version\_ids.

To identify each ARS number we use the following expression:

$$\text{ARS\_id} = 150(\text{line} - 1) + 6(\text{floor} - 1) + \text{arslink}. \quad (\text{B.2})$$

Where *line* stands for the line number of the apparatus, ranging from 0 to 11, and *floor* stands for the floor number of each line, ranging from 0 to 24; while *arslink* is the number of each ARS of one floor, ranging from 0 to 5. We have to remember that there are 2 ARS for each optical module and three optical modules in each floor. These value are stored in the Data Base in the table `antares.geography`.

The distribution of missing ARS is reported in the figure B.11.

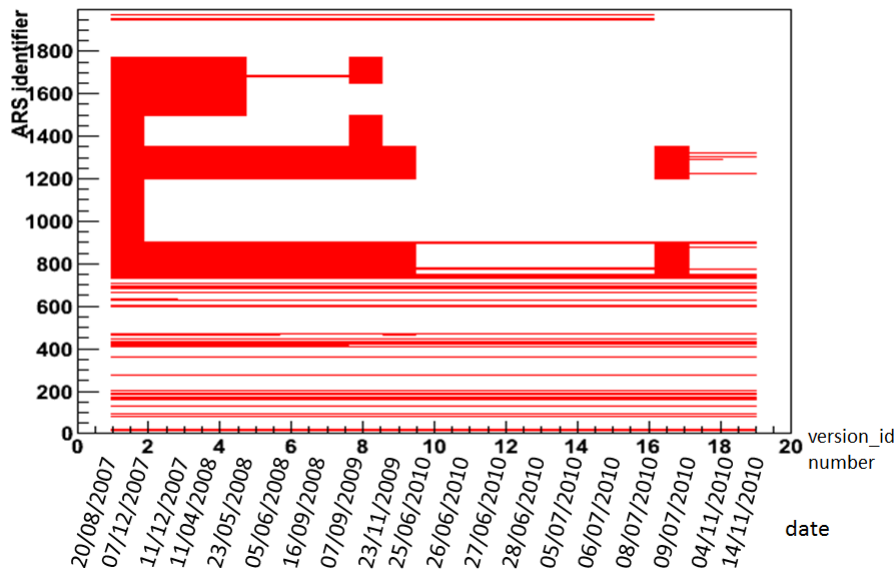


**Figure B.11.** The distribution of the missing ARS of the apparatus.

Next step is to show the distributions of the XT main parameters: TVC\_MEAN and XT\_SLOPE. The distributions for all the 19 version\_ids are reported in the figure B.12.

The purpose of the analysis is to evaluate the possible time evolution of the XT parameters. In order to evaluate this relative evolution, and if the evolution is stable in time, we evaluate the differences of these parameters for consecutive version\_ids.

It means to compute, for example, the difference of XT\_SLOPE between the version\_id 1 and the version\_id 2, then the difference between the version\_id 2 and the version\_id 3 and so on for all the 19 version\_ids.

These differences distributions are shown in the figure B.13.

As can be seen from the figure B.13, the parameters seem to be very stable: the differences show a pronounced peak at zero. It means that a difference equal to zero is equivalent to a not variable parameter, thus a stable value.

### B.3.2 The second part of the analysis

Although the condition of the data acquisition for the cross-talk parameters seem to be quite stable only from August 2009 [28]. Before this time there are some behaviours that are still not understood.

Thus, the ANTARES collaboration decided to take into account for this analysis only the version\_ids following this time. Also only the version\_ids with the large number of ARS and with no particular trigger selection are used.

So, to fix the universal values we use only the last entries. At the end we are

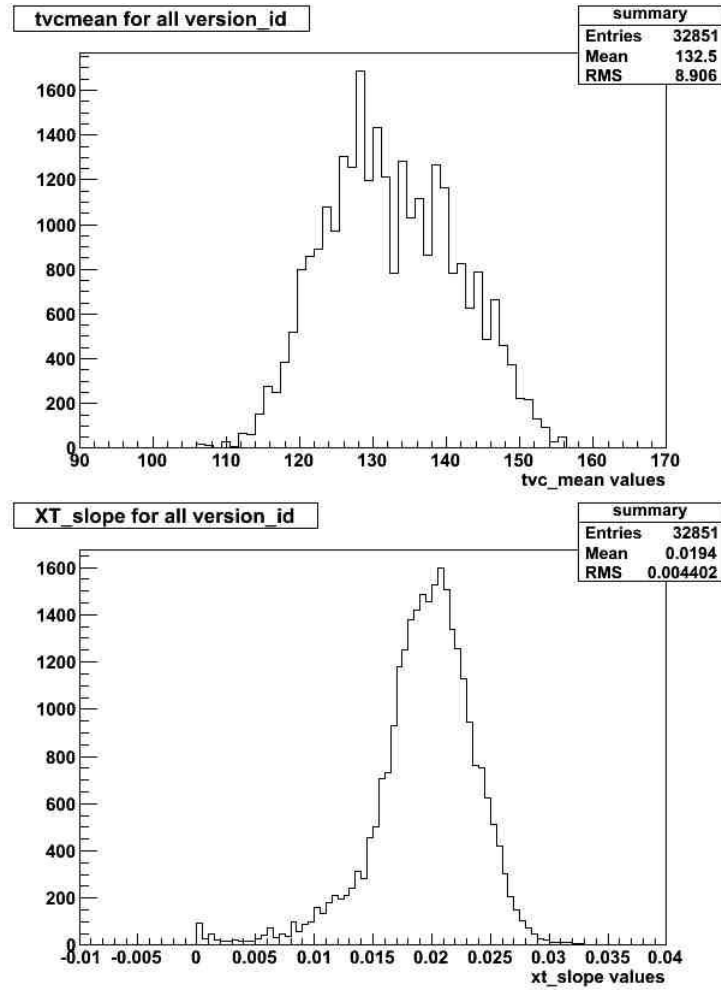


**Figure B.12.** The distribution of the cross-talk parameters TVC\_MEAN and XT\_SLOPE.

managing only four version\_ids (see table B.2).

The second step of the analysis is to repeat the calculations and plots we have shown above for only these four version\_id.

However there is a new parameter that has been taken into account: the  $\chi^2$  of the fit done to extract the XT parameters.

Now we select only the ARS with  $\text{calibOK} = 1$  and with a  $\chi^2$  value available.

In the figure B.14 is shown the distribution of these parameters for the first version\_id.

Then we evaluate the relative errors (called sigma  $\sigma$ ) between each ARS of each version\_id. We calculate this difference in this way:  $(ARS_i - \langle ARS \rangle) / \langle ARS \rangle$ , where  $\langle ARS \rangle$  is evaluated for each ARS of the four version\_id.

The results are reported in the figure B.15.

All the distribution have no problem. For the TVC\_MEAN shape it does not seem so surprising since its values are linked to the uniform distribution of TVC which define the time and which in the code have a limited precision to 0.25. This stability is one of the reasons which makes us want to perform a time independent

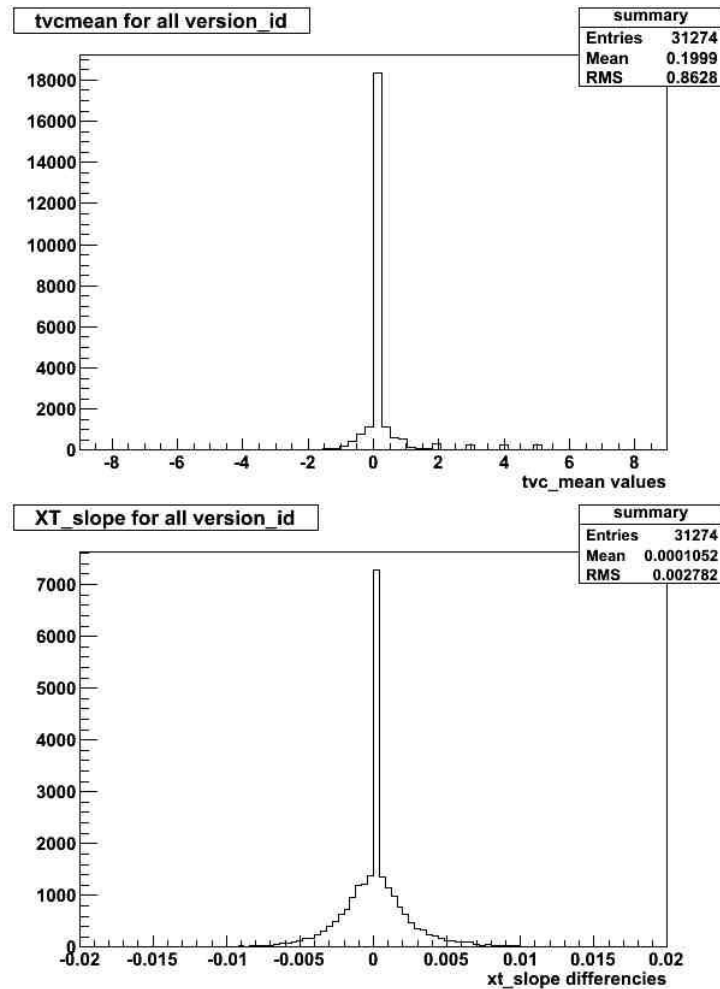


**Figure B.13.** The distribution of the differences of the cross-talk parameters TVC\_MEAN and XT\_SLOPE.

correction. From now on we do not more consider the study on the TVC\_MEAN parameter.

Then we evaluate the relative differences, like we did before, for the four version\_id. These differences are shown in figure B.16: three differences for 4 version\_ids.

Now we evaluate the mean distributions for the cross-talk parameters over the 4 version\_ids. The result is shown in the figure B.18.

We have to notice that we used as the total number of ARS of the full detector the number of them present in the fourth version\_id, that is the one with the bigger number (1703) as shown above. It is an underestimation.

In the figure B.17 is reported the number of counts used doing the mean value calculus: if an ARS is present in all the four version\_ids thus count = 4 and so on.

We have several solution to freeze the correction: to consider the same correction for all ARS taken from the mean of the distribution of all ARS, with several version\_ids; take for each ARS the mean correction over version\_ids; take for each

**Table B.2.** The new 4 selected version\_id. The first column represent the version\_id number. In the second column the version\_id number identifiers, in the third column there are the correspondent dates and in the fourth the correspondent number of working ARS.

#	version_id	date	working ARS
1	59186564	07/09/2009	1442
2	59186544	23/11/2009	1412
3	50421296	09/07/2010	1414
4	56470388	14/11/2010	1703

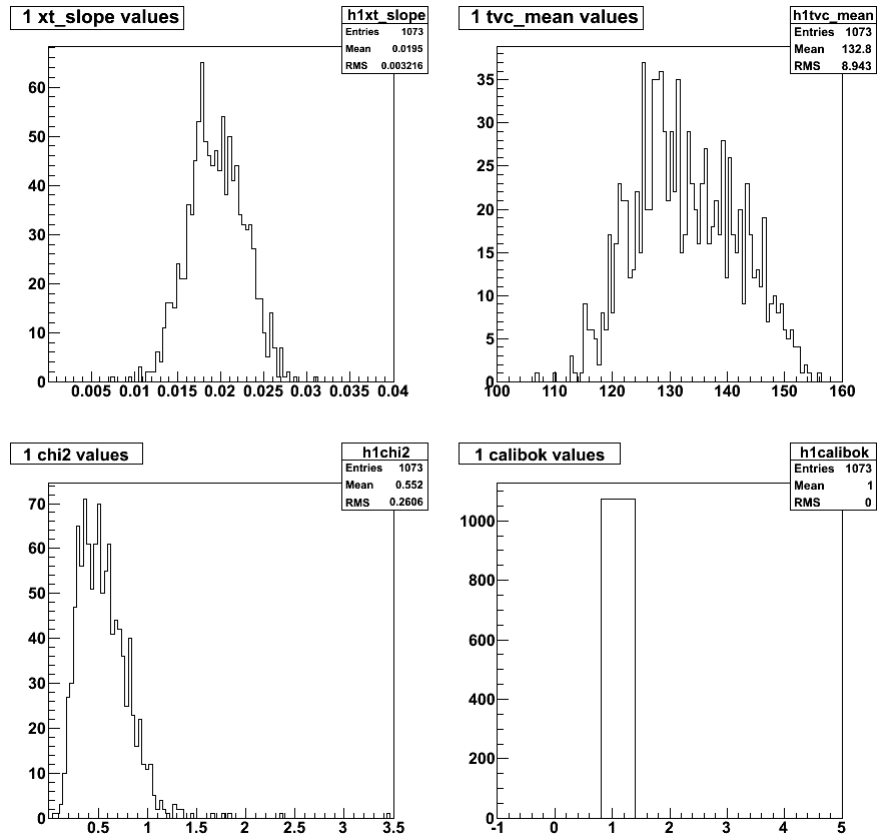


**Figure B.14.** The distribution of the cross-talk parameters for the version\_id = 59186564. In the upper left plot the XT\_SLOPE distribution, in the upper right the TVC\_MEAN, in the bottom left the  $\chi^2$  and in the bottom right the calibOK.

ARS the mean over version\_ids but discarding bad values.

The first solution is quite brutal and not accurate. Between the other two we use the second one that we just used in the previous calculations.

In order to check also the third hypothesis, we try to test the correlation between the parameters and the  $\chi^2$  values. In this way we can see if there are some ARS that have always bad values for the respective parameters.

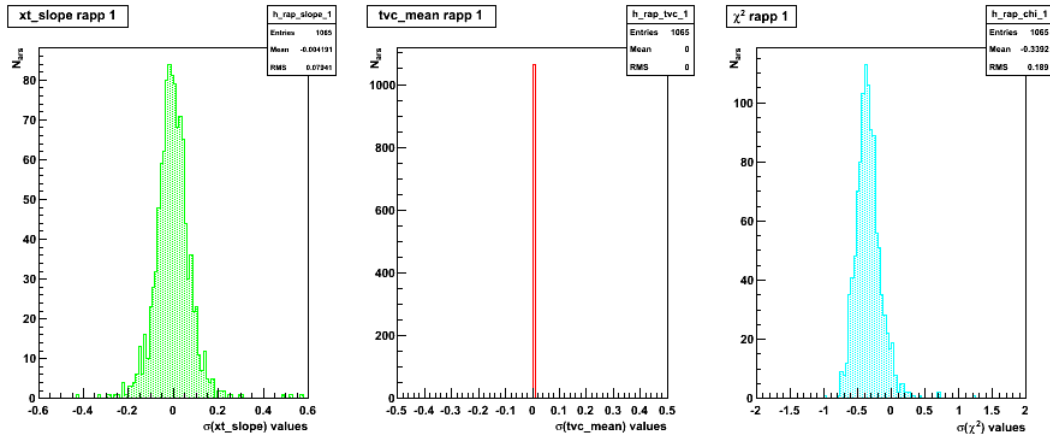


Figure B.15. The distribution of the relative difference of the cross-talk parameters for the version\_id = 59186564. In the left plot the XT\_SLOPE distribution, in the central plot the TVC\_MEAN, in the right plot the  $\chi^2$ .

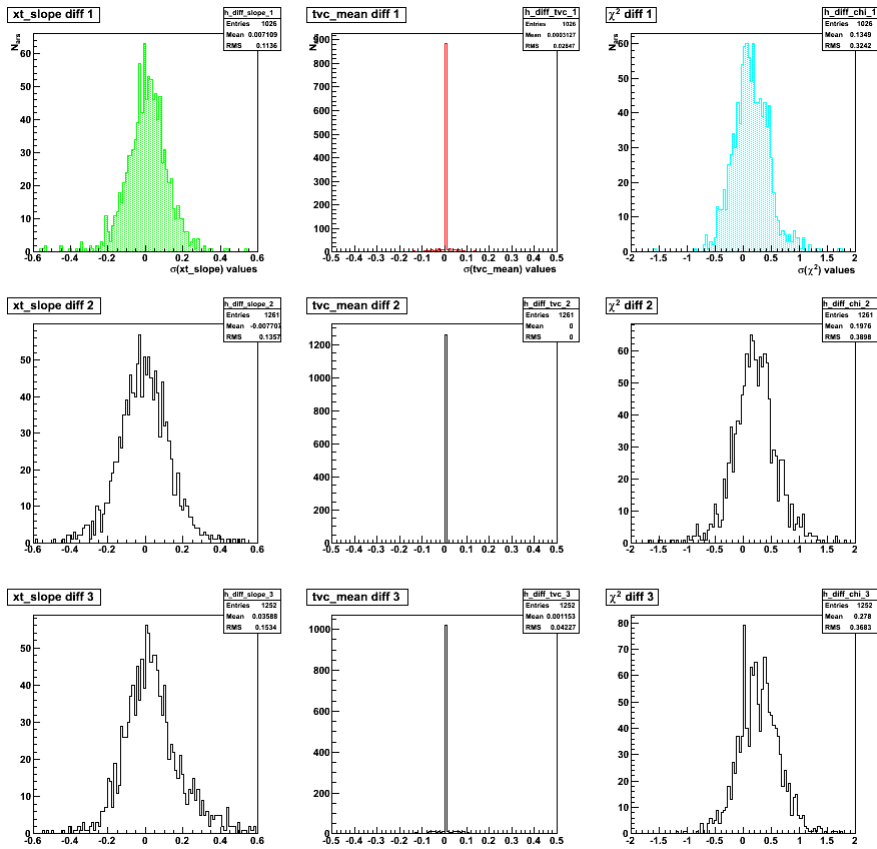


Figure B.16. The 3 relative differences between the 4 version\_ids. In the left column the XT\_SLOPE difference distribution, in the central column TVC\_MEAN, in the right column the  $\chi^2$  distribution.

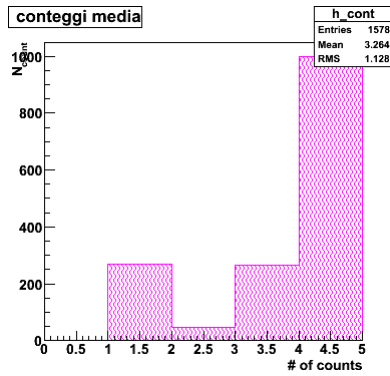


Figure B.17. The ARS counts distribution.

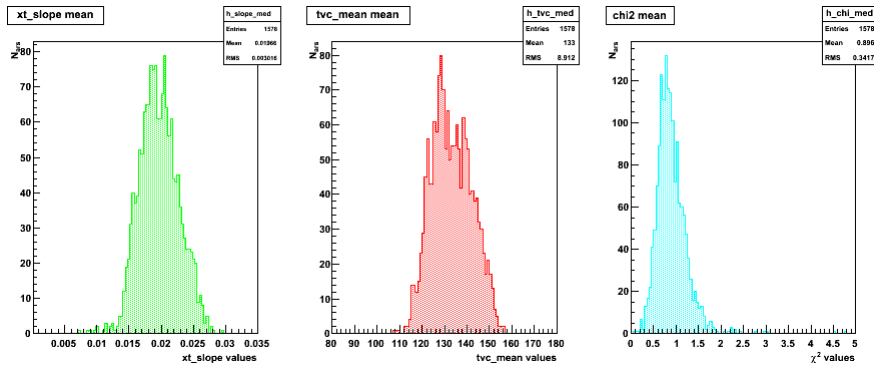


Figure B.18. The mean distributions of the cross-talk parameters (XT\_SLOPE, TVC\_MEAN,  $\chi^2$  respectively).

In the following figures B.19 and B.20 we show these correlation plots. As can be seen in all the figures there is not any correlation between the parameters and the  $\chi^2$ .

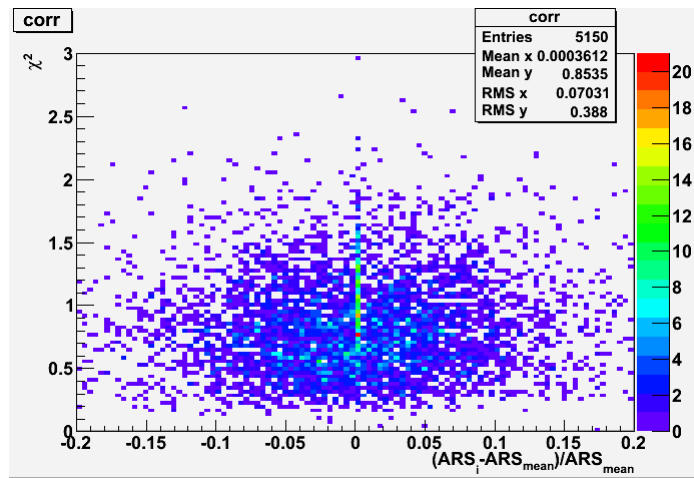
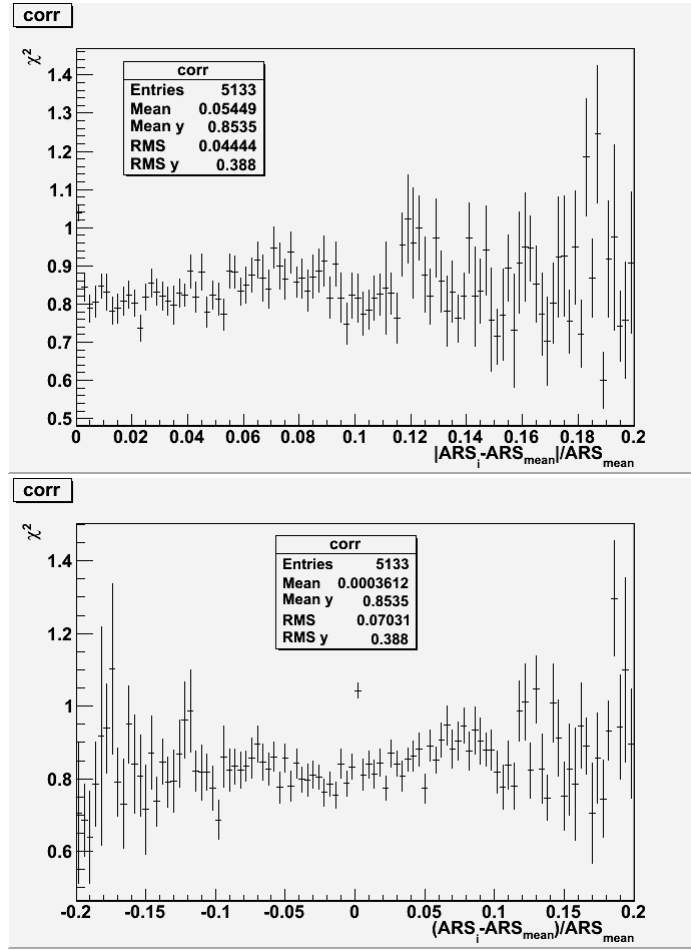


Figure B.19. The correlation between the ARS and the  $\chi^2$ .



**Figure B.20.** The correlation profile for the quantity  $(ARS_i - \langle ARS \rangle) / \langle ARS \rangle$ , with (top) and without (bottom) absolute value, and the  $\chi^2$ . The errors are of the standard type  $\sigma/\sqrt{n}$  for each bin of the histogram.

After evaluating the possible correlation, and found that there is no correlation, we proceed trying to estimate again the evolution in time of the XT\_SLOPE parameter with the same method we use above.

In the figures B.21, the relative differences between the four version\_ids is reported.

In the next two plots B.22 are shown the distribution of the parameter for each version\_id. The plots are weighted with the number of ARS of each version\_id (in this case the weight it is equal to  $w = 1/\#ARS$ ). The total number of ARS for each version\_id is reported above together with the version\_ids numbers identifier.

After all these plots and checks we can at the end define the mean cross-talk parameters values that can be used as general values for calibration purpose.

- XT\_SLOPE =  $0.019 \pm 0.06$ ;
- TVC\_MEAN =  $127.38 \pm 0.046$ .

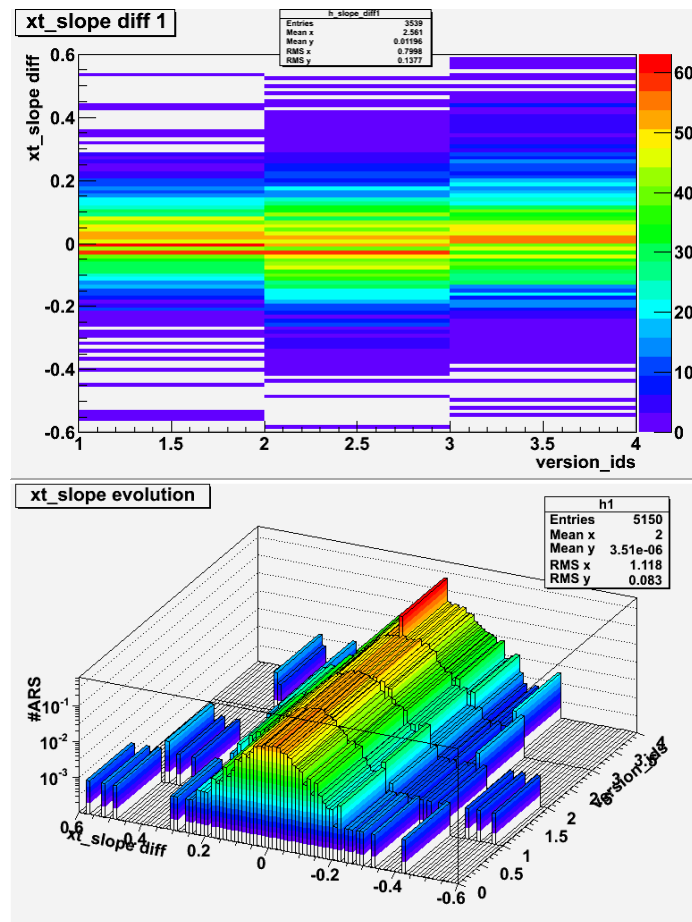


Figure B.21. The relative difference between the four version\_ids for the XT\_SLOPE parameter.

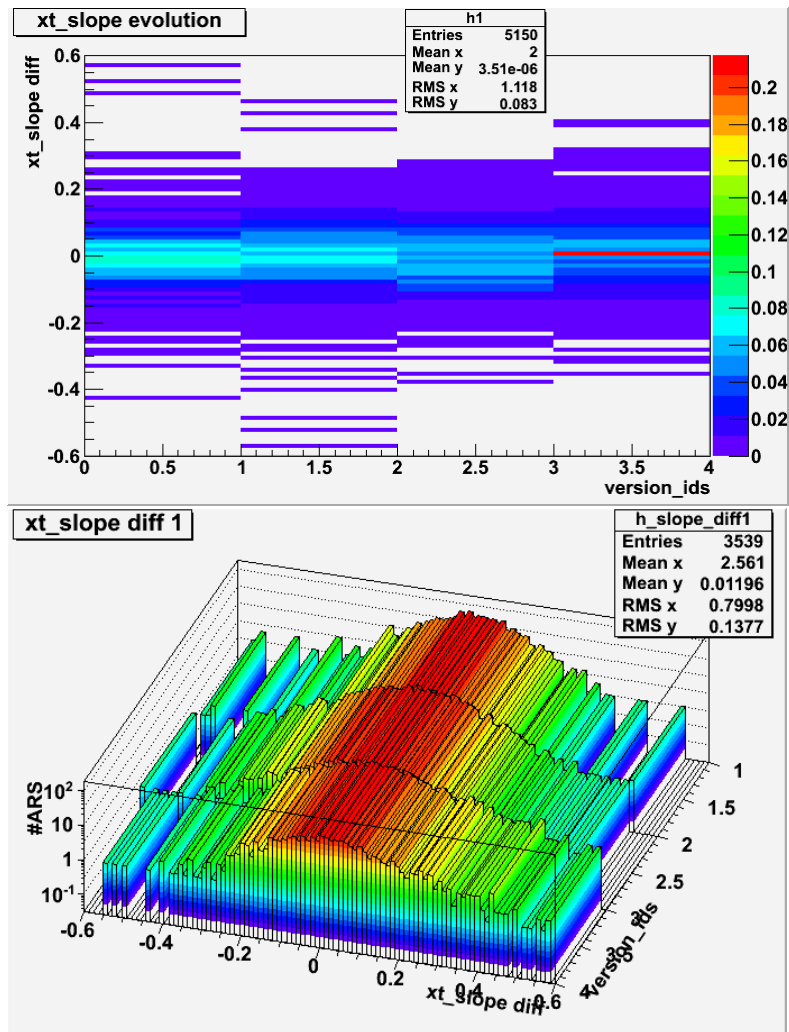


Figure B.22. The distributions of the XT\_SLOPE parameter with the ARS weight.



# Bibliography

- [1] <http://fermi.gsfc.nasa.gov/>.
- [2] <http://icecube.wisc.edu>.
- [3] <http://h1.desy.de>.
- [4] <http://www-zeus.desy.de>.
- [5] <http://gcn.gsfc.nasa.gov>.
- [6] <http://visual.merriam-webster.com/astronomy/astronomical-observation/celestial-coordinate-system.php>.
- [7] <http://astronomy.swin.edu.au/cosmos/N/North+Galactic+Pole>.
- [8] ABDO A. A. ET AL. Measurement of the cosmic ray e+ plus e- spectrum from 20 gev to 1 tev with the fermi large area telescope. *Phys. Rev. Lett.*, **102**, 181101, (2009). [arXiv:astro-ph/0905.0025v1](https://arxiv.org/abs/astro-ph/0905.0025v1).
- [9] ADRIANI O. ET AL. New measurement of the antiproton-to-proton flux ratio up to 100 gev in the cosmic radiation. *Phys. Rev. Lett.*, **102**, 051101; *Nature*, **458**, 607, (2009). <http://prl.aps.org/pdf/PRL/v102/i5/e051101>.
- [10] AGUILAR J. A. ET AL. Performance of the front-end electronics of the ANTARES Neutrino Telescope. *Nucl. Instrum. Meth.*, **A 622**, 59-73, (2010). [arXiv:astro-ph.IM/1007.2549v2](https://arxiv.org/abs/astro-ph.IM/1007.2549v2).
- [11] AGUILAR J. A. ET AL. A fast algorithm for muon track reconstruction and its application to the ANTARES neutrino telescope. *Astrop. Phys.*, **34**, 652, (2011). [arXiv:astro-ph/1105.4116](https://arxiv.org/abs/astro-ph/1105.4116).
- [12] AHMED T. ET AL. First measurement of the charged current cross-section at hera. *Phys. Lett.*, **B324**, 241, (1994).
- [13] AHMED Z. ET AL. A search for wimps with the first five-tower data from cdms. *Phys. Rev. Lett.*, **102**, 011301, (2009). [arXiv:astro-ph/0802.3530v2](https://arxiv.org/abs/astro-ph/0802.3530v2).
- [14] AHRENS J. ET AL. Sensitivity of the IceCube detector to astrophysical sources of high energy muon neutrinos. *Astropart. Phys.*, **20**, 507, (2004).

- [15] AL SAMARAI, I. *Search for neutrinos from transient sources with the ANTARES neutrino telescope and optical follow-up observations - Development of hemispheric hybrid photomultipliers for astroparticle experiments*. Ph.D. thesis, Marseille University (2011).
- [16] ALLEN S. W. ET AL. Improved constraints on dark energy from Chandra X-ray observations of the largest relaxed galaxy clusters. *MNRAS*, **383**, 879, (2008). [arXiv:astro-ph/0706.0033v2](https://arxiv.org/abs/astro-ph/0706.0033v2).
- [17] ALPHER R. A., BETHE H., GAMOW G. The origin of chemical elements. *Phys. Rev.*, **73**, 803, (1948). [http://astrophysics.fic.uni.lodz.pl/100yrs/html/chap/fs2\\_07009.htm](http://astrophysics.fic.uni.lodz.pl/100yrs/html/chap/fs2_07009.htm).
- [18] ALPHER R. A., HERMAN R. C. On the relative abundance of the elements. *Phys. Rev.*, **74**, 1737, (1948). [http://prola.aps.org/pdf/PR/v74/i12/p1737\\_1](http://prola.aps.org/pdf/PR/v74/i12/p1737_1).
- [19] ALPHER R. A., HERMAN R. C. Remarks on the evolution of the expanding universe. *Phys. Rev.*, **75**, 1089, (1949). [http://astrophysics.fic.uni.lodz.pl/100yrs/html/chap/fs2\\_07012.htm](http://astrophysics.fic.uni.lodz.pl/100yrs/html/chap/fs2_07012.htm).
- [20] AMALDI U., DE BOER W., FURSTENAU H. Comparison of grand unified theories with electroweak and strong coupling constants measured at lep. *Phys. Lett.*, **B260**, 447, (1991).
- [21] ANGELETTI L., GIANNONE P. *Esercizi e complementi di Astronomia*. Edizioni nuova cultura, second edn. (2007).
- [22] ARNAUD, A. *CALIBRATION DATA STORAGE, version 2.5*. ANTARES internal pages, ORACLE Database Webinterface.
- [23] ARNAUD, M. X-ray observations of galaxies. *To appear in Proc. Enrico Fermi, International School of Physics Course CLIX, eds. F. Melchiorri & Y. Rephaeli.*, (2005). [arXiv:astro-ph/0508159](https://arxiv.org/abs/astro-ph/0508159).
- [24] ARPESELLA C., BASA S., MONTENET F. Test results of a 14 stage 8" Hamamatsu photomultiplier (R5912-02). ANTARES internal note, ANTARES-OPM0-1997-005.pdf (1997).
- [25] ASTIER P. ET AL. The supernova legacy survey: measurement of  $\omega_m, \omega_\Lambda$  and  $w$  from the first year data set. *Astron. Astrophys.*, **447**, 31, (2006). [arXiv:astro-ph/0510447v1](https://arxiv.org/abs/astro-ph/0510447v1).
- [26] BAILEY, D. J. L. Km3 v2r1 : User guide. ANTARES internal note, ANTARES-SOFT-2002-006.pdf (2002).
- [27] BARBIERI R. A., GIUDICE G. F. *Nucl. Phys.*, **B306**, 63, (1988).
- [28] BARET, B. News on ARS. ANTARES collaboration meeting, Cern, February, Calibration session (2011).

- [29] BARWICK S. W. ET AL. Measurements of the cosmic-ray positron fraction from 1 to 50 gev. *Astrophys. J.*, **482**, L191, (1997). <http://iopscience.iop.org/1538-4357/482/2/L191>.
- [30] BERGSTROM L., EDSJÖ J., GONDOLO P. Indirect detection of dark matter in km-size neutrino telescopes. *Phys. Rev. Lett.*, **D58**, 103519, (1998). [arXiv: hep-ph/9806293](https://arxiv.org/abs/hep-ph/9806293).
- [31] BERNABEI R. ET AL. Technical aspects and dark matter searches. *Eur. Phys. J.*, **C56**, 333, (2008). [arXiv:ins-det/0912.4200v1](https://arxiv.org/abs/ins-det/0912.4200v1).
- [32] BERTONE G., HOOPER D., SILK J. Particle dark matter: evidence, candidates and constraints. *Phys. Rept.*, **405**, 279, (2005). [arXiv:hep-ph/0404175](https://arxiv.org/abs/hep-ph/0404175).
- [33] BERTONE G., NEZRI E., ORLOFF J., SILK J. Neutrinos from dark matter annihilations at the galactic centre. *Phys.Rev.*, **D70**, 063503, (2004). [arXiv: astro-ph/0403322](https://arxiv.org/abs/astro-ph/0403322).
- [34] BLAKE C. ET AL. Cosmological baryonic and matter densities from 600000 SDSS Luminous Red Galaxies with photometric redshifts. *MNRAS*, **374**, 1527, (2007). [arXiv:astro-ph/0605303v2](https://arxiv.org/abs/astro-ph/0605303v2).
- [35] BLENNOW M., EDSJÖ J., OHLSSON T. Neutrinos from WIMP annihilations obtained using a full three-flavor Monte Carlo approach. *JCAP* 0801:021, (2008). [arXiv:hep-ph/0709.3898v2](https://arxiv.org/abs/hep-ph/0709.3898v2).
- [36] BOGAZZI C., HEIJBOER A. Point source search with 2007-2010 data. ANTARES internal note, ANTARES-PHYS-2011-005.pdf (2011).
- [37] BOLIEV M. M. ET AL. *Phys. Ser.*, **55**, 126, (1991).
- [38] BORGANI, S. Cosmology with clusters of galaxies. *Lecture notes in Physics, Springer*, 287, (2006). [arXiv:astro-ph/0605575](https://arxiv.org/abs/astro-ph/0605575).
- [39] BRONIATOSWSKI A. ET AL. A new high-background-rejection dark matter ge cryogenic detector. *Phys.Lett.*, **B681**,305, (2009). [arXiv:0905.0753](https://arxiv.org/abs/0905.0753).
- [40] BRUN R., RADEMAKERS F. ROOT - an object oriented data analysis framework. *Proceedings AIHENP'96 Workshop, Lausanne, Sep. 1996, Nucl. Inst. and Meth. in Phys. Res.*, **A389**, 81-86, (1997). See also <http://root.cern.ch/>.
- [41] BRUNNER, J. Updated tag list for the new ANTARES event format. ANTARES internal note, ANTARES-SOFT-1999-003.pdf (1999).
- [42] BRUNNER, J. Cherenkov Light from HE Electromagnetic and Hadronic Showers. ANTARES internal note, ANTARES-SOFT-2002-015.pdf (2002).
- [43] BRUNNER, J. Analysis of 2007 and 2008 data with BBfit. ANTARES internal note, ANTARES-PHYS-2009-006.pdf (2009).
- [44] BRUNNER, J. The BBFit reconstruction algorithm. ANTARES internal note, ANTARES-SOFT-2010-005.pdf (2009).

- [45] CARMINATI G., MARGIOTTA A., SPURIO M. MUPAGE: a MUon GEnerator from PArametric formulas. ANTARES internal note, ANTARES-SOFT-2006-003.pdf (2006).
- [46] CARMINATI G., MARGIOTTA A., SPURIO M. MUPAGE User Guide. ANTARES internal note, ANTARES-SOFT-2007-004.pdf (2007).
- [47] CARR J., ESCOFFIER S., ZABOROV D. Proposition for an alternative trigger based on the t3 cluster trigger. ANTARES internal note, ANTARES-SOFT-2007-016.pdf (2007).
- [48] CLINE, J. M. 130 GeV dark matter and the Fermi gamma-ray line. (2012). [arXiv:astro-ph/1205.2688](https://arxiv.org/abs/1205.2688).
- [49] CLOWE D. ET AL. A direct empirical proof of the existence of dark matter. *Astrophys. J.*, **648**, L109, (2006). [arXiv:astro-ph/0608407v1](https://arxiv.org/abs/astro-ph/0608407v1).
- [50] COLES P., LUCCHIN F. *Cosmology: the origin and evolution of cosmic structures*. John Wiley & sons, second edn. (2002).
- [51] COTTINI, N. *Detection of low energy neutrinos and Dark Matter search in ANTARES*. Ph.D. thesis, Pisa University (2006).
- [52] DE JONG, M. Antares data formats. ANTARES internal note, ANTARES-SOFT-2004-006.pdf (2004).
- [53] DE JONG, M. The antares trigger software. ANTARES internal note, ANTARES-SOFT-2005-005.pdf (2005).
- [54] DE JONG, M. The Trigger Efficiency program. ANTARES internal note, ANTARES-SOFT-2009-001.pdf (2009).
- [55] DIXON D. ET AL. *New Astron.*, **3**, 539, (1998).
- [56] DODELSON, S. *Modern cosmology*. Academic Press (2003).
- [57] DREES M., GERBIER G. Dark matter. *Journal of Phys.*, **G37**, 255, (2010).
- [58] DUNKLEY J. ET AL. Five-Year WMAP observations: likelihoods and parameters from the WMAP data. *Astrophys. J. Supp*, **180**, 306, (2009). [arXiv:astro-ph/0803.0586v2](https://arxiv.org/abs/astro-ph/0803.0586v2).
- [59] EBERL T., KOPPER C. The seatray software framework. ANTARES internal note, ANTARES-SOFT-2009-013.pdf (2009).
- [60] EDSJÖ, J. WimpSim Neutrino Monte Carlo. [http://www.fysik.su.se/~sim\\$edsjo/wimpsim/](http://www.fysik.su.se/~sim$edsjo/wimpsim/).
- [61] EDSJÖ, J. *Aspects of neutrino detection of neutralino dark matter*. Ph.D. thesis, Uppsala University (1997). [arXiv:hep-ph/9704384v1](https://arxiv.org/abs/hep-ph/9704384v1).
- [62] EDSJÖ, J. *Calculation of neutrino cross sections and the nusigma neutrino-nucleon scattering Monte Carlo* (2007). <http://copsosx03.physto.se/wimpsim/code/nucross3.pdf>.

- [63] EDSJÖ, J. *WIMPSIM: WIMPANN and WIMPEVENT. Simulation of WIMP annihilation in the Earth/Sun and propagation to a neutrino telescope* (2012). <http://copsosx03.physto.se/wimpsim/code/wimpsim-3.00.pdf>.
- [64] ESCOFFIER, S. Bioluminescence studies with the antares prototype sector line. ANTARES internal note, `ANTARES-SITE-2005-001.pdf` (2005).
- [65] FAYET, P. *Phys. Lett.*, **B69**, 489, (1977).
- [66] FELDMAN G. J., COUSINS R. D. Unified approach to the classical statistical analysis of small signals. *Phys.Rev.*, **D57**:3873-3889, (1999). [arXiv:physics/9711021v2](https://arxiv.org/abs/physics/9711021v2).
- [67] FERMANI, P. Tips on charge calibration. ANTARES site, INTERNAL PAGES, Calibration section, Charge calibration.
- [68] FERMI-LAT COLLABORATION. Fermi LAT Search for Dark Matter in Gamma-ray Lines and the Inclusive Photon Spectrum. (2012). [arXiv:astro-ph/1205.2739](https://arxiv.org/abs/astro-ph/1205.2739).
- [69] FERRARI, G. Lectures notes of the course of general relativity (2006).
- [70] FORERO D. V., TÓRTOLA M., VALLE J. W. F. Global status of neutrino oscillation parameters after recent reactor measurements. (2012). [arXiv:hep-ph/1205.4018v2](https://arxiv.org/abs/hep-ph/1205.4018v2).
- [71] FREEDMAN W. L. ET AL. Final result from the Hubble space telescope key project to measure the Hubble constant. *Astrophys.J.*, **553**, 47, (2000). [arXiv:astro-ph/0012376](https://arxiv.org/abs/astro-ph/0012376).
- [72] GAISSER, T. K. *Cosmic Ray and Particle Physics*. Cambridge University Press (1999).
- [73] GALOUMIAN P., BERTHIER R., LAMARE P., LOUCATOS S. Glass and gel transparency tests. ANTARES internal note, `ANTARES-OPM0-1998-004.pdf` (1998).
- [74] GAMOW, G. Expanding universe and the origin of elements. *Phys. Rev.*, **70**, 572, (1946). [http://astrophysics.fic.uni.lodz.pl/100yrs/html/chap/fs2\\_07006.htm](http://astrophysics.fic.uni.lodz.pl/100yrs/html/chap/fs2_07006.htm).
- [75] GANDHI R. ET AL. Ultrahigh energy neutrino interactions. *Astropart. Phys.*, **5**, 81, (1996).
- [76] GAULT M., VECCHI M., RIVIÈRE C. Run-by-Run Monte Carlo and Data Quality. ANTARES internal note, `ANTARES-SOFT-2011-016.pdf` (2011).
- [77] GIANNONE, P. *Elementi di Astronomia*. Pitagora Editrice Bologna, second edn. (2004).
- [78] GONDOLO P. ET AL. Darksusy: computing supersymmetric dark matter properties numerically. *JCAP*, **0407**, 008, (2004). [arXiv:astro-ph/0406204v1](https://arxiv.org/abs/astro-ph/0406204v1).

- [79] GONDOLO P., SILK J. Dark matter annihilation at the galactic center. *Phys. Rev. Lett.*, **83**, 1719, (1999). [arXiv:astro-ph/9906391](https://arxiv.org/abs/astro-ph/9906391).
- [80] GREISEN, K. End to the Cosmic-Ray spectrum? *Phys. Rev. Lett.*, **16**, 748, (1966). [http://prl.aps.org/abstract/PRL/v16/i17/p748\\_1](http://prl.aps.org/abstract/PRL/v16/i17/p748_1).
- [81] GUTH, A. H. The inflationary universe: a possible solution to the horizon and flatness problems. *Phys. Rev.*, **D23**, 347, (1981). [http://prd.aps.org/abstract/PRD/v23/i2/p347\\_1](http://prd.aps.org/abstract/PRD/v23/i2/p347_1).
- [82] HABER, H. E. Supersymmetric particle searches. *Journal of Phys.*, **G37**, 1292, (2010).
- [83] HALZEN F., MARTIN A. D. *Quarks & leptons*. John Wiley & Sons (1984).
- [84] HEIJBOER, A. *Track reconstruction and point source searches with ANTARES*. Ph.D. thesis, Amsterdam University (2004).
- [85] HILL G. C., RAWLINS K. Unbiased cut selection for optimal upper limits in neutrino detectors: the model rejection potential technique. *Astropart. Phys.*, **19**, 393-402, (2002). [arXiv:astro-ph/0209350v1](https://arxiv.org/abs/astro-ph/0209350v1).
- [86] HINSHAW G. ET AL. Five-Year WMAP observations: data processing, sky maps and basic results. *Astrophys. J. Supp*, **180**, 225, (2009). [arXiv:astro-ph/0803.0732v2](https://arxiv.org/abs/astro-ph/0803.0732v2).
- [87] HUBBLE E., HUMASON M. L. The velocity-distance relation among Extra-Galactic Nebulae. *Astrophys. J.*, **74**, 43, (1931). <http://articles.adsabs.harvard.edu/full/1931ApJ....74...43H>.
- [88] JAMES F., ROOS M. Minuit: a system for function minimization and analysis of the parameter errors and correlations. (1975).
- [89] JUNGMAN G., KAMIONKOWSKI M., GRIEST K. Supersymmetric dark matter. *Phys. Rep.*, **267**, 195, (1996). [arXiv:hep-ph/9506380](https://arxiv.org/abs/hep-ph/9506380).
- [90] KAMIONKOWSKI, M. Energetic neutrinos from heavy-neutralino annihilation in the sun. *Phys. Rev.*, **D44**, 3021, (1991).
- [91] KAMIONKOWSKI M., KINKHABWALA A. Galactic halo models and particle dark-matter detection. *Phys. Rev.*, **D57**, 3256, (1998). [arXiv:hep-ph/9710337v1](https://arxiv.org/abs/hep-ph/9710337v1).
- [92] KANE G. L., KOLDA C. F., ROSZKOWSKI L., WELLS J. D. Study of constrained minimal supersymmetry. *Phys. Rev.*, **D49**, 6173, (1994). [arXiv:hep-ph/9312272](https://arxiv.org/abs/hep-ph/9312272).
- [93] KOHRI K., LYTH D. H., MELCHIORRI A. Black hole formation and slow-roll inflation. *JCAP*, **0804**, 038, (2008). [arXiv:0711.5006](https://arxiv.org/abs/0711.5006).
- [94] KOLB E. W., TURNER M. S. *The early Universe*. Addison Wesley (1990).

- [95] KOMATSU E. ET AL. Five-Year WMAP observations: cosmological interpretation. *Astrophys. J. Supp*, **180**, 330, (2009). [arXiv:astro-ph/0803.0547v2](#).
- [96] KOROLKOVA E. V., THOMPSON L. Monte Carlo simulation of cosmic ray muons at sea level with CORSIKA. ANTARES internal note, ANTARES-SOFT-2003-002.pdf (2003).
- [97] KOUCHNER, A. *ANTARES: etallonnage de l'électronique frontale, étude de muons atmosphériques et recherche de neutrinos cosmiques* (2010).
- [98] LACHARTRE, D. Ars1 analogue ring sampler & ars\_conv users manual version 1.9. ANTARES internal note, ANTARES-ELEC-2000-6.pdf (2000).
- [99] LAMBARD G., ZORNOZA J. D., HERNÁNDEZ-REY J. J. Indirect dark matter search in the sun direction using the data 2007-2008 for the two common theoretical frameworks (cmssm, mued). ANTARES internal note, ANTARES-PHYS-2011-012.pdf (2011).
- [100] LIM, G. M. A. *Searching for Dark Matter with the Antares Neutrino Telescope*. Ph.D. thesis, Amsterdam University (2011).
- [101] LINDER, E. V. Cosmology with X-ray cluster baryons. *JCAP*, **0704**, 004, (2006). [arXiv:astro-ph/0606602](#).
- [102] LUNDMARK, K. The determination of the curvature of space-time in de sitter's world. *MNRAS*, **84**, 747, (1924).
- [103] LYKKEN, J. D. Introduction to supersymmetry. *FERMILAB-PUB-96/445-T*, (1996). [arXiv:hep-th/9612114](#).
- [104] MAMBRINI Y., MUÑOZ C. A comparison between direct and indirect dark matter search. *JCAP*, **0410**, 003, (2004). [arXiv:hep-ph/0407352v2](#).
- [105] MATHER J. ET AL. Calibrator design for the coBE far infrared absolute spectrophotometer (firas). *Astrophys. J.*, **512**, 511, (1999). <http://iopscience.iop.org/0004-637X/512/2/511/>.
- [106] MAYER-HASSELWANDER H. ET AL. High-energy gamma-ray emission from the galactic center. *Astron. Astrophys.*, **335**, 161, (1998). <http://adsabs.harvard.edu/abs/1998A%26A...335..161M>.
- [107] MCNUTT J., CADE A. More  $\mu$ -metal cage studies. ANTARES internal note (1997).
- [108] MELCHIORRI A., MANGANO G. Present bounds on the relativistic energy density in the universe from cosmological observables. *JCAP*, **0703**, 006, (2007). [arXiv:astro-ph/0612150v2](#).
- [109] MOBLEY, C. D. *Light and Water (Radiation Transfer in Natural Water)*. Academic Press (1994).
- [110] MONTARULI T., SOKALSKI I. A. A tau neutrino generator: first results. ANTARES internal note, ANTARES-SOFT-2003-003.pdf (2003).

- [111] NAKAMURA K. ET AL. Particle Data Group. *Journal of Phys.*, **G37**, 075021, (2010).
- [112] NAVARRO J. F. ET AL. The structure of cold dark matter halos. *Astrophys. J.*, **463**, 563, (1996). [arXiv:astro-ph/9508025](https://arxiv.org/abs/astro-ph/9508025).
- [113] NAVAS S., THOMPSON L. KM3 user guide and reference manual. ANTARES internal note, ANTARES-SOFT-1999-011.pdf (1999).
- [114] NEYMAN, J. Outline of a theory of statistical estimation based on the classical theory of probability. *Phil. Trans. R. Soc. Lond.*, **A 236**, 333-380, (1937). <http://rsta.royalsocietypublishing.org/content/236/767/333>.
- [115] OLIVE K. A., PEACOCK J. A. Big-Bang cosmology. *Journal of Phys.*, **G37**, 230, (2010).
- [116] OPPER, R. Ten major challenges in cosmology. *Invited talk at X-th Brazilian School of Cosmology and Gravitation, Rio de Janeiro*, (2003). [arXiv:astro-ph/0304369](https://arxiv.org/abs/astro-ph/0304369).
- [117] PENZIAS A. A., WILSON R. W. A measurement of excess antenna temperature at 4080 Mc/s. *Astrophys. J.*, **142**, 419, (1965). <http://articles.adsabs.harvard.edu/full/1965ApJ...142..419P>.
- [118] POLONSKY, N. Supersymmetry: structure and phenomena. *Lect. Notes Phys.*, **M68**, 1, (2001). [arXiv:hep-ph/0108236v1](https://arxiv.org/abs/hep-ph/0108236v1).
- [119] POVH B. ET AL. *Particelle e nuclei*. Bollati Boringhieri (2002).
- [120] REED, C. Physics and Real (CalReal) release v2r0. ANTARES internal note, ANTARES-SOFT-2008-006.pdf (2008).
- [121] REID D. ET AL. The picture of our Universe: a view from modern cosmology. (2002). [arXiv:astro-ph/0209504](https://arxiv.org/abs/astro-ph/0209504).
- [122] REIN D., SEGHAL L. M. Neutrino excitation of baryon resonances and single pion production. *Ann. of Phys.*, **133**, 79, (1981).
- [123] RHODES W. ET AL. Limits on the flux of very high energy neutrinos with the Fréjus detector. *Astropart. Phys.*, **4:3**, 217, (1996).
- [124] RIES A. G. ET AL. Type Ia supernova discoveries at  $z > 1$  from the Hubble space telescope: evidence or past deceleration on dark energy evolution. *Astrophys. J.*, **607**, 665, (2004). [arXiv:astro-ph/0402512](https://arxiv.org/abs/astro-ph/0402512).
- [125] RYDEN, B. *Introduction to cosmology*. Addison Wesley (2004).
- [126] S. WEINBERG. *The quantum theory of fields. Vol. 3: Supersymmetry*. Cambridge University Press (2000).
- [127] SAHNI, V. Dark matter and dark energy. *Lect. Notes Phys.*, **653**, 141, (2004). [arXiv:astro-ph/0403324](https://arxiv.org/abs/astro-ph/0403324).

- [128] SCHÜSSLER F., PAYET K., VANNONI G. Analysis utilities for AntDST. ANTARES internal note, ANTARES-SOFT-2010-004.pdf (2010).
- [129] SCHÜSSLER F., PAYET K., VANNONI G. AntDST: Data Summary Trees for reconstructed and simulated Antares events. ANTARES internal note, ANTARES-SOFT-2010-003.pdf (2010).
- [130] SCHUTZ, B. F. *A first course in general relativity*. Cambridge University Press, eighteenth edn. (2006).
- [131] SCOTT D., SMOOT G. F. Cosmic microwave background. *Journal of Phys.*, **G37**, 261, (2010).
- [132] SIKIVIE, P. Experimental tests of the "invisible" axion. *Phys. Rev. Lett.*, **52**, 695, (1984). [http://prl.aps.org/pdf/PRL/v52/i8/p695\\_2](http://prl.aps.org/pdf/PRL/v52/i8/p695_2).
- [133] SILK J., OLIVE K., SREDNICKI M. The photino, the sun, and high-energy neutrinos. *Phys. Rev. Lett.*, **55**, 257, (1985). [http://prl.aps.org/pdf/PRL/v55/i2/p257\\_1](http://prl.aps.org/pdf/PRL/v55/i2/p257_1).
- [134] SJOSTRAND T., MRENNNA S., SKANDS P. PYTHIA 6.4 Physics and Manual. *JHEP 0605:026*, (2006). [arXiv:hep-ph/0603175](http://arxiv.org/abs/hep-ph/0603175).
- [135] SLIPHER V. M. Spectrographic observations of nebulae. *Pop. Astr.*, **23**, 21, (1915).
- [136] SUSSKIND, L. The gauge hierarchy problem, technicolor, supersymmetry, and all that. *Phys. Rep.*, **104**, 181, (1984).
- [137] TAOSO M., BERTONE G., MASIERO A. Dark matter candidates: a ten-point test. *JCAP*, **0803**,022, (2008). [arXiv:astro-ph/0711.4996v2](http://arxiv.org/abs/astro-ph/0711.4996v2).
- [138] TEMPEL E., HEKTORA A., RAIDALA M. Fermi 130 GeV gamma-ray excess and dark matter annihilation in sub-haloes and in the Galactic Centre. (2012). [arXiv:astro-ph/1205.1045](http://arxiv.org/abs/astro-ph/1205.1045).
- [139] THE ANTARES COLLABORATION. Antares internal pages. <http://antares.in2p3.fr>.
- [140] THE ANTARES COLLABORATION. *A deep sea telescope for high energy neutrinos* (1999). [arXiv:astro-ph/9907432](http://arxiv.org/abs/astro-ph/9907432).
- [141] THE ANTARES COLLABORATION. *ANTARES physics analysis plan* (2009).
- [142] THORNE K. S., MISNER C. W., WHEELER J. A. *Gravitation*. W. H. Freeman, second edn. (1973).
- [143] TROTTA R., MELCHIORRI A. Indication for primordial anisotropies in the neutrino background from wmap and sdss. *Phys.Rev.Lett.*, **95**, 011305, (2005). [arXiv:astro-ph/0412066v2](http://arxiv.org/abs/astro-ph/0412066v2).
- [144] VAN ALBADA T. S. ET AL. Distribution of dark matter in the spiral galaxy NGC 3198. *Astrophys. J.*, **395**, 305, (1985).

- 
- [145] VERNIN, P. Celestial coordinate systems: definition and conversion algorithms. ANTARES internal note, ANTARES-SOFT-2007-018.pdf (2007).
- [146] WENIGER, C. A Tentative Gamma-Ray Line from Dark Matter Annihilation at the Fermi Large Area Telescope. (2012). [arXiv:astro-ph/1204.2797v2](https://arxiv.org/abs/1204.2797v2).
- [147] WESS J., BAGGER J. *Supersymmetry and Supergravity*. Princeton University Press (1983).
- [148] WEST, P. *Introduction to Supersymmetry and Supergravity*. World Scientific (1986).
- [149] WHITE M., SCOTT D., SILK J. Anisotropies in the cosmic microwave background. *Ann. Rev. Astron. & Astrophys.*, **32**, 329, (1994). <http://ned.ipac.caltech.edu/level5/March02/White/frames.html>.
- [150] ZATSEPIN G. T., KUZ'MIN V. A. Upper limit of the spectrum of Cosmic Rays. *JETP Lett.*, **4**, 78, (1966).

# List of Figures

1.1	Constraints on $\Omega_\Lambda, \Omega_m$ from SNIa measures . . . . .	9
1.2	Constraint on the baryon density from Big Bang Nucleosynthesis . .	11
1.3	CMB temperature anisotropies sky maps observed by COBE and Planck . . . . .	13
1.4	Pie scheme of the energy components of the Universe . . . . .	14
1.5	Observed rotational curve of the galaxy NGC 3198 . . . . .	15
1.6	The merging bullet cluster evidences the presence of dark matter . .	16
1.7	Time evolution of the comoving WIMP number density . . . . .	19
1.8	Mechanism scheme of how WIMPs are trapped into celestial bodies .	24
3.1	Distance over which protons and photons can propagate in the cosmic space as a function of the energy. . . . .	34
3.2	In this image is shown the importance of the neutrino astronomy. Neutrinos are the only particles that can travel over large distances in the Universe without losing the information on the source that they carry on with themselves. . . . .	34
3.3	Zenith angle distribution of the muon flux above 1 $TeV$ for atmospheric muons and atmospheric neutrino induced muons . . . . .	36
3.4	Averaged charged current cross-section for $\nu N$ interactions for different sets of parton distribution functions [140]. The data point correspond to the average of the measurements by H1 and ZEUS at HERA. . .	38
3.5	The effect of the medium molecules polarization when a charged particle pass through the medium with a velocity that exceeds the speed of light in the medium. . . . .	39
3.6	This image show the cone of Cherenkov light induced in the medium.	40
3.7	The angular distribution of light scattering in the deep Mediterranean Sea for $(400 \leq \lambda \leq 500) nm$ [109]. . . . .	41
3.8	The track reconstruction scheme is shown. The arrow indicate the muon's trajectory, $\theta_C$ is the angle under which the Cherenkov photons are emitted, $B$ represents the position of the $i$ th PMT. The reference system is also reported. . . . .	42
3.9	Angular difference between the initial neutrino direction and that of the reconstructed muon track. . . . .	43

3.10	The angular resolution as a function of the neutrino energy. The red solid line represents the angle between the muon track reconstructed and the track generated in the MC simulation. The blue dashed line, instead, represents the angle between the neutrino direction and the one of the produced muon [139]. . . . .	44
3.11	Average range of the muon in standard rock as a function of the initial neutrino energy [140]. . . . .	45
3.12	The location of the ANTARES experiment . . . . .	46
3.13	Scheme of the detector array. The structure of the 12 standard lines and the IL is shown. In the little photo are showed also the storeys. . . . .	47
3.14	Scheme of a detector string with all the principal components shown. The acronyms are presented and described in the text. [140] . . . . .	49
3.15	In the left image is shown the scheme of a storey with the three OMs, in the centre a picture of an OM over a mirror, in the right image the different components of an OM are reported. . . . .	50
3.16	Attenuation length of: Benthos sphere (a), silicone gel (b), sea water (c), quantum efficiency (d) for the Hamamatsu PMT tubes [73]. . . . .	51
3.17	In the figure the two main contribution to the optical noise on the PMT are shown. The constant line represents the contribution of the Potassium decay, while the peak are caused by the sea fauna. . . . .	55
3.18	Sky observable by ANTARES in galactic coordinates. Some high energy sources are reported. The area in the inner of the red curve is always visible, while the grey zone is never seen by the detector. The sources comes from the third EGRET catalogue [55]. . . . .	56
3.19	The muon effective area as a function of the energy. . . . .	57
4.1	The equatorial coordinates system [6]. . . . .	63
4.2	The galactic coordinates system [7]. . . . .	64
4.3	The DATA distributions in four different coordinates systems. Top: local detector coordinates; bottom: horizontal coordinates. . . . .	65
4.4	The DATA distributions in four different coordinates systems. Top: equatorial coordinates; bottom: galactic coordinates. . . . .	66
4.5	The Monte Carlo energy distribution for neutrinos. Our selection choice is shown. . . . .	73
4.6	Comparison of the three parameters which point out the goodness of the fit quality ( $t\chi^2$ , $b\chi^2$ and $M$ ) for a sample selection of runs belonging to the 12 lines period. . . . .	78
4.7	The effects of some types of cuts on the $t\chi^2 = tchi2$ distribution of a 9 period DATA sample. . . . .	80
4.8	The DATA-MC comparison for the $t\chi^2$ parameter. Only events with $t\chi^2 < 5$ are considered. . . . .	85
4.9	The DATA-MC comparison for the $t\chi^2$ parameter. Only events with $t\chi^2 < 1.4$ are considered. . . . .	85
4.10	The DATA-MC comparison for the $b\chi^2$ parameter. Only events with $t\chi^2 < 3$ are considered. . . . .	86
4.11	The DATA-MC comparison for the $b\chi^2$ parameter. Only events with $t\chi^2 < 1.4$ are considered. . . . .	86

4.12	The DATA-MC comparison for the number of used hits in the reconstruction fit. Only events with $t\chi^2 < 5$ are considered. . . . .	87
4.13	The DATA-MC comparison for the number of used lines in the reconstruction fit. Only events with $t\chi^2 < 5$ are considered. . . . .	87
4.14	The DATA-MC comparison for the $\cos(\text{zenith})$ parameter. Only events with $t\chi^2 < 3$ are considered. . . . .	88
4.15	The DATA-MC comparison for the $\cos(\text{zenith})$ parameter. Only events with $t\chi^2 < 1.4$ are considered. . . . .	88
4.16	The angular resolution for an example set of neutrino MC events. . .	89
4.17	The effective area for neutrino MC events of line 9 configuration. . .	90
4.18	The neutrino spectra for the WIMP mass of 50 GeV and the two available annihilation channels: $b\bar{b}$ and $\tau^+\tau^-$ . . . . .	94
4.19	The neutrino spectra for the WIMP mass of 200 GeV and the three available annihilation channels: $b\bar{b}$ , $\tau^+\tau^-$ and $W^+W^-$ . . . . .	94
4.20	The neutrino spectra for the WIMP mass of 500 GeV and the three available annihilation channels: $b\bar{b}$ , $\tau^+\tau^-$ and $W^+W^-$ . . . . .	95
4.21	The neutrino spectra for the WIMP mass of 1 TeV and the three available annihilation channels: $b\bar{b}$ , $\tau^+\tau^-$ and $W^+W^-$ . . . . .	95
4.22	The stripe of signal around the Galactic Centre motion in the horizontal coordinates (A,z). Only for the anti-neutrino signal events. . .	98
4.23	The plot show the effect of the $t\chi^2 < b\chi^2$ cut. The black point represents DATA events, the red point the muon events, the green points the background neutrino events and the blue points the signal neutrino events. . . . .	99
4.24	The distributions of the different types of particles: DATA, MC muons, MC background neutrinos and MC signal neutrino. . . . .	100
4.25	The Galactic Centre visibility in the horizontal system (A,h). . . . .	101
4.26	The trajectory of the GC plotted over the distribution of the up-going neutrino events in the horizontal coordinate system space (A,z). . . . .	102
4.27	The distribution of DATA and MC events as a function of the half-cone angle for the whole data set. A $t\chi^2 < 3$ cut was applied. The agreement, as already noticed, is not sufficient for larger values of $t\chi^2$ . . . . .	104
4.28	The distribution of DATA and MC events as a function of the half-cone angle for the whole data set. A $t\chi^2 < 1.4$ cut was applied. . . . .	104
4.29	The behaviour of $\bar{\mu}_{90}$ as a function of the half-cone angle for different values of $t\chi^2$ . . . . .	107
4.30	The different distributions of $\bar{\mu}_{90}$ , $b$ and $n_s$ as a function of the half-cone angle . . . . .	108
4.31	The MRF distribution in the $t\chi^2$ -half-cone angle parameter space for a Dark Matter composed by WIMP with mass = 500 GeV and for the hard annihilation channel $W^+W^-$ . . . . .	109
4.32	The sensitivity (in $cm^{-2}s^{-1}$ ) of the ANTARES detector as a function of the WIMP mass for the three different annihilation channels chosen. . . . .	111
4.33	The sensitivity (in $km^{-1}yr^{-1}$ ) of the ANTARES detector as a function of the WIMP mass for the three different annihilation channels chosen. . . . .	111
A.1	Confidence belt construction and its use [66]. . . . .	116

A.2	Ratio between Gauss and Poisson distributions. . . . .	119
A.3	Relative difference between Poisson and Gauss distributions. . . . .	119
A.4	Here an example for the average upper limit $\bar{\mu}_{90}$ as a function of the background $b$ . The black curve represents the Poisson distribution, the red one the Gauss distribution. The green curve show the behaviour of the mixed regime: Poissonian until $b = 10$ and Gaussian up to the end. In the thesis we chose a value $b = 24$ . . . . .	120
A.5	The trend of $\bar{\mu}_{90}$ as a function of the background. . . . .	120
B.1	The ARS circuit scheme [10]. . . . .	124
B.2	ARS structure and working principle [10]. . . . .	125
B.3	The TVC working scheme [97]. . . . .	126
B.4	The working method of the integrator when a signal pass the L0 threshold [97]. . . . .	127
B.5	The integration by parts of the charge signal [97]. . . . .	127
B.6	Cross-Talk: origin and effect. In the left figure is represented the pipeline scheme at the origin of the cross-talk effect between time (TVC) and charge (AVC). The effect is represented in the right figure in which the trend of the AVC as a function of the time is shown [97].	128
B.7	An example of the fit to correct the cross-talk effect (bottom right) together with the measure of the 1pe peak (bottom left). . . . .	129
B.8	The distribution of the CalibOK parameters occurrences . . . . .	131
B.9	The percentage of occurrence of the calibOK new flags. . . . .	132
B.10	The distribution of the calibOK values as a function of the selected version_ids. . . . .	132
B.11	The distribution of the missing ARS of the apparatus. . . . .	133
B.12	The distribution of the cross-talk parameters TVC_MEAN and XT_SLOPE.	134
B.13	The distribution of the differences of the cross-talk parameters TVC_MEAN and XT_SLOPE. . . . .	135
B.14	The distribution of the cross-talk parameters for the version_id = 59186564. In the upper left plot the XT_SLOPE distribution, in the upper right the TVC_MEAN, in the bottom left the $\chi^2$ and in the bottom right the calibOK. . . . .	136
B.15	The distribution of the relative difference of the cross-talk parameters for the version_id = 59186564. In the left plot the XT_SLOPE distribution, in the central plot the TVC_MEAN, in the right plot the $\chi^2$ . . . . .	137
B.16	The 3 relative differences between the 4 version_ids. In the left column the XT_SLOPE difference distribution, in the central column TVC_MEAN, in the right column the $\chi^2$ distribution. . . . .	137
B.17	The ARS counts distribution. . . . .	138
B.18	The mean distributions of the cross-talk parameters (XT_SLOPE, TVC_MEAN, $\chi^2$ respectively). . . . .	138
B.19	The correlation between the ARS and the $\chi^2$ . . . . .	138
B.20	The correlation profile for the quantity $(ARS_i - \langle ARS \rangle) / \langle ARS \rangle$ , with (top) and without (bottom) absolute value, and the $\chi^2$ . The errors are of the standard type $\sigma/\sqrt{n}$ for each bin of the histogram. . . . .	139

---

B.21 The relative difference between the four version_ids for the XT_SLOPE parameter. . . . .	140
B.22 The distributions of the XT_SLOPE parameter with the ARS weight.	141



# List of Tables

2.1	Standard model particles and their super-partners [61]. . . . .	28
4.1	The different configurations in lines of the apparatus with their durations for the data sample used in this analysis. . . . .	67
4.2	Total number of runs for each configuration period. Only runs with DQ used . . . . .	69
4.3	Comparison of the data lifetimes before and after the Data Quality selection. . . . .	70
4.4	Standard MC runs for each configuration period. Only runs with DQ used . . . . .	73
4.5	Low energy MC runs for each configuration period. Only runs with DQ used . . . . .	74
4.6	Selected events for each detector line configuration, event and particle type. . . . .	81
4.7	Oscillation parameters considered in the WIMPSIM B scenario [60] . .	91
4.8	Optimization values. . . . .	110
A.1	Upper limits for a required 90% C.L. as a function of the background $b$ . The first column represent the background, the second the average upper limit, the third the number of steps necessary for convergence and the last the C.L. probability reached at the moment of the convergence. As can be seen a lot of upper limits are conservative. .	121
B.1	The first block of the 19 selected version_id. The first column represent the version_id number. In the second column the version_id number identifiers are reported, while in the third column there are the correspondent dates. . . . .	130
B.2	The new 4 selected version_id. The first column represent the version_id number. In the second column the version_id number identifiers, in the third column there are the correspondent dates and in the fourth the correspondent number of working ARS. . . . .	136